Residual dipolar couplings: a complementary tool for stereochemistry determination of drug compounds

Zur Erlangung des akademischen Grades einer

DOKTORIN DER NATURWISSENSCHAFTEN

(Dr. rer. nat)

von der KIT-Fakultät für Chemie und Biowissenschaften

des Karlsruher Instituts für Technologie (KIT)

genehmigte

DISSERTATION

von

Dipl.-Chem. Emine Sağer
aus Langres – Frankreich

1. Referent: Prof. Dr. Bukhard Luy
2. Referent: Prof. Dr. Joachim Podlech

Tag der mündlichen Prüfüng: 7. Februar 2019

To my beloved niece, Defne Özgören,

Uğurlu meleğim Defne Özgören'e,

Ağacın dalında oturan kuşun, “dal kırılacak” diye bir endişesi olmaz.
Çünkü inanıp güvendiği dal değil kanatlarıdır. (Unknown)

A bird sitting on a tree is never afraid of the branch breaking, because
its trust is not on the branch but on its own wings. (Unknown)

***F-E-A-R** has two meanings:*
***F**orget **E**verything **A**nd **R**un or **F**ace **E**verything **A**nd **R**ise.*
The choice is yours. (Unknown)

Ich versichere wahrheitsgemäß, die Arbeit selbstständig angefertigt, alle benutzten Hilfsmittel vollständig und genau angegeben und alles kenntlich gemacht zu haben, was aus Arbeiten anderer unverändert oder mit Änderungen entnommen wurde. Weiterhin versichere ich, dass der Inhalt dieser Arbeit bis auf die unten angegebenen Teilpublikationen noch nicht veröffentlicht wurde und dass ich eine solche Veröffentlichung nicht vor Abschluss des Promotionsverfahrens vornehmen werde.

Karlsruhe, 07.01.2019

....

(Dipl.-Chem. Emine Sağer)

List of Publications

Lewis, I., Schaefer, M., Wagner, T., Oberer, T., Sager, E., Wipfli, P. and Vorherr, T., *A Detailed Investigation on Conformation, Permeability and PK Properties of Two Related Cyclohexapeptides.* Int J Pept Res Ther, 2015. 21(2): p. 205-221.

The topic covered in this publication is not part of the following PhD-thesis.

Abstract

NMR spectroscopy is one of the most powerful technique employed in chemistry and structural biology to characterize molecular properties such as the constitution, configuration and conformation of organic compounds and their interaction with drug targets. High-resolution standard NMR parameters such as chemical shift, ^{3}J couplings and NOEs allow the structural elucidation of the majority of samples in isotropic solution. To study samples for which structural determination is not possible with these standard approaches, utilization of complementary parameters such as residual dipolar couplings (RDCs) is considered an attractive option.

Anisotropic parameters are measurable only with the introduction of alignment. Therefore, the use of specific equipment such as adjustable stretching devices is necessary to generate strained gels, which are providing a tuneable anisotropic environment. For efficient assessment of small amounts of sample, a new 3 mm stretching device has been developed based on the design of the existing 5 mm stretching device and is described in this thesis. In addition, a swelling device has been built to control the swelling of a gel for NMR experiments. The new stretching device has been tested and shows encouraging results regarding the ability to adjust the degree of alignment to the right strength and for the determination of anisotropic parameters with high accuracy.

Since residual dipolar couplings depend on the distance and orientation between atoms, they can be used for structure elucidation of molecules with several stereocenters. In this thesis, making use of RDCs, the relative configurations of multiple natural products with several stereocenters have been successfully demonstrated including the determination of the relative stereochemistry of tertiary amines. In this context, next to standard static fitting procedures, also molecular dynamics simulations with tensorial orientational constraint were used to identify the correct configurations.

Finally, the indispensable determination of the absolute configuration has been attempted. The conventional method of choice is X-ray crystallography with its limitations like the necessity of obtaining a crystal and unpredictable timelines. Further method development for studying the absolute configuration of molecules is needed to overcome these limitations. By measuring RDCs of several enantiomeric pairs, a new method to determine the absolute configuration of molecules was investigated and preliminary promising data is presented.

Zusammenfassung

NMR-Spektroskopie gehört zu den etabliertesten und leistungsfähigsten Methoden in Chemie und Strukturbiologie, und die Kenntnis der Konstitution, Konfiguration und oft auch der Konformation von Molekülen ist von zentraler Bedeutung für die Entdeckung neuer Wirkstoffe. NMR-Standardparameter wie chemische Verschiebung, ^3J-Kopplungskonstanten und NOEs erlauben es, die Mehrzahl der organischen Moleküle strukturell aufzuklären. Verbindungen, die sich einer Strukturaufklärung mit Hilfe dieser Parameter entziehen, lassen sich oft durch Heranziehen komplementärer Parameter wie dipolarer Restkopplungen (RDCs) analysieren.

Für die Messung von anisotropen NMR-Parametern werden Orientierungsmedien verwendet wie zum Beispiel mechanisch gespannte Gele, die Anisotropie in der Lösung induzieren. Darüber hinaus sind zur Anpassung der Anisotropie Dehnungsvorrichtungen hilfreich. Für effiziente Messungen von kleinen Probenmengen wurde in dieser Arbeit eine neue Apparatur entwickelt: ausgehend von der vorhandenen 5mm-Dehnungsvorrichtung wurde die Entwicklung einer 3 mm-Dehnungsvorrichtung durchgeführt. Um ebenfalls den Quellschritt des Gels steuern zu können, wurde eine neuartige Quellvorrichtung geschaffen. Die neue Dehnungsvorrichtung wurde in der Praxis getestet und zeigt ermutigende Ergebnisse für die Anpassung der Anisotropie an die passende Stärke. Darüber hinaus wurden Messungen von anisotroper Parametern mit hoher Genauigkeit erreicht.

RDCs liefern wertvolle globale-Informationen, zum Beispiel über die Orientierung internuklearer Vektoren innerhalb eines Moleküls. Mit Hilfe von RDCs wurden in der vorliegenden Arbeit die relativen Konfigurationen von Naturstoffen mit mehreren Stereozentren bestimmt, einschließlich der relativen Konfigurationen von tertiären Aminen. Zur Bestimmung der Konfigurationen wurden neben Standardmethoden auch molekular-dynamische Simulationen durchgeführt, in denen experimentelle RDCs als orientierende, tensorielle Randbedingungen verwendet wurden.

Die Bestimmung von absoluten Konfigurationen eines Moleküls ist unverzichtbar in der Arzneimittelforschung. Die wichtigste Methode hierzu ist die Röntgenstrukturanalyse, deren Anwendung jedoch durch die Verfügbarkeit eines hochwertigen Kristalls und dem oft hohen Zeitaufwand limitiert ist. Die Entwicklung von weiteren Methoden zur Aufklärung der Stereochemie ist aus diesem Grund ein aktives Forschungsfeld. In dieser Arbeit werden hierzu vorläufige, vielversprechende Daten zur Bestimmung der absoluten Konfiguration von Enantimerenpaare mit Hilfe von RDCs in chiralen Orientierungsmedien präsentiert.

Table of Contents

List of Publications I

Abstract..I

Zusammenfassung...III

Table of Contents V

1. Introduction.. 1

1.1. Commonly used techniques for structure elucidation 1

1.2. Molecular composition...3

1.3. Molecular constitution..3

1.4. Molecular configuration 4

1.5. Molecular conformation 7

1.6. Scope of the work...8

1.7. Outline of the thesis..9

2. Theoretical background and methodology 11

2.1. Theory 11

  2.1.1. Dipolar Coupling 12

  2.1.2. Liquid crystals 19

  2.1.3. Stretched gels for alignment 20

2.2. Experimental section 21

  2.2.1. Deuterium experiment 21

  2.2.2. Adjustment of the alignment 23

    2.2.2.1. Modification of the gel..23

    2.2.2.2. Variable Angle Sample Spinning...24

    2.2.2.3. Gel Apparatus 26

  2.2.3. NMR measurements to obtain the experimental RDCs 29

  2.2.4. The interpretation of anisotropic parameters 35

    2.2.4.1. Fitting experimental RDCs using Singular Value Decomposition.....................35

    2.2.4.2. Molecular dynamics with orientational tensorial constraints 37

3. Materials and methods 39

3.1. Equipment 39

3.2. Software 40

3.3. NMR Method 40

4. 3 mm stretching and swelling devices 43

4.1. Design of the 3 mm stretching device 43

  4.1.1. Properties of the silicone rubber tube 43

4.1.2. Properties of the Teflon plug 45
4.1.3. The Teflon lock 45
4.2. Evaluation of the 3 mm stretching device 46
4.2.1. Molecule 46
4.2.2. Alignment medium 47
4.2.3. Experimental part 48
4.2.3.1. Sample preparation 48
4.2.3.2. NMR experiments 48
4.3. The swelling device 54
4.4. Conclusion 55

5. Relative configuration determination of natural products 57
5.1. Stereochemistry determination of Selfotel 60
5.2. Experimental data for the Reserpine derivatives 64
5.2.1. Sample preparation 64
5.2.2. NMR measurements 65
5.2.2.1. NMR Spectra for assignment in the isotropic phase 65
5.2.2.2. NMR spectra for RDC measurements 65
5.2.3. Generation of 32 possible configurations 67
5.3. Relative stereochemistry determination of RD-1 68
5.3.1. Single conformer single alignment tensor SVD approach 68
5.3.2. Multiple conformers single alignment tensor SVD approach 70
5.3.3. Molecular dynamic simulation with orientational constraints (MDOC) 72
5.3.4. X-ray Data 77
5.4. Determination of the relative stereochemistry of RD-2 78
5.4.1. Single conformer single alignment tensor SVD approach 78
5.4.2. Multiple conformers single alignment tensor SVD approach 80
5.4.3. Molecular dynamic simulation with orientational constraints (MDOC) 81
5.4.3.1. MDOC with ${}^{1}D_{\mathrm{CH}}$ constraints 81
5.4.3.2. MDOC with ${}^{1}D_{\mathrm{CH}}$ and ${}^{3}J_{\mathrm{HH}}$ constraints 82
5.4.3.3. MDOC with ${}^{1}D_{\mathrm{CH}}$, ${}^{3}J_{\mathrm{HH}}$ and distance constraints 85
5.5. Discussion 88
5.6. Conclusion 93

6. Absolute configuration determination of small chiral compounds 95
6.1. Existing methods for absolute configuration determination 95
6.1.1. Chemical synthetic methods 95
6.1.2. Anomalous X-ray diffraction 96

6.1.3. Chiroptical spectroscopy 96
6.1.4. Chromatographic methods 97
6.1.5. NMR based methods 97
6.2. Experimental methods 99
6.2.1. Alignment medium 99
6.2.2. Enantiomeric molecules studied 99
6.2.3. Sample preparation 101
6.2.4. NMR measurement 103
6.3. Alignment tensors of the enantiomeric pairs 109
6.4. Molecular Dynamics (MD) simulation methods 111
6.4.1. Molecular dynamics simulation of HMIP in *vacuo* 111
6.4.2. Molecular dynamics simulations with explicit co-solvent 115
6.5. Discussion 119
6.6. Variable angle sample spinning NMR in PBLG 122
6.7. Conclusion 126

7. Summary and outlook 129

8. Bibliography 133

9. Appendix 143

9.1. List of Figures 143
9.2. List of Tables 147
9.3. List of Abbreviations and Symbols 149
9.4. Appendix 155
9.4.1. Isotropic NMR spectra of Selfotel 155
9.4.2. Anisotropic NMR spectra of Selfotel. 159
9.4.3. NMR spectra of RD-1 and RD-2 160
9.4.4. MSpin and COSMOS results for all configurations of RD-1 163
9.4.5. MSpin and COSMOS results for all configurations of RD-2 165
9.4.6. Isotropic NMR spectra of HMIP with assignments 169
9.4.7. Isotropic NMR spectra of POMT with assignments 170
9.4.8. Isotropic NMR spectra of borneol with assignments 171
9.4.9. Isotropic NMR spectra of camphor with assignments 172
9.4.10. Isotropic NMR spectra of quinuclidinol with assignments 173

Acknowledgements 175

1. Introduction

The complete description of the chemical structure of organic molecules including the characterization of the three-dimensional structure is essential in drug discovery. Without complete structural characterization, no relevant new drug could become available on the pharmaceutical market. Indeed, the guidelines to follow for the submission of a new drug according to the Food and Drug Administration (FDA) are strict and detailed concerning the description of the structure of the new molecular entity [1]. The information to be submitted to the authorities ensure continued highest drug substance and drug product quality regarding identity, quality, purity and potency. Different information such as the name according to the IUPAC nomenclature, the structure, general drug substance properties, structural characterization and stability have to be included according to precise requirements. To be included on regulatory documents, the composition, constitution, configuration and conformation of those molecules need to be defined.

1.1. Commonly used techniques for structure elucidation

There are several techniques used for structure elucidation, with the most commonly used ones briefly described in this paragraph. As some are more preferred than others due their efficiency and practicality, advantages and limitations are discussed.

Mass spectrometry (MS) and the more accurate version high-resolution mass spectroscopy (HR-MS) allow the determination of the elementary composition of the molecule. This technique provides the exact mass, more precisely the mass number divided by the charge number of the fragment (m/z), which is used to determine the chemical sum formula of the compound. Other MS techniques are able to determine fragments of a molecule. The fragmentation of a molecule causes characteristic pattern in the mass spectrum used to derive structural information of the molecule. Thus, the elementary composition of the molecule can be determined but more details are needed and for that other complementary techniques are used such as optical spectroscopy (OS).

Infrared spectroscopy (IR), Raman spectroscopy and UV-VIS spectroscopy are used to study how atoms and bonds interact with light. The energy at which any peak in an absorption spectrum appears corresponds to the frequency of a vibration or an electronic transition of a part of the molecule. Each band is caused by the absorbed energy from that particular frequency of IR radiation to excite bonds in the molecule to a higher state of vibration – either stretching or bending.

IR is a reliable technique and is also used in quality control providing information such as the functional groups present in the structure. In addition, IR spectroscopy provides a fingerprint of the sample which can be used to identify the molecular family or even entire organic molecules in case the IR spectrum already exists in the IR database. Ultraviolet-visible (UV-Vis) spectroscopy is useful for the quantitative analysis of samples. UV-Vis spectroscopy allows to obtain qualitative information about the type of the bonds in the sample but also to determine the concentration of the molecule absorbing in the corresponding spectral range. It is a non-destructive and a fast technique. In summary, optical spectroscopy provides information, such as the presence of functional groups in the structure.

Since sample purity is an important parameter directly influencing the accuracy of these different techniques, high performance liquid chromatography (HPLC) is used for the molecular characterization by determining the purity of the sample. HPLC is a technique used for the purification and separation of the different molecules in a mixture and the quantification of the molecules. An HPLC system is composed of a pump to pass a pressurized liquid solvent containing the sample mixture through a column filled with a solid adsorbent material. As different molecules interact differently with the stationary phase, the molecules are eluted at different times leading to their separation. This *so-called* retention time provides information about the molecule, for example, whether the molecule is polar or apolar.

Nuclear magnetic resonance (NMR) spectroscopy is complementary to the previously described techniques. The fragments determined by MS and the functional groups determined by OS can be connected to each other via NMR spectra. This allows to precisely determine the complete two dimensional structure, which includes constitution and configuration, but not the conformation of the molecule. Another advantage of NMR is the ability to acquire through space correlations, allowing the determination of the 3D structure. Therefore, NMR spectroscopy is the only method providing atomic resolution in solution.

Last but not least, X-ray crystallography provides all information previously described. Indeed, a small molecule X-ray structure contains a complete description of the molecular structure, each atom and bond, as well as the conformation in solid phase and in a particular environment. It is a very robust technique, but the accessibility of X-ray equipment is often limited and the application is restricted because of the need of a crystal.

Very recently, Jones *et al.* showed that a Cryo electron microscopy method called MicroED allows to unambiguously identify small molecules [2, 3]. This technique uses electron diffraction to obtain structural information from simple powders without a special and time consuming sample preparation and was developed first for structure determination of biomolecules [4, 5]. Data are collected as the X-ray diffraction method and then backwards prediction works is performed to figure out the structures from the diffracted data. This emerging technique shows great potential but it is still in development state. Further investigations and optimizations are required before a more widespread use by a greater scientific community can be realized.

In conclusion, in order to elucidate a structure, the combination of the techniques cited before is essential. In practice, the choice of methods being applied also depends on the instrumentation availability and the nature of the data needed such as the composition, the constitution, the configuration and or the conformation.

1.2. Molecular composition

There are different ways to represent a molecule by name, empiric formula, molecular formula and/or structural formula. The empiric formula provides the ratio of the elements in the molecule while the molecular formula provides the exact amount of each elements which constitute the molecule. The structural formula allows showing how these elements are structured, that means in addition the different bonds allowing to attach each elements is given, that represents the molecular constitution and configuration.

1.3. Molecular constitution

The constitution of a molecule is defined by its atomic composition and the connecting bonds, which together describe the 2D structure.

The choice of the techniques needed for the determination of the constitution depends on the complexity of the molecule and the number of different 2D arrangements that can be obtained with the same atomic composition. Compounds with the same molecular formula with different constitution are called isomers. For example, if the difference between two molecules with the same chemical formula is just the position of a methyl group as shown in **Figure 1**, they are called regioisomers. These two molecules have the same elementary composition, but different functional groups. Their monoisotopic mass is 109.05 Da as determined by HR-MS. IR and NMR methods yield the correct determination of the position of the methyl (8) group. Molecule **A** contains a tertiary amide while the molecule **B** an ether. Hence, these two molecules will have different physicochemical properties and bioactivity.

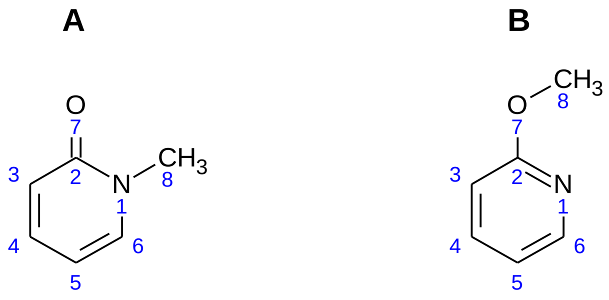

Figure 1: Chemical structures of two regioisomers with the chemical formula C_6H_7NO.

1.4. Molecular configuration

In addition, the atoms of a given molecule display a specific spatial arrangement, which constitutes the stereochemistry of a molecule and is called configuration. The configuration plays an essential role in the interaction of a compound with biomolecules like enzymes, structural proteins and antibodies. The bioactivity depends on the strength and the localization of the interaction with the biomolecule which is the reason why the determination of the configuration is an important step in drug discovery. Molecules with the same constitution but different configurations are called stereoisomers, which comprise both enantiomers and diastereoisomers. Enantiomers are molecules having the same constitution and identical internal dimensions but they are mirror images and non-superimposable. Diastereoisomers have different internal dimensions defined by the distances between non-bonded atoms and dihedrals angles. These stereoisomers are defined by the relative or the absolute configuration. Relative configuration refers to the configuration of a molecule in relation to other atoms on the same molecule, in relation to other molecules or in relation to another form of the same molecule. The most important types of relative configurations are: *E* (*Entgegen*) and *Z* (*Zusammen*) used for the description of double bonds (row **A** on the **Figure 2**), *D* (*Dextrorotatory*) and *L* (*Levorotatory*) used for the description of carbohydrates and amino acid (row **B** on the **Figure 2**), and *cis*- and *trans*- used for non-planar molecules having two faces such as cyclohexane or cyclopentane (row **C** on the **Figure 2**). Furthermore, rarely appearing types of configuration are planar chirality as *e.g.* found in paracyclophanes (row **D** on the **Figure 2**) as the aromatic rings are not free to rotate and the molecules consequently contain no plane of symmetry [6]. In helical arrangements as for example found in helicenes (row **E** on the **Figure 2**), there is an axial dissymmetry and hence this type of molecule are also enantiomers. The absolute configuration provides the precise spatial position of atoms or groups around a stereocenter as determined by the Cahn-Ingold-Prelog rules and is designated as *R*- (*Rectus*) or *S*- (*Sinister*) (Row **F** on the **Figure 2**). Diastereoisomers have different physicochemical properties and different bioactivities whereas on the contrary, enantiomers have the same physicochemical properties except the interaction with an achiral environment or polarized light. As biological molecules are mostly chiral, it is essential to correctly identify and distinguish enantiomers and diastereoisomers. A famous and at the same time tragic example showing different bioactivity of two enantiomers is the molecule thalidomide [7] (Row **G** on the **Figure 2**). During the 1950s and 1960s, the drug thalidomide was used against nausea, especially for pregnant women; however, it was discovered that it caused severe birth malformations and even the death of the embryo. This molecule contains an acidic chiral hydrogen which can racemize in the order of several minutes which results in the presence of both enantiomers during the residence time of the drug in the body. While the two stereoisomers have the same physicochemical properties, the bioactivities remarkably differ. *S*-thalidomide has the desired bioactivity of reducing nausea, *R*-thalidomide causes the birth malformations. This tragic case led to the development of stricter regulations and controls before the launch of a drug on the market. Indeed, nowadays every possible enantiomer has to be prepared in pure form. Each stereocenter has to be known and the quantitative isomeric composition of the material used in pharmacological, toxicological, and clinical studies known. As enantiomers have identical physicochemical properties, it is not always easy to analyse them.

A	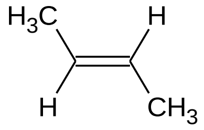 (2*E*)-but-2-ene	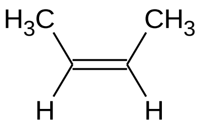 (2*Z*)-but-2-ene
B	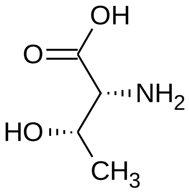 *D*-threonine	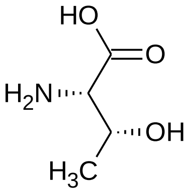 *L*-threonine
C	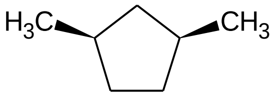 (1*R*,3*S*)-1,3-dimethylcyclopentane *cis*-1,3-dimethylcyclopentane	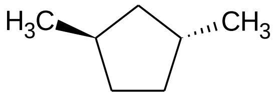 (1*R*,3*R*)-1,3-dimethylcyclopentane *trans*-1,3-dimethylcyclopentane
D	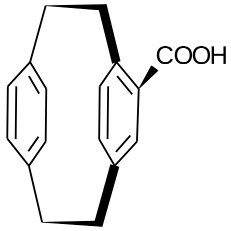 [2.2]paracyclophanecarboxylic acid	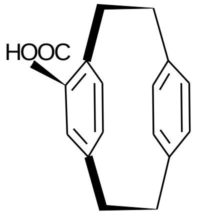 [2.2]paracyclophanecarboxylic acid
E	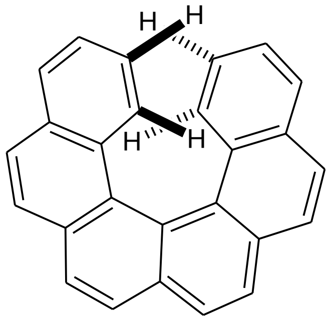 *S_h*-hexahelicene	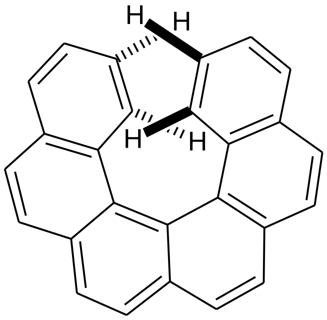 *R_h*-hexahelicene
F	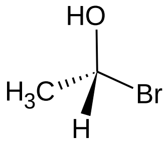 (1*S*)-1-bromoethanol	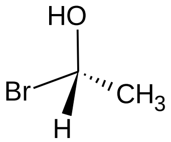 (1*R*)-1-bromoethanol
G	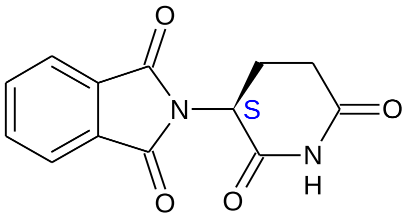 *S*-thalidomide	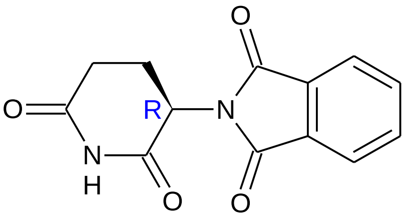 *R*-thalidomide

Figure 2: Example of stereoisomers.
Molecules in rows **A** and **C** represent diasteroisomers and rows **B**, **D**, **E**, **F** and **G** contain enantiomers.

1.5. Molecular conformation

Moreover, a molecule having the same constitution and configuration can have different conformations, *i.e.* different temporary spatial arrangements resulting from rotation of its constituent group of atoms around single bonds overcoming a rotational energy barrier. This rotational energy barrier is influenced by the substituent attached to the bond. There are different dynamic conformational changes with more or less high energy barriers. An amide bond, for example, has two main conformations, a (*Z*)- and a (*E*)- conformation with a rotation barrier in the range of 15-23 kcal/mol in the gas phase and in solution attesting the restriction of the amide bond rotation (**Figure 3**) [8]. The example also shows a difficulty in distinguishing conformation from configuration, as even two conformations might be separable under favourable conditions. However, conformational differences are usually characterized as different 3D structures that can be transformed into each other without breaking a bond.

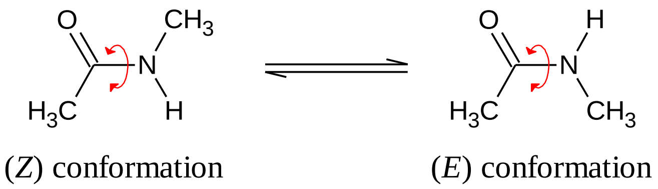

Figure 3: Example of conformers.

Other prominent moieties adopting different conformations are aliphatic rings. For example, cyclohexane can adopt multiple well-known conformations, namely chair, half-chair, boat and twist-boat. In solution, mainly the chair and boat conformations are being populated and the molecule can go through these different shapes easily as the rotational barrier in the range of 5-10 kcal/mol. Small molecules can be very flexible and once substituted with different functional groups and other moieties, they are able to contribute to a big set of different conformations. That is why a more complex molecule coming from the association of these different groups can adopt different conformations in solution and as a consequence can have different, time dependent 3D arrangements, *e.g.* U-shape, a linear conformation, or more complex conformations. As the spatial arrangement has an important role in the binding process of the drug-like molecules to the target, the determination of the molecular conformation in solution is an important step in drug discovery.

1.6. Scope of the work

As described above, the 3D structure plays a critical role in drug development, as the compound shape as well spatial arrangement and presentation of functional groups in solution are essential features towards its bioactivity. 3D structures can be obtained via X-ray crystallography and NMR spectroscopy which are complementary methods. For X-ray crystallography, obtaining a crystal of a molecule is essential; however, this is not always achievable. In addition, the X-ray technique yields the 3D conformation and configuration of the molecule in solid phase. The conformation strongly depends on the crystallization conditions, the particular solvent as well as the temperature. This can lead to a situation where the determined X-Ray structure is different from the state in aqueous buffer solution in which the bioactivity is usually tested. In addition, crystal structures are affected by inter-molecular packing, which may lock the structure into a particular conformation of the molecule, whereas in solution, the molecule can adopt the conformations which are populated according to their energy levels and the Boltzmann distribution. The biggest advantage of NMR spectroscopy is that it offers the characterization of the molecules in solution state and the easier accessibility of NMR spectrometers makes it also more commonly used than X-ray diffraction.

Classical structure elucidation by NMR is based on the determination of short proton-proton distances by acquiring nuclear Overhauser enhancement (NOE) experiments and measuring scalar coupling constants (*J*) between NMR active nuclei, which provide information on the rotation of a bond connecting the atoms. Although this approach can be employed to solve the structure of a vast number of molecules, using NOEs and coupling constants is sometimes not sufficient to resolve ambiguities in the structure, such as the stereochemistry or the conformation of the molecule in solution. This is because both $^3J_{HH}$ couplings and NOEs provide only short range information since atoms connected by dihedral angles comprised of three covalent bonds can only be approximately 4 Å apart and NOEs can be only observed in a sphere of 5 Å. If these short range correlations do not form a continuous network, for example because a linker between two parts of molecule does not possess NMR active nuclei, classical NMR approaches may fail in the determination of configuration and conformation. Therefore, it becomes necessary to use other NMR parameters which provide long range information.

Dipolar couplings are such parameters, as they provide long range angular information relative to the static magnetic field, thus allowing correlations of distant parts in a molecule. However, this parameter is only obtainable in the solid state since in the liquid state dipolar couplings are averaged to zero due to the fast rotation of the molecule. This limitation can be overcome by measuring *so-called* Residual Dipolar Couplings (RDCs), which represent an anisotropic parameter measurable in an intermediate state between liquids and solids. RDCs provide spatial correlations between different parts of a molecule that are not in close proximity and therefore can substantially enable the three-dimensional structure determination of molecules which cannot be elucidated by standard NMR spectroscopy or X-Ray crystallography. This thesis explores the incorporation as RDCs as structural parameters as an alternative method to standard NMR spectroscopy or X-Ray crystallography in case these techniques are inconclusive.

1.7. Outline of the thesis

Traditionally, RDC measurements were mostly used for the refinement of 3D structures of large biomolecules [9]. For example, RDCs of the amide N-H bond are frequently acquired on ^{15}N enriched protein samples. However, in order to apply these techniques to small organic molecules, the existing techniques and devices need to be adapted. Since organic molecules are rarely isotopically enriched and the RDCs of at least one bond CH couplings are required for structure characterization, the concentration of the sample has to be increased in order to record ^{1}H, ^{13}C correlation spectra with high enough signal to noise. This is easily achieved for soluble compounds available in large quantities. However, in drug discovery, solubility and quantity of substance available are often limiting factors which is why the improvement of several existing techniques has been required in order to apply them in the field of small molecule drug discovery.

In the first part of this thesis, the theoretical background, the experimental approach and the software used working with RDCs are explained and summarized.

Next, the development of a miniaturized device for measuring RDCs in stretched alignment medium is described and the initial results obtained with this device are presented. As in drug discovery often a quantity limitation is encountered, a miniaturization of the device is an important step toward the implementation of RDC based techniques in drug related analytics. In addition, a new swelling device is described, followed by a discussion on the advantages and limitations of the novel devices.

Subsequently, the determination of the relative configuration of complex natural products with the use of RDCs is discussed. The studied natural products are partially flexible and contain several stereocenters including a tertiary amine. In order to identify the correct relative configuration, the use of experimental RDC data as orientational constraints in molecular dynamics simulations is explored and explained in detail. The different steps of the methodology from data acquisition and processing to computational analysis are also described.

In the last part, a new method to determine the absolute configuration of chiral molecules is investigated. The majority of the natural products and synthesized drugs have chiral stereocenters [10]. Thus, as illustrated previously on the thalidomide example, it is of high importance to develop a method for determination of the absolute configuration. Different existing methods to determine absolute stereochemistry, such as X-ray diffraction, vibrational circular dichroism (VCD) [11], Mosher ester analysis by NMR [12], and chromatographic methods are discussed. Nevertheless, due to their specific limitations, further method development is required for the determination of the absolute stereochemistry. Enantiomers have already been distinguished by RDCs by performing alignment in a chiral medium [13], but the determination of absolute chirality has not been reached until today. The greatest limitations are presently the available computational models, and the inherent complexity of the solute alignment, as well as the fact that such a prediction of the chiral alignment has not been published to date. Ten pairs of enantiomers were measured as first step to attempt to determine their absolute configurations. Two different molecular dynamics (MD) methods towards obtaining the theoretical RDCs were tested and evaluated.

2. Theoretical background and methodology

The determination of the 3D configuration and conformation is an important area of research and various techniques such as NMR, X-ray and modelling are used in the field. In NMR, the standard parameters such as chemical shift, $^3J_{HH}$ couplings and NOEs provide classical information about the constitution, relative configuration and conformation of a molecule. Chemical shift is the primary parameter in NMR spectroscopy for atomic characterization of the molecule. It describes the resonance frequency of a nucleus relative to a reference value in a magnetic field. Its value varies according to the local electronic environment and the local geometry *e.g.* the bond lengths, angles between bonds and the moiety present on this bond. Scalar coupling arises due to indirect interaction between two nuclear spins mediated by the electrons of the covalent bond connecting these nuclei. The NOE is a through space interaction and is caused by the transfer of nuclear spin polarization from one spin to another spin via cross relaxation. The combination of NOEs and $^3J_{HH}$ scalar couplings is insufficient for certain molecules as it is not always possible to determine the molecular arrangement with these parameters. Therefore, there is a need for further information, which could be provided by anisotropic NMR parameters like RDCs. In this section, the conditions and experimental parameters necessary to determine RDCs will be explored as well as the obtainable 3D data described.

2.1. Theory

The discovery of RDCs and their increased utilization allows a good understanding of the development of the application of RDCs in research. A. Saupe and G. Englert pioneered the measurement of molecules in alignment media in 1963, publishing the first spectrum showing a split NMR signal of benzene which was aligned in a liquid crystal [14]. Their work focused on the properties of the polymers which give strong alignment to the solvent. In 1964, A. Saupe described the theory of dipolar couplings in liquid crystals [15] which was the starting point of various works in liquid crystalline phases with chloroform. In order to have the possibility to measure a large variety of molecules and not being limited to the solvent chloroform, other alignment media have been explored such as polymer gels. In 1981, Deloche and Samulski measured the first deuterium quadrupolar splitting of D_2O in a polymer gel and this proved that the alignment provided by stretched polymer gels was sufficient for the measurement of anisotropic parameters [16].

The properties of polymer gels were studied with deuterium NMR by Samulski during the next decade [17]. Since then, these gels have been used to partially align a multitude of solutes and solvents. Another way to align molecules is the use of bicelles [18-20] or phages [21, 22] as water-compatible lyotropic mesophases commonly used for biomolecules. The first gel used as alignment medium for the study of a protein was a polyacrylamide gel (PAA) in 2000 [23]; the method using a stretched gel to align the molecule has been called strain induced alignment in a gel (SAG). The gel straining induces anisotropy and thus prevents the signal averaging of the dipolar couplings to zero observed in the isotropic case. The advantage of the gel is the possibility to arbitrarily scale the alignment allowing to find a good balance between the size of RDCs and spectral resolution.

2.1.1. Dipolar Coupling

Contrary to scalar couplings which result from the interaction through bonds, dipolar couplings represent through space interactions. This direct dipole-dipole interaction takes place between two spins which are schematically shown as I and S in **Figure 4**. These spins can be considered as two magnets with an inherent rotation at the Larmor frequency. The orientation of each of these spins with respect to the static B_0 field will be the source of a local magnetic field, which either adds or subtracts to the static magnetic field. Consequently, each local magnetic field felt by the nuclei will lead to a D_{IS}^{Int} positive or negative shift of resonance frequencies, depending on the orientation of coupled spins. As the parallel and antiparallel orientations are approximately equally populated for each spin, the dipole-dipole interaction *i.e*. the dipolar coupling D_{IS} will result in a split of their frequency with twice the dipolar coupling D_{IS}^{Int}.

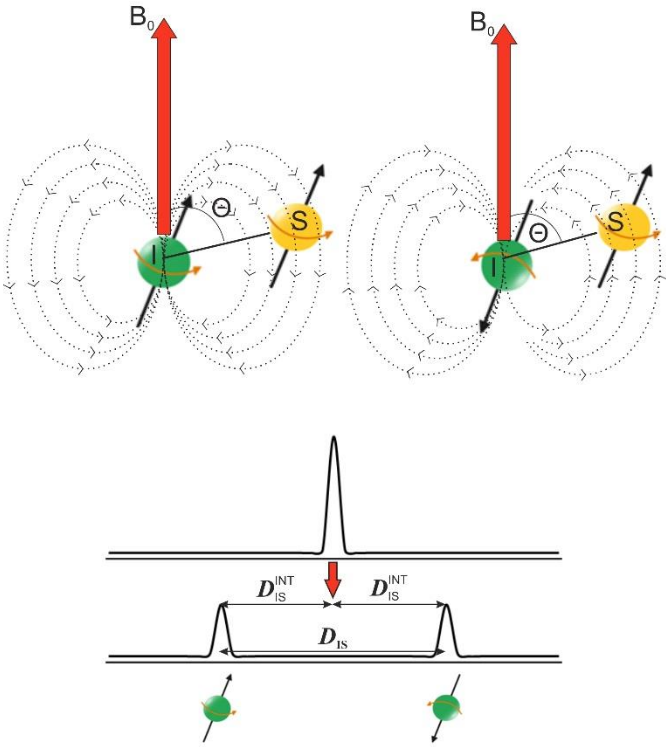

Figure 4: Magnetic dipole (I) – dipole (S) coupling interaction (D_{IS}) and the spectrum obtained with the dipolar coupling.

For a simplified model comprised of only two isolated spins, the dipolar coupling D_{IS} (assuming averaging to zero is omitted) is dependent on the distance r_{IS} between the two nuclei (which can be bonded or non-bonded) and the angle Θ of their internuclear vector $\overrightarrow{r_{IS}}$ relative to B_0 [24]:

$$D_{IS} = -\frac{\hbar\gamma_I\gamma_S\mu_0}{16\pi^2}\left(\frac{1}{r_{IS}^3}(3cos^2\theta - 1)\right) \quad (1)$$

where γ_I and γ_S correspond to the gyromagnetic ratios of the two spins, ħ corresponds to the Planck constant divided by 2π and μ_0 to the permeability of vacuum.

In liquid state, dipolar couplings vanish because molecules tumble freely and the vector $\overrightarrow{r_{IS}}$ points equally in all direction resulting in dipolar coupling being averaged to zero and causing the loss of precious structural information. In the solid state, dipolar couplings are on the order of several thousand hertz. The presence of many dipolar couplings leads to very broad lines due to the presence of several couplings, which causes dipolar couplings to be hardly measurable and usable. Indeed, equation (1) describes the dipolar coupling for static molecules *i.e.* in solid state. According to this equation, the biggest value of $^1D_{CH}$ is approximately -46 kHz when the CH bond is parallel to the magnetic field. Dipolar couplings can be positive or negative and even zero when θ reaches 54.74 degrees, the *so-called* magic angle, where the component $(3cos^2\theta - 1)$ is equal to zero. In order to measure dipolar couplings at higher resolution, an intermediate state between solid and liquid has to be reached keeping sufficient resolution of the signals. This state can be obtained using alignment media such as stretched gels, liquid crystals, paramagnetic ions, phages or micelles allowing a partial orientation of the molecule. While molecular tumbling is still present, the interaction with the alignment medium leads to the existence of preferred orientations with respect to all possible orientations of the molecule (**Figure 5**). Thus, in the alignment medium, the internuclear vectors are not averaged to zero and the resulting net vector gives rise to a residual dipolar coupling (RDC). By tuning the strength of the alignment, the RDCs can be reduced to a value of 0-20 Hz which is in the range of the biggest $^3J_{HH}$ couplings.

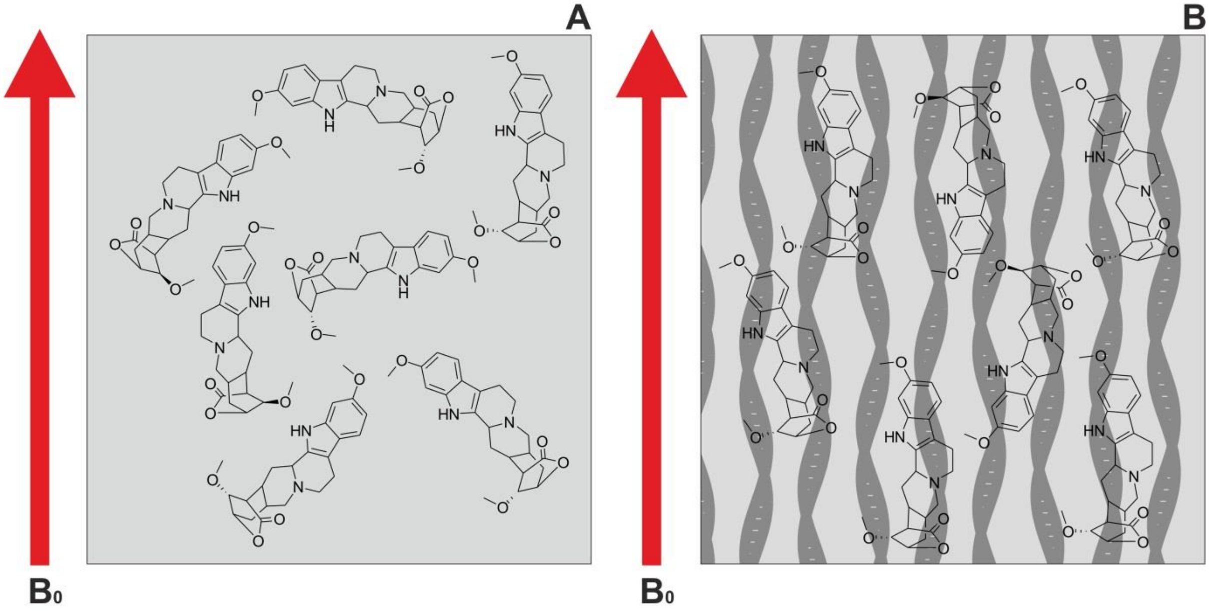

Figure 5: Comparison between isotropic and the anisotropic conditions.
In the isotropic state (**A**), there is no preferred orientation with respect to B_0 and dipolar couplings are averaged to zero. In the anisotropic case (**B**), solute molecules diffused into the alignment medium will be partially oriented.

There are 3 different ways to align a molecule for the measurement of RDCs: alignment in a liquid crystalline phase (PBLG for example), alignment in stretched gels (*e.g.* stretched polyacrylamide gel) and orientation via paramagnetic ions, which will be described later.

In isotropic medium, the simplification of equation (1) with the averaging of the angle θ is only due to molecular tumbling and equation (1) can be written as following:

$$D_{IS} = -\frac{3\hbar\gamma_I\gamma_S\mu_0}{16\pi^2 r_{IS}^3}\left(\langle cos^2\theta\rangle - \frac{1}{3}\right) \tag{2}$$

D_{IS} is thus the average value in solution of the residual dipolar coupling with all possible orientations defined by the angle θ while assuming constant distance r_{IS} between the coupled nuclei. An averaging to zero in isotropic medium is a result of θ adopting all possible values and thus the dipole vector pointing in all directions in the laboratory frame (x^L, y^L, z^L). The averaged $\langle cos^2\theta\rangle$ is time dependent and equal to $\frac{1}{3}$ in isotropic medium.

In 2004, Kramer *et al.* gave a detailed and comprehensive introduction to the alignment tensor which describes the average orientation of the molecule with respect to the magnetic field [24]. The alignment tensor with its orientation and its three principal components allows calculating theoretical RDCs.

In order to describe the orientational averaging, it is necessary to use an arbitrary frame of the molecule (x^M, y^M, z^M) instead of the laboratory frame (x^L, y^L, z^L). The molecular frame is a reference frame that is fixed in the molecule. The orientation of the molecular frame is arbitrary, but defined. In the laboratory frame, the orientation of the magnetic field is fixed along z-axis, while in this arbitrary frame the magnetic field orientation is not fixed along a defined axis. The molecule and its rotation define the orientation of the molecular frame axes as represented in **Figure 6**.

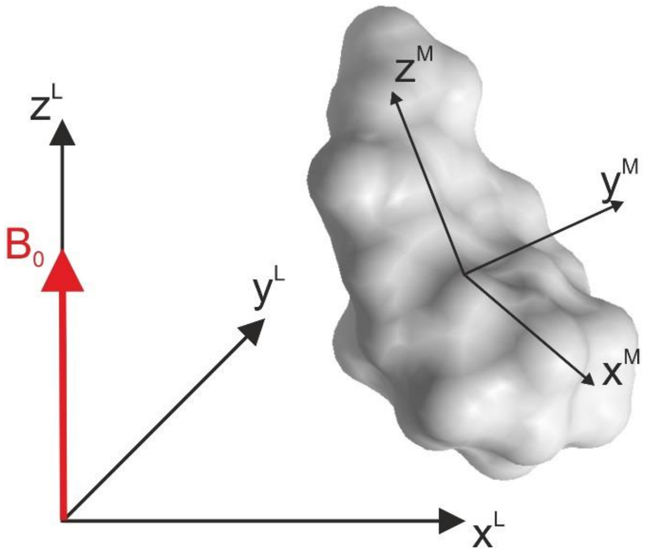

Figure 6: Schematic representation of laboratory and molecular frames.
Figure adapted from [24].

With the three Cartesian components $cos\,\theta_x$, $\cos\theta_y$ and $\cos\theta_z$, the term $\langle cos^2\theta\rangle$ can be represented in terms of the probability tensor **P** as follows:

$$\langle cos^2\theta\rangle = P_x\theta_x^2 + P_y\theta_y^2 + P_z\theta_z^2 = \frac{1}{3} \tag{3}$$

The probability tensor corresponds to the distribution probability of the B_0 field in the molecular frame. P_x P_y and P_z represent the probabilities to have the magnetic field B_0 along the corresponding axis of the arbitrary frame. In an isotropic solution, the magnetic field B_0 is equally distributed in all the spatial directions. Hence in the molecular frame, B_0 will be equally aligned in time along the 3 axis x,y,z, *i.e.* $P_{xx} = P_{yy} = P_{zz} = \frac{1}{3}$. This probability tensor will allow defining the alignment tensor A as followed where U is the unitary tensor:

$$\boldsymbol{A} = \boldsymbol{P} - \frac{1}{3}\boldsymbol{U} \tag{4}$$

The alignment tensor is equal to zero in isotropic solution, *i.e.* the degree of alignment is null as follows:

$$A = \begin{pmatrix} 1/3 & 0 & 0 \\ 0 & 1/3 & 0 \\ 0 & 0 & 1/3 \end{pmatrix} - \frac{1}{3}\begin{pmatrix} 1 & 0 & 0 \\ 0 & 1 & 0 \\ 0 & 0 & 1 \end{pmatrix} \tag{5}$$

A_x, A_y and A_y are the three components of the alignment tensor A, and they are defined as follows:

$$A_x = P_x - \frac{1}{3}$$

$$A_y = P_y - \frac{1}{3}$$

$$A_z = P_z - \frac{1}{3} \tag{6}$$

According to the alignment tensor and equation (2), the dipolar coupling can be written as follows:

$$D_{IS} = -\frac{3\hbar\gamma_I\gamma_S\mu_0}{16\pi^2 r_{IS}^3}\left(\langle cos^2\theta\rangle - \frac{1}{3}\right) = -\frac{3\hbar\gamma_I\gamma_S\mu_0}{16\pi^2 r_{IS}^3}\, r^T A r \tag{7}$$

Hence, the only variable in this equation is the alignment tensor which is a tensor A with 9 unknown variables:

$$A = \begin{pmatrix} A_{xx} & A_{xy} & A_{xz} \\ A_{yx} & A_{yy} & A_{yz} \\ A_{zx} & A_{zy} & A_{zz} \end{pmatrix} \tag{8}$$

As the alignment tensor is traceless, the following conditions apply:

$$A_{xx} + A_{yy} + A_{zz} = 0 \tag{9}$$

and hence,

$$A_{xx} + A_{yy} = - A_{zz} \tag{10}$$

The alignment tensor is also symmetric with respect to the diagonal, so:

$$A_{yx} = A_{xy}$$

$$A_{xz} = A_{zx}$$

$$A_{yz} = A_{zy} \tag{11}$$

Because of the symmetry and the interdependence of diagonal terms, the number of unknown variables to solve the matrix of the alignment tensor decreases to five for a rigid molecule. Thus, in order to determine the alignment tensor of a given molecule, at least five independent RDCs are required. Out of these five RDCs, not more than three RDCs should be in a common plane and the five RDCs must not be parallel or antiparallel to each other.

With the purpose to obtaining sufficient RDCs with appropriate size, the molecules need to be aligned in a solution with a certain degree of order. For the alignment of the molecules by means of paramagnetic ions, mostly lanthanides are being used. The ion needs to be in the proximity of the molecule. This application is mostly used in biomolecular NMR, as for bigger molecules only a fraction of the signals are close to the paramagnetic ion so that enough RDCs can still be obtained. In addition, the tag itself would change a lot the properties of a small molecule. This disappearance of signals is caused by the free electron of the paramagnetic ion which broadens the lines due to relaxation. Thus, the extraction of RDCs for small molecules becomes almost impossible. Consequently, using paramagnetic ions for small molecules is usually impractical; instead, liquid crystals and stretched or compressed gels are the preferred media. Therefore, these approaches are used throughout this thesis. The majority of liquid crystals can be used with apolar organic solvents (*e.g.* $CDCl_3$) and aqueous solutions. Their advantages and limitations will be discussed below. Last but not least, the stretched gels have more widespread use for small molecules, as they allow the use of a wide range of solvents and are typically easier to handle compare to liquid crystal for which a critical concentration is needed with substantial minimum alignment [25].

2.1.2. Liquid crystals

Liquid crystalline (LC) phase is the fourth state of matter in addition to the known states of solid, liquid, and gas. It is a unique state between the solid (crystalline) and liquid (isotropic) states. There are two main types of liquid crystal: thermotropic and lyotropic. The thermotropic liquid crystals exhibit liquid crystalline mesophases when melting from the crystal phase or cooling from the isotropic liquid, whereas the lyotropic materials exhibit liquid crystalline mesophases when mixed with a particular solvent at a critical concentration. Depending on their overall 3D shape, molecules in LC phase could retain some possibility to tumble as they freely do in solution. However, due to the viscosity increase in LC samples, this flexibility is severely reduced. LCs align in strong magnetic field; therefore, they are anisotropic, which means that their physical properties are not identical in all directions. This property is transferred to the analysed molecule and enforces some alignment of this molecule. This makes the measurement of residual dipolar couplings possible.

For the work presented in this thesis, lyotropic material, more precisely poly-γ-benzyl-*L*-glutamate (PBLG), is used (See **Figure 7**).

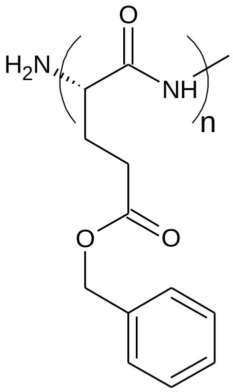

Figure 7: Chemical structure of poly-γ-benzyl-*L*-glutamate (PBLG).

PBLG is a lyotropic polypeptide liquid crystal which forms an α-helical conformation in apolar solvents like $CDCl_3$. It will adopt a liquid crystalline phase when the polymer exceeds a certain concentration in solution and is limited to a very narrow temperature range [26]. More detailed information on the use of LC alignment medium and the results obtained using it are given in section 6.

2.1.3. Stretched gels for alignment

Deloche and Samulski measured an anisotropic parameter in stretched polymer gels studying a polymer for the first time in 1981 [27]. For biomolecules, the use of stretched gels was first described in the year 2000 by Tycko *et al.* [23] and Sass *et al.* [28]. Both authors used a polyacrylamide gel swollen in water as alignment medium. However, small molecules are mainly soluble in organic solvents which explains why there was a need to generate additional gels extending their use beyond water based matrices. In 2004, Luy *et al.* introduced polystyrene (PS) [29] and polydimethylsiloxane (PDMS) [30] gels allowing the RDCs measurement of organic molecules in apolar solvents like $CDCl_3$ and CD_2Cl_2. One year later, gels compatible with DMSO and other polar organic solvents were published [31, 32]. In 2007, Kummerlöwe *et al*. developed an easily scalable, uncharged DMSO compatible alignment medium applicable to a wide range of molecules, polyacrylonitrile (PAN) gel [33], which is used in section 5.

To prepare a sample, a cross-linked polymer network is added to a NMR tube in form of a stick, and the polymer then swells after addition of the solvent. During the swelling process, the gel will first reach the wall of the tube and will then continue to expand in the vertical direction. The degree of alignment is defined by the stick properties and solvent together with the interaction with the molecule and therefore cannot be controlled directly. The options for varying the strength of the alignment are limited to changing the measurement temperature, the initial dry stick diameter, and the degree of cross linking. The test molecule can be added simultaneously with the solvent or after the swelling. When limited sample amounts are available it is important to add the molecule into the gel slowly and carefully after the swelling stage as during the swelling step which can take several weeks, the gel can break or shrink leading even to the loss of the molecule. In case that only the size of the polymer stick or cross linking density are utilized to tune the alignment, several individual samples have to be prepared. In order to avoid this shortcoming, different devices have been designed which allow to stretch or compress the gel enabling tuning of the alignment using only a single sample. A tuneable compressing device was developed by Gil *et al*. in 2010 [34] based on previous work of Tycko *et al.* [23] and Grzesiek *et al.* [28], which introduced the approach to achieve alignment by preventing the gel to swell freely by a plunger. Consequently, the gel will just swell in the radial direction and up to the plunger which can be placed according to the desired alignment. Alternatively, a stretching device can be used. In this case, the dry stick is placed in a stretchy tube which is placed in an open cut NMR tube. This allows arbitrarily stretching the polymer stick and thus varying the alignment strength. The first prototype was developed by Kuchel *et al.*[35] and further improved by Kummerlöwe *et al.*[36]. In this thesis, the stretching device has been used and adapted for use of small sample quantities (section 4).

2.2. Experimental section

2.2.1. Deuterium experiment

A deuterium (1D ^{2}H) spectrum is typically used to measure the quadrupolar coupling $\Delta\nu_{Q}$ of the solvent which allows an assessment of the stretching of the gels and if the liquid crystalline phase is achieved. The quadrupolar coupling is observed due to the interaction between the quadrupole moment of a nucleus with a spin larger than ½ and the electric field gradient (EFG) at the nucleus. $\Delta\nu_{Q}$ is also an anisotropic parameter in NMR, so in the solution it is averaged to zero. However, in anisotropic medium, $\Delta\nu_{Q}$ leads to splitting of the solvent signal enabling the experimental determination of the quadrupolar coupling. This value is then utilized to monitor the alignment strength of the orienting medium. The size of the splitting depends mainly on the size of the EFG on deuterium nuclei of the molecules and on the degree of alignment. For example, chloroform ($CDCl_3$) is a solvent with one of the strongest EFG, hence, it will give bigger $\Delta\nu_{Q}$ compared to DMSO-d_6. This is the reason why $\Delta\nu_{Q}$ values from different samples (containing different solvents or media) cannot be directly compared. However, from the same sample the $\Delta\nu_{Q}$ and RDCs behave linear. The deuterium spectrum is needed to evaluate the anisotropy of the medium and the sample equilibration before collecting RDCs. Adjusting the value of $\Delta\nu_{Q}$ by using another gel or a stretching device will allow finding a balance between the spectral resolution and the alignment strength. Indeed, a too strong alignment leads to broad signals *i.e.* less accuracy of the measured values, mainly due to the high number of ^{1}H, ^{1}H-RDCs. Because of the resulting spectral overlap and the broad signals, the extraction of the coupling constants becomes more difficult or even impossible. On the other hand, a too weak alignment will give a good resolution, but small RDC values, which are on the order of the experimental error. As a consequence, a modulation of the alignment is needed and this can be realized with the stretching device or variable angle NMR described in the following section.

While the 1D ^{2}H spectrum of deuterated solvent is used to roughly characterize the strength and homogeneity of the alignment, no spatial information can be extracted. In case inhomogeneity is observed, it is important to know the underlying reason. Major reasons are an inhomogeneous magnetic field (suboptimal shims) or an inhomogeneity of the sample itself (*e.g.* if the gel or LC are not equilibrated), as well as a combination of the two. To address this, a ^{2}H imaging experiment is used for monitoring the quality of the gels or the LCs [37]. This experiment allows the detection of broken gels or of inhomogeneity in the gels or LCs by probing the spatial distribution of the ^{2}H quadrupolar splitting along the *z* direction of anisotropic samples (**Figure 8**).

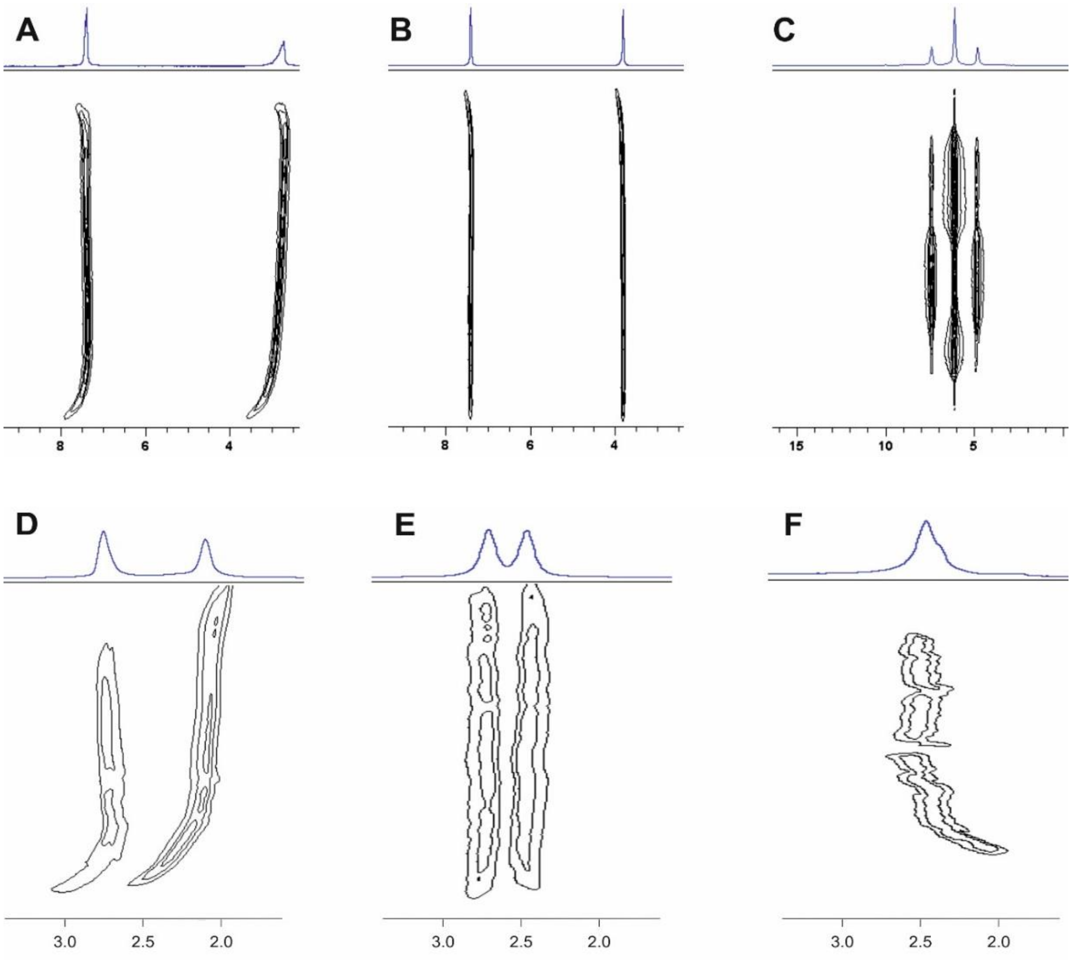

Figure 8: Several ^{2}H imaging spectra of deuterated solvent measured with LC in $CDCl_3$ (**A B** and **C**) and gel samples in DMSO-d_6 (**D, E** and **F**).
Spectra shown in panels **B** and **E** indicate that the measured samples were well-equilibrated and well shimmed. **A** and **D** are imaging spectra of samples acquired with bad shims. Spectrum in panel **C** shows different alignments due to concentration gradients and the presence of isotropic solvent. Panel **F** shows a spectrum of a broken gel.

2.2.2. Adjustment of the alignment

2.2.2.1. Modification of the gel

A complementary approach to vary the degree of alignment is the modification of the alignment medium itself, *i.e.* increasing or decreasing the alignment strength by modulating the amount of cross linker (**Figure 9**). The gels used as alignment media are typically obtained from polymer units, radical starters, and cross linkers. The alignment strength will increase with the number of cross linking points and the length of the polymer chain will decrease with the number of radical starters, equally causing a decrease in alignment [29]. A variation of the temperature can change the viscosity of the gel and as the alignment strength depends on the density of the gel, the variation of the temperature may also allow the scaling of the alignment [38].

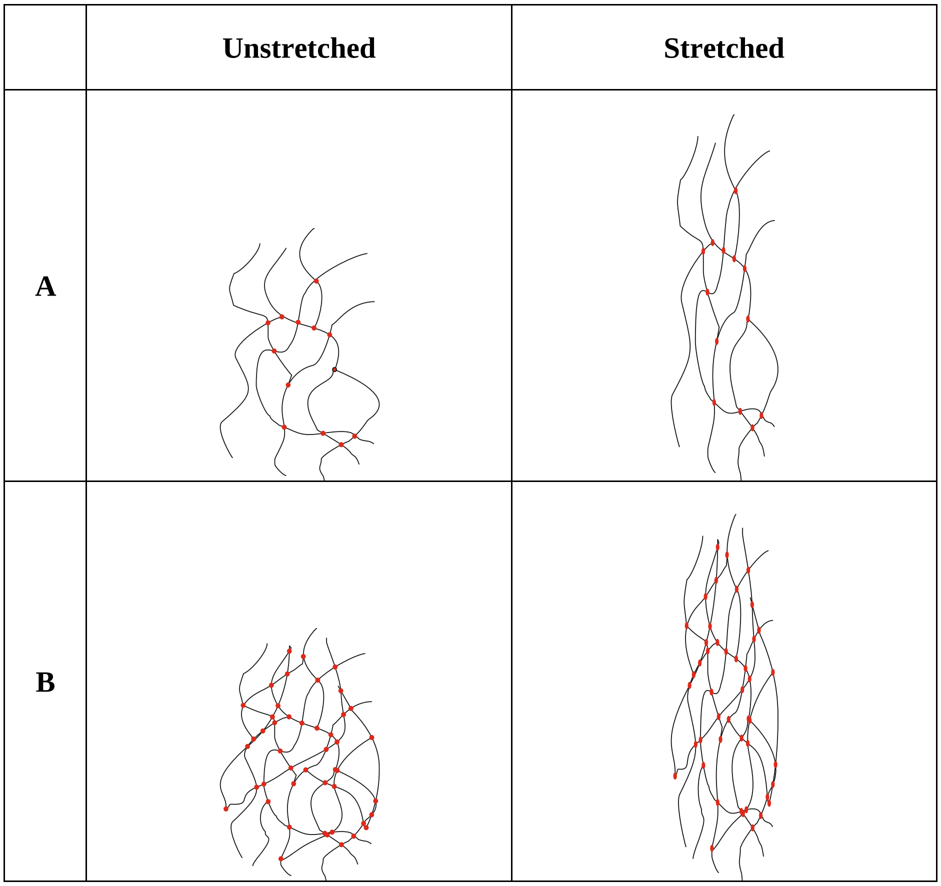

Figure 9: Modulation of the alignment strength by using different degrees of cross-linking.
The cross linkers are indicated as red dots in both states, unstretched and stretched. Row **B** illustrates a situation in which more cross linker was used compared to row **A** resulting in increased alignment a shown in the stretched state.

The polymer gels used for the alignment of small molecules are synthesized directly with different diameters then dried and cut in the desired length resulting in a dry stick; according to their diameter, the stretching of the gel will be different; therefore, the alignment can be scaled by using gels with different diameters. Since stretching is performed in the direction of the external magnetic field B_0 the alignment with the field directly depends on the degree of the stretching. In addition, the solvent plays an important role for gel stretching, as polymer gels swell differently depending on the solvent used [38].

As it has been shown, using modification of the polymer stick, the alignment can be tuned. However, each modification requires the preparation of a new sample. This is not only time consuming but it also requires a large quantity of sample. Often, in particular with natural products, the available sample amount is limited. In such cases, other methods are needed in order to vary the alignment without preparing a new sample, such as stretching devices or variable angle sample spinning NMR (VASS).

2.2.2.2. Variable Angle Sample Spinning

RDCs are measurable in an alignment medium. In a conventionally used probe head, for both liquid crystalline and stretched gel samples liquid crystal samples, the direction of the alignment coincides with the axis of B_0 field. If this average director deviates by the angle Θ_{VASS} relative to the magnetic field, equation (2) for the determination of the dipolar couplings has to be rewritten as follows:

$$D_{IS} = -\frac{\hbar\gamma_I\gamma_S\mu_0}{16\pi^2 r_{IS}^3}\left(\frac{3}{2}\cos^2\Theta_{VASS} - \frac{1}{2}\right)\langle(3\cos^2\Theta_{BM} - 1)\rangle \qquad (12)$$

where Θ_{BM} is the angle between the vector of the RDCs within the molecule and the average director of the alignment medium. In 1964, Saupe *et al.* [15] showed that the scaling of the RDCs was possible if the orientation of the alignment tensor was varied independently of the static magnetic field. For a liquid crystalline phase, this variation of the director is achieved by the use of a Variable Angle Sample Spinning (VASS) probe head [39]. The liquid crystalline sample is placed in a rotor used also in conventional high-resolution magic angle spinning (MAS) NMR. Such rotors are used for sample in semi solid state NMR and usually rotate around an axis at the magic angle and at a given frequency in the kHz range. When used with these conditions, the liquid crystalline phase sample displays an alignment tensor director which is parallel to the magic angle (MA), *i.e.* to 54.74°. According to equation (12), the first term in the bracket will approximate zero and hence no dipolar couplings can be observed. In order to be able to measure RDCs, the rotor has to be placed outside the MA and the magnetic field orientation as schematized in the **Figure 10**.

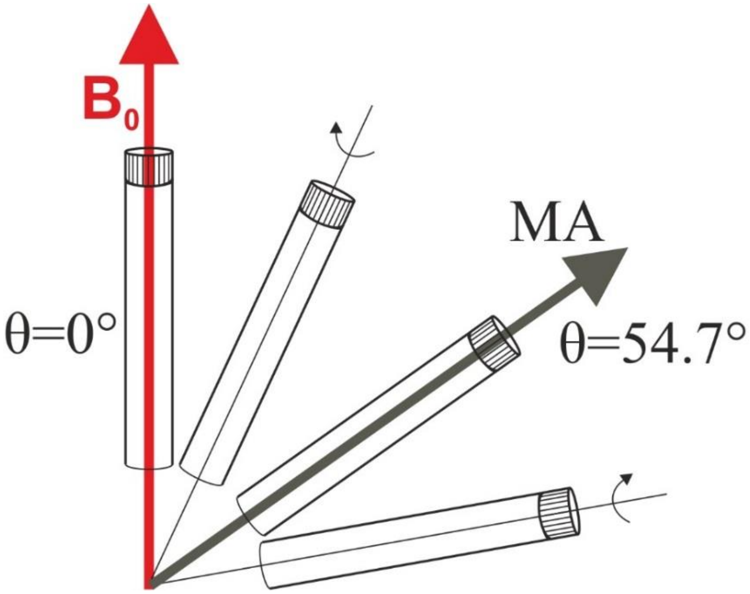

Figure 10: Scaling of the alignment with variable angle sample spinning (VASS).

The orientation of the alignment tensor in liquid crystalline phases is either parallel or perpendicular to the magnetic field depending on the liquid crystal used and the sign of the anisotropy of the magnetic predisposition [40]. Spinning non-parallel to the magnetic field is a known way to vary the alignment tensor for liquid crystalline phases. By spinning the sample at a different angle than the magic angle 54.74°, the alignment strength can be modified and thus the best balance between the resolution and the size of the RDCs can be determined using the same sample. It is also important to spin the rotor not too fast (below 1000 Hz according to the specification of the probe head); otherwise, the alignment can be lost because the magic angle spinning becomes the predominant effect on the director orientation [39]. The evaluation of the VASS approach compared to the standard liquid state NMR measurements in PBLG is described in section 6 of this thesis.

2.2.2.3. Gel Apparatus

A gel apparatus allows elongation or compression of the gel and hence to modify the alignment strength of polymer-based alignment medium. Ishii *et al*. introduced a compression method for gels in 2001 [41] which utilizes a Shigemi plunger to modulate the pressure on the gel. In 2010, Gil *et al.* developed an optimized version of the compressing device based on previous work of Tycko *et al*. [23] and Grzesiek *et al*. [28] which can be used with specific gels [34]. Depending on the gel used, the compression has to be handled very carefully as pushing back a swollen gel is difficult and can lead to breaking of the gel. The first stretching device, a simple funnel-like apparatus squeezing the gel into an open cut NMR tube via the opening, was published by Chou *et al.* in 2001 [42]. However, changing the scaling of the alignment is not possible with this device. In 2006, Kuchel *et al.* proposed a different stretching device [35] composed of a flexible silicone rubber tube, an open cut NMR tube and a rubber plug. The gel is in the silicone tube, which is placed in an open cut NMR tube and closed by the rubber plug. By stretching the silicone tube, the swollen gel will be stretched to the desired length. In order to fix and modulate the stretched gel, a screwing device is used, allowing fast and reversible alignment adjustment. Thus, with the same sample, measurements with different degree of alignment strength are possible.

Kuchel *et al.* defined the *so-called* extension factor (Ξ) to quantify the degree of gel stretching in the apparatus [43]. It is calculated from the length of the stretched and non-stretched gel (equation (13)):

$$\Xi = \frac{length\ of\ stretched\ gel}{length\ on\ unstretched\ gel} - 1 \tag{13}$$

The extension factor Ξ is equal to zero if the gel is unstretched and it is equal to one for a gel stretched to twice its original length. The quadrupolar splittings measured for the solvents of stretched gels are linear with the extension factor as shown in **Figure 11**.

A	Quadrupolar Splitting [Hz]	Gel Length [cm]	Extension factor
Unstretched	0	3.5	0
First stretching	2	4	0.143
Second stretching	5.8	5	0.429
Third stretching	9.6	6	0.714
Maximal stretching	17	8	1.286

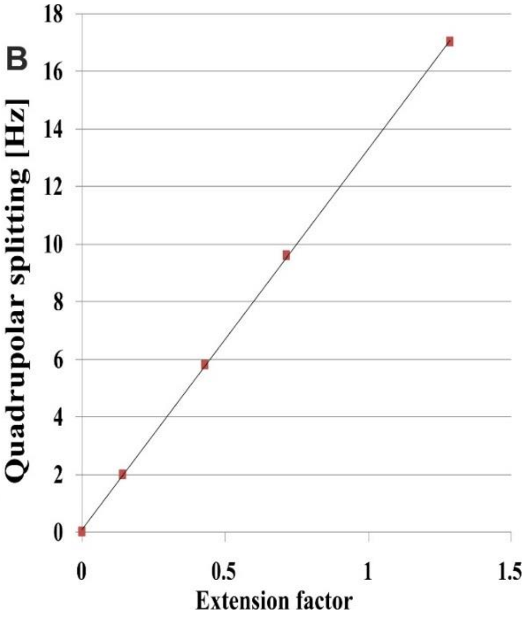

Figure 11: Scaling of the alignment strength of a polyacrylamide gel with the 5 mm stretching device.
Table **A** contains the gel lengths obtained by different stretchings, the corresponding extension factors and the measured quadrupolar splittings $\Delta\nu_Q$. The Graph in panel **B** demonstrates the linearity of Ξ to the increased alignment strength ($\Delta\nu_Q$).

To increase the options of measuring with different solvents and gels and to adapt the device for use in standard 5 mm NMR probe heads, the stretching device of Kuchel *et al.* has been slightly redesigned by Kummerlöwe *et al.*[36]. The principle is the same: a silicone tube is placed inside an open cut 5 mm NMR tube and fixed with a Teflon plug at the bottom. A Polychlorotetrafluoroethylene (PCTFE) lock with nylon screws allow to fix the pulled silicone tube at the top of the device and hence to adjust the alignment strength. A photograph of the actual device is shown in the **Figure 12**.

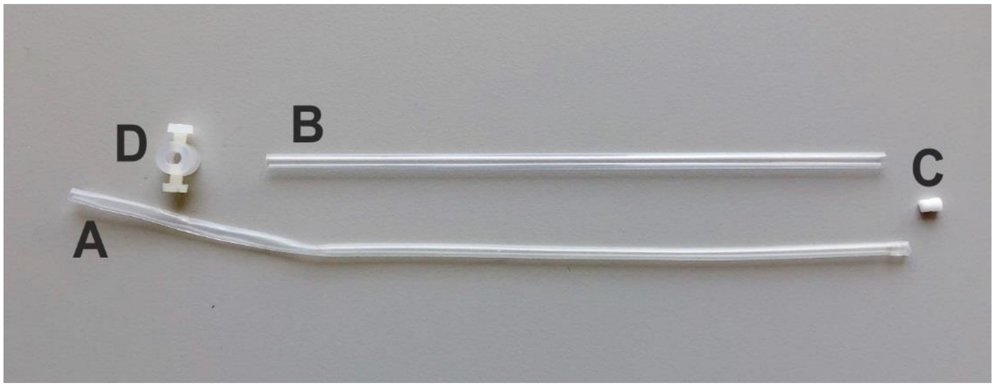

Figure 12: 5 mm stretching device designed by Kummerlöwe for polar solvents.
The device is composed of a silicone tube (**A**), an open cut 5 mm NMR tube (**B**), a Teflon plug (**C**), and a PCTFE lock with 2 nylon screws (**D**) [36].

The gel inside the tube is then mechanically stretched by pulling the silicone tube. As a result, anisotropic parameters can be measured. One of the shortcomings of this device is that the silicone rubber tubing allows the diffusion of water into the sample, and reversely the evaporation of solvent out of the gel. For example, the PAN gel is hydrophobic and as DMSO is a hygroscopic solvent, the quantity of water increases in the silicone tubing which leads to gel shrinking, making the gel unusable. Since the slow contamination with water cannot be avoided when using silicone tubing, such stretching devices cannot be used for water sensitive samples measured in DMSO-d_6 [36]. Another limitation of the silicone rubber is its property to swell with apolar solvents like chloroform, dichloromethane or benzene, which are often used for NMR experiments of organic molecules. These issues have been addressed with the use of tubing made of perfluorinated elastomer material as, *e.g.* Viton® or Kalrez®. Such materials are chemically resistant, water tight and enable measurements in a wide temperature range up to approximately 275 °C [44]. These devices are also composed of an open cut 5 mm tube, a flexible perfluorinated elastomer tube, a specially designed Polychlorotetrafluoroethylene (PCTFE) screw at the bottom allowing the fixation of the tubing, and a PCTFE device with nylon screws at the top used to adjust the stretching. PCTFE is hard enough, easy to process and chemically resistant, making it an ideal material the stretching device (**Figure 13**). Compared to the silicone tubing, the perfluorinated elastomer has no signal in proton spectra and can be used with all common NMR solvents, while the use of silicone tubing is limited when measuring in chloroform or similar solvents due to swelling.

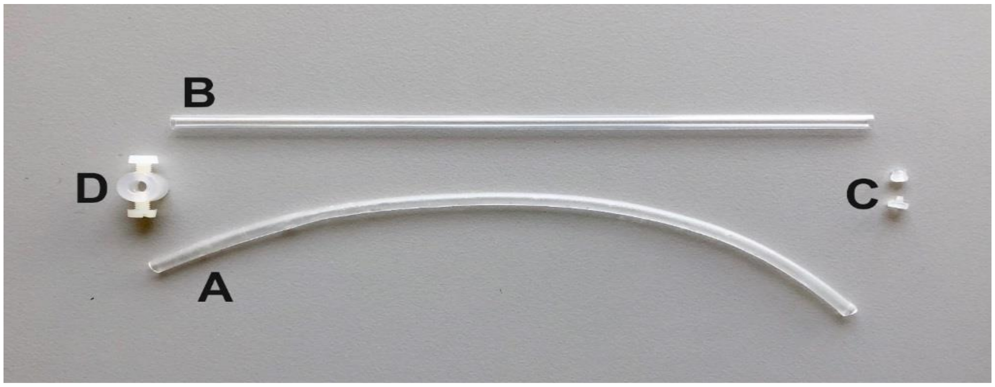

Figure 13: 5 mm stretching device designed by Kummerlöwe for all commonly used solvents.
The device is composed of a Kalrez tube (**A**), an open cut 5 mm NMR tube (**B**), a specially designed Polychlorotetrafluor ethylene (PCTFE) screw (**C**) and a Kel-F/PCTFE cap with 2 screws (**D**).

In conclusion, the most convenient way to vary the alignment of a stretched polymer gel when aiming to use only a single sample is the utilization of a stretching device. As described above, such devices are already available for 5 mm NMR tubes. However, when a reduction of the sample quantity is required and/or increased sample homogeneity is desired, the use of a smaller sized tube would be highly advantageous. One aim of this work is to miniaturize the existing stretching device for 3 mm NMR tube, which will be described in section 4.

2.2.3. NMR measurements to obtain the experimental RDCs

For the measurement of anisotropic parameters *e.g. residual* dipolar couplings (RDCs), the acquisition of spectra in isotropic and anisotropic states is needed, since the value obtained in the anisotropic state corresponds to the coupling in isotropic state plus the anisotropic coupling contribution. In equation (14), T corresponds to the *total* splitting observed in the anisotropic state and is the sum of the scalar coupling J (obtained in the isotropic state), obtained under the same measurement conditions, and the residual dipolar splitting D. Hence, the differences of T and J values will provide the desired anisotropic parameters, here RDCs.

$$T = J + D \tag{14}$$

As a consequence, two measurements are required: One in isotropic and one in the anisotropic state. Either two separate samples are prepared or methods allowing the acquisition of spectra in both states simultaneously are used. In addition, NMR experiments which allow accurate determination of the desired scalar J and total coupling T are needed. RDCs of the one bond heteronuclear couplings ${}^{1}D_{\mathrm{CH}}$ *or* ${}^{1}D_{\mathrm{NH}}$ are frequently assessed since the bond length is well-known and fixed [45-47, 20, 48]. As shown in equation (14), they can be derived from the difference between the total splitting of the anisotropic sample (${}^{1}T_{\mathrm{CH}}$ or ${}^{1}T_{\mathrm{NH}}$) and the corresponding scalar couplings (${}^{1}J_{\mathrm{CH}}$ *or* ${}^{1}J_{\mathrm{NH}}$). The obtained RDCs contain pure angular information only if the distance between the two spins is already known. Thus, when coupling over more than two bonds (*e.g.* geminal or ${}^{2}J_{\mathrm{CH}}$ couplings) is measured, the distance information has to be obtained separately from X-ray structures or from minimized structures obtained from *ab initio* and/or molecular dynamics simulation.

Various NMR experiments allowing the determination of scalar couplings were described previously. In this work, the CLIP-HSQC [49] is used as it suppresses dispersive antiphase components prior to detection. An improved version of the CLIP-HSQC containing broadband pulses to excite more uniformly the full spectral width (mainly for ^{13}C and ^{15}N) is implemented. The **Figure 14** displays an excerpt of a CLIP-HSQC acquired on a reserpine derivative molecule studied in section 5 of this thesis. These pulses are BEBOP [50, 51] for 90 degree excitation, BIBOP [52] as inversion pulses (180 degrees) and BURBOP [53] as universal rotation pulses (180 degrees). The need to use broadband pulses becomes more severe with the increase of the magnetic field strength, for example from 400 to 800 MHz spectrometers as it is the case within this thesis. In this case the typical spectral width of ^{13}C of 180 ppm to be covered by an excitation pulse is 18 kHz for 400 MHz and is doubled *i.e.* 36 kHz for a 800 MHz spectrometer. Thus the requirements for the pulse duration and power to excite this bandwidth are outside of the standard probe head limits. In this case the use of broadband type pulses is necessary and allows proper and accurate coupling constants extraction. When using non-broadband enough pulses, *e.g.* the spectral width is not fully excited, the problem for accurate coupling extraction is more severe at the spectral edges as demonstrated by Enthart *et al.* [49].

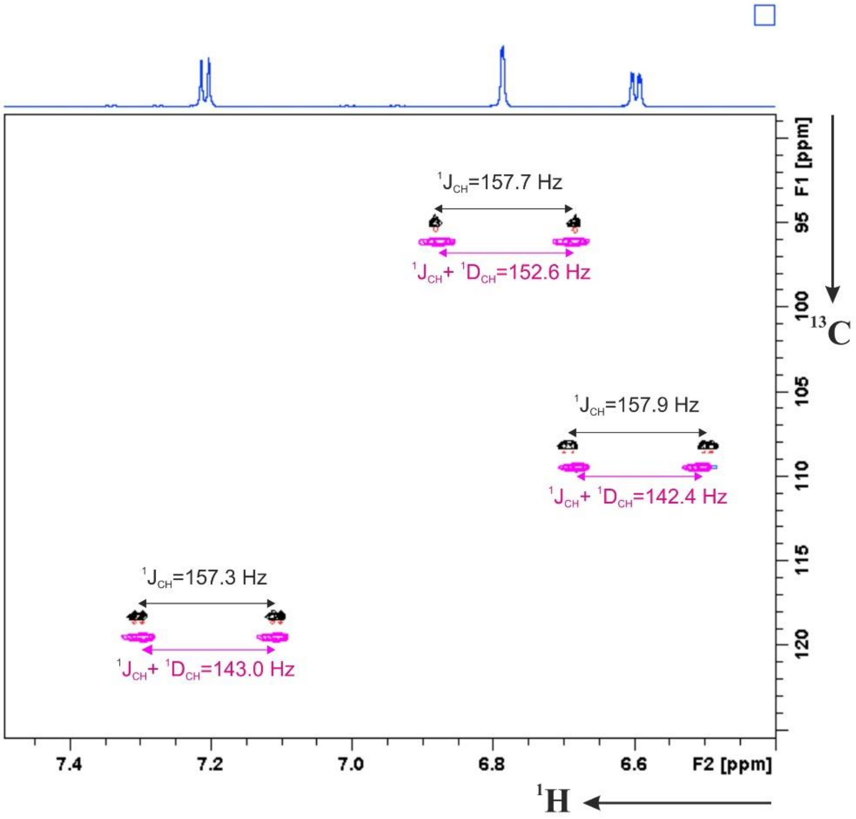

Figure 14: Excerpt of a CLIP-HSQC acquired on a reserpine derivative molecule studied in section 5. RDCs are obtained by comparing the spectrum recorded in the isotropic state (black) and the anisotropic state (achieved by using a stretched PAN gel pink), with a quadrupolar splitting of $\Delta\nu_Q$ = 7.95 Hz (DMSO-d_6).

The resulting spectra allow extraction of the couplings from the splittings acquired in the isotropic and anisotropic states. The method to extract the couplings is as follows: first a row of the indirect carbon frequency is selected from the CLIP-HSQC, extracted and saved as a 1D spectrum. This 1D spectrum is overlaid with a copy of itself and then manually shifted in order to overlap the centre of the α-component of the doublet with the centre the β-component. The value of the shift obtained in Hz corresponds to the total splitting $^{1}T_{CH}$ in the anisotropic state and to the scalar coupling $^{1}J_{CH}$ to the isotropic state. In order to estimate the error, a shift of one of the signals to the furthest right and the furthest left are required. The value obtained corresponds to the individual maximum error estimate (MEE) of the coupling in Hz. The methodology has been developed by Kummerlöwe [54] and is demonstrated in **Figure 15**.

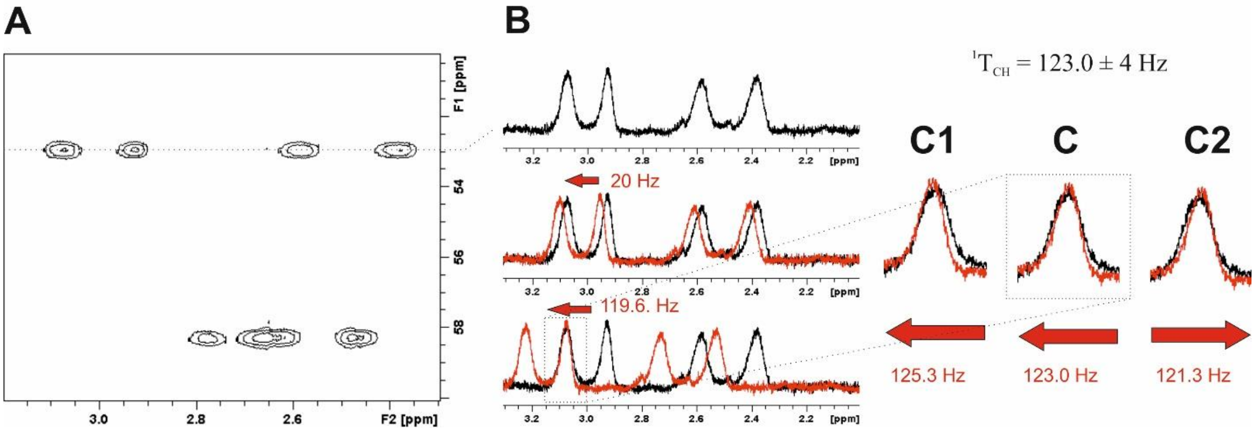

Figure 15: Illustration of the extraction of $^{n}J_{CH}/^{n}T_{CH}$ values and of the corresponding error estimation. Panel **A** shows an excerpt of the CLIP-HSQC of a reserpine derivative in PAN/DMSO-d_6 gel (described in detail in section **5**). The signal around 53 ppm corresponds to the geminal proton of a CH_2 group. The slice at this carbon chemical shift is extracted (**B**, top row) and a copy of this slice (in red) is overlaid with it (**B**, middle row). A shift of 20 Hz is shown in order to indicate the direction of the spectral shift. The peak is shifted until the two components of the peak are on top of each other; the required shift now corresponds to the observed coupling (**C**). The individual alignments to the left (**C1**) and to the right (**C2**) sides allow the estimation of the maximum individual error.

Another experiment used for the extraction of RDC values is the P.E.HSQC [55]. In the isotropic case in addition to the $^{1}J_{CH}$ for methylene groups the $^{2}J_{HH}$ coupling could be measured. The experiment is based on the use of the E. COSY principle applied for heteronuclear case [56-59]. The use of the displacement of the signals in the E. COSY multiplet allows the measurement of the sign for the geminal coupling. A negative sign for the coupling means that the tilt of the signals of the multiplet is to the right as demonstrated in **Figure 16** section **A**. An opposite (positive) sign of the geminal coupling would lead to a tilt to the left as shown in section **B** of the same picture. These properties of the P.E.HSQC experiment are especially valuable in the anisotropic case. The

${}^2T_{HH}$ could be either positive or negative and without sign sensitive experiment like the P.E.HSQC the change of the sign of this coupling could become unnoticed and therefore the further calculation will be performed with a wrong ${}^2D_{HH}$ value. In the example from **Figure 16**, if ${}^2T_{HH}$ = -20.1 Hz with ${}^2J_{HH}$ = -13.4 Hz, hence ${}^2D_{HH}$ = -6.7 Hz and if ${}^2T_{HH}$ = 20.1 Hz with ${}^2J_{HH}$ = -13.4 Hz and thus ${}^2D_{HH}$ = 33.5 Hz. In addition in case of anisotropic samples with the alignment, the protons of the methyl groups are not equivalent and thus this experiment allows the measurement of the respective ${}^2D_{HH}$ for the methyl group protons together with its sign based on the same displacement in the P.E.HSQC experiments. This coupling can only be observed in anisotropic phase as ${}^2J_{HH}$ for the methyl group is averaged to zero in solution.

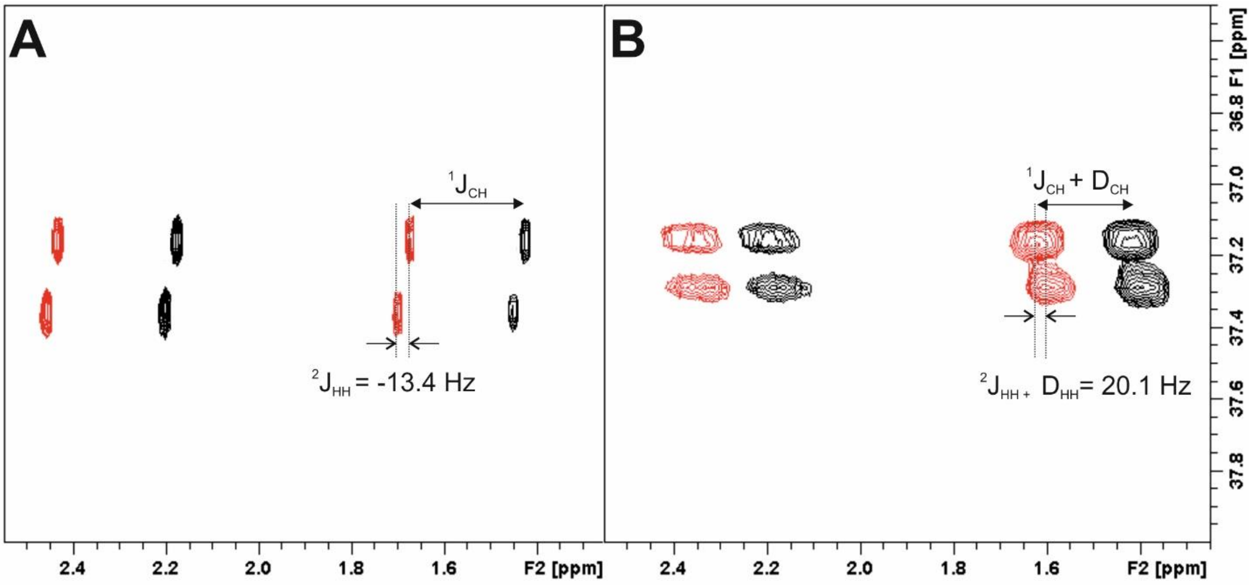

Figure 16: Excerpt of a P.E.HSQC recorded on the POMT molecule described in section 6 aligned in PBLG/$CDCl_3$.
This experiment allows the simultaneous extraction of ${}^2J_{HH}/{}^2T_{HH}$ and ${}^1J_{CH}/{}^1T_{CH}$ values. A methylene group is visible in the isotropic (**A**) and the anisotropic spectra (**B**). The sign of the homonuclear coupling is given by the tilt of the multiplet which changes in the alignment case due to the increased positive ${}^2D_{HH}$ coupling. ${}^2D_{HH}$ = 20.1+13.4 =33.5 Hz.

Another important information related to structural properties of large and flexible small molecules is provided by long range heteronuclear couplings ${}^nJ_{CH}$ and the corresponding ${}^nD_{CH}$ RDCs [60, 21, 61, 20]. In contrast to the determination of ${}^3J_{CH}$ coupling constants in isotropic samples, for long range couplings it is crucial to determine the sign in addition to the value. HSQC-TOCSY experiments are generally utilised to assess long range heteronuclear RDCs. In the studies presented in this thesis, the IPAP-type HSQC-TOCSY experiment [62, 63] has been used which allows measuring the sign of the couplings by the introduction of spin state selectivity [64, 65]. The α- and β-components of the $^{1}J_{\mathrm{CH}}$ couplings in these experiments are selected via spin state selective coherence transfer as described in [66, 67]. The IPAP-type HSQC-TOCSY experiment is recorded always as a set of two experiments: HSQC-TOCSY A contains both the α- and β-components for each multiplet, while the HSQC-TOCSY B is a reference experiment which allows the separation of the components. By the addition or the subtraction of these two experiments, the α- and β-components are obtained in separate experiment copies. For the extraction of the $^{\mathrm{n}}J_{\mathrm{CH}}$ coupling constants, a stepwise procedure has to be followed as schematized in **Figure 17** where the individual steps are described. The HSQC-TOCSY-IPAP experiments often contain cross peaks of different intensities, especially if the spectra have signals in the aromatic and aliphatic region. This difference in intensities has to be corrected for each row. To achieve this, identical rows are extracted from the HSQC-TOCSY A and B spectra and their intensities are scaled to adopt the same intensity. The average value of the scaling factors is then used for the addition and the subtraction of two HSQC-TOCSY experiments. The resulting subspectra are used for the extraction of $^{n}J_{\mathrm{CH}}$ coupling constants by simply measuring the displacement of a certain cross peak in the two subspectra. When this procedure is applied identically to isotropic and anisotropic samples, the extracted couplings are sign sensitive relative to the direct $^{1}J_{\mathrm{CH}} + {}^{1}D_{\mathrm{CH}}$ coupling which is usually a positive sign.

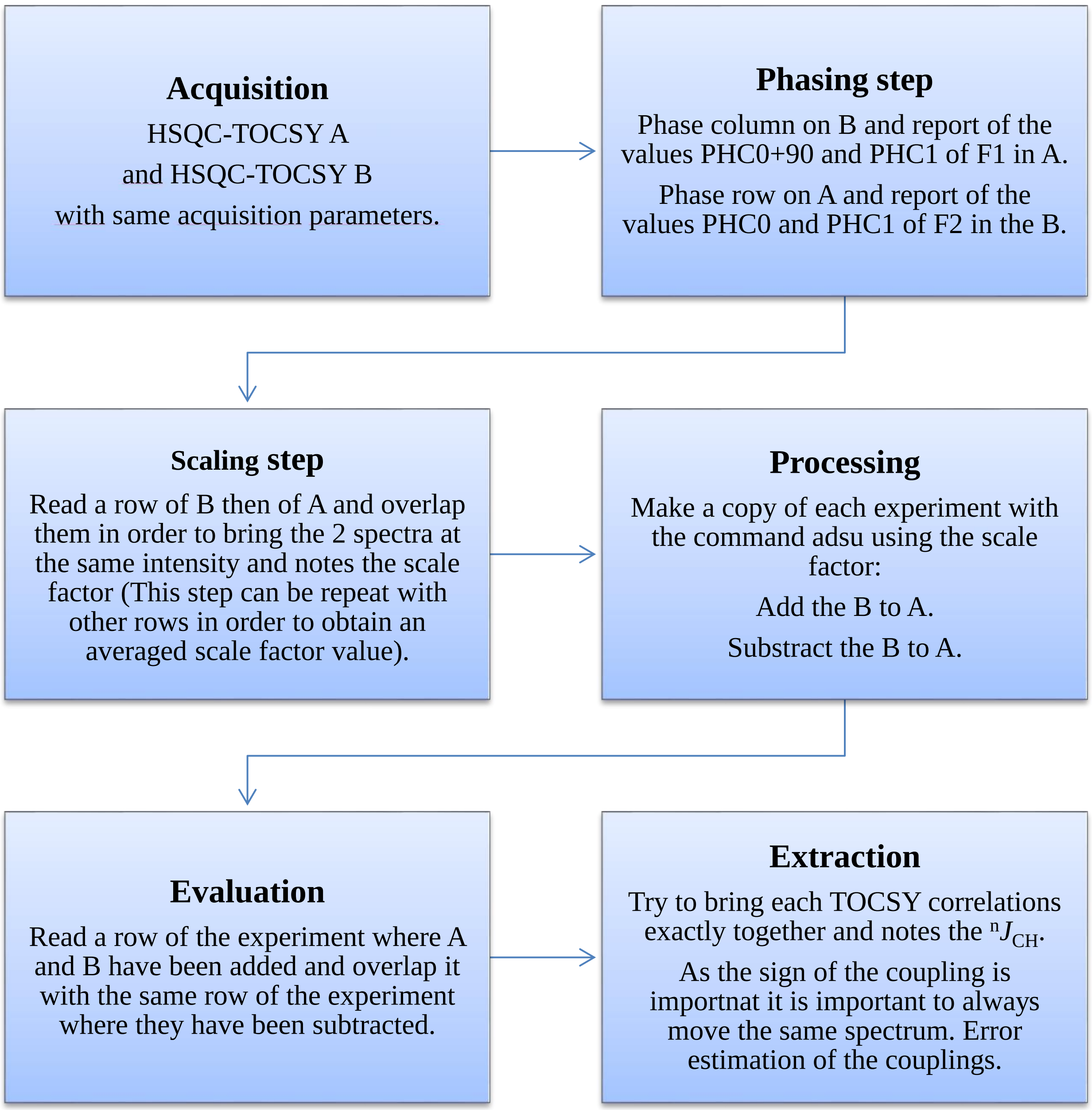

Acquisition

HSQC-TOCSY A

and HSQC-TOCSY B

with same acquisition parameters.

Phasing step

Phase column on B and report of the values PHC0+90 and PHC1 of F1 in A.

Phase row on A and report of the values PHC0 and PHC1 of F2 in the B.

Scaling step

Read a row of B then of A and overlap them in order to bring the 2 spectra at the same intensity and notes the scale factor (This step can be repeat with other rows in order to obtain an averaged scale factor value).

Processing

Make a copy of each experiment with the command adsu using the scale factor:

Add the B to A.

Substract the B to A.

Evaluation

Read a row of the experiment where A and B have been added and overlap it with the same row of the experiment where they have been subtracted.

Extraction

Try to bring each TOCSY correlations exactly together and notes the $^{n}J_{CH}$.

As the sign of the coupling is importnat it is important to always move the same spectrum. Error estimation of the couplings.

Figure 17: Procedure for the extraction of the long range RDCs $^{n}J_{CH}$ from HSQC-TOCSY experiments.

2.2.4. The interpretation of anisotropic parameters

Depending on the degree of flexibility of the studied molecule, there are different ways to analyse anisotropic parameters. The basic information which can be derived from experimentally determined anisotropic parameters such as RDCs is the averaged molecular alignment with respect to the external magnetic field.

2.2.4.1. Fitting experimental RDCs using Singular Value Decomposition

For a rigid molecule, the orientation of the molecule can be described by the alignment tensor which can be derived by mathematical methods like the singular value decomposition (SVD) [68] if a minimum set of five independent experimental RDCs are available per rigid fragment. This is the case if no more than three internuclear vectors are in a same plane and if no vectors are parallel. The alignment tensor can be also approximated by the TRAMITE prediction, with this approach the alignment tensor is assumed to coincide with the tensor of inertia [69]. Thus back calculated RDCs depend on the molecular geometry but are independent from the experimental RDCs. There are different programs that have the SVD approach being implemented, such as PALES [70, 71] and MSpin [72] with the latter being used in this thesis. MSpin program works with either single or few preselected fixed 3D conformations of the molecule under study applying the single conformer single alignment tensor fitting approach or the multiple conformer single alignment tensor fitting approach, respectively. The experimental RDCs are given as input data to the program MSpin, which allows determining the global alignment tensor using the SVD approach with the fitting of a single geometry optimized configuration or a combination of low-energy conformations. Then the alignment tensor is used to calculate the theoretical RDCs, which are compared to the experimentally determined RDCs, allowing the validation of the fitting or not. For the latter approach, a common coordinate system for all conformations is determined by the superposition of the different geometries. In this thesis, the different conformers imported to MSpin are generated for a given configuration and weighted with the energies as calculated by Maestro (Maestro, Schrödinger, LLC, New York, NY, 2016) using the molecular force-field OPLS_2005 [73, 74] in Macromodel (Schrödinger Release 2014-2: Macromodel, Schrödinger, LLC, New York, NY, 2016). The non-flexible part of the molecule in the conformational search allows defining a common frame. In this method, the single tensor approach allows the calculation of RDCs based on a single alignment tensor for an ensemble of conformers of a given configuration.

In any case, fitting a single alignment tensor to a conformational ensemble is an approximation, which successfully led to several correct configuration determinations in the past [75-77].

With the two methods implemented in MSpin for the SVD approaches, first the alignment tensor is defined using the experimental RDCs followed by back calculation of the RDCs and comparison with experimental data. The MSpin software package uses the Q value introduced by Cornilescu *et al*. [78] as a fitting criterion. This quality factor allows the relative evaluation of structural models of a predefined set with respect to each other:

$$\mathrm{Q} = \sqrt{\frac{\sum_{\mathrm{i}}\left(D_{\mathrm{calc}}^{\mathrm{i}} - D_{\mathrm{exp}}^{\mathrm{i}}\right)^2}{\sum_{\mathrm{i}}\left(D_{\mathrm{exp}}^{\mathrm{i}}\right)^2}} \tag{15}$$

However, no absolute evaluation of the fulfilment of the experimental constraints is possible. This can be much better achieved by using the quality factor n/χ^2 where n is the number of experimental RDCs and χ^2 is defined as:

$$\chi_{\mathrm{i}}^2 = \left(\frac{D_{\mathrm{calc}}^{\mathrm{i}} - D_{\mathrm{exp}}^{\mathrm{i}}}{\Delta D_{\mathrm{exp}}^{\mathrm{i}}}\right)^2 \tag{16}$$

$$\frac{\mathrm{n}}{\chi^2} = \mathrm{n}\sum_{\mathrm{i}=1}^{\mathrm{n}} \frac{1}{\chi_{\mathrm{i}}^2} \tag{17}$$

where i runs over all data points, $D_{\mathrm{calc}}^{\mathrm{i}}$ and $D_{\mathrm{exp}}^{\mathrm{i}}$ are the back calculated and the experimental values, respectively, and $\Delta D_{\mathrm{exp}}^{\mathrm{i}}$ are the experimental errors of each $D_{\mathrm{exp}}^{\mathrm{i}}$.

In this thesis, the agreement between experimental and back calculated RDCs was expressed with the value n/χ^2. A structural model that fully complies with experimental data within the experimental errors results in $\mathrm{n}/\chi^2>1$, so a value below 1 indicates that at least one experimental value is outside its corresponding experimental error which is termed an “outlier” [79]. Therefore, all $1/\chi^2$ values have to be larger than 1, which is used as a strict criterion for accepting or rejecting a solution. In addition to the n/χ^2 quality factor, the number of such outliers is provided for every structural model as another important parameter for evaluation. In the experiments described in this thesis, all experimental errors have been provided as maximum error estimates using the procedure defined by Kummerlöwe *et al.* [54]. As these error estimates correspond to a very high confidence level of approximately three times the standard deviation (3σ), a single outlier is in principle sufficient to falsify a structural model, as the model does not reproduce the experimental data within the error range.

It should be noted that RDC data interpretation using the alignment tensor concept is limited to rigid structures and only works approximately for molecules with little vibrational amplitudes. For treatment of more flexible molecules, different approaches like molecular dynamics with orientational constraints (MDOC) have to be used, as will be discussed in more detail in section 5.3.3.

2.2.4.2. Molecular dynamics with orientational tensorial constraints

The program package COSMOS used in this study has a specialized protocol for time averaged molecular dynamics (MD) simulations using orientational constraints and includes a molecular mechanics force field [80]. The orientation encoded in the tensorial constraints derived from experimental RDC values is used as a parameter for the generation of pseudo forces, which constrain the orientation of the molecule within the MD [79]. For each MDOC step, a full tensorial orientation is calculated and compared with the experimental data. Based on analytical solutions for the first and second derivative of the tensor with respect to the laboratory frame axes x, y, and z, the individual C-H bond vectors will be rotated to improve the overall pseudo energy, which depends on the difference between each calculated and experimental RDC. Setting up the MD calculation, different parameters have to be optimized, *e.g.* the maximal strength of the weighting factor (WF) of the pseudo forces and the scaling factor s_{AM}, which reduces the calculation time by avoiding unnecessary computation of isotropic tumbling of the molecule of interest. The duration of the MD has to be chosen in order to reach good convergence of the orientational constraints. During the MDOC run, the calculated $^1D_{CH}$ RDCs are written into an output file at discrete time points as defined in the MDOC settings. At the evaluation step of the MDOC run, these $^1D_{CH}$ couplings are arithmetically averaged. The n/χ^2 is then calculated from these averaged values neglecting the first nanosecond of the MDOC trajectory, which is needed for initial system equilibration. In addition, at an appropriate time, a geometry snapshot and different tests are saved as a control for the MD run. The corresponding text files contain different data such as distances between different atoms, energies, RDCs and torsion angles. The coordinates are used to evaluate the molecular modification during the MD *e.g.* the flexibility of the molecule, *i.e.* the conformational changes.

3. Materials and methods

3.1. Equipment

All NMR experiments described in this thesis were acquired at 300 K on the spectrometers listed in **Table 1**. Data processing was performed using TOPSPIN.

Table 1: NMR spectrometers used to acquire experiments described in the thesis and their specifications.

Identification	**Location**	**^{1}H Field strength**	**Console**	**Probe head with z-gradient**	**Frequency [Hz]**
A	Novartis	500 MHz	Avance III	5 mm BBFO	^{1}H: 500.09 ^{13}C: 125.75 ^{31}P: 202.44 ^{2}H: 76.77
B	Novartis	800 MHz	Avance III HD	5 mm cryo CPTCI	^{1}H: 800.15 ^{13}C: 201.20 ^{15}N: 81.08 ^{2}H: 122.83
C	Novartis	600 MHz	Avance III HD	1.7 mm cryo CPTCI	^{1}H: 600.13 ^{13}C: 150.90 ^{2}H: 92.12
D	KIT	600 MHz	Avance III	5 mm cryo CPTCI	^{1}H: 599.7 ^{13}C: 150.81 ^{2}H: 92.06
E	KIT	600 MHz	Avance II	5 mm BBI 4 mm VASS	^{1}H: 600.19 ^{13}C: 150.93 ^{2}H: 92.13

3.2. Software

Software packages used for analysis of data described in this thesis are listed in **Table 2**.

Table 2: Software packages used for data analysis.

Software	Reference/Origin	Version	Complementary Information
Topspin	Bruker Biospin GmbH, Germany	3.2 and 3.5	
MSpin	Mestrelab Research S.L. Spain http://www.mestrelab.com	Rev_201	Courtesy of Armando Navarro-Vázquez [72]
COSMOS	Cosmos GmbH http://www.cosmos-software.de	6	SVN 763
Maestro-Macromodel	Schrodinger, LLC	2015-4 2018-3	
MatLab	Mathworks	R2015a	Non-standard script of Dr. S. Ehni further modifications by Dr. P. Tzvetkova: a36_readmathematica_w.m
Mathematica	Wolfram Research	10	Non-standard script of Dr. S. Ehni further modifications by Dr. P. Tzvetkova: 05_all_Trajectories_fixJ_v1.1.nb
ACD	Advanced Chemistry Development, Inc.	2014	
MestReNova	Mestrelab Research S.L.	2012-2018	

3.3. NMR Method

Resonance assignment

For resonance assignment of spectra recorded on samples in isotropic phase, standard Bruker sequences were used to acquire 1D and 2D NMR experiments such as 1D-^{1}H, 1D-^{13}C, edited-^{1}H-^{13}C-HSQC, COSY, TOCSY, ROESY, and ^{1}H-^{13}C-HMBC.

Recorded NMR Experiments

The NMR experiments summarized in **Table 3** were carried out.

Table 3: NMR experiments recorded for the resonance assignment.

Experiments	**Standard Bruker Pulse Programs**	**Specifications**	**References**
^{1}H-NMR	zg30	1D ^{1}H experiment with 30-degree pulse	
^{13}C-NMR	zgpg	1D ^{13}C experiment with ^{1}H-broadband-decoupling	
^{1}H,^{1}H-COSY	cosygpmfphpp	2D homonuclear phase sensitive experiment with double quantum filter	[81]
^{1}H,^{1}H-ROESY	h-roesy_2.3_pp	2D homonuclear phase sensitive experiment with 180x/180-x spin-lock including a purge pulse	[82, 83]
^{1}H,^{13}C-ed-HSQC	hsqcedetgpsisp2.2	2D HSQC experiment with multiplicity editing, ^{1}H detection and z-gradient	[84]
^{1}H,^{13}C-HMBC	hmbcgplpndqf	2D HMBC experiment with ^{1}H detection and z-gradient	[85]
^{1}H,^{15}N-HMBC	hmbcgplpndqf	2D long range ^{1}H,^{15}N correlation. HMBC experiment with ^{1}H detection and z-gradient	[85]
^{31}P-NMR	zgpg30	1D ^{31}P experiment with power-gated decoupling using 30 degree	

4. 3 mm stretching and swelling devices

In biomedical research, tested compounds are typically synthetic or natural products which can be challenging to analyse because of their structural complexity due to the presence of several chiral centres, several rings, and non-active NMR nuclei. Often only a small quantity is dedicated for analytical characterization. To elucidate the correct structure and stereochemistry, RDC measurements can be determined to complement the standard NMR parameters such as chemical shifts (CS), scalar couplings and NOEs. To measure RDCs, a preferred orientation has to be introduced in the sample, which is achieved via a weak alignment in an anisotropic medium. The strength of the alignment and its adjustment play a crucial role in achieving the best resolution and precise RDC measurements, as described in detail in the previous sections, and the most convenient way to vary the alignment, using only a single aligned sample, is the usage of a stretching device. Such devices were developed and implemented for 5 mm tubes. However, in case the sample is only available in limited quantities and increased sample homogeneity is desired, it would be advantageous to utilize smaller tubes. In this chapter, the development of a stretching device with a novel lock suitable for 3 mm NMR tubes is presented. In addition, a swelling device is described which was developed to prevent sample loss due to unsuccessful alignment of the sample.

4.1. Design of the 3 mm stretching device

The original 5 mm stretching device of Kummerlöwe *et al.* [36] has been used as a template for the design of the 3 mm device. Like the 5 mm device, a flexible silicone rubber tube is placed in an open-cut 3 mm NMR tube and fixed at the bottom with a Teflon® plug but the upper fixing of the stretched state is achieved with a novel Teflon lock for the 3 mm NMR tubes. All these components have been adapted and redesigned.

4.1.1. Properties of the silicone rubber tube

The three and five mm silicone rubber tubes were purchased from J. Lindemann GmbH in Germany (www.lindemannsilikon.de). The three mm silicone tube has an inner diameter (ID) of 1 mm and a wall thickness (WS) of 0.5 mm; hence, the outer diameter of the silicone tube is 2 mm and it has a hardness of 60° Shore A (for a schematic representation see **Figure 18**). The silicone needs to be stretchable, but strong enough to avoid a breakage of the silicone during stretching.

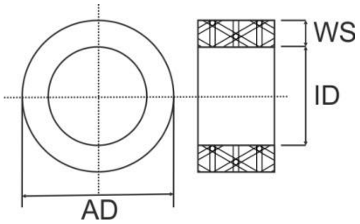

Figure 18: Technical description of the silicone rubber tube.
ID for inner diameter, WS for the wall thickness and AD for the outer diameter. For the 3 mm stretching device ID=1 mm, WS=0.5 mm and AD=2 mm was used.

An important consideration is the compatibility with the used solvents. Like the silicone used for the 5 mm stretching device, the silicone rubber tube used for the 3 mm device swells in apolar solvents like $CDCl_3$ while in DMSO the length and the diameter of the silicone tube remains unchanged (**Figure 19**). Therefore, the use of the stretching device is recommended for polar solvent only.

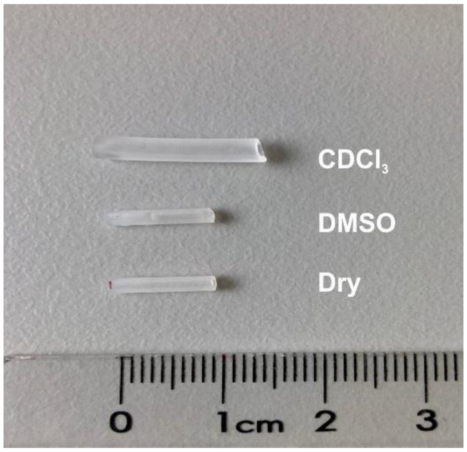

Figure 19: Impact of apolar solvents on silicone tubes used in this study.
1 cm of silicone rubber tubing was left in DMSO and $CDCl_3$ for 4 hours at room temperature in closed vials. The silicone is swelling in both horizontal and perpendicular directions by approximately 50% of the original size in presence of $CDCl_3$ while it stays at the original size in DMSO.

4.1.2. Properties of the Teflon plug

The T-shaped Teflon plug is similar to the plug used for the 5 mm; however it has been reduced in size in order to be compatible with smaller silicone tube. The plug reduction has been performed by Matthias Brechbuehl from the engineering centre of NOVARTIS. In **Figure 20**, the blueprints of the plug as seen from above (A) and from the side (B) are shown together with a photograph of the plug (C). The dimensions are given with letters and they are summarized in the **Table 4** for the 3 and 5 mm devices.

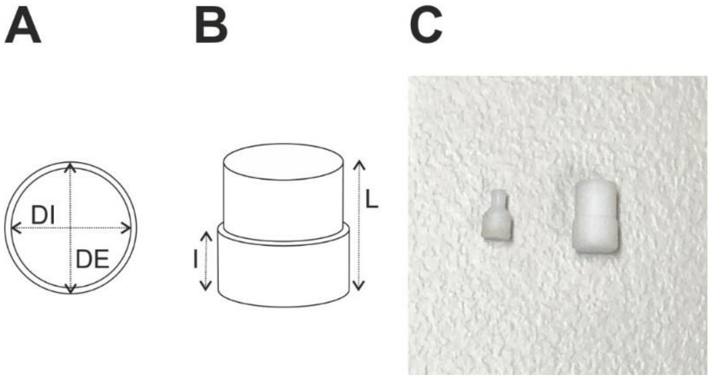

Figure 20: T-shaped Teflon plug.
In panel **A**, a blueprints from the top of the plug is shown and in panel **B** a blueprint from the side and in panel **C** a photograph of the 3 and 5 mm plugs. DI corresponds to the diameter of the small cylinders and DE of the big cylinders of the plugs.

Table 4: Dimensions of the T-shaped Teflon plugs for 3 and 5 mm stretching devices.

	For 3 mm device [mm]	**For 5 mm device [mm]**
DI	1.2	3.6
DE	3.0	4.0
L	4.0	5.3
l	2-0	2.0

4.1.3. The Teflon lock

The novel Teflon lock consists of a cylinder with a hole in the middle allowing the silicone rubber tube to let through (**Figure 21A**). Once inserted, the stretched tube will be blocked and closed with a removable arm (**Figure 21B**). In **Figure 21C**, a photograph of the Teflon lock is shown. The lock has been designed in order to be placed on the 3 mm cap which also has a hole allowing the silicone rubber tube to let it through. This design enables the Teflon lock to be stabilized using it on top of Bruker SampleJet caps.

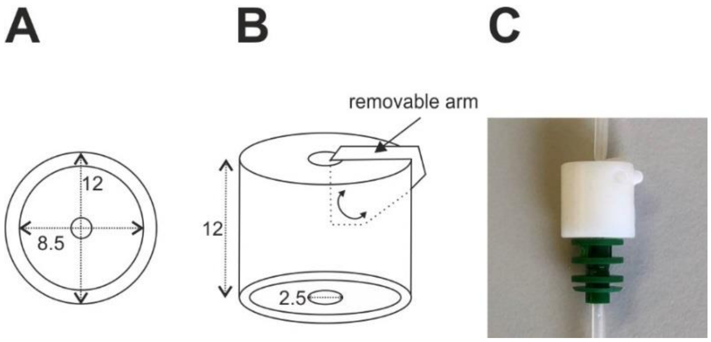

Figure 21: Design and dimension of the novel Teflon lock.
Panels **A** and **B** show the lock from the top and the side, respectively, and provide the individual dimensions in mm. A photograph of the white Teflon lock with the rest of the stretching device is shown in panel **C**.

4.2. Evaluation of the 3 mm stretching device

To demonstrate the applicability of the newly developed 3 mm device, a small molecule with two chiral centres was aligned in a PAA gel prepared with the desired diameter. Once the sample was equilibrated, different NMR experiments were acquired and the performance of stretching device assessed by feasibility of measuring RDCs and assigning the relative stereochemistry of the molecule.

4.2.1. Molecule

4-(Phosphonomethyl)-2-piperidinecarboxylic acid is an approved drug commercialized under the name Selfotel and was used as a test molecule as racemic mixture. It is soluble in water, contains two stereogenic centers and enables the determination of more than 5 independent ${}^{1}D_{CH}$ RDCs. The structure and the numbering used are depicted in **Figure 22**.

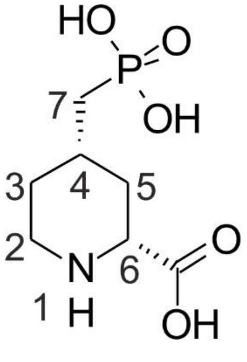

Figure 22: Chemical structure and numbering of 4-(Phosphonomethyl)-2-piperidinecarboxylic acid.

4.2.2. Alignment medium

A polyacrylamide (PAA) gel was chosen as alignment medium due to its easy preparation [41, 28, 23]. The gel was prepared by the standard polymerization reaction (**Figure 23**) using the quantities of the individual components provided in **Table 5**.

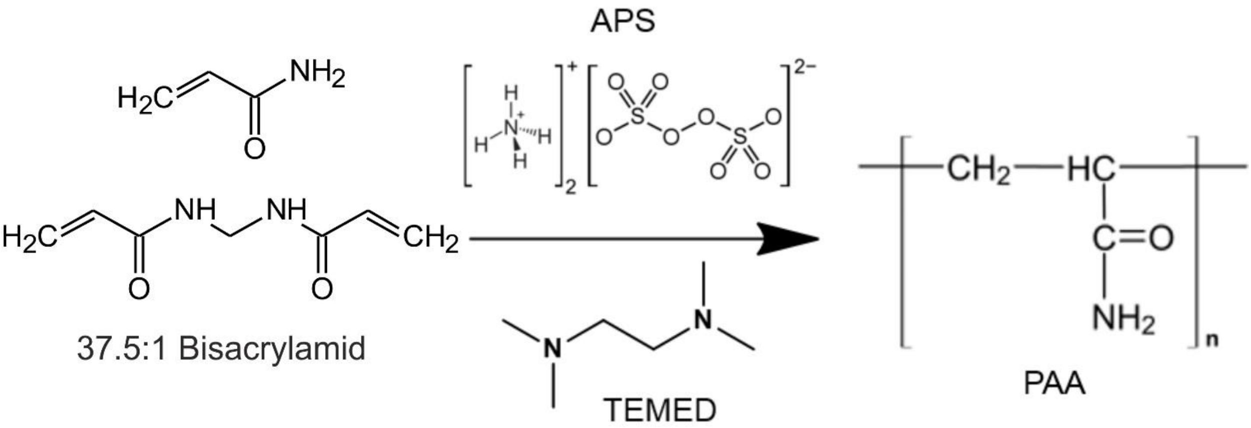

Figure 23: Chemical reaction for the preparation of the polyacrylamide gel.
37:1 Bisacrylamid corresponds to a mixture of acrylamide (primary amid) and bis-acrylamide (secondary amide) with a ratio of 37.5:1

Table 5: Reactants and reagents used for the synthesis of the PAA gel.
Rotiphorese® Gel 30 (37.5:1) Art Nr: 3029.1 from ROTH is ready-to-use, gas stabilized and contains aqueous, 30 % acrylamide and bisacrylamide stock solution at a ratio of 37.5:1.

	Molecular Formula	**Molecular Weight [g/mol]**	**Volume [µL]**	**Density**
Rotiphorese® Gel 30 (37.5:1)			336	
Ammonium-persulfate APS	$(NH_4)_2S_2O_8$	228.18	2	1.98 g/cm^3
Tetramethylethylenediamine TEMED	$C_6H_{16}N_2$	116.20	1	0.7765 g mL^{-1} (at 20 °C)

The three reactants were mixed in an Eppendorf tube and transferred quickly into the tubing (3 or 5 mm) in order to obtain the desired diameter during the polymerization. Then, they were placed horizontally into a hood until the polymerization was finished in approximately one day, and subsequently cut to the desired length. Gels for the 3 and the 5 mm devices were prepared simultaneously for side-by-side comparison.

4.2.3. Experimental part

4.2.3.1. Sample preparation

The NMR sample for the assignment of the molecule was prepared by dissolving 2.2 mg of Selfotel (Novartis compound archive) in 280 µL deuterium oxide containing TSP-d_4 (1 mg/mL) as a reference substance. 40 µL of this solution was transferred into a 1.7 mm NMR sample tube and a set of isotropic reference and assignment NMR experiments was performed.

For measuring RDCs with the 3 and the 5 mm devices, a stock solution of Selfotel was prepared by dissolving 8 mg in 1 mL of deuterium oxide (D_2O) leading to a final concentration of 35.86 mM. The isotropic and anisotropic samples were prepared from the stock solution for the extraction of RDCs. 3 and 5 mm stretching devices were prepared with a 15% polyacrylamide gel at as described in section 4.2.2. Once completely dried, the gel was placed into the stretching device, then 250 µL and 70 µL of Selfotel stock solution were added to the 5 and 3 mm stretching device, respectively. Afterwards, the stretching devices were left for one week at room temperature in order to let the gel swell and to achieve a homogeneous distribution of the molecule within the gel.

4.2.3.2. NMR experiments

For the assignment and validation of the compound structure, ^{1}H and ^{13}C detected 1D and 2D NMR spectra were recorded at 300K using a Bruker 600 MHz AVANCE III HD spectrometer equipped with a 1.7 mm CPTCI inversely detected ^{1}H,^{13}C,^{15}N triple resonance cryogenically cooled probe with actively shielded z-gradients (spectrometer C in **Table 1**). ^{31}P NMR spectra were recorded on a Bruker Avance III spectrometer (spectrometer B in **Table 1**) with a 5 mm BBFO probe. All spectra were referenced setting the TSP methyl group signal to 0 ppm. ^{31}P and ^{15}N shifts were referenced by using phosphoric acid and urea as external standards by setting their signals to 0.0 ppm (^{31}P) and 75.0 ppm (^{15}N), respectively.

The ^{1}H NMR spectrum of Selfotel contained 8 signal groups besides the D_2O (4.77 ppm) and TSP (0 ppm) background signals. Integration of these 8 groups showed the presence of 10 protons. The ^{13}C NMR spectrum shows a total of 7 signals besides the TSP (0 ppm) resonance, while one nitrogen signal was observed in ^{1}H-^{15}N-HMBC spectra, as expected.

Structural elements and the molecular constitution were determined based on chemical shift values and identified spin systems. The connectivity of the individual elements was determined based on COSY, ROESY and HMBC data. The obtained ^{1}H, ^{13}C and ^{15}N chemical shifts and integration values are summarized in **Table 6**.

Table 6: ^{1}H, ^{13}C, ^{15}N, and ^{31}P NMR assignments of Selfotel in D_2O.
Atom numbering is according to **Figure 22**, and the following abbreviation are used: br (broad), s (singlet), d (doublet), t (triplet), q (quartet), m (multiplet), ^{a} overlaid).

Atom	**Group**	**^{1}H**				**^{13}C**	**^{15}N**	**^{31}P**
		δ [ppm]	Mult	*J* [Hz]	*Int*	δ [ppm]	δ [ppm]	δ [ppm]
1	N						43.1	
2	CH_2	3.04	t	12.1, 14.8	1H	46.3 (s)		
		3.47	d	12.1	1H			
3	CH_2	1.41	m^{a}		1H	31.8 (d, *J* = 8.7 Hz)		
		2.15	d	14.3	1H			
4	CH	2.03	m		1H	33.1 (d, *J* = 2.9 Hz)		
5	CH_2	1.41	m^{a}		1H	36.7 (d, *J* = 12.4 Hz)		
		2.45	d	14.0	1H			
6	CH	3.74	dd	12.9, 1.4	1H	61.4 (s)		
7	CH_2	1.67	m		2H	36.9 (d, *J* = 133.2 Hz)		
8	C					176.3 (s)		
9	P							23.8
10	OH	Not Visible						
12	OH	Not Visible						
14	OH	Not Visible						

The observed connectivities are illustrated in the correlation scheme in **Figure 24**. ^{1}H, ^{13}C and ^{15}N spectra are consistent with the number and type of protons and carbons defined by the depicted structure of Selfotel. The ^{1}H, ^{13}C, ^{31}P and 2D spectra of Selfotel are shown in section 9.4.1, in the appendix.

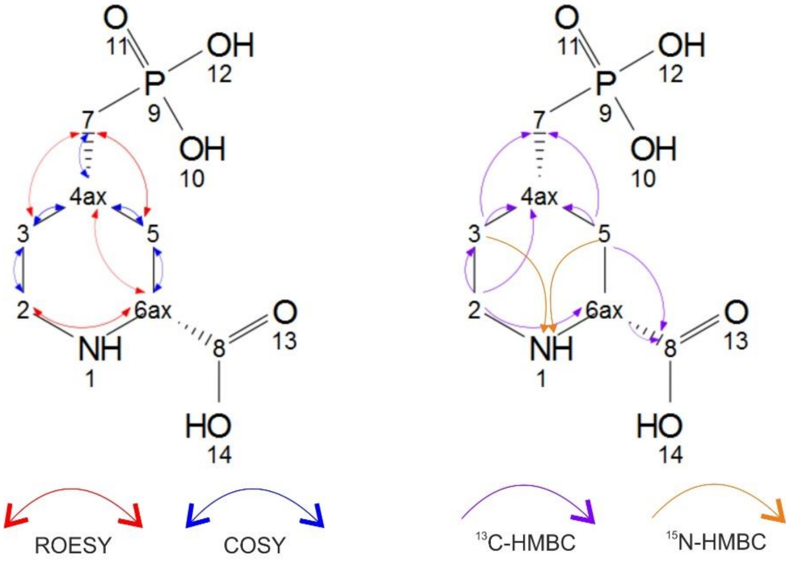

Figure 24: Correlation schemes showing NMR connectivities.
On the left side, the homonuclear ROESY and COSY correlations are given with red and blue arrows, respectively. On the right side the heteronuclear ^{13}C- and ^{15}N-HMBC are given with violet and orange arrows, respectively.

Selfotel can have two different relative configurations in which the protons 4 and 6 can be either *trans*- or *cis*-. According to the observed NOE between protons 4 and 6 and the coupling constant of these two protons, 12.9 Hz for CH-6, it can be concluded that they are both axial and in the same plane. Hence, Selfotel is present in the *cis*-configuration and the piperidine has the chair conformation.

Experimental set up for the 3 mm device:

In order to compare the 3 mm device with the 5 mm device with regards to the linearity of the quadrupolar splittings with the extension factor, both samples were measured at different stretching states. The splitting and homogeneity was assessed by observing the deuterium signal of the solvent. A well equilibrated and aligned sample will display a symmetric solvent signal and an appropriate linewidth which is not too broad at half height. The set of deuterium spectra measured using the 3 and 5 mm devices at different gel lengths are shown in **Figure 25**.

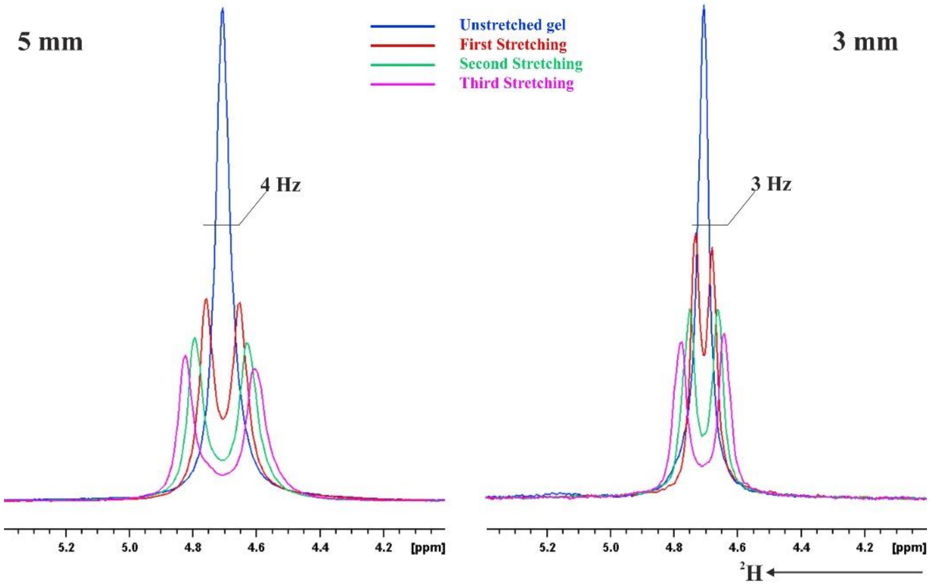

Figure 25: Deuterium spectra of D_2O measured at different stretching strengths with the 3 and the 5 mm stretching devices.
In black is the deuterium spectra obtained without stretching the gel. The D_2O peak is symmetric and has a linewidth of approximately 3 Hz and 4 Hz at half height in all cases with the 3 and 5 mm devices, respectively.

The extension factors Ξ calculated from the equation (13) proportional to the gel lengths and the quadrupolar splittings obtained from these spectra allow to show the linearity of the stretching for the 3 and 5 mm devices (see **Figure 26** and **Table 7**). Indeed, the quadrupolar splitting varies linearly with the extension factor (Ξ) for both stretching devices as shown on **Figure 26**. The signal obtained from the 3 mm device are much sharper with a linewidth of 3 Hz at half height while for the 5 mm device the best linewidth reached is 4 Hz. A better resolution with the 3 mm device is reached, this can be explained by easier shimming with the smaller tube and a more homogeneous gel in the smaller volume.

Table 7: Extension factors obtained from the gel lengths in the 3 and 5 mm devices.
The gels were stretched to different lengths, and the corresponding extension factors and measured quadrupolar splittings are reported.

	3 mm device			**5 mm device**		
	Gel Length [cm]	**Quadrupolar Splitting [Hz]**	**Extension Factor Ξ**	**Gel Length [cm]**	**Quadrupolar Splitting [Hz]**	**Extension Factor Ξ**
Unstretched	4.60	0	0	5.2	0	0
1st Stretching	5.15	3.9	0.12	5.6	2.3	0.08
2nd Stretching	6.00	6.8	0.30	6.3	8.0	0.21
3rd Stretching	6.60	10.6	0.43	7.0	12.7	0.35
4th Stretching				8.5	16.9	0.44

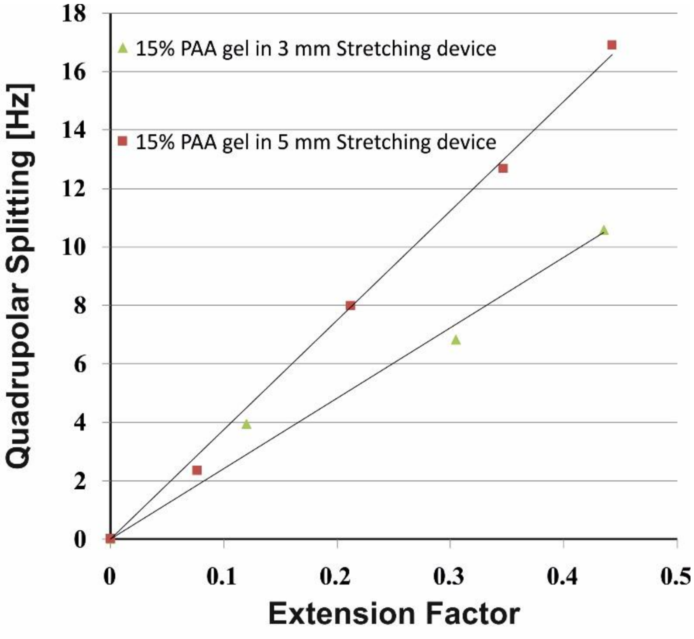

Figure 26: Scaling of the alignment strength dependent on the extension factor with the 3 and 5 mm stretching devices.
The quadrupolar splittings $\Delta\nu_Q$ of the solvent signal were measured at different gel lengths and plotted against the extension factor.

Once the homogeneity of the gels and linearity were demonstrated, CLIP-HSQC experiments were measured on samples in both the 5 and 3 mm devices using the spectrometer B in **Table 1** (For the spectra see **Figure 75** and **Figure 76** in the appendix). Next, the total couplings $^1T_{CH}$ Selfotel from the anisotropic samples were extracted and the values obtained according to the process described in section 2.2.3 are reported in **Table 8**. In addition, a sample of Selfotel dissolved in D_2O was measured to obtain the scalar couplings $^1J_{CH}$ in the isotropic state (**Figure 74** in the appendix).

Table 8: Chemical shifts of Selfotel in D_2O and one-bond ^1H, ^{13}C-couplings for Selfotel in D_2O and in the stretched 15 %-PAA/D_2O-gels.
Atom numbering is according to **Figure 22**. Several couplings were not determined due to overlap of Selfotel signals with the signal of the gel.

	Isotropic Sample				**Anisotropic Samples**					
	5 mm NMR Tube				**3 mm device $\Delta\nu_Q$ = 9.5 Hz**			**5 mm device $\Delta\nu_Q$ = 23 Hz**		
Assignment	**δ(H) [ppm]**	**δ(C) [ppm]**	**$^1J_{CH}$ [Hz]**	**Error [Hz]**	**$^1T_{CH}$ [Hz]**	**Error [Hz]**	**$^1D_{CH}$ [Hz]**	**$^1T_{CH}$ [Hz]**	**Error [Hz]**	**$^1D_{CH}$ [Hz]**
CH(3’)	1.37	28.8	128.39	0.3	130.78	2.0	2.40	129.22	0.3	0.83
CH(3”)	2.08	28.8	132.51	0.4	126.93	0.3	-5.58	134.40	0.8	1.89
CH(4)	2.00	29.9	132.65	0.3	134.55	3.0	1.90	130.41	1.2	-2.24
CH(5’)	1.40	33.3	129.03	0.5				130.09	1.0	1.06
CH(5”)	2.43	33.3	135.90	1.0	132.77	2.0	-3.13	130.99	1.0	-4.91
CH(7’)	1.66	33.0	125.34	0.5						
CH(7”)	1.64	34.1	124.23	0.5						
CH(2’)	3.00	43.4	142.93	0.6				145.34	0.3	2.41
CH(2”)	3.43	43.4	145.91	0.3	143.47	1.0	-2.44	142.19	0.6	-3.72
CH(6)	3.80	57.7	144.75	0.3	144.68	0.3	-0.07	148.36	2.0	3.61

Residual dipolar couplings were obtained from the 15% PAA gel with the 3 and 5 mm devices. The RDCs obtained are small and in the range of the errors of the largest error between the scalar and the total couplings. Therefore, these anisotropic data were not used in order to determine the stereochemistry of Selfotel which was done with a 30% PAA gel in order to increase the alignment of Selfotel in a 5 mm stretching device. The results are given in the section 5. As the goal of this study was the development of the 3 mm stretching device and its evaluation, supplementary steps have not yet been performed for Selfotel in the 3 mm device.

The preparation of 3 mm gels is currently subject to further improvement, because gel swelling and equilibration can take up to several weeks. Without a defined and robust protocol for gel preparation, there is a chance of breaking the gel in the process, making it unusable. Therefore, it is advantageous to swell the gel in the absence of the analyte molecule, which is then added after the gel is fully equilibrated. In this case, the gel is prepared outside the NMR tube in a dedicated swelling device, which is described in the following section.

4.3. The swelling device

For a valuable sample, it is preferable to swell the gel before the addition of the compound. In principle, this could be done directly in the stretching device, but if the swelling and the equilibration of the gel takes an extended time (several weeks), it is preferable to perform this in a watertight environment. The swelling device is made of Kel-F/PCTFE, a material resistant to major organic solvents. It is a cylinder with a hole of 2.80 mm inside with two screws caps, the design and all dimensions are given in **Figure 27**. This devices has been designed in collaboration with Muhammet Ali Sağer and made by Matthias Brechbuehl from the engineering centre of NOVARTIS.

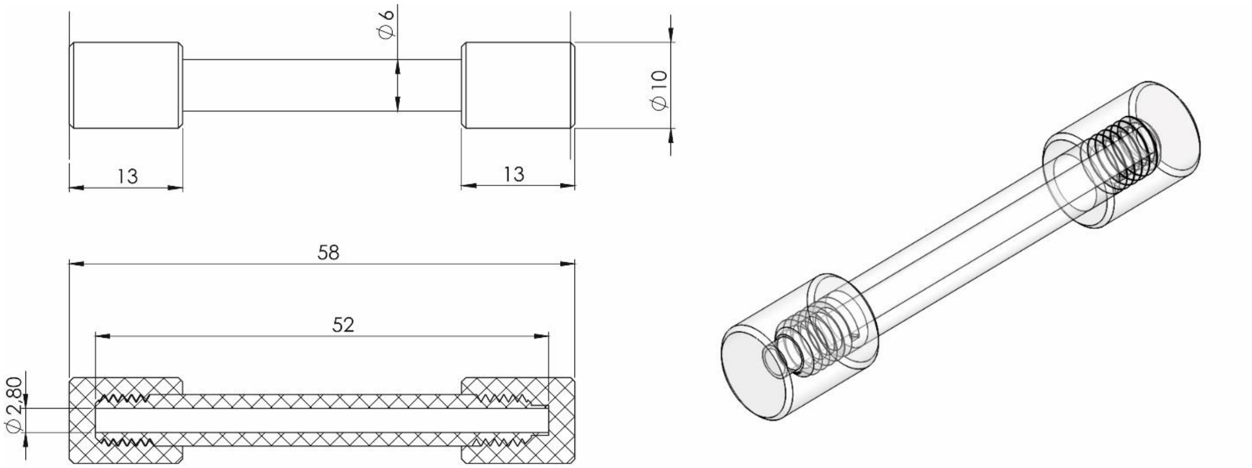

Figure 27: Design and dimensions of the swelling device.
The dimensions are given in mm.

The gel and the desired solvent are introduced in the device which is closed and it is left to swell. Once swollen, the gel is transferred into the flexible tube by pushing it or with the help of a syringe (**Figure 28**).

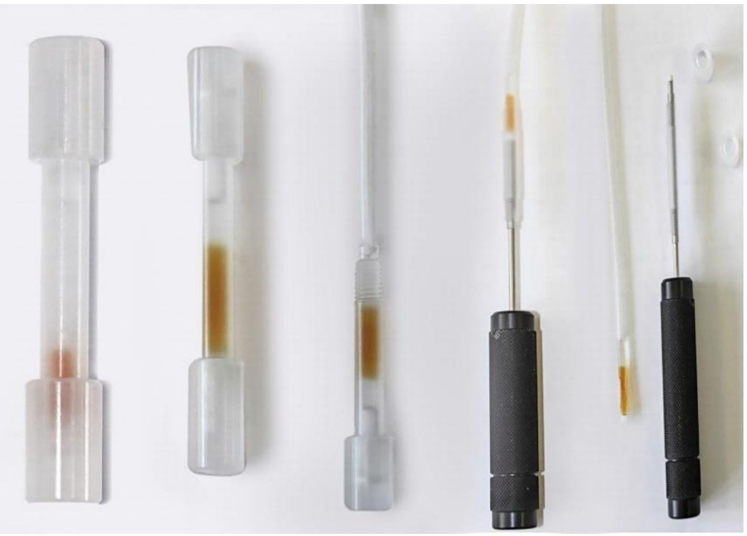

Figure 28: Procedure to transfer a swollen gel from the swelling device to the tubing.

4.4. Conclusion

The 3 mm stretching device allows adjusting the degree of alignment to the right strength in order to measure anisotropic parameters with high accuracy. The advantages are the requirement for less substance, the homogeneity of the alignment, and potentially the use of shorter radiofrequency (rf) pulses. With the 3 mm device, the shimming steps between each stretching steps were faster compare to the 5 mm device. In addition, the linewidths at half height for the spectra obtained with the 3 mm devices were smaller compared to the spectra obtained with the 5 mm device. One disadvantage is the increased measurement time due to use of less substance. Due to the diminution of the inner diameter compare to the 5 mm silicone tubing, the sample volume will also decrease, which becomes even more significant when the silicone is stretched.

The gel swelling equilibration is the longest and least controllable step during sample preparation. The novel swelling device allows swelling the gel in advance and in the absence of the analyte. Therefore, the gel can be transferred and tested before the addition of the molecules to be studied. The way to use it is straightforward. The device is produced for the moment only for the 5 mm stretching device and it is not available for a 3 mm stretching device. The preparation of a corresponding swelling device with 1 mm inner diameter turns out to be difficult using standard mechanical tools but might be possible with specialized techniques, which are currently under investigations.

5. Relative configuration determination of natural products

Natural products play a critical role in drug discovery as they provide access to new chemotypes and structural diversity. Such substances are derived from a large range of organisms and tested for the desired *in vitro* or *in vivo* activity towards molecular targets or in disease models. In order to take advantage of natural products as potential drug candidates, their exact chemical structure and configuration need to be known. This knowledge will allow to synthetize them in larger quantities and to consider structural isomers allowing structure activity relationship exploration (SAR). The analysis of SAR enables the determination of the chemical group responsible for evoking a target biological effect in the organism. Structure and configuration determination can be achieved by X-ray crystallography, if sufficient material is available and diffracting crystals are obtained. The crystallisation step is a time consuming process and in many cases it is not possible at all. Therefore, NMR spectroscopy is a prevalent technique for determining the chemical structure of natural products. However, investigating the configuration of molecules containing many stereocenters is often not possible based on traditional NOE data and coupling patterns. In such cases, complementary NMR data needs to be recorded and interpreted. In recent years, residual dipolar couplings have become an attractive source of such additional data [34, 86, 77, 87]. In this section, 3 different natural products were studied: Selfotel (**Figure 22**) which allowed evaluating the 3 mm stretching device in the section 4 of this thesis and 2 derivatives of the natural product Reserpine.

The investigated reserpine derivatives RD-1 and RD-2 have the systematic name: (1*S*,4*R*,5a*S*,14b*R*,15a*S*,16*R*)-12,16-dimethoxy-4,5,5a,6,8,9,14,14b,15,15a-decahydro-1,4-methanoindolo[2,3-a]oxepino[4,5-g]quinolizin-2(1H)-one and (1*S*,4*R*,5a*S*,14b*S*,15a*S*,16*R*)-16-hydroxy-12-methoxy-2-oxo-1,4,5,5a,6,7,8,9,14,14b,15,15a-dodecahydro-2H-1,4-methanoindolo[2,3-a]oxepino[4,5-g]quinolizin-7-ium. The structure and the numbering used in this study are depicted in **Figure 29** for RD-1 and in **Figure 30** for RD-2 (please note the numbering scheme deviates from the IUPAC numbering of the compound).

The reserpine derivatives 1 and 2 (RD-1 and RD-2) represent natural product where the assignment of the relative stereochemistry was not possible using traditional NMR analysis. Reserpine is a well-known alkaloid found in the roots of *Rauwolfia serpentina* and *Rauwolfia vomitoria* [88, 89]. Pseudoreserpic acid derivatives are useful as sedatives and antihypertensives [90, 91].

All these molecules contain a tertiary amine, which is part of a quinolizidine system (see **Figure 29**), *i.e.* two fused cyclohexane rings with a nitrogen at the bridgehead position. RD-1 and RD-2 have the same skeleton, RD-1 has a methoxy group on the oxygen numbered 28 while for RD-2 at this position there is an alcohol. RD-2 is a hydrochloride salt protonated on the amine of the quinolizidine while RD-1 is the neutral form. These two reserpines were chosen due to their differences concerning their chirality which play a role in the flexibility.

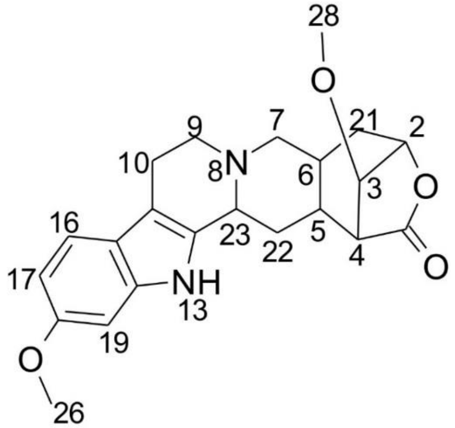

Figure 29: Chemical structure and numbering used in this study of Reserpine Derivate 1 (RD-1).

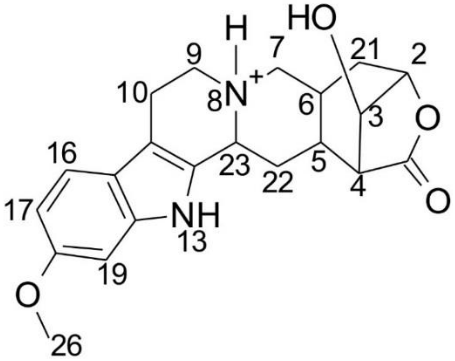

Figure 30: Chemical structure and numbering used in this study of Reserpine Derivate 2 (RD-2).

In total, the two molecules each contain 7 stereocenters including the tertiary amine, which is treated as an additional chiral centre. It is known that inversion of the nitrogen pyramid in amines can readily take place via a change in sp^3 hybridization of the nitrogen atom by passing through a planar sp^2 state [92, 93]. While in most amines this inversion process is too fast to be detectable by NMR, in some cases suitable substituents can sufficiently stabilize the two interchanging states and allow the separation of the two isomers. The timescale of interconversion was not known for RD-1 and RD-2 at the beginning of the study, indeed the proton NMR spectrum of RD-1 shows only one conformer, while two conformers are visible for RD-2 on the ^{1}H NMR spectrum while the LC-MS spectrum shows only one compound as shown on **Figure 31**. The scalar couplings of the CH around the amine for the reserpine derivatives allow supposing a stabilization of the tertiary amine. For these two molecules, it was initially not obvious which of the cases applies, fast inversion or presence of just one conformation. RD-2 is protonated on the tertiary amine, indeed it is a hydrochloride salt while RD-1 is the neutral form, the second conformer presents for RD-2 can be due to the chirality of the NH+.

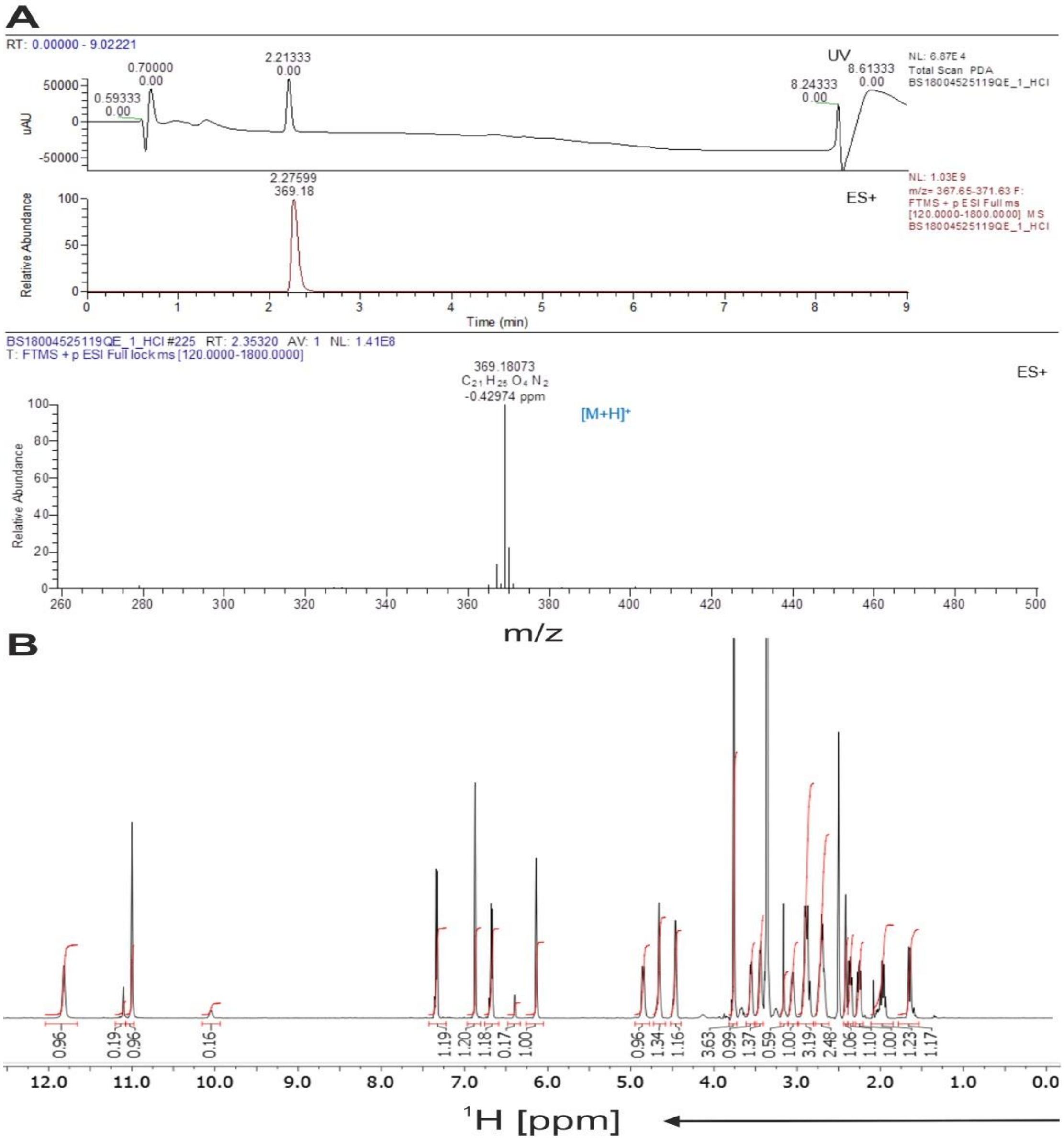

Figure 31: LC-MS and ^{1}H proton NMR spectrum of RD-2.
On the panel **A**, LC-MS spectrum of RD-2 is given and in panel **B** the ^{1}H proton NMR spectrum of RD-2 is shown where two conformers are visible.

The aim of the study was the reliable determination of the relative stereochemistry of the reserpine derivatives (RD-1 and RD-2) and the determination of the interconversion of the tertiary amine. The establishment of a protocol that could be applied in the same way to other similar relatively complex molecules which exhibits a certain degree of flexibility is described. To achieve this, first the relative stereochemistry of Selfotel has been studied then the more complex Reserpine derivatives. Different computational methods for RDC-based configurational analysis using the programs MSpin [72] and COSMOS [94, 95] were also compared.

The following work shows that the determination of the relative stereochemistry of the two seven stereocenter reserpine derivatives RD-1 and RD-2 and of Selfotel can be achieved by all three applicable MSpin and COSMOS RDCs analytical methods. However, significant differences were observed concerning the fulfilment of experimental constraints and the related treatment of the inherent flexibility of the reserpine derivatives. The potential inversion and stereochemistry of the tertiary amine by $^1J_{CH}$ and $^1D_{CH}$ couplings is revealed and a detailed comparison of the static versus the molecular dynamics based approaches as tools for the analysis of relative configuration and conformation of complex molecules with inherent flexibility is given. The NMR-based configuration is verified by X-Ray analysis which has been performed simultaneously.

5.1. Stereochemistry determination of Selfotel

A sample was prepared with a 30% PAA gel in order to increase the alignment of Selfotel and measured in the 5 mm stretching device while the samples in the section 4 were prepared with a 15% PAA gel. With this sample, a quadrupolar splitting of 51 Hz was achieved for the D_2O signal and larger RDCs were obtained for the test compound as summarized in **Table 9**.

Table 9: Chemical shifts of Selfotel in D_2O and one-bond ^{1}H, ^{13}C-couplings for Selfotel in D_2O and in the stretched 30 %-PAA/D_2O-gels.

Atom numbering is according to **Figure 22**. Several couplings were not determined due to overlap of Selfotel signals with the signal of the gel.

	Isotropic medium				**Anisotropic medium**		
	5 mm NMR tube				**5 mm device - $\Delta\nu_Q$ = 51 Hz**		
Assignment	**δ(H) [ppm]**	**δ(C) [ppm]**	**$^1J_{CH}$ [Hz]**	**Error [Hz]**	**$^1T_{CH}$ [Hz]**	**Error [Hz]**	**$^1D_{CH}$ [Hz]**
CH(3’)	1.37	28.8	128.4	0.3	137.4	1.5	9.0
CH(3”)	2.08	28.8	132.5	0.4	134.5	0.5	2.0
CH(4)	2.00	29.9	132.6	0.3	141.0	1.2	8.4
CH(5’)	1.40	33.3	129.0	0.5	137.5	6.0	8.5
CH(5”)	2.43	33.3	135.9	1.0	129.9	0.5	-6.0
CH(7’)	1.66	33.0	125.3	0.5			
CH(7”)	1.64	34.1	124.2	0.5			
CH(2’)	3.00	43.4	142.9	0.6	149.2	2.0	6.3
CH(2”)	3.43	43.4	145.9	0.3	135.5	0.8	-10.4
CH(6)	3.80	57.7	144.8	0.3	151.9	1.0	7.1

The relative configuration of Selfotel was verified by applying the experimentally derived RDCs with the programs MSpin and COSMOS as described in section 2.2.4. The calculated values obtained via the two software packages are summarized in **Table 10**.

Table 10: Experimental and computed RDC values for Selfotel.

Atom numbering is according to **Figure 22**. [a] Experimental values. [b] Experimental errors [c] computed values obtained with MDOC approach and [d] values obtained by SVD approach.

	Experimental Data		**COSMOS**		**MSpin**	
Couplings	**D_{exp} [Hz][a]**	**Error [Hz][b]**	**D_{calc} [Hz][c]**		**D_{calc} [Hz][d]**	
			cis	*trans*	*cis*	*trans*
CH(3’)	9.0	1.5	8.5	8.3	8.5	6.6
CH(3”)	2.0	0.5	1.7	1.4	2.2	1.5
CH(4)	8.3	1.2	8.2	7.1	7.0	7.8
CH(5’)	8.5	6.0	7.8	7.4	7.9	7.5
CH(5”)	-6.0	0.5	-6.5	-7.1	-6.3	-6.5
CH(2’)	6.3	2.0	8.8	8.9	7.3	7.5
CH(2”)	-10.5	0.8	-9.2	-9.7	-10.2	-10.5
CH(6)	7.1	1.0	7.1	7.1	8.4	8.8

Subsequently, the n/χ^2 quality factor values were calculated based on the output of the two approaches and summarized as shown in **Figure 32**. n/χ^2 values are above 1 for the *cis*-conformation with both COSMOS and MSpin, whereas values are below for the *trans*-conformation. This substantiates the earlier finding which was based on analysis of NOE data. A plot displaying calculated and experimental RDCs shows qualitatively good correlation of the data for the *cis*-conformation (**Figure 33**). A detailed analysis revealed that 2 calculated values don’t fit the corresponding experimental data for the *cis*-conformation, while for the *trans*-conformation four calculated values are outside its corresponding experimental error (highlighted in red in **Figure 33**).

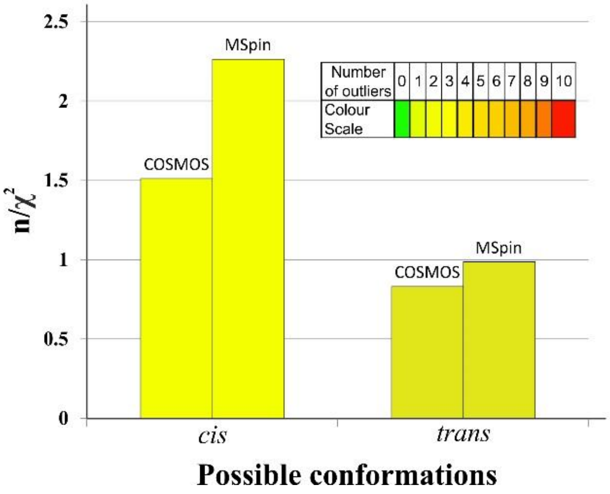

Figure 32: Quality factors n/χ^2 calculated for *cis*- and *trans*-conformations of Selfotel.

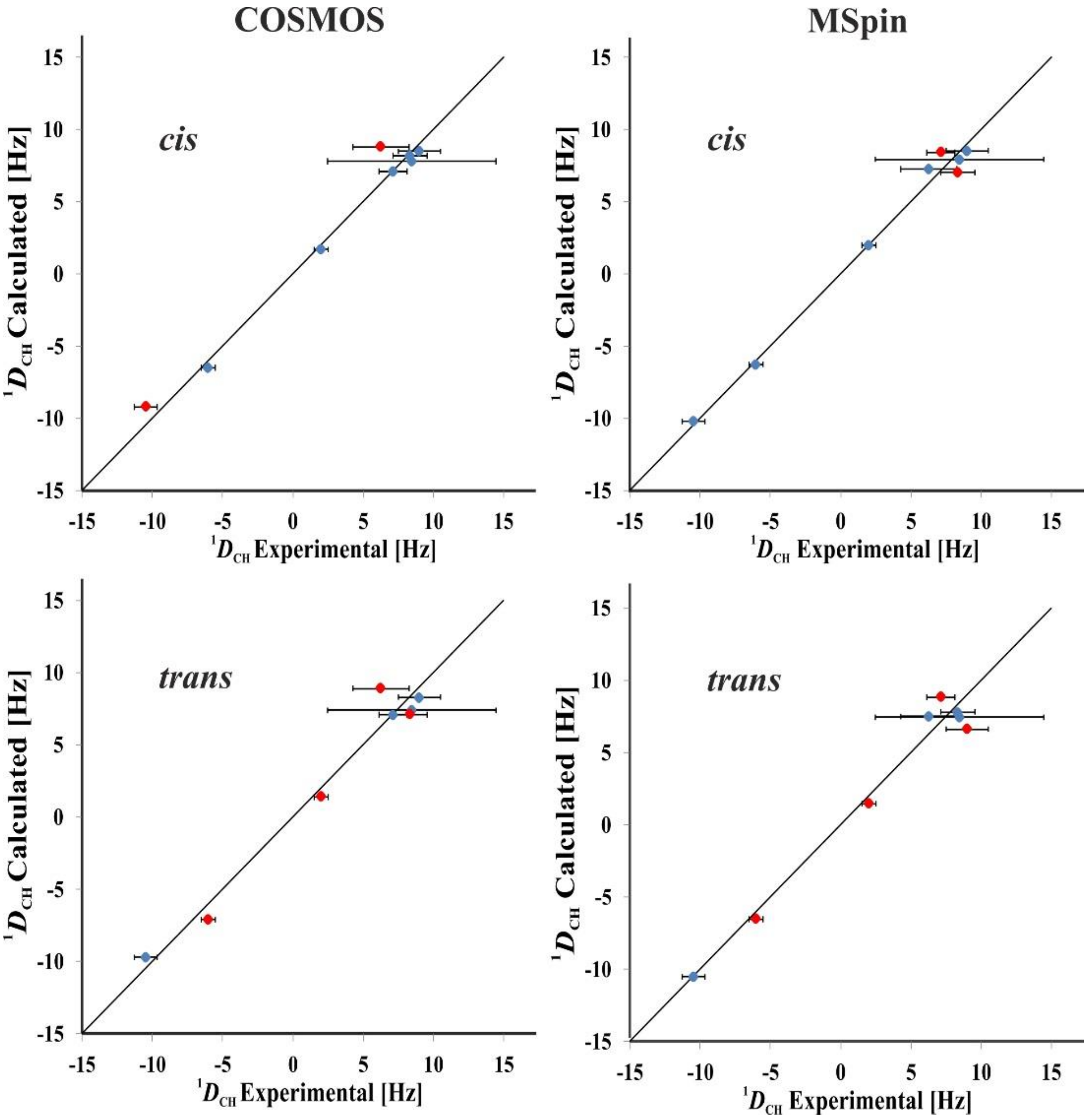

Figure 33: Experimental RDCs for the *cis*- and *trans*-conformations of Selfotel plotted against back calculated RDCs obtained with MSpin and COSMOS.
Errors are shown as horizontal lines, and outliers are coloured red.

An optimization of the MDOC approach and a more precise measurement of the experimental RDCs would probably provide an agreement of all experimental constraints with the calculated values within the experimental errors.

5.2. Experimental data for the Reserpine derivatives

5.2.1. Sample preparation

The composition of the isotropic and anisotropic samples of RD-1 and RD-2 are summarized in **Table 11**. Partial alignment of the sample was achieved using a polymer-based alignment medium. While a large number of polymer gels [30, 34, 96] and liquid crystalline phases [97, 98] have been reported in the literature, polymer gels in combination with a rubber-based stretching device [35] provide the best flexibility in adjusting the alignment strength (see section 2.2.2.3). As DMSO-d_6 was used as solvent for the isotropic measurements, a polyacrylonitrile (PAN) gel [33, 99] has been used as the alignment medium for the anisotropic sample. A dry PAN polymer stick of 3 mm diameter irradiated with accelerated electrons (200 kGy) was used, which was placed inside the Kalrez tubing of the stretching apparatus with DMSO-d_6 (See **Figure 13**). The sample were tightly closed in order to avoid that the quantity of water increased in the devices, indeed, in the presence of too much water the PAN gel shrinks. The sample were equilibrated for approximately 3 weeks. For RD-2, after one month the gel was shrunk. RD-2 is a salt and protonated on the tertiary amine, hence the sample contained already too much water, and it is why before the preparation of the second sample the sample was lyophilized to reduce the quantity of water.

Table 11: Properties of isotropic and anisotropic sample of RD-1 and RD-2.

	RD-1		**RD-2**	
	Isotropic	**Anisotropic**	**Isotropic**	**Anisotropic**
Quantity [mg]	2.8	10	3.0	8
Solvent/Gel	DMSO-d_6	DMSO-d_6/PAN	DMSO-d_6	DMSO-d_6/PAN
Volume [mL]	0.5	0.3	0.5	0.3
Monoisotopic Mass [g/mol]	382.2		369.2	
Concentration [mM]	14.7	87.2	16.3	72.2

5.2.2. NMR measurements

5.2.2.1. NMR Spectra for assignment in the isotropic phase

All NMR measurements for the assignment of RD-1 in DMSO-*d₆* were recorded at 300 K on a Bruker 500 MHz Avance III spectrometer (spectrometer **A** in **Table 1**) equipped with a 5 mm BBFO probe head with actively shielded z-gradients. For RD-2, the measurements were recorded at 300K on a Bruker 600 MHz AVANCE III HD spectrometer equipped with a 1.7 mm CPTCI inversely detected ^1H,^{13}C,^{15}N triple resonance cryogenically cooled probe with actively shielded z-gradients (spectrometer C in **Table 1**). For the assignment of RD-2 another isotropic sample was prepared with 1.5 mg in 40 µL DMSO-d_6 leading to an approximate concentration of 101.6 mM (for details and assignment of RD-1 and RD-2 see Appendix (section 9.4.3)). The ^1H NMR spectrum was acquired by using 64k data points at a spectral width of 12 kHz, and a 1.5 s repetition delay. 2D ^1H,^{13}C-correlation spectra were recorded with 2k data points in the ^1H dimension and 128 points in the ^{13}C dimension. 2D ^1H,^1H-correlation spectra were recorded with 2k data points in the direct and 128 points in the indirect dimension, respectively. The repetition delay for the 2D experiments was 1 second.

5.2.2.2. NMR spectra for RDC measurements

For RD-1 and RD-2, the NMR spectra were recorded on Bruker 800 MHz Avance III HD spectrometer equipped with a 5 mm CPTCI inversely detected ^1H,^{13}C,^{15}N triple resonance cryogenically cooled probe with actively shielded z-gradients. (Spectrometer B in **Table 1**) The temperature was controlled with a Bruker SmartVT-unit to be at 300 K.

Residual dipolar coupling $^1D_{CH}$ values of the reserpine derivatives were calculated from the difference between the scalar couplings $^1J_{CH}$ of the isotropic sample and the total splitting of the anisotropic sample ($^1T_{CH}={}^1J_{CH}+D_{CH}$) as measured by CLIP-HSQC [49] and P.E.HSQC [55] experiments according to the process described in section 2.2.3. In addition a P.E.HSQC spectrum is measured in order to compare and confirm the residual dipolar couplings obtained from the CLIP-HSQC and extract the geminal $^2D_{HH}$ dipolar couplings.

To assess the introduced alignment using the stretching device, a deuterium spectrum was recorded showing quadrupolar splittings of $\Delta\nu_Q$ = 6.3 Hz for RD-1 and $\Delta\nu_Q$ = 6.7 Hz for RD-2, respectively. Thus a balanced state enabling sufficient spectral resolution and residual dipolar coupling size was reached. The homogeneity of the alignment media was controlled by a deuterium imaging experiment [37] as explained in section 2.2.1. All 2D spectra were acquired with 32k points in the direct ^{1}H dimension and 512 points in the indirect ^{13}C dimension, unless stated otherwise. The repetition delay was set to 1s. The ^{1}H, ^{13}C-CLIP-HSQC spectrum in isotropic condition was acquired with a 64k points in the direct ^{1}H dimension and 512 points in the indirect ^{13}C dimension, while the P.E.HSQC of the isotropic sample was acquired with 1.5k points in the indirect dimension. All spectra were processed using the software Topspin 3.2 and were apodized by a sine squared window function with SSB 2 for ^{13}C and ^{1}H, with linear prediction of 512 points and zero filling to 2k points. The couplings and their errors were measured as described in section 2.2.3. For RD-1, a total of 21 $^1J_{CH}$ and corresponding $^1D_{CH}$ couplings ranging from -25.6 to 32.1 Hz could be extracted with errors ranging between 0.3 and 5 Hz (**Table 12**) as determined by the procedure for maximum error estimate described by Kummerlöwe *et al.*[54].

Table 12: Experimental $^1J_{CH}$, $^1T_{CH}$, and $^1D_{CH}$ coupling constants of RD-1.

	Isotropic conditions		**Anisotropic conditions**		**Experimental $^1D_{CH}$**	
Couplings	**$^1J_{CH}$ [Hz]**	**Error [Hz]**	**$^1T_{CH}$ [Hz]**	**Error [Hz]**	**D_{exp} [Hz]**	**Error [Hz]**
$C_{10}H_{10B}$	127.02	0.5	141.36	5.0	14.3	5.0
$C_{10}H_{10A}$	128.45	1.0	151.19	5.0	22.7	5.0
$C_{21}H_{21A}$	129.62	0.3	125.64	0.3	-4.0	0.3
$C_{21}H_{21B}$	126.43	0.3	144.63	0.3	18.2	0.3
C_5H_5	132.45	0.3	156.54	1.3	24.1	1.3
C_6H_6	130.95	0.3	156.79	1.0	25.8	1.0
$C_{22}H_{22A}$	128.02	0.3	153.40	0.3	25.4	0.3
$C_{22}H_{22B}$	127.80	0.3	120.26	0.3	-7.5	0.3
C_4H_4	145.83	0.3	131.99	0.6	-13.8	0.6
C_9H_{9B}	128.74	0.3	160.79	1.5	32.1	1.5
C_9H_{9A}	136.36	0.3	123.03	0.3	-13.3	0.3
C_7H_{7B}	128.39	0.3	154.78	5.0	26.4	5.0
C_7H_{7A}	137.06	0.3	120.49	5.0	-16.6	5.0
$C_{23}H_{23}$	130.82	0.3	157.55	0.3	26.7	0.3
CH_{3-28}	142.44	0.3	145.53	0.4	3.1	0.4
CH_{3-26}	143.36	0.3	144.79	0.3	1.4	0.3
C_2H_2	159.64	0.3	133.99	1.8	-25.6	1.8
C_3H_3	150.96	0.3	155.91	0.3	5.0	0.3
$C_{19}H_{19}$	157.71	0.3	152.47	0.3	-5.2	0.3
$C_{17}H_{17}$	157.94	0.3	138.52	1.0	-19.4	1.0
$C_{16}H_{16}$	157.31	0.3	151.21	1.0	-6.1	1.0

For RD-2, a total of 18 $^{1}J_{CH}$ and corresponding $^{1}D_{CH}$ couplings ranging from -21.0 to 30.0 Hz were determined with errors ranging between 0.3 and 4 Hz. All experimental data are summarized in **Table 13** for RD-2. Two dipolar coupling $^{1}D_{CH}$ are not extractable for RD-2 due to overlapping which correspond to the CH_2-10 according to the numbering on the **Figure 30**.

Table 13: Experimental $^{1}J_{CH}$, $^{1}T_{CH}$, and $^{1}D_{CH}$ coupling constants of RD-2.

	Isotropic conditions		**Anisotropic conditions**		**Experimental $^{1}D_{CH}$**	
Couplings	**$^{1}J_{CH}$ [Hz]**	**Error [Hz]**	**$^{1}T_{CH}$ [Hz]**	**Error [Hz]**	**D_{exp} [Hz]**	**Error [Hz]**
$C_{21}H_{21A}$	131.26	1.0	128.59	0.4	-2.7	1.0
$C_{21}H_{21B}$	128.71	1.0	138.24	1.5	9.5	1.5
$C_{5}H_{5}$	137.45	1.8	147.73	0.3	10.3	1.8
$C_{6}H_{6}$	118.48	1.8	148.44	2.0	30.0	2.0
$C_{22}H_{22A}$	134.07	1.0	130.02	1.0	-4.1	1.0
$C_{22}H_{22B}$	128.50	1.0	146.78	0.5	18.3	1.0
$C_{4}H_{4}$	147.30	0.5	146.14	0.6	-1.2	0.6
$C_{9}H_{9B}$	144.44	1.8	161.61	0.5	17.2	1.8
$C_{9}H_{9A}$	146.66	1.8	141.38	0.7	-5.3	1.8
$C_{7}H_{7B}$	147.98	1.8	145.29	0.3	-2.7	1.8
$C_{7}H_{7A}$	141.79	2.5	151.65	4.0	9.9	4.0
$C_{23}H_{23}$	145.37	1.0	162.41	1.0	17.0	1.0
$CH_{3\text{-}26}$	143.74	0.3	144.50	0.3	0.8	0.3
$C_{2}H_{2}$	160.44	0.6	142.92	3.0	-17.5	3.0
$C_{3}H_{3}$	150.42	0.6	156.06	0.3	5.6	0.6
$C_{19}H_{19}$	159.22	0.6	155.27	0.7	-4.0	0.7
$C_{17}H_{17}$	158.87	0.6	137.83	1.5	-21.0	1.5
$C_{16}H_{16}$	159.05	0.6	155.94	0.6	-3.1	0.6

5.2.3. Generation of 32 possible configurations

RD-1 and RD-2 contain 7 chiral centres of which two (at atom 2 and 4 in **Figure 29** and **Figure 30**) are within a sterically hindered lactone ring. Therefore, only 32 out of the 64 theoretically possible configurations are sterically accessible (**Table 14**) and were evaluated (neglecting all enantiomer with *S*-configuration at C2).

Static structural models of the 32 different configurations were generated with the program CORINA [100] and subsequently optimized using the program Maestro of the Schrödinger software package (Release 2014-2, Maestro, Schrödinger, LLC, New York, NY, 2016). Corresponding 3D structures with minimal energies as well as ensembles of energy minimized structures were used for the subsequent MSpin calculations and as initial structures for COSMOS MDOC runs.

Table 14: Possible relative configurations of RD-1 and RD-2.
[a] Running number identifying the configurations [b] *R* and *S* identify the configuration of the stereocenters in the following sequence: C_2 C_3 C_4 C_5 C_6 N_8 C_{23}. Note that for each relative configuration a mirror image (enantiomer) exists that is not listed and for which the same analysis can be applied.

Configuration[a]	$\mathbf{C_2C_3C_4C_5C_6N_8C_{23}}$[b]	**Configuration**[a]	$\mathbf{C_2C_3C_4C_5C_6N_8C_{23}}$[b]
1	*RRSSSSS*	17	*RRSSSRS*
2	*RSSSRSS*	18	*RSSSRRS*
3	*RRSSRSS*	19	*RRSSRRS*
4	*RRSRSSR*	20	*RRSRSRR*
5	*RSSRSSR*	21	*RSSRSRR*
6	*RSSSSSS*	22	*RSSSSRS*
7	*RRSRRSR*	23	*RRSRRRR*
8	*RSSRRSR*	24	*RSSRRRR*
9	*RSSRRSS*	25	*RSSRRRS*
10	*RRSRRSS*	26	*RRSRRRS*
11	*RRSSSSR*	27	*RRSSSRR*
12	*RSSSSSR*	28	*RSSSSRR*
13	*RSSRSSS*	29	*RSSRSRS*
14	*RRSRSSS*	30	*RRSRSRS*
15	*RRSSRSR*	31	*RRSSRRR*
16	*RSSSRSR*	32	*RSSSRRR*

5.3. Relative stereochemistry determination of RD-1

5.3.1. Single conformer single alignment tensor SVD approach

Each geometry-optimized configuration was fitted in MSpin to determine a global alignment tensor using the SVD option as described in section 2.2.4.1. Based on the outcome, RDCs were back calculated and compared with experimental data.

The resulting quality factors for the single best conformers of the 32 configurations of RD-1 are summarized in **Figure 34**. The *RRSSSSR* configuration (number 11) showed unambiguously the best n/χ^2 value for RD-1, clearly identifying this configuration as the best fitting one out of the set of 32 single conformers for RD-1 (for details see section 9.4.4 in the appendix). For most practical applications, this result might be sufficient, however, the low value of $n/\chi^2=0.093$ and more than 10 outliers demonstrate that the model is by far not sufficient to fully represent the experimental results. As the overall fit of experimental *vs.* back calculated RDCs correlates well (see **Figure 35**), the most probable reason for the insufficient fulfilment of experimental data using the single conformer approach is the presence of some degree of flexibility in the RD-1 molecule. As dynamics cannot be included in a single conformer approach, the extension to a multiple conformer analysis was therefore attempted in a next step.

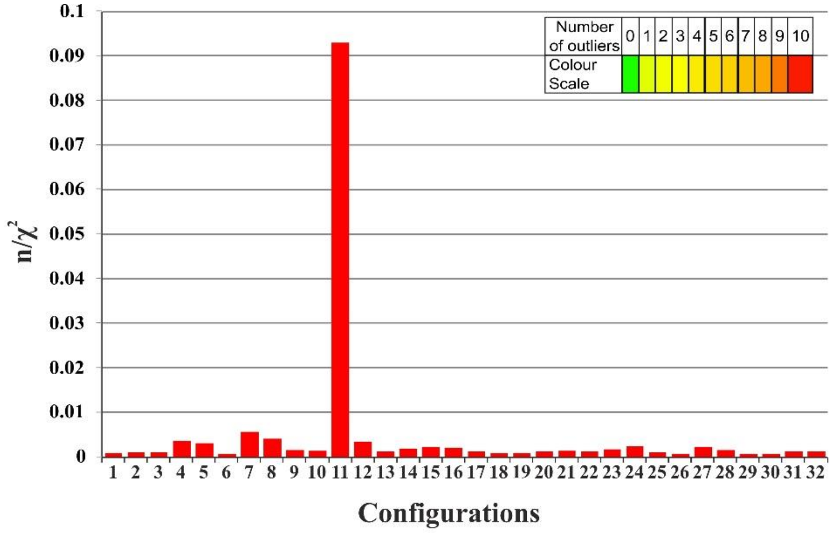

Figure 34: MSpin (SVD) quality factors n/χ2 calculated for all possible configurations of RD-1.
On the horizontal axis, the 32 different configurations are listed using the numbering shown in **Table 14.** The colour of the bar encodes the number of outliers from the measured RDC values, as shown in the colour scale on the upper right. Even the best static structural model has at least 10 RDCs that do not comply with the data within experimental errors.

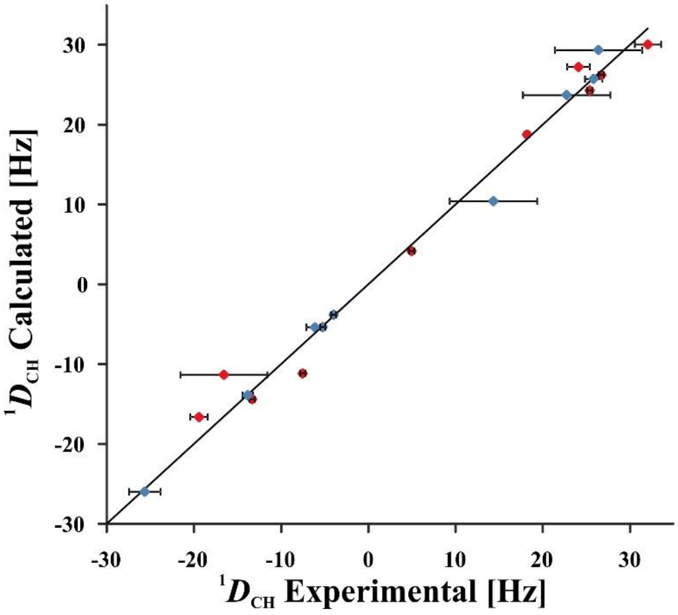

Figure 35: Plot of back calculated RDCs obtained with MSpin (SVD), against experimental RDCs for the best configuration 11 (*RRSSSSR*).
Although experimental and calculated data correlate well based on the correlation coefficient of 0.99, 10 out of the 19 RDCs are not within the error range of the experimental data (red data point). The diagonal line represents $D_{\text{calc}} = D_{\text{exp}}$. Only 19 out of 21 experimental RDCs were used in MSpin, because the two methoxy groups (26 and 28 in Fig. 1) cannot be used for the analysis with this software.

5.3.2. Multiple conformers single alignment tensor SVD approach

The multiple conformer single alignment tensor SVD-based fitting procedure is the only viable of the existing approaches using multiple conformations as insufficient data are available for a multi tensor approach. It allows the calculation of RDCs based on a single alignment tensor for an ensemble of conformers of a given configuration. Clearly, fitting a single alignment tensor to a conformational ensemble is an approximation, which, however, successfully led to several configuration determinations in the past [75-77].

In this study, a number of different conformers was generated from a conformational search for each configuration with the Monte Carlo-based program Maestro. Using the default settings and the OPLS_2005 force field, all conformations with an energy difference below a threshold of 6.0 kcal/mol relative to the lowest energy structure were calculated. In a first round, all of these low-energy conformers were combined to ensembles by weighing the population of each conformer according to its energy. The theoretical RDCs were then calculated using the single tensor approach. The correlation of the resulting RDCs with the experimental values did not show an improvement compared to using a single conformer single alignment tensor fit and is therefore not shown. In a next step, the conformer population of the input ensemble were optimized since the calculated energy differences might not represent the actual energies. With this approach, configuration 11 remained to display the best n/χ^2 value (**Figure 36**) with an apparent good correlation between the back calculated and experimental RDCs (**Figure 37**). However, the number of outliers was unchanged with 10 calculated RDCs being still outside the range of the maximum error estimates of the experimental RDCs. Overall, the result obtained for the best configuration 11 did not significantly improve compared to the SVD approach using a single conformer. For this configuration, four different conformers are obtained with Maestro. These, however, only differ in the position of the methoxy groups *i.e.* the core frame of the molecule is essentially the same for the different conformers and therefore very similar D_{calc} and consequently n/χ^2 values are obtained. On the other hand, for some other configurations up to 16 different conformers are obtained by the Maestro software, partially with significant differences in the core frame. For example, configuration 1 has 16 conformers and the SVD approach led to an improvement in n/χ^2 from 0.0008 of a single conformer to approximately 0.002 for the multiple conformer fit. The multiple conformer single alignment tensor approach could therefore very slightly improve the overall quality of structural models, but consistency with experimental results could not be achieved.

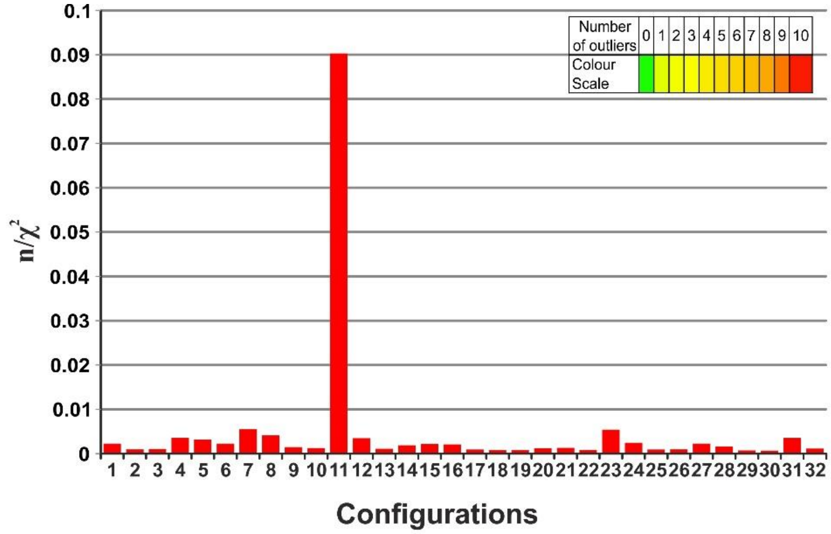

Figure 36: MSpin (SVD) quality factors n/χ^2 calculated for all possible configurations of RD-1 from multiple conformers.

On the horizontal axis the 32 different configurations are listed using the numbering shown in **Table 14**. The colour of the bar encodes the number of outliers from the measured RDCs values, as shown in the colour scale on the upper right. Even the best static ensemble has at least 10 RDCs that do not fit the data within experimental errors.

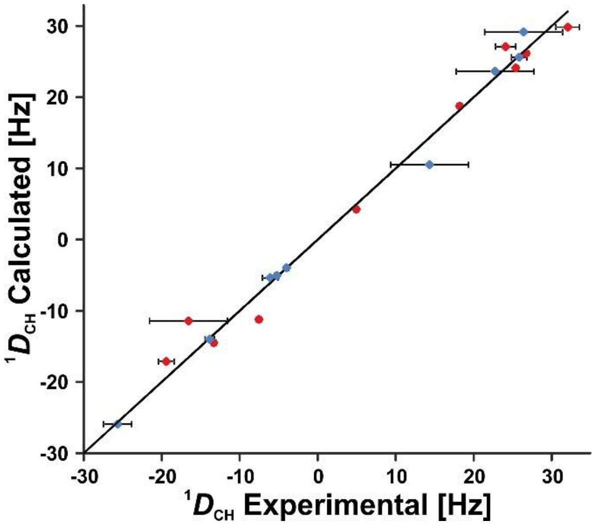

Figure 37: Plot of back calculated RDCs obtained with MSpin (Single Tensor Fit), against experimental RDCs for the best configuration 11 (*RRSSSSR*).

Although the overall fit of experimental against calculated data shows a good correlation with R = 0.99, 10 out of the 19 RDCs are not within the range of maximum error estimates of the experimental data (outliers are coloured red, and error ranges indicated by a horizontal line). The diagonal line represents the case of full correlation of experimental and calculated data. Only 19 out of 21 experimental RDCs are used in MSpin, because the two flexible methoxy groups (26 and 28 in **Figure 29**) have been excluded for the analysis with this software.

5.3.3. Molecular dynamic simulation with orientational constraints (MDOC)

As described in section 2.2.4.2, several parameters have to be fine-tuned during the set-up of the MD calculations. For RD-1, we found that setting the WF to $5.5.10^{-4}$ and the scaling factor s_{AM} to 4.10^{-3} resulted in calculated RDC values in the range of $^{1}D_{CH}$ = -25.7 to 31.4 Hz (see **Table 20** for the value of the configuration 11 and in the Appendix section 9.4.4 for the individual values of each configuration), which are in the same range as the experimentally determined values. In addition, MD runs were chosen to last 80 ns in order to reach good convergence of the orientational constraints.

During the MDOC runs, the calculated $^{1}D_{CH}$ RDCs were written into an output file every 20 ps. When evaluating MDOC runs, these $^{1}D_{CH}$ couplings were arithmetically averaged. The n/χ^2 was then calculated from these averaged coupling constants neglecting the first nanosecond of the MDOC trajectory, which is needed for initial system equilibration. Furthermore, a geometry snapshot is saved every 40 ps as control of the evolution of different parameters of the molecular geometry such as the dihedral angles or the distances between atoms.

The parameter file for COSMOS contains the experimental RDCs and the different groups enabling to define atoms involved in the constraints or the others groups needed for the understanding of the resulting data, such as the evolution of different dihedral angles. The first run was realized without any fixing. The results obtained are summarized in **Figure 38**, where the configurations having a different stereochemistry just for the amine are grouped as defined in **Table 14**.

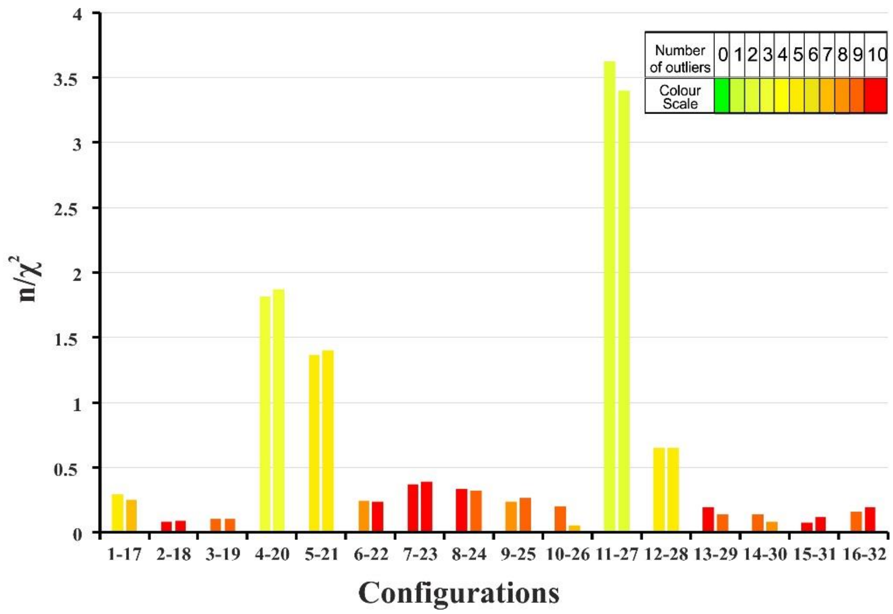

Figure 38: COSMOS quality factors n/χ^2 calculated for all possible relative configurations of RD-1 defined in **Table 14**.

On the horizontal axis, the 32 different configurations are listed using the numbering of **Table 14**. The colour of the bar encodes the number of outliers of the measured RDCs values taken from $1/\chi^2$ values below 1.

The configurations, which differ just at the amine N_8, have approximately the same n/χ^2, what allows suggesting an eventual inversion of the amine during the MDOCs. The measurement of the dihedral angle C_{11}-C_{12}-C_{23}-N_8 for the configuration 11 and 27 shows approximately an identical distribution for the configuration 11 and 27 as represented on the panel A and B of the **Figure 39**. Hence, the inversion of the amine took place during the MDOC what explains the result obtained for COSMOS.

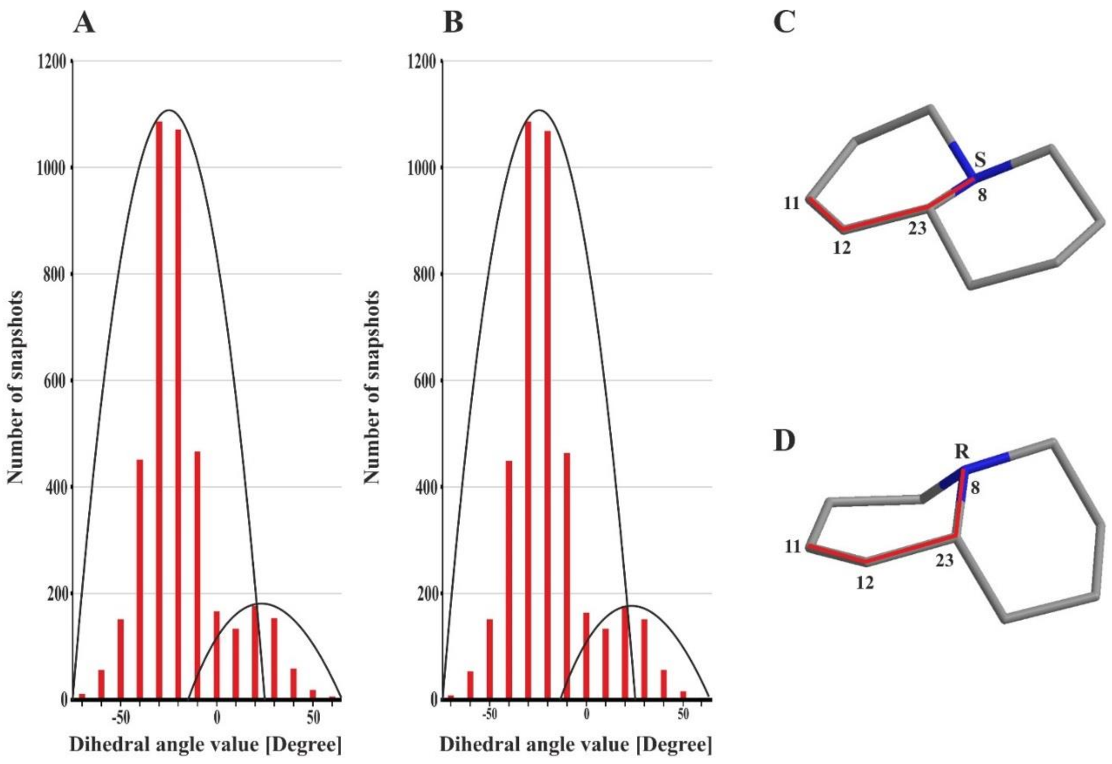

Figure 39: Study of the dihedral angle C$_{11}$-C$_{12}$-C$_{23}$-N$_8$ during the MDOC run for the configurations 11 and 27 of RD-1.

The configuration of the quinolizidine system is given in the Panel **C** and **D** for the configuration 11 and 27, respectively. On the panel **A** and **B**, the distribution of the angle C$_{11}$-C$_{12}$-C$_{23}$-N$_8$ obtained during the MDOC is given for the configuration 11 and 27, respectively.

The configuration preferred for the amine in the quinolizidine system is the *S*- configuration according to the distributions obtained from the MDOC run. From the 4000 angles measured during the MDOC, 88 percent have the configuration *S*- and 12 percent the configuration *R*-. At this stage, further investigations were required to experimentally determine the presence or absence of amine inversion.

In isotropic conditions, the determination of the configuration at the amine N8 was not possible using classical NMR methods like NOE-derived distances and dihedral angles derived from ^3J-couplings due to overlapping signals in the NMR spectra and flexibility of the molecule. While the aliphatic CH$_2$ and CH groups at positions 7, 9, and 23 provide significant stabilization of the tertiary amine, a potential rapid inversion cannot be excluded *a priori* (See **Figure 40**). A theoretical structural search for conformations with inverted amines showed little differences in energies of the two isoforms, more precisely 25.8 kcal/mol and 28.5 kcal/mol for the configuration 11 and 27, respectively, which differ only from each other by the configuration of the amine.

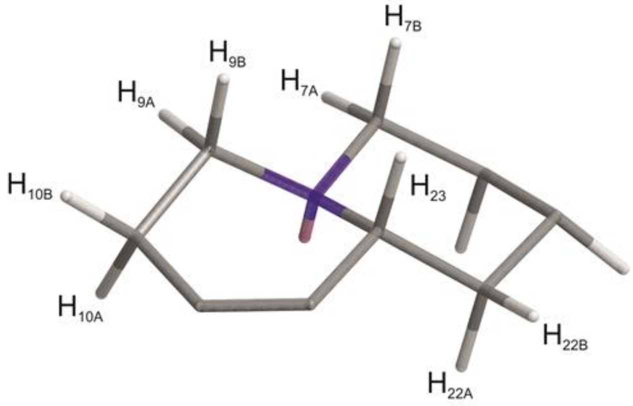

Figure 40: Quinolizidine system of RD-1.

The unambiguous resolution of this question was found when analysing the one-bond measurements: if rapid inversion occurred, all structural parameters such as chemical shifts and in particular scalar couplings of neighbouring aliphatic groups should be averaged. The experimentally determined ${}^{1}J_{CH}$ coupling constants of the axial protons of CH_2 7 and 9 (128.4 and 128.7 Hz respectively) are smaller than the ${}^{1}J_{CH}$ couplings of the corresponding equatorial protons (137 and 136.4 Hz respectively). Equally, chemical shifts are significantly different for the protons within the CH_2 9, namely 2.93 ppm for the equatorial proton and 2.39 ppm for the axial proton (the experimental results for selected CH and CH_2 groups surrounding the amine are summarized **Figure 40** and **Table 15**). Therefore, the amine is present in a defined configuration and potential inversion was neglected in the subsequent studies.

Table 15: Experimental data for the CH_2 and CH in close proximity of the amine of RD-1.
Atom numbering is according to **Figure 29** [a] Proton chemical shift in ppm [b] Carbon chemical shift in ppm [c] one bond CH scalar couplings in Hz.

Couplings	δ(^{13}C) [ppm][a]	δ(^{1}H) [ppm][b]	$^{1}J_{CH}$ [Hz][c]
C_9H_{9B} (ax)	52.9	2.38	128.7
C_9H_{9A} (eq)		2.93	136.4
C_7H_{7B} (ax)	58.5	2.50	128.4
C_7H_{7A} (eq)		2.62	137.1
$C_{23}H_{23}$	54.6	3.46	130.8
$C_{10}H_{10B}$ (ax)	21.8	2.53	127.0
$C_{10}H_{10A}$ (eq)		2.71	128.5
$C_{22}H_{22B}$ (eq)	35.0	2.35	127.8
$C_{22}H_{22A}$ (ax)		1.74	128.0

As inversion for RD-1 could be excluded, a second COSMOS run was performed in which the distance between the carbons 23, 7 and 9 was fixed in the parameters in order to prevent the inversion of the amine. As a result, a different outcome was obtained as compared to the previous run in which a configuration with amine N_8 inversion was used (quality factors are shown in **Figure 41**). While three configurations (4, 5, and 11) have overall quality factors n/χ^2 above 1 and therefore potentially comply with the experimental data, a detailed analysis revealed that only configuration 11 (*RRSSSSR*) fulfilled all experimental constraints within the experimental errors, while the other two best matching structural models have two and five outliers, respectively. The comparison of measured and calculated RDCs, as shown in **Figure 42**, further supports the stereochemistry of configuration 11 (*RRSSSSR*) as the correct one.

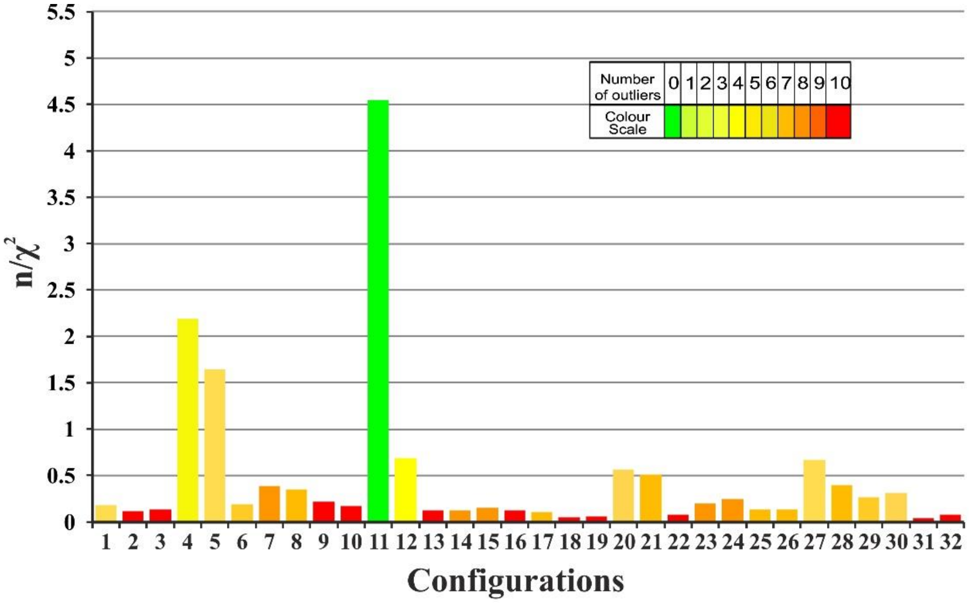

Figure 41: COSMOS quality factors n/χ^2 calculated for all possible configurations of RD-1.
On the horizontal axis the 32 different configurations are listed using the numbering of **Table 14**. The colour of the bar encodes the number of outliers of the measured RDC values taken from $1/\chi^2$ values below 1.

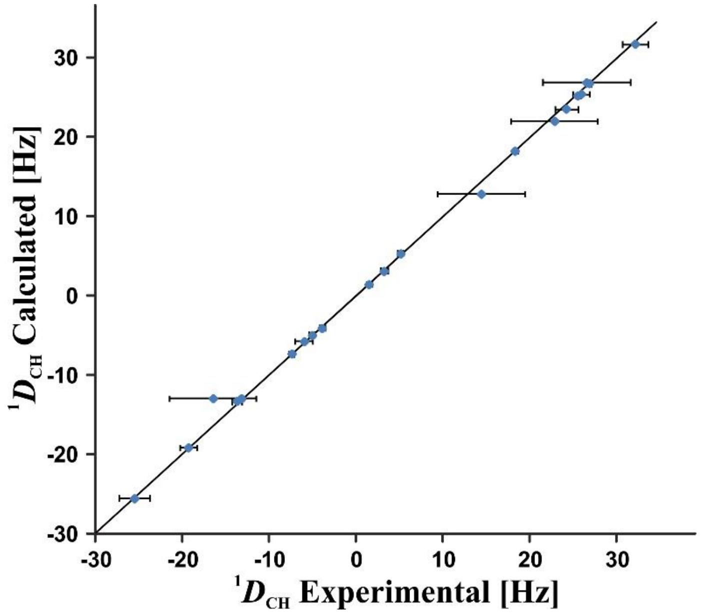

Figure 42: Plot of averaged back calculated RDCs obtained with COSMOS against experimental RDCs for configuration 11 (*RRSSSSR*) of RD-1.
All averaged calculated RDCs are inside the error range of the experimentally determined data.

5.3.4. X-ray Data

In parallel to the NMR efforts, the structure of RD-1 was determined by X-ray crystallography. The structure analysis revealed the configuration of RD-1 to be *RRSSSSS* (configuration 11 from NMR-based analysis in **Figure 14**) which is in full agreement with the RDC-based NMR analysis of all seven stereocenters. Based on the presence of anomalous scatters oxygen and nitrogen, the absolute configuration of RD-1 could be unambiguously assigned as C_2*R*, C_3*R*, C_4*S*, C_5*S*, C_6*S*, N_8*S*, C_{23}*R* (**Figure 43**). The result is supported by a Flack x parameter of 0.02 (13) [101]. The X-ray structure elucidation of RD-1 was done by Ina Dix at Novartis.

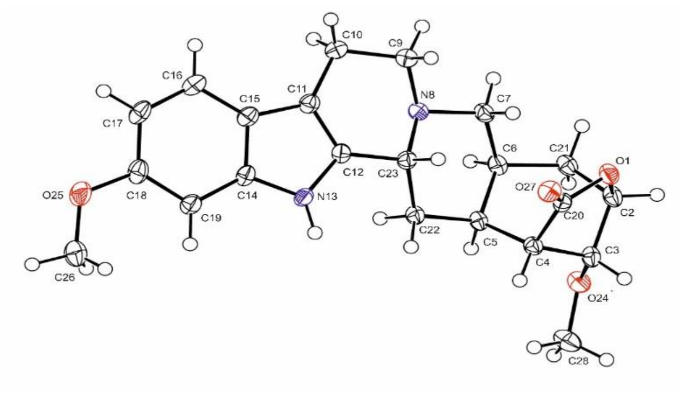

Figure 43: The crystal structure of RD-1.
Non-H atoms are represented by displacement ellipsoids drawn at 50% probability level.

5.4. Determination of the relative stereochemistry of RD-2

The same protocol used for the stereochemistry elucidation of RD-1 has been applied to the molecule RD-2.

5.4.1. Single conformer single alignment tensor SVD approach

Each geometry-optimized configuration of RD-2 was fitted in MSpin to determine a global alignment tensor using the SVD option of MSpin as described in the section 2.2.4.1 of this thesis. Resulting RDCs were back calculated and compared with the experimentally determined data (All results are provided in the Appendix section 9.4.5).

Quality factors obtained from the MSpin calculations for the single best conformers of the 32 configurations of RD-2 are summarized in **Figure 44**. The *RRSSSSS* configuration has clearly the best n/χ^2 value identifying this configuration as the best fitting one out of the set of 32 single configurations for RD-2. For most practical applications, this result might be sufficient. However, the value for $n/\chi^2=0.459$ also implies that the model is not sufficiently good to describe fully the experimental data. Compared to RD-1, the $n/\chi2$ value suggests an approximately 5 times better fitting, while at the same time RD-2 is more flexible than RD-1. This can be explained as follows: for RD-2, the error values are larger and the RDC values of the CH_2-10 cannot be extracted, while for RD-1, the error values are smaller and all experimental RDCs are available. This means that the tolerance of the model towards improper back calculation of the RDCs is much higher that for the RD-1 calculations. Nevertheless, the overall quality factor is below 1 and 4 outliers disqualify the structural models. As the overall fit of experimental *vs.* back calculated RDCs correlates well (see **Figure 45**), the most probable reason for the insufficient fulfilment of experimental data using the single conformer approach is the presence of some degree of flexibility in the RD-2 molecule. As dynamics cannot be included in a single conformer approach, the extension to a multiple conformer analysis was attempted in a next step.

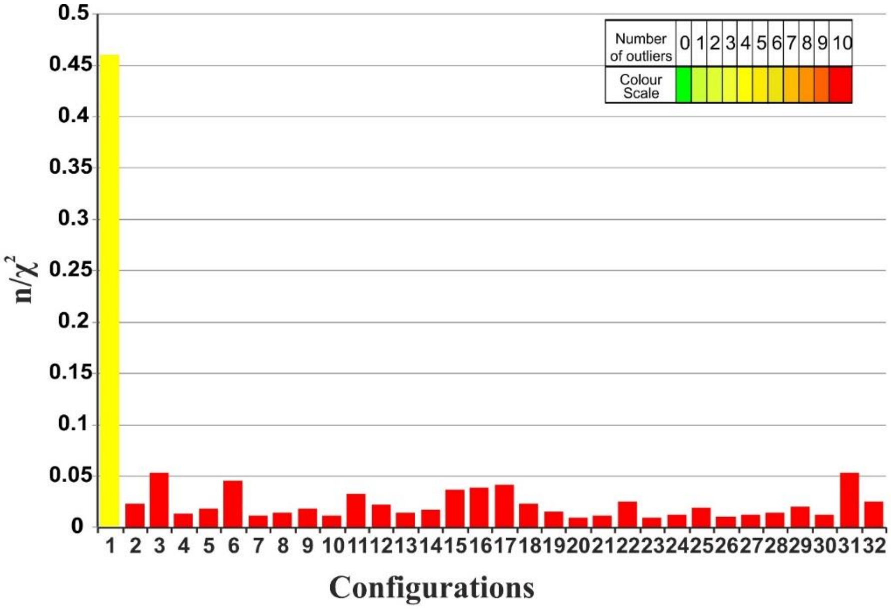

Figure 44: MSpin (SVD) quality factors n/χ^2 calculated for all possible configurations of RD-2.

On the horizontal axis, the 32 different configurations are listed using the numbering shown in **Table 14.** The colour of the bar encodes the number of outliers from the measured RDCs values, as shown in the colour scale on the upper right. Even the best static structural model has at least 4 RDCs that do not agree with the data within experimental errors.

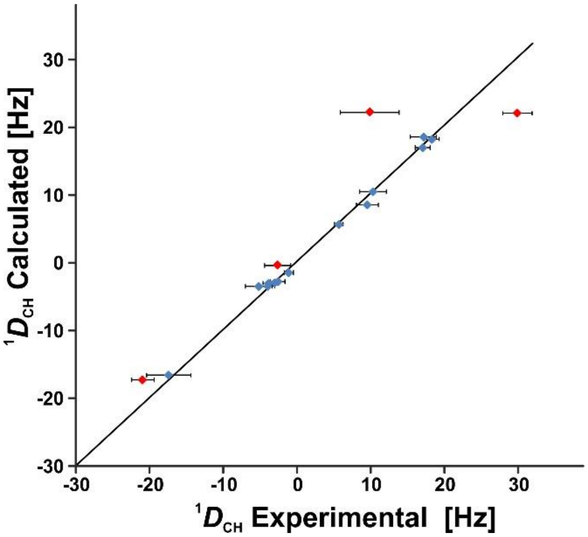

Figure 45: Plot of back calculated RDCs obtained with MSpin (SVD), against experimental RDCs for the best configuration 1 (*RRSSSSS*) of RD-2.

Although the overall fit of experimental *vs.* calculated data shows a good correlation, 4 out of the 17 RDCs are not within the error range of the experimental data (coloured in red on the graph). The diagonal line represents the unity line where $D_{\mathrm{calc}} = D_{\mathrm{exp}}$. Only 17 out of 18 experimental RDCs are used in MSpin, because the methoxy group 26 (**Figure 30**) can't be used for the analysis when using this software.

5.4.2. Multiple conformers single alignment tensor SVD approach

As for RD-1, a set of conformers generated with Maestro for all configurations were used for the calculation of RDCs based on a single alignment tensor obtained from a conformational ensemble. All conformers were weighted according to their energy. Resulting RDCs did not improve as significantly as observed for RD-1, and the configuration 1 has still the best n/χ^2 value as presented in **Figure 46**. For the configuration displaying the highest n/χ^2, 26 conformers are obtained with Maestro, and the total n/χ^2 obtained is almost the same than the n/χ^2 obtained from single conformer analysis. The number of outliers increased from four to five (see **Figure 46**). Hence, the flexibility of RD-2 cannot be characterized with these 26 conformers, so the MDOC approach was tried next in order to improve the description of the experimental data with an accurate model.

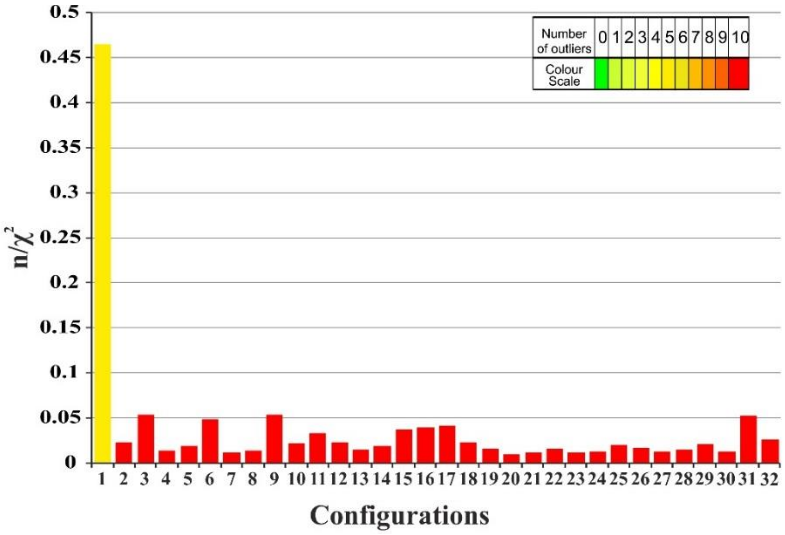

Figure 46: MSpin (SVD) quality factors n/χ^2 calculated for all possible configurations of RD-2 from multiple conformers.

On the horizontal axis the 32 different configurations are listed using the numbering shown in **Table 14**. The colour of the bar encodes the number of outliers from the measured RDCs values, as shown in the colour scale on the upper right. Even the best static ensemble has at least 5 RDCs that do not agree with the data within experimental errors.

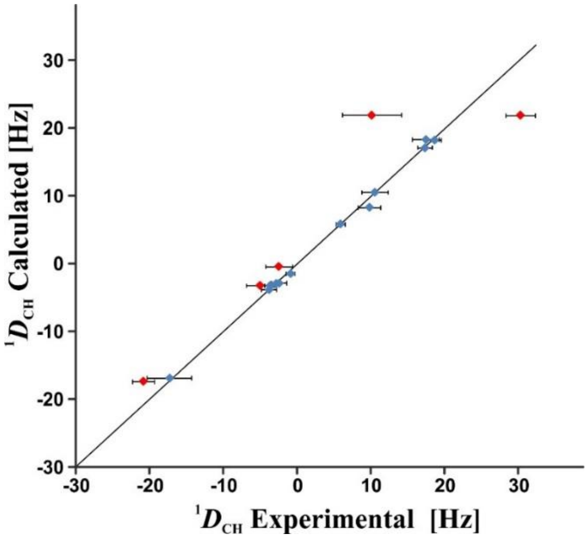

Figure 47: Plot of back calculated RDCs obtained with MSpin (SVD) against experimental RDCs for the ensemble of conformers for the best configuration 1 (*RRSSSSS*) of RD-2.
Although the overall fit of experimental *vs.* calculated data shows a good correlation, 5 out of the 17 RDCs are not within the error range of the experimental data (coloured in red on the graph). The diagonal line represents the unity line where $D_{calc} = D_{exp}$. Only 17 out of 18 experimental RDCs are used in MSpin, because the methoxy group 26 in **Figure 30** can't be used for the analysis when using this software.

5.4.3. Molecular dynamic simulation with orientational constraints (MDOC)

5.4.3.1. MDOC with $^1D_{CH}$ constraints

As RD-2 is more flexible compared to RD-1, the scaling factor s_{AM} was increased to 7.10^{-3} while for RD-1 4.10^{-3} was used, and the pseudo force WF was set to 6.10^{-4}. With this variation of the scaling factor the molecule flexibility and observed conformational variations can be better compensated as demonstrated in [79]. The weight factor WF contributes to scale the forces during the MD. The calculated RDCs values fluctuated between $^1D_{CH}$ = -21.3 and 28.1 Hz, which are in the same range as the experimentally determined values. The other parameters are the same compared to RD-1 and the runs are evaluated in the same way. The result of the first run is summarized in **Figure 48**. Three configurations full-filled the experimental data and 8 configurations have good n/χ^2 values (values superior than the half of the best n/χ^2). This shows that the flexibility of the molecule can lead to agreement of calculated RDCs and experimental data resulting in acceptable quality factors even for wrong configurations. Only with RDCs constrains, the method failed due to flexibility, therefore other orientational constraints such as scalar couplings were used to avoid too much flexibility for RD-2.

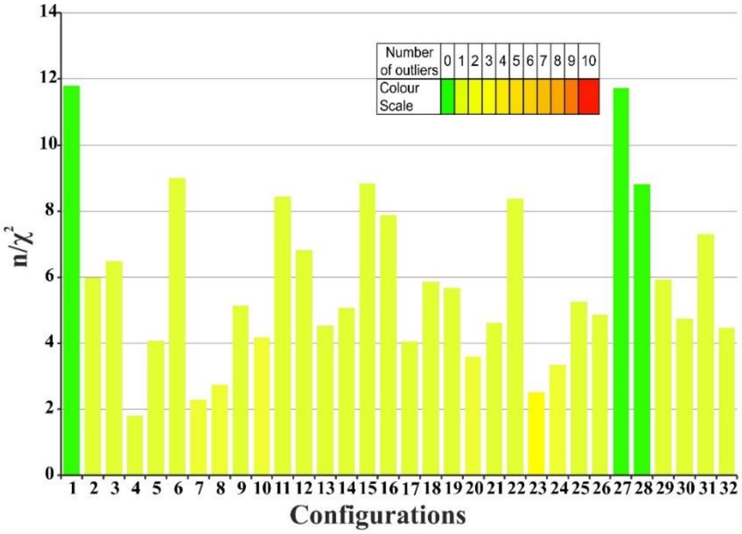

Figure 48: COSMOS quality factors n/χ^2 calculated for all possible configurations of RD-2 with only ${}^1D_{\mathrm{CH}}$ orientational constraints.

On the horizontal axis the 32 different configurations are listed using the numbering of **Table 14**. The colour of the bar encodes the number of outliers of the measured RDC values taken from individual $1/\chi^2$ values below 1.

5.4.3.2. MDOC with ${}^1D_{\mathrm{CH}}$ and ${}^3J_{\mathrm{HH}}$ constraints

The coupling constant between 2 vicinal protons provides detailed information about the spatial orientation. The ${}^3J_{\mathrm{HH}}$ values are mostly positive and they vary widely from 0 Hz up to 22 Hz depending on structural and conformation details [102-104]. The Karplus equation correlates ${}^3J_{\mathrm{HH}}$ couplings constants with different stereochemical parameters such as bond angle, bond length, substituent electronegativity and orientation, and most importantly with the torsion angle between the vicinal protons. The Karplus equation is reliable for conformational analysis of ring systems. RD-2 is composed of several rings, a quinolizidine, a cyclohexane, and a γ-lactone ring. The experimental vicinal coupling constants extracted for RD-2 are listed in **Table 18**.

The experimentally determined scalar couplings were used as additional orientation constraints alongside the dipolar couplings during the MDOC. The calculated ${}^1D_{\mathrm{CH}}$ RDCs and ${}^3J_{\mathrm{HH}}$ scalar couplings were written into a file every 20 ps. For the RDCs, the same WF and s_{AM} were used as employed in the previous MDs. The WF used for the scalar couplings was set to 15. For the subsequent evaluation, the obtained ${}^1D_{\mathrm{CH}}$ and ${}^3J_{\mathrm{HH}}$ were arithmetically averaged. The n/χ^2 values were then calculated from these averaged numbers. The results obtained from this simulation are provided in **Figure 49** for all possible configurations of RD-2.

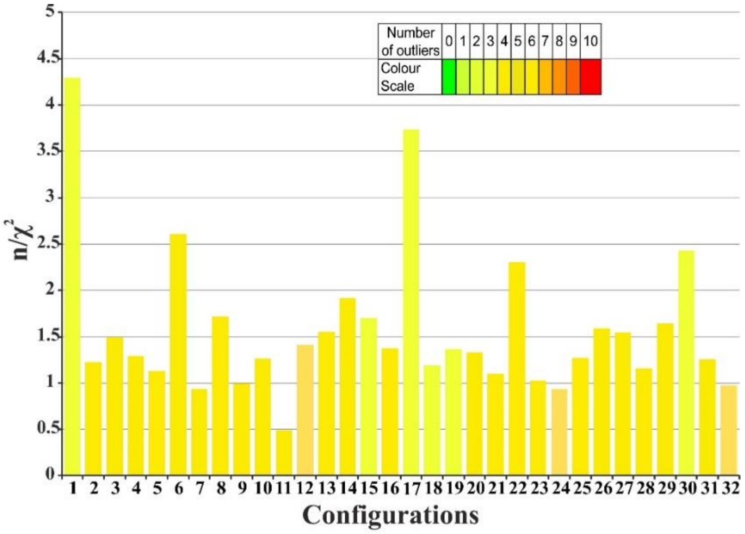

Figure 49: COSMOS quality factors n/χ^2 calculated for all possible configurations of RD-2 with $^1D_{CH}$ and $^3J_{HH}$ orientational constraints.
On the horizontal axis the 32 different configurations are listed using the numbering of **Table 14**. The colour of the bar encodes the number of outliers of the measured RDC values taken from individual 1/χ^2 values below 1.

A better discrimination compared to the previous run without $^3J_{HH}$ coupling constraints was achieved, with configurations 1 and 17 having the best n/χ^2 values which differ only on the configuration of the amine. However, these 2 configurations still have 3 outliers and the configuration of the amine has to be determined, *e.g.* if the amine inversion does not occur. One-bond measurements of scalar couplings of neighbouring aliphatic groups don't allow determining if the amine for RD-2 is present in a defined configuration, while this was possible for RD-1. Indeed, the experimentally determined $^1J_{CH}$ coupling constants of the axial protons of CH_2 7 and 9 (141.8 and 144.4 Hz respectively) are very close to the $^1J_{CH}$ couplings of the corresponding equatorial protons (148.0 and 146.7 Hz respectively). The chemical shifts of the axial and equatorial protons of CH_2 9 and CH_2 7 are different, respectively, namely 3.57 ppm and 3.45 for the equatorial protons and 3.07 ppm and 2.71 for the axial proton, however this it is not sufficient to exclude the inversion of the amine (the experimental results for selected CH and CH_2 groups surrounding the amine are summarized **Figure 50** and **Table 16**). For CH_2 22, the axial and equatorial $^1J_{CH}$ couplings and their chemical shifts are significantly different, revealing less flexibility in the proximity of this CH_2, while the corresponding values for the CH_2 7 and 9 indicate flexibility around the amine.

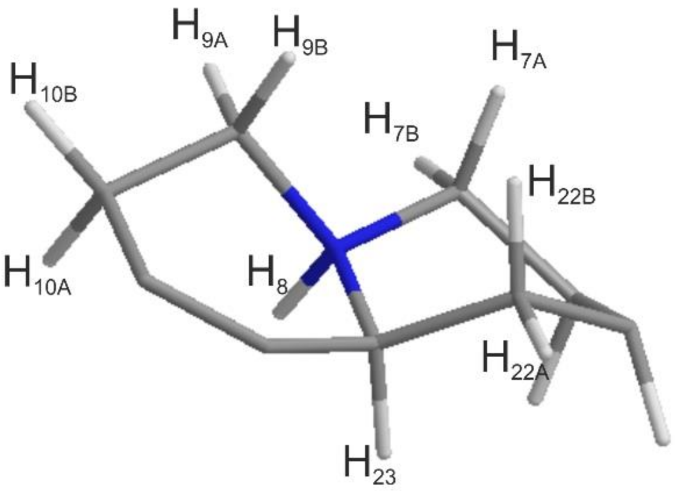

Figure 50: Quinolizidine system of RD-2

Table 16: Experimental data for the CH_2-7 and 9 and CH-23 in close proximity of the amine of RD-2. Atoms are numbered according to **Figure 30**. Value in bracket correspond to the same value of RD-1.

Coupling	δ(^{13}C) [ppm]	δ(^{1}H) [ppm]	$^{1}J_{CH}$ [Hz]
C_9H_{9B} (ax)	48.1	3.07 (2.38)	144.44 – (128.7)
C_9H_{9A} (eq)		3.57 (2.93)	146.66 – (136.4)
C_7H_{7A} (ax)	55.0	2.71 (2.50)	141.79 – (128.4)
C_7H_{7B} (eq)		3.45 (2.62)	147.98 – (137.1)
$C_{23}H_{23}$	51.4	4.86 (3.46)	145.37 – (130.8)
$C_{22}H_{22A}$ (eq)	26.4	2.37 (2.35)	134.07 – (127.8)
$C_{22}H_{22B}$ (ax)		1.97 (1.74)	128.50 – (128.0)

The use of $^{1}D_{CH}$ and $^{3}J_{CH}$ couplings allows determination of the relative configuration of RD-2, with the exception of the configuration of the tertiary amine. The configuration 1 and 17 differs only on the configuration of the amine, for which no dipolar coupling is available, and the dihedrals angles derived from the scalar couplings $^{3}J_{HH}$ fit for the two configurations. This is why, in addition to these constraints, distances between protons through space determined from ROESY experiments are used as constraints in further MDOC simulations, as described in the next subsection.

5.4.3.3. MDOC with ${}^{1}D_{CH}$, ${}^{3}J_{HH}$ and distance constraints

A ROESY experiment was used for the determination of distances between protons within the RD-2 molecule. This experiment is suitable for analyses of intermediate sized molecules, like RD-2 [105]. ROE data are measured by integration of cross peaks in ROESY spectrum [106]. Using the invariant distance between the aromatic protons H16 and H17 as a reference with a distance of 2.45 Å, the distance r_{ij} between a pair of hydrogens i and j is determined from the ROESY peak integral a_{ij} according to:

$$r_{ij} = r_{ref}\left(\frac{a_{ref}}{a_{ij}}\right)^{1/6} \qquad (18)$$

where r_{ref} and a_{ref} are the distance and peak integral of the reference protons, respectively. The obtained distances are provided in **Table 19**.

These distances were added as constraints to the MD simulations, in addition to the ${}^{1}D_{CH}$ and ${}^{3}J_{HH}$.based constraints. Altogether, a total of 44 constraints were used (18 dipolar couplings, 10 scalar couplings and 16 distances), with the results obtained being summarized in **Figure 51** (for details see section 9.4.5 and 9.4.4 in the appendix).

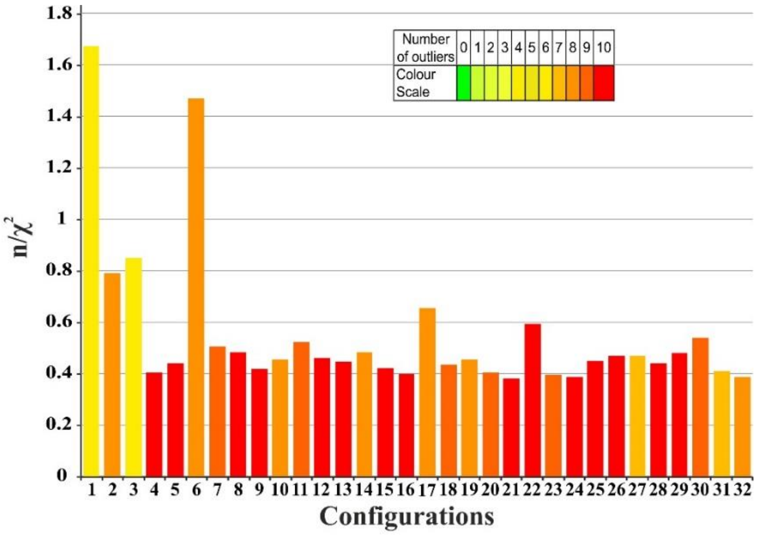

Figure 51: COSMOS quality factors n/χ^2 calculated for all possible relative configuration of RD-2 defined in **Table 14**.
On the horizontal axis, the 32 different configurations are listed using the numbering of **Table 14**. The colour of the bar encodes the number of outliers of the measured RDCs values taken from individual $1/\chi^2$ values below 1.

The configurations 1 (*RRSSSSS*) and 6 (*RSSSSSS*) have overall quality factors n/χ^2 above 1, while the other 30 configurations have all n/χ^2 below 1. These two configurations differ only on the configuration of the CH-3 present on the γ-lactone ring (**Figure 52**). They don't fulfil all experimental constraints within the experimental errors, displaying 6 and 8 outliers, respectively. Configuration 17 (*RRSSSRS*), which had high quality criterion in the previous MDs runs and differs only on the configuration of the amine compared to configuration 1, has now a quality factor n/χ^2 below 1 with 8 outliers. Clearly the addition of the ROE distances as constraint allowed the assignment of the relative configuration of the amine, showing that the amine is present in a defined configuration and potential inversion can be excluded.

On **Figure 52**, the two configurations 1 and 6 are illustrated, for the configuration 6 the distance between the proton H5 and H3 is approximately 2.5 Å, while for the configuration 1 this distance is about 3.8 Å.

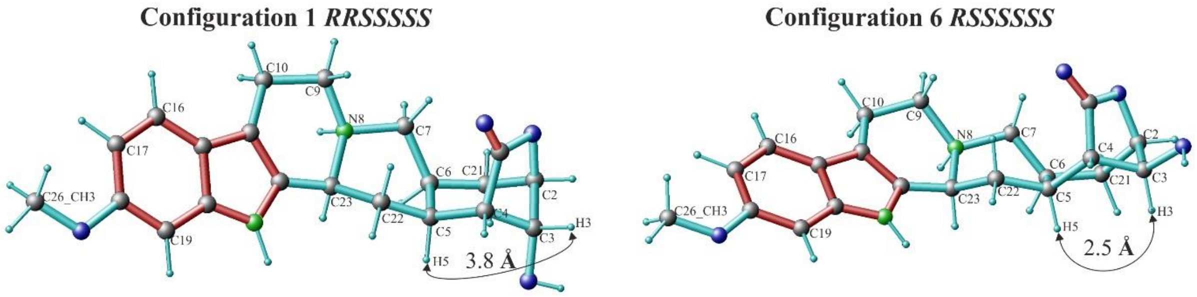
Configuration 1 *RRSSSSS*

Configuration 6 *RSSSSSS*

Figure 52: Three-dimensional representation of configurations 1 (*RRSSSSS*) and 6 (*RSSSSSS*) of RD-2.

In the ROESY spectra, no correlation is visible between protons 5 and 3, while for configuration 6, these two protons are close enough in order to have a correlation (2.5 Å, **Figure 52**). In addition, the scalar coupling constants $^3J_{\mathrm{HH}}$ of H3 with H4 and H3 with H2 fit slightly better with configuration 1. Indeed, the experimental values of these two $^3J_{\mathrm{HH}}$ are 4.6 and 5.2 Hz, respectively, and the average calculated values are 4 and 5.2 Hz for configuration 1 and 3.6 and 3.3 Hz for configuration 6. Thus, the comparison of measured and calculated $^1D_{\mathrm{CH}}$, $^3J_{\mathrm{HH}}$ and intramolecular proton distances derived from ROESY experiment, as shown in **Figure 52** and **Figure 51**, supports the stereochemistry of configuration 1 (*RRSSSSS*) as the correct one. However, configuration 1 doesn't fulfil all experimental constraints within the experimental errors. Indeed, it has 6 outliers, one from a $^1D_{\mathrm{CH}}$ value, two from $^3J_{\mathrm{HH}}$ coupling constants and 3 from ROESY-derived distances (**Table 17**, **Table 18** and **Table 19**). As the calculated values for these couplings are close to be within the experimental error, it should be possible to decrease the numbers of outliers with proper further optimization of the pseudo forces for the different constraints.

Table 17: Experimental *vs*. calculated ${}^{1}D_{CH}$ values for configuration 1 *RRSSSSS* of RD-2.
[a] Experimental values. [b] Experimental errors. [c] Averaged MDOC back calculated values [d] Single conformer (SC) SVD back calculated values [e] Multiple conformers (MC) SVD back calculated values.
Values which don't reach the error range compared to the experimental data ($1/\chi^2 < 1$ outliers) are marked with an asterisk (*).

	Experimental Data		**MDOC**	**SVD (SC)**	**SVD (MD)**
Coupling	D_{exp} **[Hz]**[a]	ΔD_{exp} **[Hz]**[b]	D_{calc} **[Hz]**[c]	D_{calc} **[Hz]**[d]	D_{calc} **[Hz]**[e]
$C_{21}H_{21A}$	-2.7	1.0	-2.6	-3.0	-3.1
$C_{21}H_{21B}$	9.5	1.5	9.5	8.2	8.1
C_5H_5	10.3	1.8	10.6	10.2	10.3
C_6H_6	30.0	2.0	27.7*	21.8*	21.6*
$C_{22}H_{22A}$	-4.0	1.0	-4.0	-3.7	-4.0
$C_{22}H_{22B}$	18.3	1.0	18.0	18.0	18.0
C_4H_4	-1.2	0.6	-1.3	-1.7	-1.7
C_9H_{9B}	17.2	1.8	17.0	18.3	18.1
C_9H_{9A}	-5.3	1.8	-5.1	-3.7	-3.5
C_7H_{7B}	-2.7	1.8	-2.4	-0.7*	-0.7*
C_7H_{7A}	9.9	4.0	12.0	21.9*	21.7*
$C_{23}H_{23}$	17.0	1.0	17.0	16.7	16.9
$CH_{3\text{-}26}$	0.8	0.3	0.7		
C_2H_2	-17.5	3.0	-17.8	16.8	-17.1
C_3H_3	5.6	0.6	5.7	5.4	5.6
$C_{19}H_{19}$	-4.0	0.7	-3.8	-3.3	-3.5
$C_{17}H_{17}$	-21.0	1.5	-20.7	-17.5*	-17.6*
$C_{16}H_{16}$	-3.1	0.6	-3.0	-3.3	-3.2

Table 18: Experimental *vs.* calculated ${}^{3}J_{HH}$ values for configuration 1 *RRSSSSS* of RD-2.
Values which don't reach the error range compare to the experimental data ($1/\chi^2 < 1$ outliers) are marked with an asterisk (*).

Coupling	${}^{3}J_{HH}$ **experimental [Hz]**	**Error**	${}^{3}J_{HH}$ **calculated [Hz]**
H_{23}-H_{22B}	12.6	1.5	11.5
H_{22B}-H_5	12.9	1.5	11.3*
H_{22A}-H_5	8.2	1.5	6.9
H_{21A}-H_2	4.0	1.0	3.6
H_{21B}-H_6	8.9	1.5	8.3
H_{21B}-H_2	3.8	1.0	3.4
H_{7A}-H_6	13.6	1.5	11.7*
H_5-H_4	4.1	1.5	3.5
H_4-H_3	4.6	1.0	4.0
H_3-H_2	5.2	1.0	5.2

Table 19: Experimental *vs*. calculated ROE distances for configuration 1 *RRSSSSS* of RD-2.
Values which don't reach the error range compare to the experimental data ($1/\chi^2 < 1$ outliers) are marked with an asterisk (*).

ROE correlation	Experimental distance [Å]	Error	Calculated distance [Å]
H_{17}-H_{16}	2.45	0.3	2.49
H_8-H_{23}	2.29	0.3	2.20
H_8-H_{9A}	2.62	0.3	2.30*
H_{24}-H_3	2.57	0.3	2.30
H_{13}-H_{23}	2.94	0.3	3.09
H_2-H_3	2.39	0.3	2.53
H_{23}-H_{22A}	2.47	0.3	2.45
H_2-H_{21B}	2.34	0.3	2.46
H_3-H_4	2.35	0.3	2.41
H_2-H_{21A}	2.33	0.3	2.52
H_{23}-H_{22B}	3.16	0.3	3.02
H_{9A}-H_{9B}	1.75	0.3	1.76
H_{9B}-H_{22B}	2.49	0.3	3.68*
H_{7B}-H_{21A}	2.30	0.3	2.60*
H_{21B}-H_{21A}	1.72	0.3	1.70
H_{22A}-H_{22B}	1.69	0.3	1.80

5.5. Discussion

Out of many previously reported direct fitting approaches for the determination of conformational ensembles based on residual dipolar couplings, only two approaches are feasible for medium-sized organic molecules with a limited set of RDCs. All other approaches are either too complex to be applied to this class of molecules, *e.g.* methods based on the mean field additive potential principle [107-109], or too few RDCs are accessible for a reliable fit, as is the case for the multiple conformer multiple alignment tensor fit. The two remaining approaches used here are both based on fitting a single alignment tensor either to a single rigid conformer or to a set of selected conformers using singular value decomposition (SVD). In both cases, a preselected ensemble of possible conformers, typically based on *ab initio* calculations or other computer aided structure elucidation approaches, is being utilized.

In contrast to these direct fitting methods, constrained molecular dynamics (MD) simulations can be used to optimize a single structure or an ensemble of structures to best fit experimental results. However, such approaches have not yet been used to determine the relative configuration of molecules. Several implementations of such methods have been reported using an approximated alignment tensor as initial input [110-115]. Again, the limitation to an alignment tensor is artificial, as, strictly speaking, a single molecular frame of reference for a flexible molecule is not appropriate. Hence, a different approach is favoured for the desired task: Sternberg *et al*. have implemented direct tensorial orientational constraints for dipolar couplings that act in the well-defined laboratory frame. In this case no alignment tensor needs to be assumed and corresponding MD simulations with orientational constraints (MDOC) are based on sound physical principles [80]. The mathematical details of the approach have been described by P. Tzvetkova *et al*. (currently under review, [79]).

The three different approaches, namely SVD-based fitting using a single alignment tensor with a single or multiple conformers and the MDOC approach were tested on the reserpine derivatives RD-1 and RD-2. The results of the 3 methods for the correct configuration are summarized in **Table 20** for RD-1. These two molecules with 7 stereogenic centres represent complex structures that at first sight might be considered relatively rigid. However, the configuration and dynamics at the amine N-8 could not be determined with NOE and ^{3}J-coupling data alone for RD-1. Only the determination of $^{1}J_{CH}$ coupling constants as a side product of the measurement of one-bond RDCs, clearly excluded a significant inversion at N-8, and resulting $^{1}D_{CH}$ couplings unambiguously led to the correct relative configuration of the amine with all three approaches used for RD-1. RD-2 is protonated on the tertiary amine and more flexible than RD-1, which explains why a combination of different experimental NMR parameters ($^{1}D_{CH}$, $^{3}J_{HH}$, and ROE distances) was needed for the determination of the relative configuration of RD-2 including the tertiary amine. Thus, the experimental data of RD-2 can be explained by a single configuration of the amine, but it might also be the result of a fast inversion at this flexible part of the molecule. Further studies will be needed to clarify this aspect.

Table 20: Experimental *vs.* calculated values for configuration *RRSSSSR* of RD-1.

[a] Experimental values. [b] Experimental errors. [c] Averaged MDOC back calculated values [d] Single conformer (SC) SVD back calculated values [e] Multiple conformers (MC) SVD back calculated values.

Values which don't reach the error range compare to the experimental data ($1/\chi^2 < 1$ outliers) are marked with an asterisk (*).

	Experimental Data		**MDOC**	**SVD (SC)**	**SVD (MD)**
Coupling	D_{exp} **[Hz]**[a]	ΔD_{exp} **[Hz]**[b]	D_{calc} **[Hz]**[c]	D_{calc} **[Hz]**[d]	D_{calc} **[Hz]**[e]
$C_{10}H_{10B}$	14.3	5.0	12.7	10.4	10.5
$C_{10}H_{10A}$	22.7	5.0	21.9	23.7	23.6
$C_{21}H_{21A}$	-4.0	0.3	-4.2	-3.8	-4.0
$C_{21}H_{21B}$	18.2	0.3	18.1	18.8^*	18.8^*
C_5H_5	24.1	1.3	23.4	27.2^*	27.1^*
C_6H_6	25.8	1.0	25.3	25.7	25.6
$C_{22}H_{22A}$	25.4	0.3	25.1	24.3^*	24.1^*
$C_{22}H_{22B}$	-7.5	0.3	-7.5	-11.2^*	-11.2^*
C_4H_4	-13.8	0.6	-13.5	-13.9	-14.0
C_9H_{9B}	32.1	0.5	31.6	30.0^*	29.9^*
C_9H_{9A}	-13.3	0.3	-13.1	-14.4^*	-14.5^*
C_7H_{7B}	26.4	5.0	26.8	29.3	29.2
C_7H_{7A}	-16.6	5.0	-13.1	-11.3^*	-11.4^*
$C_{23}H_{23}$	26.7	0.3	26.6	26.2^*	26.2^*
$CH_{3\text{-}28}$	3.1	0.4	3.0		
$CH_{3\text{-}26}$	1.4	0.4	3.0		
C_2H_2	-25.6	1.8	-25.7	-26.0	-25.9
C_3H_3	5.0	0.3	5.2	4.2^*	4.3^*
$C_{19}H_{19}$	-5.2	0.3	-5.1	-5.4	-5.1
$C_{17}H_{17}$	-19.4	1.0	-19.3	-16.6^*	-17.1^*
$C_{16}H_{16}$	-6.1	1.0	-5.9	-5.4	-5.4

Both alignment tensor approaches led to virtually identical results: from the preselected conformers of all possible 32 relative configurations of RD-1, the correct one clearly fitted the data best, demonstrating again the enormous potential of RDCs for structure and in particular configuration determination. However, the preselected conformers did not allow generating a structural ensemble that fully agreed with experimental data. Even in the best case, more than 10 RDCs were outside the error margins of the experiment. Apparently, additional conformers would have to be taken into account that were not part of the standard conformational search procedure. The MDOC approach, in contrast, has no pre-assumptions concerning the conformational space and the correct structure results in a conformational ensemble that fully reproduces the experimental data. It turns out that at least one minor conformation with approximately 10 % population is present (**Figure 53**).

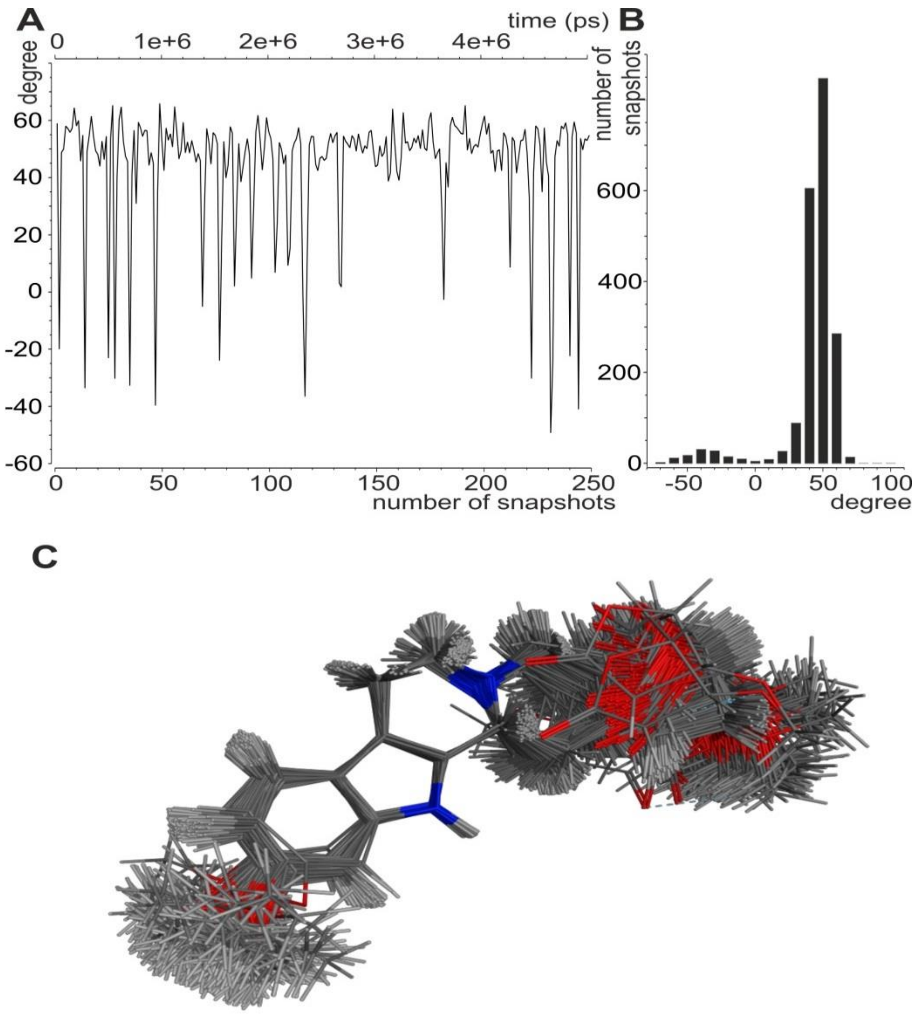

Figure 53: Structural ensemble derived from experimental RDC constraints of RD-1.
(**A**, **B**) The dihedral angle H_{10A}-C_{10}-C_9-H_{9A} is indicative for at least one minor conformation with a population of roughly 10 %. A graph with the evolution of the angle over a part of the MDOC run (**A**) as well as the population of the angles over the entire MDOC run is shown (**B**). (**C**) Visualization of the structural ensemble of the correct relative configuration of RD-1 from 250 individual conformations from the MDOC run. Structures are overlaid at the indole ring.

Since the corresponding conformer is missing in the preselection of the alignment tensor fitting approaches, it can be expected that even the multiple conformers approach is unable to reproduce the experimental constraints. Nevertheless, as the full accessible conformational space is only restricted by RDC constraints in the MDOC approach, the ability to discriminate the different relative configurations must necessarily be reduced. Besides the correct configuration 11, the relative configurations 4 and 5 also achieved n/χ^2 values above 1, however with 2 and 5 outliers, *i.e.* with back calculated RDC constraints outside the experimental error range, which falsified these two configurations. The large n/χ^2 values of these two wrong configurations can be explained by the fact that they cause significant changes only in the bridged lactone-ring, which contains only few RDC constraints due to low number of protons in the ring system. Obviously, additional constraints derived from both theory and experiment could be added to further discriminate configurations, but in this study we limited ourselves to one-bond RDCs which still allow sufficient discrimination – solely based on experimental constraints and unbiased by theory. For RD-2, the same protocol was followed, however, additional constraints were needed because fewer $^1D_{CH}$ constraints were available compared to RD-1. The RDCs for the CH_2-10 were not extractable due to signal overlap, and in addition the amine is protonated. In RD-2, the proton 5, 6 and 23 are in the same plane (-*cis*) making the molecule more flexible, while for RD-1, the proton 23 is -*trans* to the protons 5 and 6 which leads to a stiffer molecular structure (**Figure 54**).

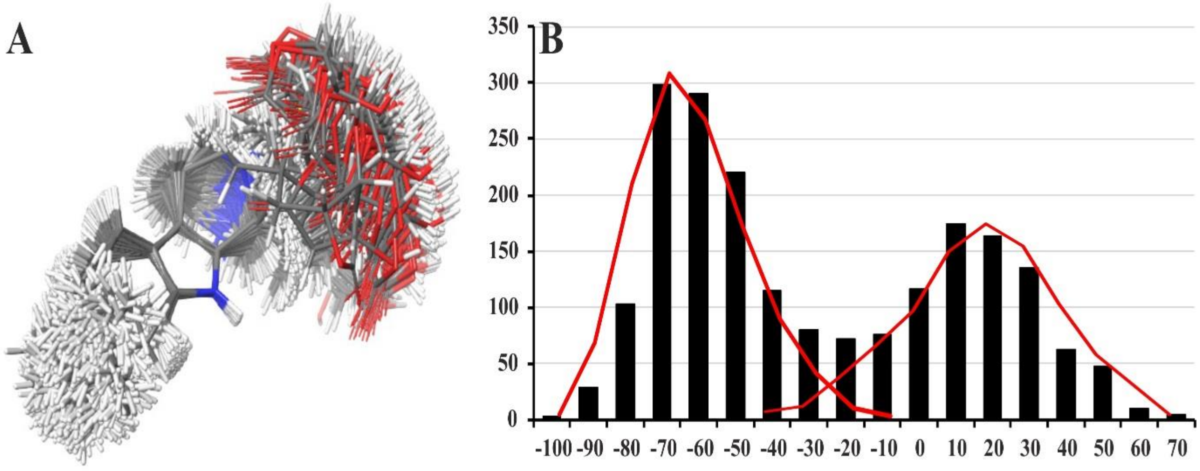

Figure 54: Flexibility of RD-2.
In panel **A**, a visualization of the structural ensemble of the correct relative configuration of RD-2 from 250 individual conformations from the MDOC run is shown. The individual structures are overlaid at the indole ring. In panel **B**, the population of the angles over the entire MDOC run is provided, the dihedral angle H_{9B}-C_9-N_8-C_7 is indicative for at least a second conformation with a population of roughly 50 %.

5.6. Conclusion

In summary, RDCs represent a valuable tool for the determination of the conformation and configuration of even very complex molecules and introduce a novel method that allows the distinction of relative configurations and the determination of a structural ensemble that fulfils all experimental constraints within error ranges. As a first the relative stereochemistry of a small molecule with 2 chiral centres, Selfotel, was determined. The elucidation of this molecule require little optimization of the MD simulation and this simple example was used with the main purpose to demonstrate the assessment of the 3 mm device. Then, the configuration of 7 stereogenic centres in a partially flexible molecule (RD-1) and a more flexible molecule (RD-2) could be determined, including the stereochemistry of an amine. This was not possible using only standard NMR data (NOEs and scalar couplings). For a partially flexible molecule as shown here, the SVD approach with preselected conformers for each configuration led to a clear discrimination of the correct *vs*. wrong configurations of RD-1 and RD-2, but experimental data could not be reproduced within their error ranges. The latter was easily achieved by the *so-called* MDOC (molecular dynamics using orientational constraints) approach for RD-1, which also provided a clear distinction unbiased by a theoretical preselection of conformers.

The configurational and conformational analysis of RD-1 was achieved solely based on one-bond RDCs and for RD-2 the use of the scalar coupling $^3J_{\mathrm{HH}}$ and the distances derived from ROE were needed in addition to the one-bond RDCs. Nevertheless, for RD-2 calculated data could not fulfilled all experimental data within their error. More anisotropic NMR parameters like long-range RDCs or residual chemical shift anisotropies (RCSAs) could be included in both SVD and MDOC calculations, but only the MDOC approach will allow the simultaneous inclusion of further experimental constraints like distances derived from NOE-data or dihedral angles obtained from the Karplus relation. In addition, also theoretically derived angular or distance constraints can be applied. MDOC may therefore be more generally applicable and extend the application range of RDC aided 3D-structure determination to especially flexible molecules. Therefore it is a great potential method in many areas of structural analysis, including for example natural product-based drug discovery as well as the structural characterization of intrinsically disordered proteins.

6. Absolute configuration determination of small chiral compounds

The first determination of the absolute configuration of stereocenters in a small molecule (tartaric acid) by X-ray crystallography was described by Bijvoet *et al.* in 1951 [116]. X-ray measurements were performed on sodium rubidium (NaRb) (+)-tartrate crystals using an emission line of Zirconium (Zr) to excite the anomalous scattering of the Rb-atoms. This method requires a well-defined crystal lattice which can be difficult, and sometimes even impossible, to obtain in sufficient quality. Nevertheless, X-ray is still the first choice for the determination of the configuration of compounds. For the substances which can be neither crystallized nor easily be converted into crystallisable derivatives, other techniques need to be applied. Such methods were comprehensively described by Allenmark *et al.* [117] and include synthetic methods [118], anomalous X-ray diffraction [116], chiroptical spectroscopy [119] and nuclear magnetic resonance methods [12]. All these methods require a reference substance with known absolute stereochemistry for comparison or accurate theoretical analysis, usually from previous measurements or other analytic methods, and are briefly described in the following paragraph.

6.1. Existing methods for absolute configuration determination

6.1.1. Chemical synthetic methods

The first method used for structural elucidation of unknown products was based on chemical synthesis with degradation and derivatization reactions in order to develop and test structural hypotheses [120]. This method can take years to be completed and requires a significant quantity of material. With the emergence of advanced spectroscopic methods, this methods lost its relevance, however, it can still be used for the absolute stereochemistry determination by degradation reaction and by converting the studied molecule into a compound with known configuration.

6.1.2. Anomalous X-ray diffraction

X-ray crystallography provides the 3D structure of a molecule, arranged in a crystal lattice, by measuring how it scatters X-ray radiation. As the dimensions of atoms and bonds lengths are in the range of 1 to 3.5 Å, X-rays having a typically a wavelength around 1 Å is appropriate for the resolution of atomic details. By measuring the intensities in the diffraction pattern, the electron density distribution in the crystal can be calculated and a molecular model can be derived [121]. A crystal corresponds to a symmetric and regular packing of a molecule which allow to distinguish enantiomers. Different ways exist to assign the absolute stereochemistry using X-Ray diffraction [122]. Single-crystal XRD using an internal chiral reference is one of the method, but an introduction of a known chiral reference moiety to the unknown chiral molecule is needed, hence a modification of the compound occurs. An alternative single crystal XRD method exploits resonant scattering, the *so-called* Flack parameter[101]. This method is based on a post refinement of the diffraction data which need to have a high quality. This latest is the preferred method nowadays [123].

6.1.3. Chiroptical spectroscopy

Chiroptical spectroscopy methods include optical rotary dispersion (ORD), electronic circular dichroism (ECD), vibrational circular dichroism (VCD), and Raman optical activity (ROA). A distinction of molecules is possible based on the differential interaction of polarized light with chiral molecules. For example, in circular dichroism (CD) spectroscopy, the employed light is circularly polarized, and the difference in absorption of right and left polarized light yields a CD spectrum. However, these methods require prior knowledge from similar scaffolds to attest the configuration. Novel compounds with several stereocenters are not easily analysed by these methods. Vibrational CD (VCD) uses infrared radiation and enables determination of absolute configuration in comparison to calculated spectra, as enantiomers will display exact opposite VCD spectra [124]. Chiroptical spectroscopy methods [119] are increasingly used for absolute stereochemistry determination as the interaction between the electromagnetic radiation and the molecules can be modelled from *ab initio* quantum mechanical modelling. However, as this requires all conformations to be known, these techniques are still mostly applied to relatively rigid compounds with few stereocenters, explaining why the use of RDCs and computational methods was explored as a complementary technique in this thesis.

6.1.4. Chromatographic methods

Chromatography allows the separation of components in a sample, carried by a liquid or gaseous phase, by sorption-desorption steps on the stationary phase. Chiral chromatography is a commonly used method for the separation of enantiomers by the formation of diastereoisomers via derivatizing agents or mobile phase additives using a chiral stationary phase. This method allows the separation of enantiomers and the assignment of the absolute configuration in case pre-existing data if related molecules is available.

6.1.5. NMR based methods

NMR-based determination of the absolute configuration can be achieved by chemical modification using chiral derivatizing agents (CDAs). While a variety of different CDAs exist (*e.g.* summarized by Seco *et al.* [12]), the Mosher's reagent Methoxy-trifluoro-methyl-phenyl-acetic acid (MTPA) is one of the most known and utilized one. Such CDAs enable the determination of the absolute configuration of molecules having different functional groups such as α-chiral secondary alcohols, β-chiral primary alcohols, α-chiral tertiary alcohols, α-chiral primary amines, secondary amines, β-chiral carboxylic acids and chiral sulfoxides. Molecules comprising chiral centres without functional groups as described above are not amenable for characterization by this method. In addition, a great care is required to ensure that neither kinetic resolution nor racemization occur during the derivatization.

In addition, NMR spectroscopy offers more direct ways to examine stereochemistry without the need for chemical modifications. The use of chiral solvating agents creates a diastereomeric environment for the enantiomers, resulting in chemical shift changes [125]. While this method was successfully applied to several lactones [126], the most significant limitation is the same as described for optical methods, namely the lack of a clear correlation between the observed spectrum and the absolute configuration of a molecule. In order to be unambiguous, the results obtained need to be compared to a reference.

Using scalar coupling constants (*J*) and nuclear Overhauser effect (NOE) is the most common way to study stereochemical and conformational relationships. As described in section 5, such NMR methods, including RDCs, only yield the relative configuration rather than absolute structures. However, it has been shown that differentiation of enantiomers is possible from anisotropic NMR parameters determined in chiral alignment media such as PBLG [127, 128], poly-ε-carbobenzyloxy-L-lysine (PCBLL) [129], gelatine [130], collagen [131, 132], e^--gelatine [133], carrageenan [134] and most recently polyacetylene gels [135-138]. Furthermore, even the *a priori* determination of the absolute configuration could be achieved in case the interaction of the solute molecules with chiral medium can be predicted with sufficient accuracy. Ziani *et al.* [139] described the determination of the absolute configuration of an epoxide by a process later called cross-fitting of residual quadrupolar couplings, RQCs [54] from very similar molecules with known chirality. A prediction of chiral alignment medium, PBLG, has been published in 2007 by Marathias *et al.* [140], however, this paper has been followed by a critical assessment publication in 2012 by the community working in the RDCs field [141].

Such predictions of residual dipolar couplings (RDCs) and other residual anisotropic NMR parameters are typically based on modelling the alignment media as an infinite wall or cylinder [68, 71], or based on the assumption that the alignment medium tensor is collinear with the inertia tensor (as in the TRAMITE approach [142]) or the tensor of gyration [143]. However, these models lack a detailed description of the solute-medium interactions and their most successful applications are limited to large molecules. Indeed, the interaction are modelled in a non-specific way (steric interaction by modelling infinite wall or cylinder), while more specialised approaches are needed for the modelling of the proper differences in the interactions of the two enantiomers with the polymer network. Only recently, a more accurate prediction of alignment has been achieved using molecular dynamic (MD) simulations for the nematic phase (rod-like molecules can organize themselves so that long axes are aligned) [144] and using a model for strain-induced alignment in a polystyrene gel in chloroform [45], which could partially reproduce the experimental data. In principle, such MD simulations are able to determine the differences in alignment for enantiomers in chiral orienting medium. In this thesis, the recently published model for a strained polymer gels is adapted to the chiral lyotropic liquid crystalline phase of a poly-γ-benzyl-*L*-glutamate (PBLG) liquid crystal in chloroform. The resulting MD simulations enable the prediction of theoretical RDCs which can then be compared to the experimental values.

6.2. Experimental methods

6.2.1. Alignment medium

In this study, a PBLG/$CDCl_3$ chiral liquid crystalline phase was used as alignment medium to distinguish enantiomers and to evaluate the possibility of determining the absolute stereochemistry. PBLG is a *pseudo* peptide composed from glutamate as shown in **Figure 7**, which forms a lyotropic mesophases and possesses an α-helical structure under the influence of strong magnetic field [128].

6.2.2. Enantiomeric molecules studied

The aim of the part of the thesis is to develop a new method for the assessment of absolute configuration with NMR spectroscopy. For this purpose, five enantiomeric pairs of molecules with different complexity, functional groups and size were selected (**Figure 55**). The systematic name of the investigated molecules is provided in **Table 21**. All of them are soluble in chloroform and therefore suitable for measurements in PBLG/$CDCl_3$. The choice of the molecule was determined according to their chemical structure and was focused of the presence either a donor or an acceptor or both for the formation of a hydrogen bond. The aim was to determine which interaction with PBLG is responsible for the possible differentiation of the enantiomers, which would allow the optimization of the MD simulations. Thus, the evaluation of a possible enantiodifferentiation based on the different hydrogen bond formation capacity of the model molecules was investigated. Borneol, camphor and quinuclidinol are small molecules containing different functional groups, namely an alcohol function in borneol and quinuclidinol (*i.e.* a donor for the formation of a hydrogen bond), a carbonyl group in camphor and a tertiary amine in quinuclidinol, respectively, which can serve as an acceptor in a hydrogen bond. PBLG itself possesses both hydrogen bond acceptors and donors which are available for interaction with the small molecules. In addition the three dimensional shape and the size of the molecules could potentially play a role and more molecular models are needed to fully address all possibilities. The complete set of molecules for this project done in collaboration with Dr. Pavleta Tzvetkova contains ibuprofen, phenylethanol and azabicyclo[2.2.1]hept-5-en-3one. Ibuprofen possess an acidic functionality, phenylethanol an alcohol and azabicyclo[2.2.1]hept-5-en-3one has an amide group, they can all formed hydrogen bonding with different strength.

The absolute stereochemistry of all compounds except for 2-Phenanthrenol, 1,2,3,4,4a,9,10,10a-octahydro-7-methoxy-1,1,4a-trimethyl (POMT) was known at the beginning of the study. The two enantiomers of POMT were isolated from a racemic mixture by the chiral separations group at Novartis. The configuration of the two enantiomers was determined by X-Ray analysis which has been performed by Ina Dix and Philippe Piechon at Novartis. All NMR experiments were performed without knowing the configuration of the two enantiomers and they were differentiated with the name *enan.* 1 and *enan.* 2 according to the names given by the chiral separations group.

Table 21: Generic and systematic names of the compound described in this section**.**

Generic Names	**Systematic Names**
HMIP	(6a*R*, 12b*R*) or (6a*S*, 12b*S*)-4,6,6a,7,812b-Hexahydro-7-methylindolo[4,3-ab] phenanthridine
POMT	2-Phenanthrenol, 1,2,3,4,4a,9,10,10a-octahydro-7-methoxy-1,1,4a-trimethyl-, (2*S* ,4a*S*,10a*R*) or (2*R* ,4a*R*,10a*S*)
Borneol	Bicyclo[2.2.1]heptan-2-ol, 1,7,7-trimethyl-, (1*S*, 2*S*, 4*S*) or (1*R*, 2*R*, 4*R*)
Camphor	Bicyclo[2.2.1]heptan-2-one, 1,7,7-trimethyl-, (1*S*, 4*S*) or (1*R*, 4*R*)
Quinuclidinol	1-Azabicyclo[2.2.2]pctan-3-ol (3*R)* or (3*S*)

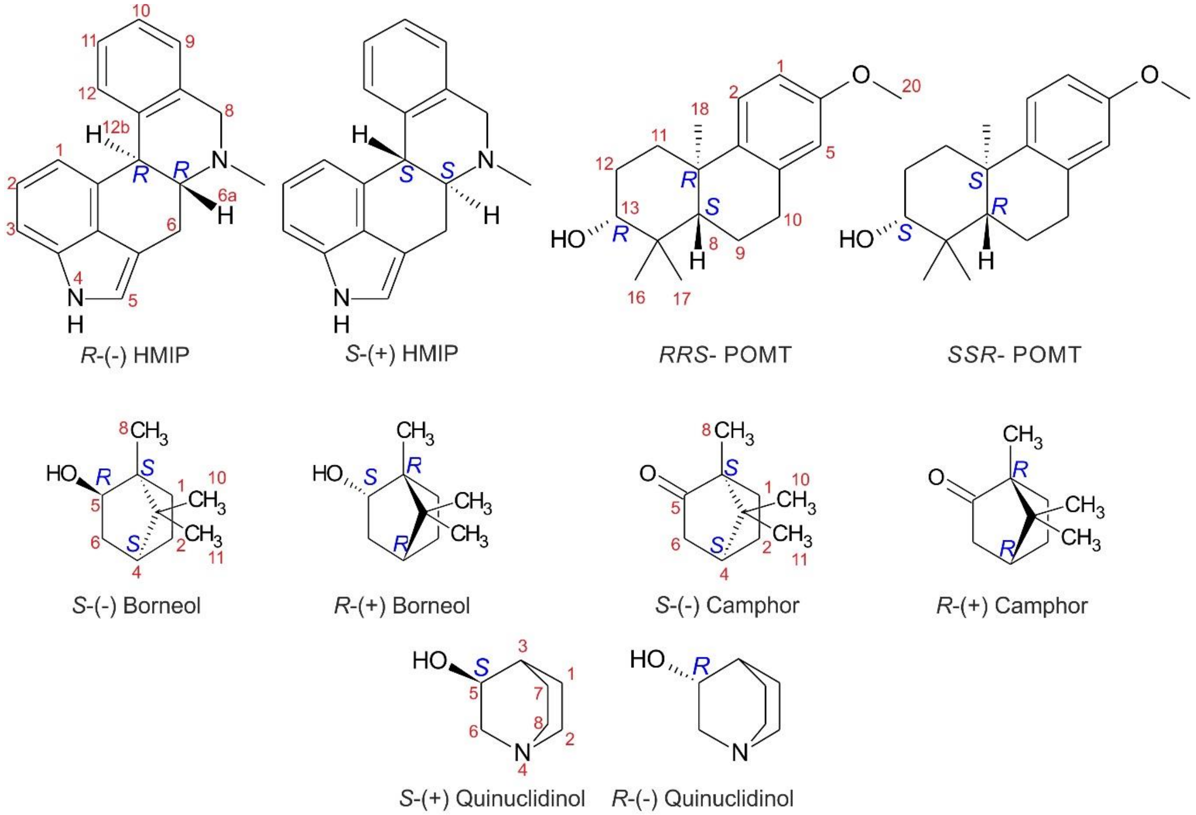
R-(-) HMIP *S*-(+) HMIP *RRS*- POMT *SSR*- POMT

S-(-) Borneol *R*-(+) Borneol *S*-(-) Camphor *R*-(+) Camphor

S-(+) Quinuclidinol *R*-(-) Quinuclidinol

Figure 55: Chemical structures, generic names and arbitrary numbering of the five pairs of enantiomers described in this study.

The absolute stereochemistry is indicated on the structure and with the generic name, while optical rotation is provided in brackets.

6.2.3. Sample preparation

To obtain experimental RDCs, isotropic and anisotropic samples were prepared as described in Section 2. For the experiments in this section, a liquid probe head and a VASS probe head were used in order to be able to measure the RDCs in different alignments. Consequently, five-millimetre tubes and 4 mm Zirconia rotors were prepared according to the information provided in **Table 22**.

Table 22: Composition and properties of isotropic and anisotropic samples of the 5 pairs of enantiomers.

	HMIP			**POMT**		
	Isotropic	**Anisotropic**		**Isotropic**	**Anisotropic**	
		R	*S*		Enan *1*	Enan *2*
Quantity [mg]	6.0	16.1	13.9	7.8	11.5	12.5
Solvent/PBLG [mg]	$CDCl_3$	$CDCl_3$/92.2	$CDCl_3$/91.9	$CDCl_3$	$CDCl_3$/90.2	$CDCl_3$/91.5
Volume [mL]	0.6	1.0		0.6	1.0	
Monoisotopic Mass [g/mol]	274.1			274.2		
Concentration [mM]	36.5	58.7	50.7	47.0	41.9	45.6

	Borneol			**Camphor**		
	Isotropic	**Anisotropic**		**Isotropic**	**Anisotropic**	
		R	*S*		*R*	*S*
Quantity [mg]	20.0	16.7	15.9	13.0	14.0	17.0
Solvent/PBLG [mg]	$CDCl_3$	$CDCl_3$/93.5	$CDCl_3$/92.9	$CDCl_3$	$CDCl_3$/90.1	$CDCl_3$/90.5
Volume [mL]	0.75	1.0		0.75	1.0	
Monoisotopic Mass [g/mol]	154.1			152.1		
Concentration [mM]	173	108	103	114	92	112

	Quinuclidinol		
	Isotropic	**Anisotropic**	
		R	*S*
Quantity [mg]	20.0	20.6	20.2
Solvent/PBLG [mg]	$CDCl_3$	$CDCl_3$/99	$CDCl_3$/98.76
Volume [mL]	0.75	1.0	
Monoisotopic Mass [g/mol]	127.1		
Concentration [mM]	210	162	159

Within a concentration range of 12 to 25% (w/v), PBLG in chloroform acts as a weakly aligning chiral medium [26]. At this concentration, the solutions are very viscous, and as a result mixing and homogenization steps take time and they have to be done carefully. However, the use of the liquid crystalline phase for an alignment medium requires a very homogeneous sample to perform experiments for NMR spectroscopy. To achieve this necessary level of homogenisation a vertical rotating shaker (360° PTR-35 Grant-Bio) was modified in order to be able to use it for 5 mm NMR tubes and to mix and homogenize the samples (**Figure 56**).

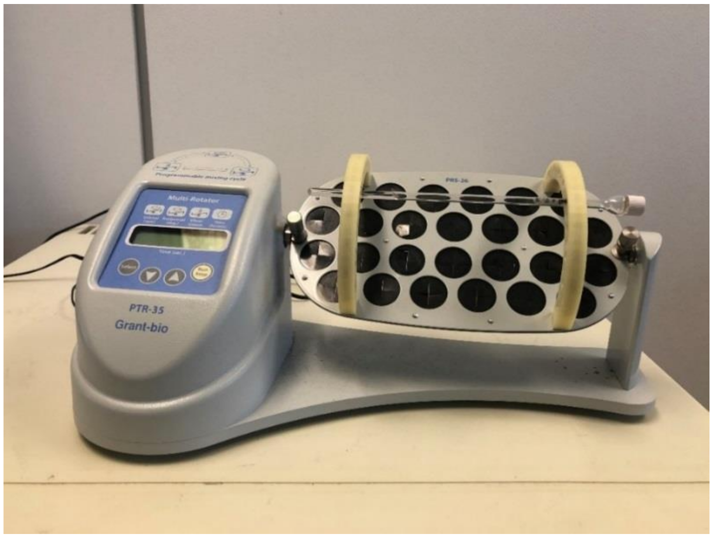

Figure 56: Vertical rotating shaker 360° PTR-35 Grant-Bio adapted for 5 mm NMR tubes.

In order to avoid the mixing and homogenization steps, once the 5 mm tube samples were measured and the spectra evaluated. The rotor samples for borneol, camphor, and quinuclidinol were directly prepared from the content of the tubes. The composition of the rotor samples were identical to the 5 mm sample tubes, indeed, 50 microliter of the 5 mm tubes samples were transferred in the rotor with a piston-operated pipette.

6.2.4. NMR measurement

NMR spectra were recorded on different spectrometers as detailed in **Table 23**.

Table 23: NMR spectrometers used to acquire experiments for the 5 pairs of enantiomers.
Borneol, camphor, and quinuclidinol samples were recorded on spectrometer **E** employed with VASS probe head.

Sample	**Spectrometer**	
	Isotropic	**Anisotropic**
HMIP	D	B and D
POMT	B	B
Borneol	A	A and E
Camphor	A	A and E
Quinuclidinol	A	A and E

^{1}H-1D and 2D CLIP-HSQC spectra were recorded on all samples in isotropic and aligned phases in order to obtain $^1T_{CH}$ coupling constants (as detailed in section 2.2.3). In addition, deuterium spectra and ^{2}H-imaging experiments were recorded on the aligned samples to measure the quadrupolar splitting and to evaluate the homogeneity of alignment, respectively. Due to very broad signals and significant signal overlap for HMIP in the aligned samples, a selectively coupled

^{13}C-detected 1D-INEPT experiment was performed to measure all $^{1}T_{CH}$ values [145] (Further modifications on the ^{13}C-detected 1D-INEPT experiment have been realised by Dr. S. Ehni and Dr. P. Tzvetkova). In **Figure 57**, the spectra obtained from HMIP for the CH-3, CH_2-8, and CH_3-21 are shown (numbering according to **Figure 55**). Antiphase multiplets are obtained with couplings corresponding to T_{CH} for CH signals, $2T_{CH}$ for a CH_2 signals and $3T_{CH}$ for CH_3 signals.

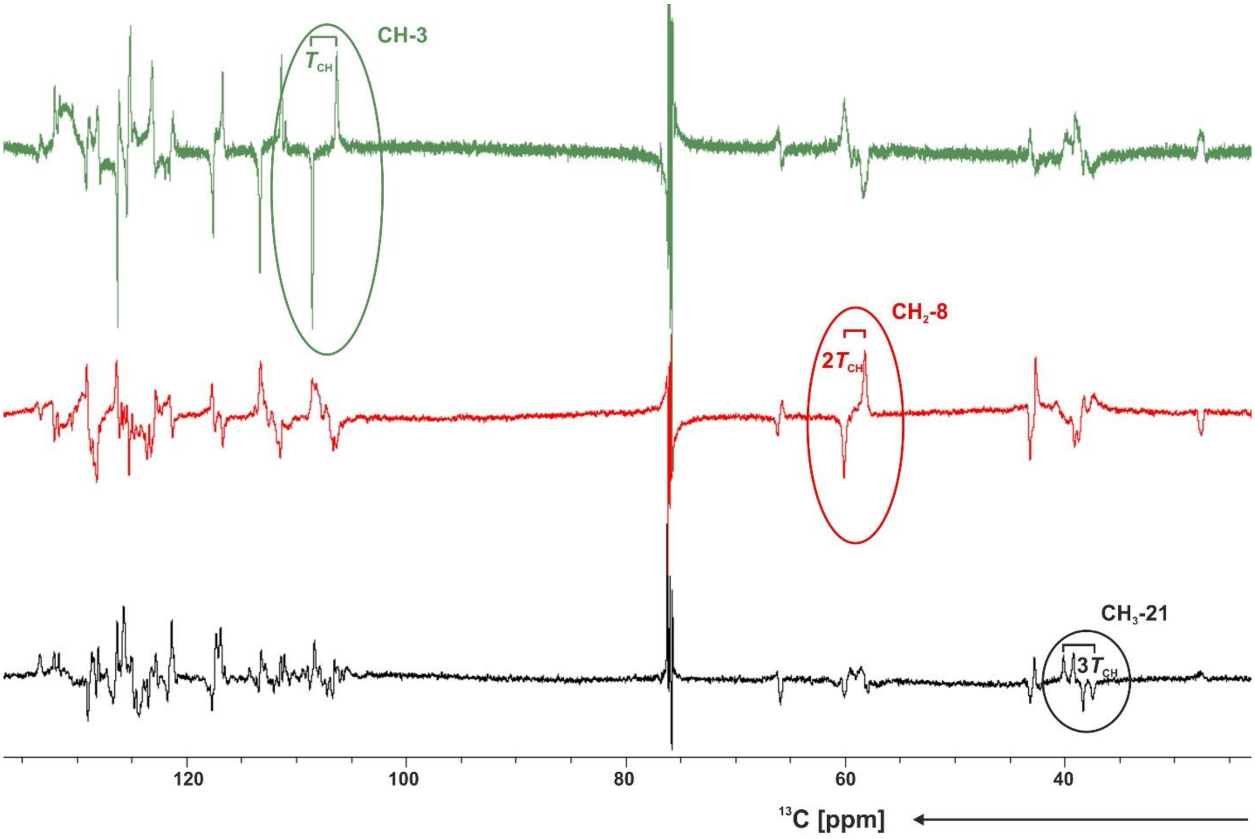

Figure 57: Selectively coupled ^{13}C-detected 1D-INEPT spectra of HMIP measured for CH_3-21, CH_2-8 and CH-3.

For the isotropic experiments, the typical proton spectral widths were 6 kHz and 12 kHz for the aligned samples, while the carbon spectral widths varied between 28 kHz to 36 kHz, with 32k time domain points recorded on the free induction decay (FID). Deuterium experiments were recorded with spectral widths of 28 kHz and 32k time domain points. CLIP-HSQC experiments were typically acquired with a spectral width between 6 kHz and 12 kHz and 16k time domain points in the direct dimension, while in the indirect dimension the spectral width was varied between 20-24 kHz with 256 increments. During data processing, zero filling to typically twice the number of points was applied in both dimensions.

Coupling constants in isotropic and aligned phases were measured according to the procedure explained in section 2.2.3. For HMIP, signals in the partially aligned sample were very broad with multiplet widths of 40 to 130 Hz and all ${}^{1}T_{CH}$ couplings were measured from selectively coupled ^{13}C-1D experiments as shown in **Figure 57**. The experimentally determined ${}^{1}D_{CH}$ residual dipolar couplings are summarized in **Table 27** for the various molecules. Three different anisotropic samples were prepared and measured for each enantiomer of HMIP, two samples in 5 mm tubes and one in 3 mm tube. For each a different quadrupolar splitting was achieved that means different alignments were reached ($\Delta\nu_Q$ = 320 Hz, 477 Hz and 642 Hz for *R*-HMIP and $\Delta\nu_Q$ = 280 Hz, 354 Hz and 623 Hz for *S*-HMIP).). For each sample, ${}^{1}T_{CH}$ RDCs were extracted from selectively coupled ^{13}C-detected 1D-INEPT experiments. In cases of weak alignment, the *total* coupling constants and their signs can be directly extracted but with HMIP in PBLG, whereas in cases of stronger alignment, the sign of the *total* couplings constant have to be checked.

The extracted ${}^{1}T_{CH}$ from the 3 anisotropic samples and ${}^{1}J_{CH}$ from the isotropic sample of *R*-HMIP and *S*-HMIP, are provided in **Table 24** and **Table 25**, respectively.

Table 24: Experimental ${}^{1}J_{CH}$ and ${}^{1}T_{CH}$ constant of *R*-HMIP obtained from 4 different samples. The scalar constants ${}^{1}J_{CH}$ were obtained from the isotropic sample and the total coupling constants ${}^{1}T_{CH}$ from 3 different anisotropic samples having a different quadrupolar splitting *i.e.* a different alignment.

Assignment	**${}^{1}J_{CH}$ [Hz] $\Delta\nu_Q$ = 0 Hz**	**${}^{1}T_{CH}$ [Hz] $\Delta\nu_Q$ = 280 Hz**	**${}^{1}T_{CH}$ [Hz] $\Delta\nu_Q$ = 354 Hz**	**${}^{1}T_{CH}$ [Hz] $\Delta\nu_Q$ = 623 Hz**
CH-5	182.12	168.39	137.50	185.03
CH_2-6 averaged	129.53	76.47	53.43	204.67
CH-6a	134.48	81.41	83.04	303.16
CH_2-8 averaged	134.76	378.35	205.75	337.62
CH-9	156.98	232.65	270.42	348.64
CH-12	156.86	198.93	249.58	305.37
CH-12b	125.82	106.75	146.63	340.09
CH-1	158.67	394.91	398.34	561.25
CH-2	158.87	-59.97	92.40	280.74
CH-3	161.50	442.91	489.21	721.61
CH_3	133.78	179.91	180.26	216.77

Table 25: Experimental $^{1}J_{\mathrm{CH}}$ and $^{1}T_{\mathrm{CH}}$ constants of *S*-HMIP obtained from 4 different samples.
The scalar constants $^{1}J_{\mathrm{CH}}$ were obtained from the isotropic sample and the total coupling constants $^{1}T_{\mathrm{CH}}$ from 3 different anisotropic samples having a different quadrupolar splittings *i.e.* a different strength of alignment.

Assignment	**$^{1}J_{\mathrm{CH}}$ [Hz] $\Delta\nu_Q = 0$ Hz**	**$^{1}T_{\mathrm{CH}}$ [Hz] $\Delta\nu_Q = 320$ Hz**	**$^{1}T_{\mathrm{CH}}$ [Hz] $\Delta\nu_Q = 477$ Hz**	**$^{1}T_{\mathrm{CH}}$ [Hz] $\Delta\nu_Q = 642$ Hz**
CH-5	182.12	172.62	172.30	264.96
CH_2-6 averaged	129.53	109.12	114.58	334.07
CH-6a	134.48	116.37	203.30	421.28
CH_2-8 averaged	134.76	426.58	192.35	476.14
CH-9	156.98	426.58	251.93	297.40
CH-12	156.86	214.20	204.70	215.33
CH-12b	125.82	204.28	295.55	394.73
CH-1	158.67	123.96	578.59	726.11
CH-2	158.87	422.39	95.46	160.10
CH-3	161.50	102.05	701.03	857.19
CH_3	133.78	513.81	215.06	224.10

In order to determine the sign of the RDCs, the correlation coefficients between the quadrupolar splittings and the $^{1}J_{\mathrm{CH}}$ / $^{1}T_{\mathrm{CH}}$ obtained for each CH is calculated with positive and negative $^{1}T_{\mathrm{CH}}$. The obtained results are summarized in **Table 26**. Since, the correlations have to be linear, the higher correlation coefficient correspond to the correct sign.

Table 26: Coefficient correlations obtained from the comparison of the quadrupolar splittings and the obtained coupling constants $^{1}J_{\mathrm{CH}}$ and $^{1}T_{\mathrm{CH}}$.

	***R*-HMIP**		***S*-HMIP**	
	Positive $^{1}T_{\mathrm{CH}}$	**Negative $^{1}T_{\mathrm{CH}}$**	**Positive $^{1}T_{\mathrm{CH}}$**	**Negative $^{1}T_{\mathrm{CH}}$**
CH-5	0.02	0.85	0.61	0.95
CH_2-6 averaged	0.43	0.98	0.64	0.97
CH-6a	0.64	0.99	0.78	0.99
CH_2-8 averaged	0.66	0.79	0.66	0.82
CH-9	0.99	0.91	0.99	0.94
CH-12	0.98	0.91	0.94	0.89
CH-12b	0.81	0.99	0.88	0.99
CH-1	0.99	0.93	1.00	0.98
CH-2	0.51	1.00	0.17	0.94
CH-3	1.00	0.96	1.00	0.98
CH_3	0.99	0.87	0.97	0.90

For the protons 5, 6, 6a, 8, 12b and 1, the correlation coefficients are better if the sign of the *total* coupling constants $^{1}T_{\mathrm{CH}}$ is changed, highlighted in green in **Table 26**, hence the negative values of these $^{1}T_{\mathrm{CH}}$ are the correct values and they are used for the interpretation of the data.

As it is experimentally almost impossible to reach an identical alignment for different samples, the RDC values of one enantiomer were scaled according to the difference in the quadrupolar splitting in order to compare the experimental RDCs between the two enantiomers.

Table 27: Experimental $^{1}D_{CH}$ coupling constants of the five pairs of enantiomers.
For Camphor, two RDCs were not extractable due to broad signals. Atoms highlighted in red are stereogenic centres. In the column with *, scaled RDCs are shown.

Assignment	***R*-(-) HMIP [Hz]**	***S*-(+) HMIP* [Hz]**
$\Delta\nu_Q$	354	477
CH-5	-319.62 ± 15	-263.01 ± 6
CH$_2$-6 averaged	-182.96 ± 10	-181.14 ± 6
CH-6a	-217.52 ± 5	-250.66 ± 7
CH$_2$-8 averaged	70.99 ± 7	42.74 ± 10
CH-9	113.44 ± 15	70.46 ± 6
CH-12	92.72 ± 15	35.50 ± 15
CH-12b	-272.45 ± 5	-312.68 ± 15
CH-1	239.67 ± 10	311.61 ± 6
CH-2	-251.27 ± 15	-188.73 ± 6
CH-3	327.71 ± 15	400.37 ± 6
CH$_3$	46.48 ± 5	60.32 ± 5

Assignment	**POMT P1 [Hz]**	**POMT P2* [Hz]**
$\Delta\nu_Q$	321	295
CH-1	-48.48 ± 1	-38.31 ± 1
CH-2	51.41 ± 1	64.12 ± 1
CH-5	50.84 ± 3	61.45 ± 1
CH-8	37.47 ± 1.5	24.00 ± 2
CH-11’	34.96 ± 3	18.29 ± 1.5
CH-11’’	11.73 ± 7	23.09 ± 10
CH-13	33.21 ± 0.5	19.03 ± 0.5
CH$_3$-16	-2.92 ± 0.8	-9.08 ± 0.5
CH$_3$-17	-1.71 ± 0.5	3.84 ± 0.5
CH$_3$-18	-15.59 ± 1	-16.29 ± 2
CH$_3$-19	2.25 ± 0.2	0.08 ± 0.3

Assignment	***S*-(-) Borneol [Hz]**	***R*-(+) Borneol* [Hz]**
$\Delta\nu_Q$	263	299
CH-5	3.34 ± 1.5	29.16 ± 0.4
CH-4	4.91 ± 0.5	-20.53 ± 2
CH$_2$-6’	-30.94 ± 2	-11.15 ± 1
CH$_2$-6’’	2.35 ± 1	-1.63 ± 1.3
CH$_2$-2’	-21.82 ± 3	-9.04 ± 2.4
CH$_2$-2’’	24.25 ± 1.5	30.45 ± 0.6
CH$_2$-1’	19.13 ± 1	10.98 ± 0.8
CH$_2$-1’’	-25.73 ± 5	-22.83 ± 1
CH$_3$-11	-1.65 ± 1.2	-0.25 ± 4
CH$_3$-10	5.92 ± 1	1.72 ± 0.4
CH$_3$-8	-1.12 ± 0.5	2.47 ± 0.5

Assignment	***S*-(-) Camphor [Hz]**	***R*-(+) Camphor * [Hz]**
$\Delta\nu_Q$	285	262
CH$_2$-6’	7.80 ± 2	11.02 ± 0.4
CH$_2$-6’’	29.40 ± 0.6	26.20 ± 0.7
CH-4	2.29 ± 3	4.11 ± 0.6
CH$_2$-1’		-26.38 ± 10
CH$_2$-1’’		-5.47 ± 10
CH$_2$-2’	1.65 ± 3	5.94 ± 2
CH$_2$-2’’	-41.51 ± 3	-52.93 ± 3
CH$_3$-10	-7.75 ± 1	-7.19 ± 1.5
CH$_3$-11	15.84 ± 1	15.73 ± 0.3
CH$_3$-8	-6.14 ± 1	-6.87 ± 0.8

Assignment	***R*-(-) Qui. [Hz]**	***S*-(+) Qui.* [Hz]**
$\Delta\nu_Q$	305	261
CH-5	22.71 ± 0.3	13.02 ± 0.3
CH$_2$-6’	-15.01 ± 1.5	-38.96 ± 0.4
CH$_2$-6’’	-25.24 ± 0.5	-0.96 ± 0.8
CH$_2$-2’	41.34 ± 0.5	30.39 ± 5
CH$_2$-2’’	-7.35 ± 0.5	-35.50 ± 5
CH$_2$-8’	-16.44 ± 1.4	-6.22 ± 0.4
CH$_2$-8’’	32.86 ± 4	28.05 ± 0.5
CH-3	-4.93 ± 0.3	5.76 ± 0.5
CH$_2$-7’	23.05 ± 1	15.04 ± 1
CH$_2$-7’’	10.52 ± 2	1.90 ± 1
CH$_2$-1’	9.10 ± 1	3.49 ± 1
CH$_2$-1’’	-26.34 ± 0.5	-17.86 ± 1

Since the agreement of the corresponding RDCs of an enantiomeric pair is expected to be low in cases the stereoisomers can be clearly distinguished, the experimental data was visualized in correlation plots (**Figure 58**). HMIP displays large RDCs up to 400 Hz, and the differences of individual couplings between the *R*- and *S*-HMIP reach 70 Hz (CH-1, CH-2, CH-3). However, the overall correlation coefficient with R=0.98 is relatively high. For borneol and quinuclidinol, the obtained correlation coefficients are smaller, with values of 0.68 and 0.78, respectively.

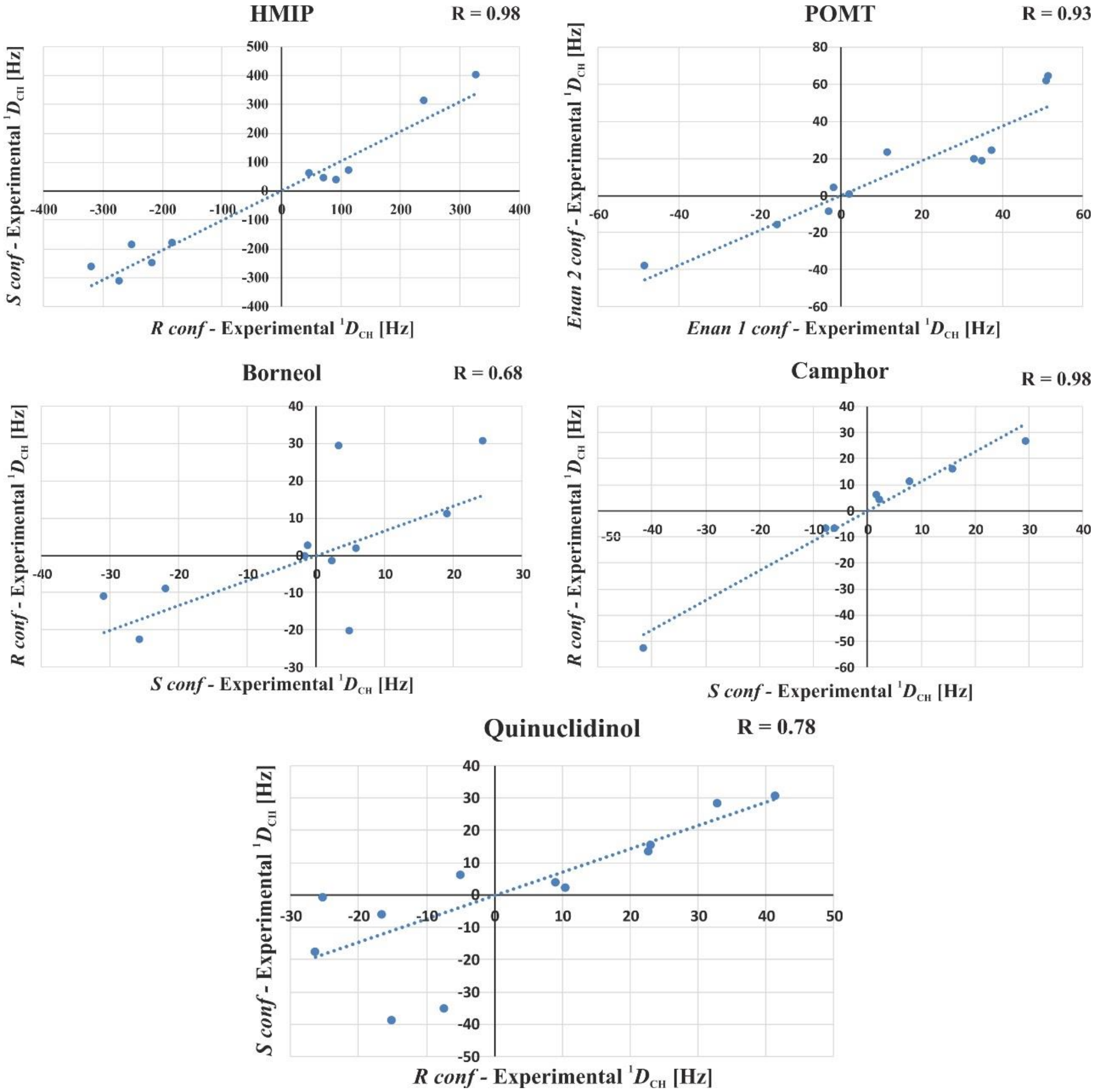

Figure 58: Comparison of the experimental RDCs extracted for the five pairs of enantiomers.
For each pair, the experimental RDCs measured for each enantiomer are plotted and a correlation coefficient (R) determined.

Correspondingly, high correlations of R = 0.98 and R = 0.93 for camphor and POMT indicate a small potential to distinguish the two enantiomers.

6.3. Alignment tensors of the enantiomeric pairs

With the MSpin program, the alignment tensor is back calculated by fitting to the experimental values using the SVD procedure [72]. The alignment tensors of all molecules were defined in order to see if a difference between each enantiomers is observable and if a correlation between the different pairs of enantiomers is noticeable. The obtained alignment tensors are illustrated in **Figure 59**, with the negative component of the alignment tensor represented in red and oriented parallel to the magnetic field B_0.

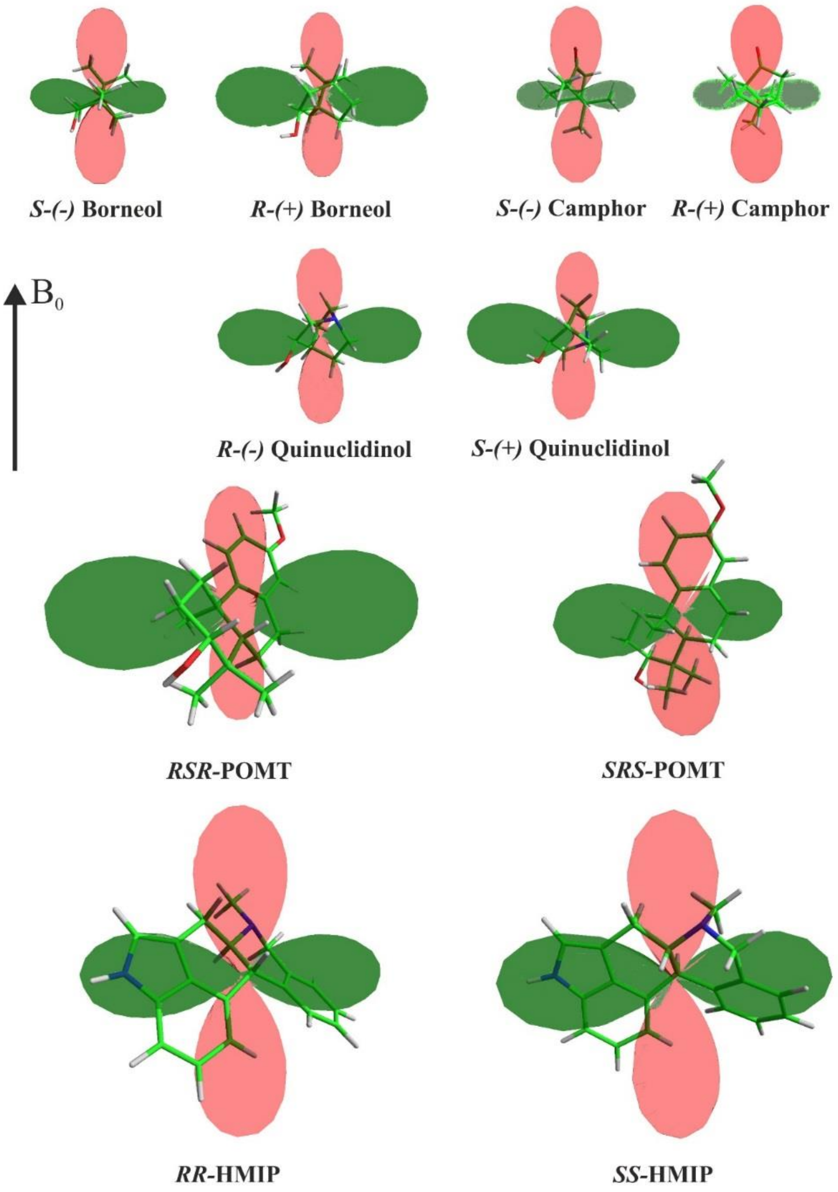
S-(-) Borneol
R-(+) Borneol
S-(-) Camphor
R-(+) Camphor
B0
R-(-) Quinuclidinol
S-(+) Quinuclidinol
RSR-POMT
SRS-POMT
RR-HMIP
SS-HMIP

Figure 59: Graphical representation of the alignment tensors of the enantiomeric pairs.
The alignment tensors are obtained from the SVD approach in MSpin with the experimental data.

The OH group of borneol, quinuclidinol and POMT point into the same direction approximately perpendicular to the static magnetic field B_0 while the carbonyl group of camphor is oriented along the magnetic field B_0. In the case of HMIP, the NH of the indole has approximately the direction of the hydroxyls but also the tertiary amine has a similar direction. As PBLG contains carbonyl groups allowing the formation of hydrogen bonds with an H-bond donor, a possible preferred interaction between the LC and the enantiomers can be hypothesized by hydrogen bonding. The correlation coefficient between the experimental RDCs of the molecules with hydroxyls is smaller compared to camphor, suggesting an interaction between the molecules and PBLG. Further investigation in a docking study between each enantiomer with PBLG could show different interactions allowing the assignment of the absolute stereochemistry. For HMIP, molecular dynamics simulation in the presence of the PBLG were run in order to determine the theoretical RDCs and to compare to the experimental RDCs to evaluate the possibility of determining the absolute configuration.

6.4. Molecular Dynamics (MD) simulation methods

The molecular dynamics simulations in vacuo were performed by Armin Widmer (Novartis) and MD runs with explicit co-solvent were performed by Dr. Konstantin V. Klenin (KIT).

6.4.1. Molecular dynamics simulation of HMIP in *vacuo*

Due to the complexity and the computational challenges associated with MD simulations of the interactions of a molecule with a chiral phase, the method development focused on a single molecule, namely HMIP. In a first step, the alignment of *R*-(-) HMIP and its (+) enantiomer induced by the presence of a single strand of PBLG was simulated *in vacuo* by a series of MD calculations with the program PyMinimaxMD (A. Widmer, Ch. Bartels unpublished) using the CHARMm force field [146]. Force field parameters and partial atomic charges for the ligands and for PBLG were assigned using the program WITNOTP (A. Widmer, unpublished). Ten molecular dynamics simulations *in vacuo* at 298 K were run for each of the two enantiomers in the presence of a 33-meric PBLG, starting from an unbound state of the ligand and from different side chain conformations of PBLG. Harmonic positional restraints were used for the 33 Cα atoms of the polymer to preserve the α-helical backbone conformation and to keep the axis of the α-helix aligned with the z-axis of the coordinate system. An additional positional restraint on a central carbon atom of the ligand was used to keep the ligand within 50 Å of the C- and N-terminal ends of the PBLG strand. The total simulation time for each of the two enantiomers was 1 μs (10 times 100 ns). During the simulations the temperature was maintained by a Langevin thermostat [147]. The alignment factor ξ for all N-H and C-H bonds of the ligand with vectors v = (x, y, z) was calculated from samples of the coordinates taken every 10 ps during the simulations using the formula:

$$\xi = \langle \frac{3z^2}{x^2 + y^2 + z^2} - 1 \rangle \tag{19}$$

From the alignment factors the RDCs ($^1D_{\mathrm{CH}}$) were calculated using the formula:

$$^1D_{CH} = s\, \frac{\kappa(\mathrm{CH})}{3r^3}\, \xi \tag{20}$$

where κ(CH) = −90.6 kHz $Å^3$ [24], r = 1.09Å, and s describes a scaling factor that takes into account the *a priori* unknown ratio of aligned *vs.* isotropic volumes of a given sample.

The values for the alignment factors ξ derived from the molecular mechanics simulations deviate from zero for several of the NH and CH bonds of the ligand, indicating that the presence of PBLG induces an anisotropic distribution of the orientations of the ligand. The values obtained with this simulation are given in **Table 28**. The values obtained for CH-2 are significantly different compared to the other values comprised between -0.58 and 0.49 (approx. 0.91 and 0.83 for *R* and *S* enantiomers respectively), consequently, these RDCs were ignored for the study. For some of the bonds to hydrogen atoms the calculated ξ values show statistically significant differences between the two enantiomers. The groups at H1, H6a, H9 and H12 have the largest differences of RDCs between the *S* and the *R* enantiomers. In all simulations the ligand changed from a remote (closest distance to PBLG > 20 Å) location to a bound state (at least one contact between ligand and PBLG non-hydrogen atoms < 4 Å) within less than 0.5 ns. Once bound to PBLG the ligand stayed in a bound state for the rest of the 100 ns simulation time with varying binding sites over time. During the simulation binding is almost always established via a hydrogen bond between the NH group of HMIP and one of the carbonyls of glutamate side chains.

To be able to compare experimental and predicted data, the value obtained from the MD simulation were scaled according to equation (20) using s as a fitting parameter for best matching $^1D_{\mathrm{CH}}$ couplings. The values are given in **Table 28**.

Table 28: Calculated $^{1}D_{CH}$ RDCs for enantiomers HMIP obtained with the MD simulation in vacuo.

MD Novartis		**Scaled in [Hz]**		**Scaled in [Hz]**
Assignment	***R*-(-) HMIP ξ**	***R*-(-) HMIP**	***S*-(+) HMIP ξ**	***S*-(+) HMIP**
NH-4	0.40 ± 0.09	666.67	0.63 ± 0.14	700.00
CH-5	-0.02 ± 0.01	-33.33	0.05 ± 0.13	55.56
CH_2-6 averaged	-0.275 ± 0.09	-458.33	-0.275 ± 0.11	-305.56
CH-6a	-0.46 ± 0.05	-766.67	-0.45 ± 0.10	-500.00
CH_2-8 averaged	0.025 ± 0.08	41.67	0.05 ± 0.12	55.56
CH-9	0.29 ± 0.09	483.33	0.05 ± 0.09	55.56
CH-10	0.19 ± 0.13	316.67	0.43 ± 0.09	477.78
CH-11	-0.06 ± 0.09	-100.00	-0.02 ± 0.10	-22.22
CH-12	0.21 ± 0.09	350.00	-0.04 ± 0.10	-44.44
CH-12b	-0.49 ± 0.05	-816.67	-0.58 ± 0.07	-644.44
CH-1	0.09 ± 0.14	150.00	0.37 ± 0.09	411.11
CH-2	0.91 ± 0.33	1516.67	0.83 ± 0.39	922.22
CH-3	0.45 ± 0.11	750.00	0.49 ± 0.15	544.44
CH_3	0.01 ± 0.04	16.67	0.03 ± 0.04	33.33

The correlation of experimental RDCs for the HMIP pair of enantiomer gives a first indication of the strength of distinction for HMIP, a large rigid molecule, which has a high correlation of corresponding RDCs. Remarkably, these qualitative measures are very well reproduced by the molecular dynamics simulation as shown in **Figure 60**. The overall correlation coefficient obtained by the least-squares linear regression analysis of calculated *R* vs *S* experimental RDCs *in vacuo* ($^{1}D_{CH}$) matches to R =0.84. This result is relatively high and close to the overall correlation coefficient obtained from experimental RDCs (R =0.98). In conclusion, the differences in the interaction of the solute molecules with the chiral alignment medium are the main effects for enantiomeric differentiation and that MD simulations might be the adequate tools for the prediction of alignment and absolute configuration.

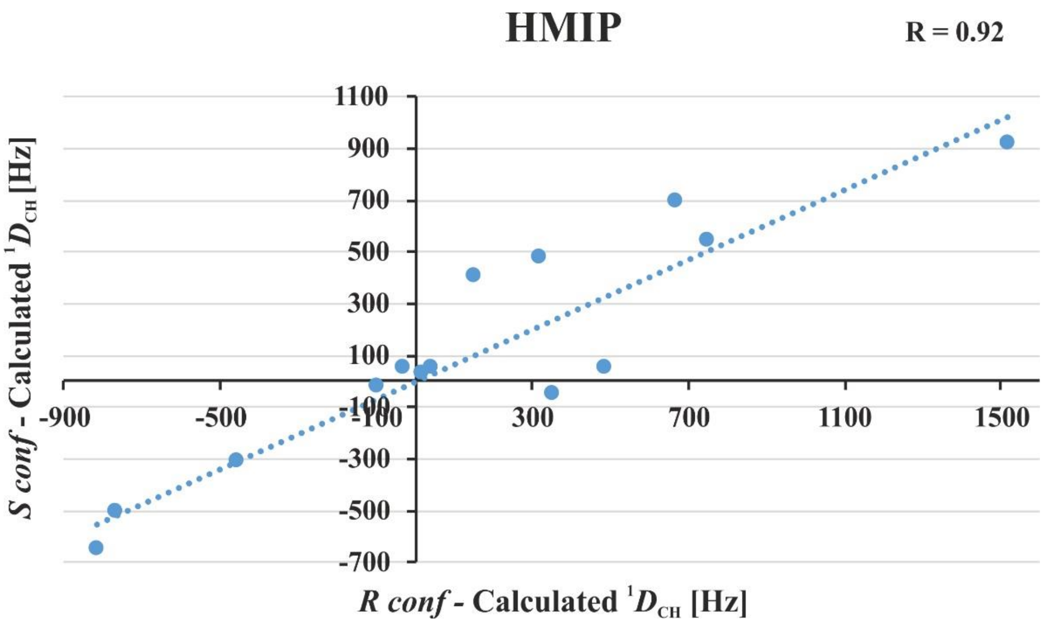

Figure 60: Comparison of the calculated RDCs for HMIP obtained from the MD simulation *in vacuo*. For HMIP, the calculated RDCs for *R* enantiomer is plotted against the calculated RDCs for the *S* enantiomer and the correlation coefficient (R) determined.

As a first test of consistency, a comparison of predicted alignment with experimental data was performed. The correlation coefficients obtained from the different possible comparisons are given in **Table 29**.

Table 29: Correlation coefficients obtained from the comparison of predicted alignment with experimental data.

		Experimental RDCs	
		R	***S***
RDCs MD	***R***	0.82	0.83
	S	0.81	0.89

This approach proved to be sufficient to generally explain differences in orientation for the two enantiomers, but the cross-fitting values obtained are also considerably high. As HMIP molecules seemed to be very closely attached to the polymer strand during the whole MD run *in vacuo*, an optimized MD simulations was attempted which took into account explicit solvent molecules.

6.4.2. Molecular dynamics simulations with explicit co-solvent

Next, the behaviour of the analyte HMIP in the presence of PBLG was simulated by an all-atom molecular dynamics simulation with explicit co-solvent (chloroform). The simulations were done with the GROMACS software package [148] using the general AMBER force field (GAFF) [149, 150]. The force field parameters for the given molecules were generated with the help of the ACPYPE tool [151]. The backbone of PBLG, represented by N = 18 monomers, was fixed in space in the α-helical conformation aligned vertically along the z axis. The side chains were allowed to be flexible. HMIP was represented by one or two molecules of different chirality. The height of the rectangular simulation box (~25 Å) was chosen in such a way that the polymer was smoothly continued by its images. The other two dimensions of the box were equal to each other and defined in the range ~35-50 Å. The number of solvent molecules was in the range 210-410, yielding the pressure of ~1 bar at the temperature of 300 K, which was maintained by the thermostat of Bussi *et al*. [152]. A single simulation step was 2 fs, with the total simulation time for the pair polymer-HMIP was 3.2 µs. Snapshots were taken every 20 ps. An example of a snapshot for HMIP in a bounded state is shown in **Figure 61**.

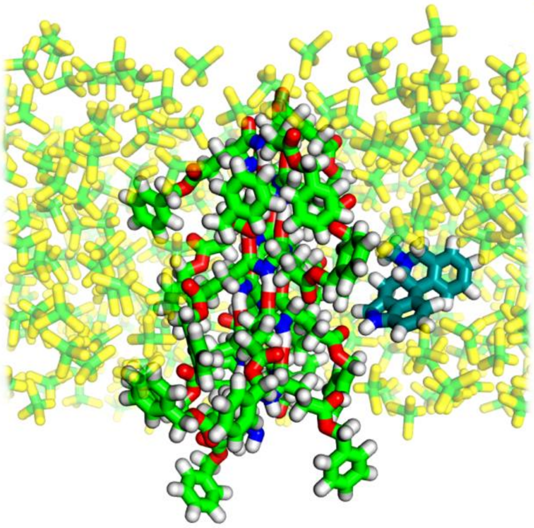

Figure 61: Snapshot from the MD simulation of *R*-(-) HMIP with PBLG in chloroform solution. Courtesy of Dr. K. Klenin and Dr. I. Kondov.

The position of the analyte was characterized by the distance to PBLG, r, which was defined as the minimum among all the distances between the centres of two atoms, one of which belonged to the analyte and the other to the polymer. The analyte was assumed to be bound to PBLG if the distance r did not exceed 3.3 Å.

The association constant per one monomer was obtained as

$$K_a = \frac{p}{Nc} \tag{21}$$

where p is the probability of the bound state and c is the average concentration of the analyte at the periphery of the simulation box. The alignment factor ξ was calculated for a set of recorded snapshots using equation (19). The alignment factors ξ for the CH vectors of the analyte were calculated separately for the analyte in all three layers: (1) with an H-bond between the analyte and the polymer; (2) with non-bonded alignment; (3) disordered layer, *i.e.* for $r > 3.3$ Å. The resulting data are summarized below. From the alignment factors, RDCs ($^1D_{\mathrm{CH}}$) were calculated from equation (21) using a scaling factor *s* that on average matched the experimental data the best. The resulting data obtained from this simulation are summarized in **Table 30**. As for the previous simulation, first the predicted data were scaled according to equation (20).

Table 30: Calculated $^{1}D_{CH}$ RDCs for enantiomers HMIP obtained with the MD simulation with explicit co-solvent.

MD KIT		**Scaled in [Hz]**		**Scaled in [Hz]**
Assignment	***R*-(-) HMIP ξ**	***R*-(-) HMIP**	***S*-(+) HMIP ξ**	***S*-(+) HMIP**
CH-5	0.14773 ± 0.01826	-184.66	0.09097 ± 0.01798	-129.96
CH_2-6 averaged	0.14639 ± 0.019055	-182.99	0.16021 ± 0.01958	-228.87
CH-6a	0.08555 ± 0.01862	-106.94	0.09526 ± 0.01853	-136.09
CH_2-8 averaged	-0.09985 ± 0.01787	124.81	-0.09368 ± 0.0183	133.83
CH-9	-0.10674 ± 0.01614	133.43	-0.03108 ± 0.02088	44.40
CH-10	-0.28132 ± 0.02400	351.65	-0.30907 ± 0.01853	441.53
CH-11	0.20267 ± 0.01837	-253.34	0.20944 ± 0.01981	-299.20
CH-12	-0.08364 ± 0.01601	104.55	0.00376 ± 0.02037	-5.37
CH-12b	0.1448 ± 0.01992	-181.00	0.18113 ± 0.01797	-258.76
CH-1	-0.16555 ± 0.02455	206.94	-0.20152 ± 0.0185	287.89
CH-2	0.34919 ± 0.01691	-436.49	0.27651 ± 0.01822	-395.01
CH-3	-0.29586 ± 0.01797	369.83	-0.32701 ± 0.01737	467.16
CH_3	-0.0672 ± 0.00602	84.00	-0.06252 ± 0.0063	89.31

Then, the least-squares linear regression analysis of calculated RDCs for *R*-HMIP and *S*-HMIP was performed. This comparison of the scaled predicted RDCs leads to a high R value of 0.97 as illustrated in **Figure 62**, a value very close to the R obtained for the experimental data (R=0.98).

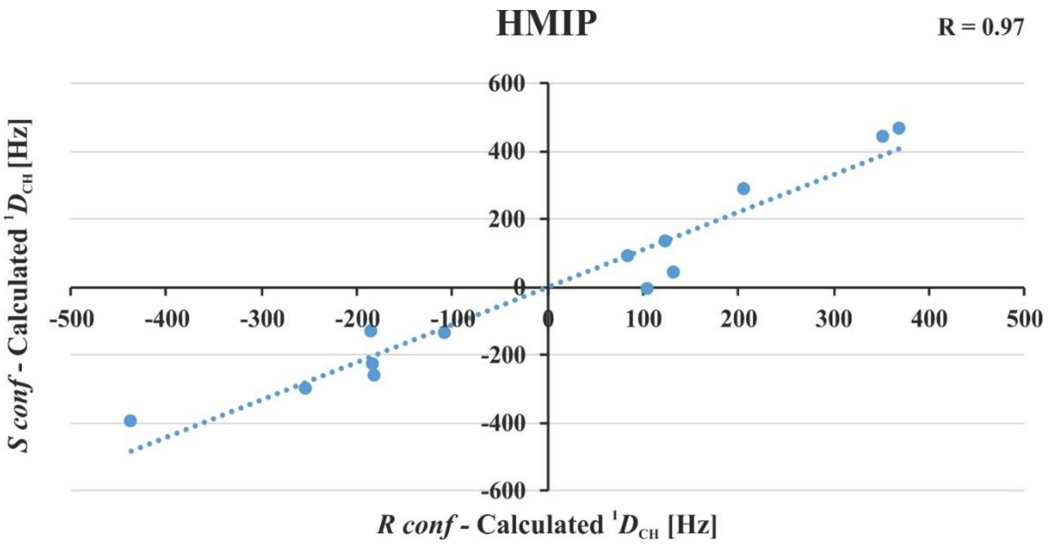

Figure 62: Comparison of the calculated RDCs for HMIP obtained from the MD simulation with explicit solvent.

For HMIP, the calculated RDCs for *R* enantiomer is plotted against the calculated RDCs for the *S* enantiomer and the correlation coefficient (R) is determined.

As for the MD simulation *in vacuo*, RDCs from scaled predictions are compared with experimental RDCs. The obtained correlation coefficients are given in **Table 31**.

Table 31: Correlation coefficients obtained from the comparison of predicted alignment with experimental data.

		Experimental RDCs	
		R	***S***
RDCs MD	***R***	0.93	0.88
	S	0.92	0.92

The comparison of the experimental RDCs with the theoretical RDCs leads to correlation coefficients bigger than the MD *in vacuo*, while for the MD *in vacuo* one value was ignored, with the MD with explicit solvent all experimental data were used. As for the simulation *in vacuo*, the cross-fitting values obtained even if they are smaller, are considerably high and close to the required R.

6.5. Discussion

Different groups have been working on developing methods to enable enantiomeric distinction by chiral alignment and the determination of the absolute configuration by NMR [153, 154, 136, 26, 155, 156]. In the present study, 5 enantiomeric pairs were measured experimentally in PBLG/$CDCl_3$ and for one pair, HMIP, the calculated RDCs were obtained from MD simulations.

HMIP is a relatively large, rigid molecule and the derived experimental RDCs have a high correlation (R=0.98). Two computational approaches were pursued, namely *in vacuo* and with explicit solvent, with both yielding high correlation of R=0.92 and R=0.97, respectively. The two approaches proved to be sufficient to generally explain differences in orientation for the two enantiomers. In both cases, a comparison of predicted alignment with experimental data led to high correlation, with R = 0.82 and R = 0.89 for the simulations *in vacuo* and R = 0.93 and R = 0.92 for the simulations with explicit solvent. However, cross-correlation of the experimental data of the *R* enantiomers with the calculated RDCs of the *S* enantiomers and *vice versa* also lead to high and similar R values as shown in **Table 29** and **Table 31**. This result was expected since a good correlation between the experimental RDCs was observed, showing little potential for differentiation.

Another possible way to interpret these data is to study the difference observed between the experimental data and the calculated data, similar to the approach using chiral derivatizing agents allowing the determination of absolute configuration [12]. This approach was named chirality-driven difference in alignment (CDDA) by Prof. Dr. Luy. The two enantiomers are aligned differently and their alignment can be defined according to the following equation:

$$A^R = A^s + \Delta A \tag{22}$$

with A^R and A^S the alignment tensor of the *R* and *S* enantiomers, respectively. ΔA corresponds to the difference in the alignment of the enantiomers.

Dipolar couplings of the *R* enantiomers can be defined as follows:

$$D_{ij}^R = d_{ij} \sum_{\alpha,\beta=a,b,c} A_{\alpha\beta}^R r_\alpha r_\beta \tag{23}$$

with
$$d_{ij} = -\frac{\hbar\gamma_I\gamma_j\mu_0}{8\pi^2 r^3} \tag{24}$$

Hence,
$$D_{ij}^{R} = d_{ij}\sum_{\alpha,\beta=a,b,c} A_{\alpha\beta}^{S} r_\alpha r_\beta + d_{ij}\sum_{\alpha,\beta=a,b,c} \Delta A_{\alpha\beta} r_\alpha r_\beta \tag{25}$$

and subsequently,
$$D_{ij}^{R} = D_{ij}^{S} + \Delta D_{ij} \tag{26}$$

To study the correlation between the experimental and the theoretical RDCs, the difference between them is calculated as follows:

$$\Delta D_{exp} = D_{exp}^{R} + D_{exp}^{S} \tag{27}$$

$$\Delta D_{calc} = D_{calc}^{R} + D_{calc}^{S} \tag{28}$$

For the experimental data, the RDCs have to be scaled to the same quadrupolar splitting $\Delta\nu_Q$. The correlation between ΔD_{exp} and ΔD_{calc} is determined according to the Pearson correlation coefficient as in the equation (29):

$$R = \frac{\sum_i (\Delta D_{exp,i} * \Delta D_{calc,i})}{\sqrt{\sum_i \Delta D_{exp,i}{}^2} * \sqrt{\sum_i \Delta D_{calc,i}{}^2}} \tag{29}$$

Depending on the obtained value, different statements are possible: if R is close to 0, no statement is possible, if R is close to 1 the absolute stereochemistry assignment is correct, and if R is close to -1 the corresponding assignment is wrong.

The experimental and theoretical differences ΔD_{CH} between the different configurations of HMIP are listed in **Table 32**. The experimental differences (*R*-*S*) are plotted against the calculated differences (*R*-*S*) and (*S*-*R*) in **Figure 63**.

Table 32: Difference of the experimental and calculated RDCs obtained for the enantiomers of HMIP.

Assignment	**ΔD_{exp} (*R-S*) [Hz]**	**ΔD_{calc} (*R-S*) [Hz]**	**ΔD_{calc} (*S-R*) [Hz]**
CH-5	-56.61	-54.71	54.71
CH$_2$-6 averaged	-1.82	45.88	-45.88
CH-6a	33.14	29.15	-29.15
CH$_2$-8 averaged	28.25	-9.02	9.02
CH-9	42.98	45.86	-45.86
CH-12	57.22	109.92	-109.92
CH-12b	40.23	77.76	-77.76
CH-1	-71.94	-80.95	80.95
CH-2	-62.54	-41.47	41.47
CH-3	-72.66	-97.33	97.33
CH$_3$	-13.84	-5.31	5.31

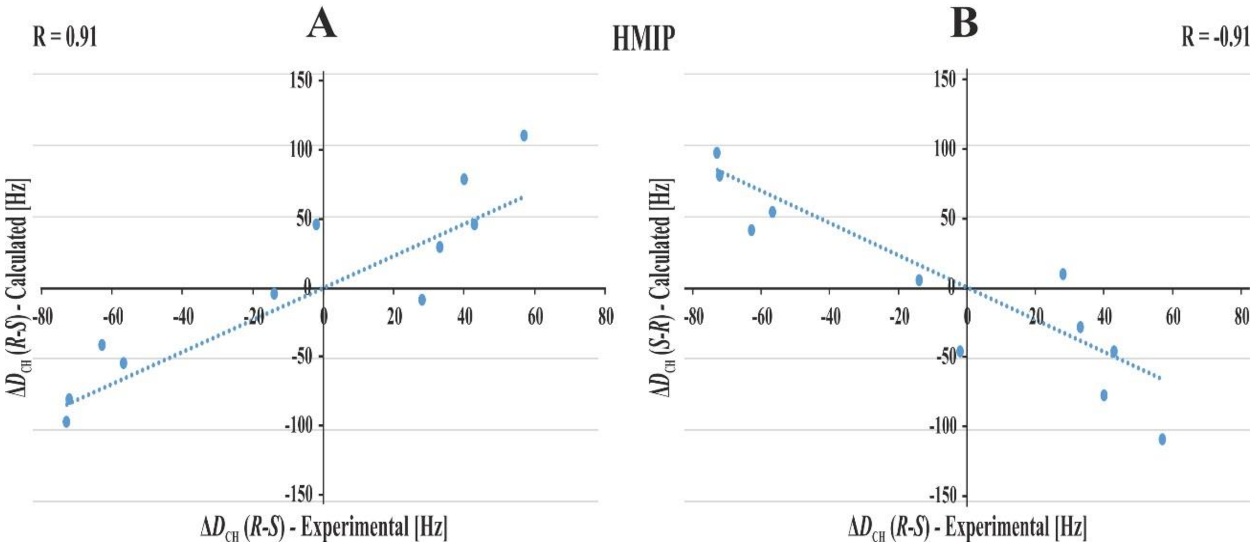

Figure 63: Comparison of the experimental RDC differences (*R*-*S*) with the calculated RDCs differences (*R*-*S*) in panel **A** and (*S*-*R*) in panel **B**.

A clearly positive correlation is obvious in panel **A** of **Figure 63** with a correlation factor of 0.91 for the comparison of the experimental *R*-D_{CH}–*S*-D_{CH} difference with the calculated *R*-D_{CH}–*S*-D_{CH} difference. The absolute stereochemistry of HMIP can thus be determined by the CDDA approach. HMIP has a relatively large dimension compared to the other small molecules, and HMIP is a primarily hydrophobic molecule with only one H-bond donor. The method need to be applied on more molecules for which the experimental data are potentially already available in order to prove the reliability of this approach. For HMIP, it was not possible to extract the RDCs in the aligned medium from the 2D-CLIP-HSQC due to a strong alignment of the molecule in PBLG/$CDCl_3$. HMIP is composed of two benzene rings which can from sandwich interaction with 2 benzyl groups of PBLG. These stacking interactions can explain the broad signals and the strong alignment which can be adjusted by using a variable angle spinning probe head (VASS) [39] allowing to reduce the size of the dipolar couplings. Borneol, camphor and quinuclidinol were also measured with the VASS probe head.

6.6. Variable angle sample spinning NMR in PBLG

One of the advantages of using a VASS probe head is the possibility to measure the scalar coupling $^1J_{\mathrm{CH}}$ and the total coupling $^1T_{\mathrm{CH}}$ in isotropic and anisotropic media on the same sample. By measuring PBLG samples in a VASS probe head, the orientation of the LC director to the magnetic field can be tuned and thus the strengths of the interactions in the sample can be modified. Therefore, the dipolar interactions can be scaled and reduced to the order of the scalar couplings by varying the spinning axis from 0° to 90° going through the magic angle (MA) of 54.74°. At the magic angle, the dipolar couplings are averaged to zero, therefore the LC phase samples behave like isotropic samples and the measured coupling constants correspond theoretically to the scalar coupling. By tuning the orientation of the rotor away from this angle, dipolar couplings are reintroduced and adjusted to the desired angle.

All VASS NMR experiments were performed on spectrometer **E**. The samples were spun at different angles at a constant spinning speed of 500 Hz. For the *R*-quinuclidinol sample, the correlation between the quadrupolar splitting and the angle was determined by measuring a deuterium spectrum at different angles, ranging from the eject position at 0° to 90°. In **Figure 64**, the reduction of the alignment ($\Delta\nu_{\mathrm{Q}}$) from 0° to the magic angle and the associated reduction of the couplings is shown. From the MA to 90°, the quadrupolar splittings increase again but less so than from 0° to MA. In these deuterium spectra, peaks of isotropic and aligned $\mathrm{CDCl_3}$ are visible, which demonstrates that the sample was not yet homogenous. In order to address this shortcoming, the subsequent samples were prepared from the 5 mm tubes used in the first part of this section.

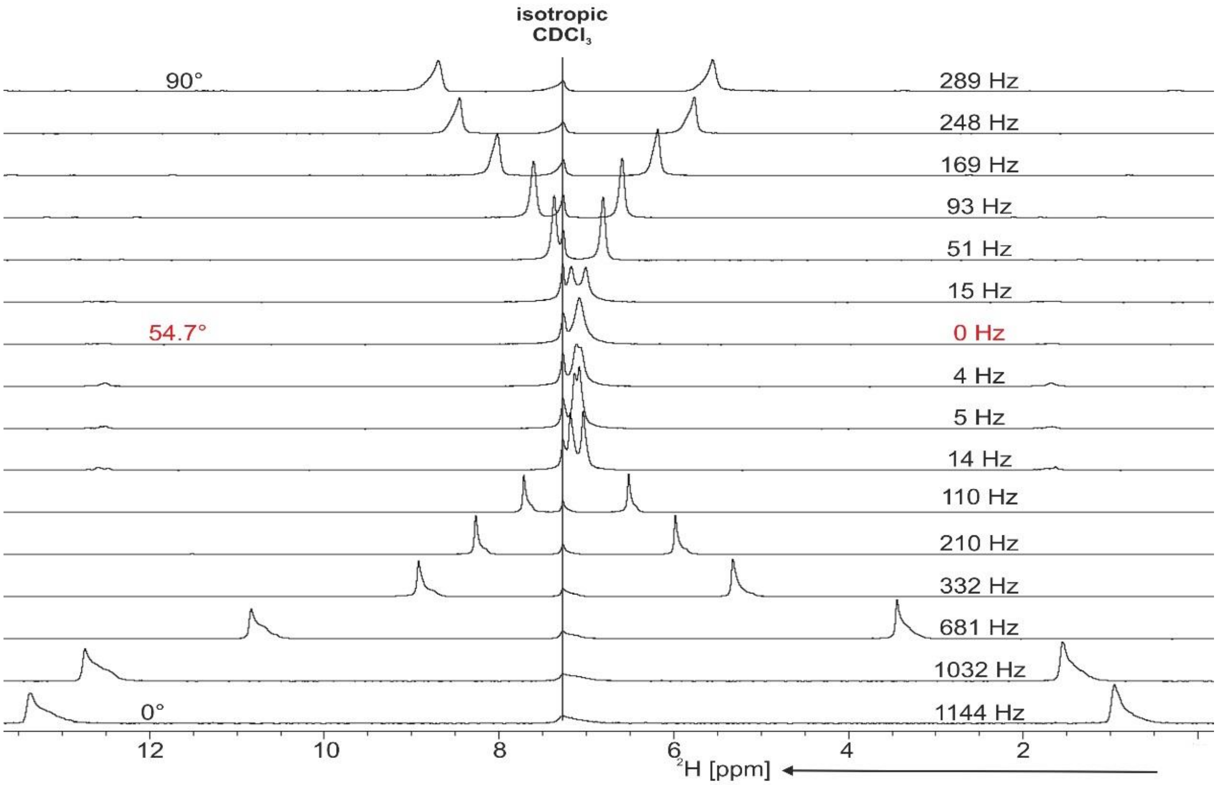

Figure 64: 1D ^{2}H NMR spectra of $CDCl_3$ in PBLG of *R*-quinuclidinol sample recorded at various angles. On the right side of each spectrum the quadrupolar splitting value is given in Hz and on the left the angle of the rotor with respect to the magnetic field B_0. The spinning speed is 500 Hz.

For the 3 enantiomeric pairs, the $^1T_{CH}$ were extracted from CLIP-HSQC and the experimental $^1D_{CH}$ coupling constants are listed in **Table 33**.

Table 33: Experimental $^{1}D_{CH}$ coupling constants of the 3 pairs of enantiomers measured with the VASS probe head.

For camphor, 4 RDCs were not extractable due to broad signals. Atoms highlighted in red are the stereogenic centre. In the column with *, scaled RDCs are shown.

Assignment	***S*-(-) Borneol [Hz]**	***R*-(+) Borneol* [Hz]**
Δν$_Q$	231	237
CH-5	-6.91 ± 2.0	47.50 ± 3.0
CH-4	-9.87 ± 0.7	-33.59 ± 5.0
CH$_2$-6’	-46.12 ± 2.0	-18.98 ± 5.0
CH$_2$-6’’	-44.12 ± 10.0	0.27 ± 1.5
CH$_2$-2’	-56.15 ± 10.0	-5.41 ± 12.0
CH$_2$-2’’	-0.37 ± 2.0	33.08 ± 2.0
CH$_2$-1’	-3.18 ± 4.0	24.15 ± 5.0
CH$_2$-1’’	-56.17 ± 8.0	-48.13 ± 3.0
CH$_3$-11	-29.69 ± 3.0	-6.55 ± 0.5
CH$_3$-10	-13.16 ± 3.0	-5.88 ± 0.5
CH$_3$-8	-14.24 ± 8.0	-1.99 ± 0.5

Assignment	***S*-(-) Camphor [Hz]**	***R*-(+) Camphor * [Hz]**
Δν$_Q$	198	209
CH$_2$-6’	0.56 ± 0.7	2.73 ± 0.5
CH$_2$-6’’	19.17 ± 4.0	17.58 ± 0.5
CH-4	9.53 ± 10.0	-2.25 ± 3.0
CH$_2$-1’		-39.94 ± 5.0
CH$_2$-1’’		-24.55 ± 5.0
CH$_2$-2’		-11.13 ± 6.0
CH$_2$-2’’		-15.96 ± 8.0
CH$_3$-10	-13.53 ± 1.3	-24.95 ± 10.0
CH$_3$-11	8.68 ± 2.0	6.03 ± 2.0
CH$_3$-8	-27.00 ± 5.0	-31.19 ± 10.0

Assignment	***R*-(-) Qui. [Hz]**	***S*-(+) Qui.* [Hz]**
Δν$_Q$	178	179
CH-5	-3.80 ± 2.5	-1.90 ± 1.2
CH$_2$-6’	16.50 ± 1.5	5.79 ± 0.4
CH$_2$-6’’	10.57 ± 2.5	-0.20 ± 1.2
CH$_2$-2’	10.13 ± 2.5	-0.21 ± 2.5
CH$_2$-2’’	12.37 ± 3.0	2.47 ± 6.0
CH$_2$-8’	7.10 ± 15.0	-1.23 ± 2.0
CH$_2$-8’’	6.76 ± 5.0	2.65 ± 2.0
CH-3	-48.83 ± 1.0	-46.94 ± 9.0
CH$_2$-7’	2.22 ± 13.0	-0.22 ± 2.0
CH$_2$-7’’	-6.82 ± 8.0	0.52 ± 1.0
CH$_2$-1’	8.02 ± 8.0	8.14 ± 8.0
CH$_2$-1’’	-8.59 ± 1.6	-7.53 ± 7.0

As for the 5 mm NMR samples, the experimental data was also visualized in correlation plots (**Figure 65**).

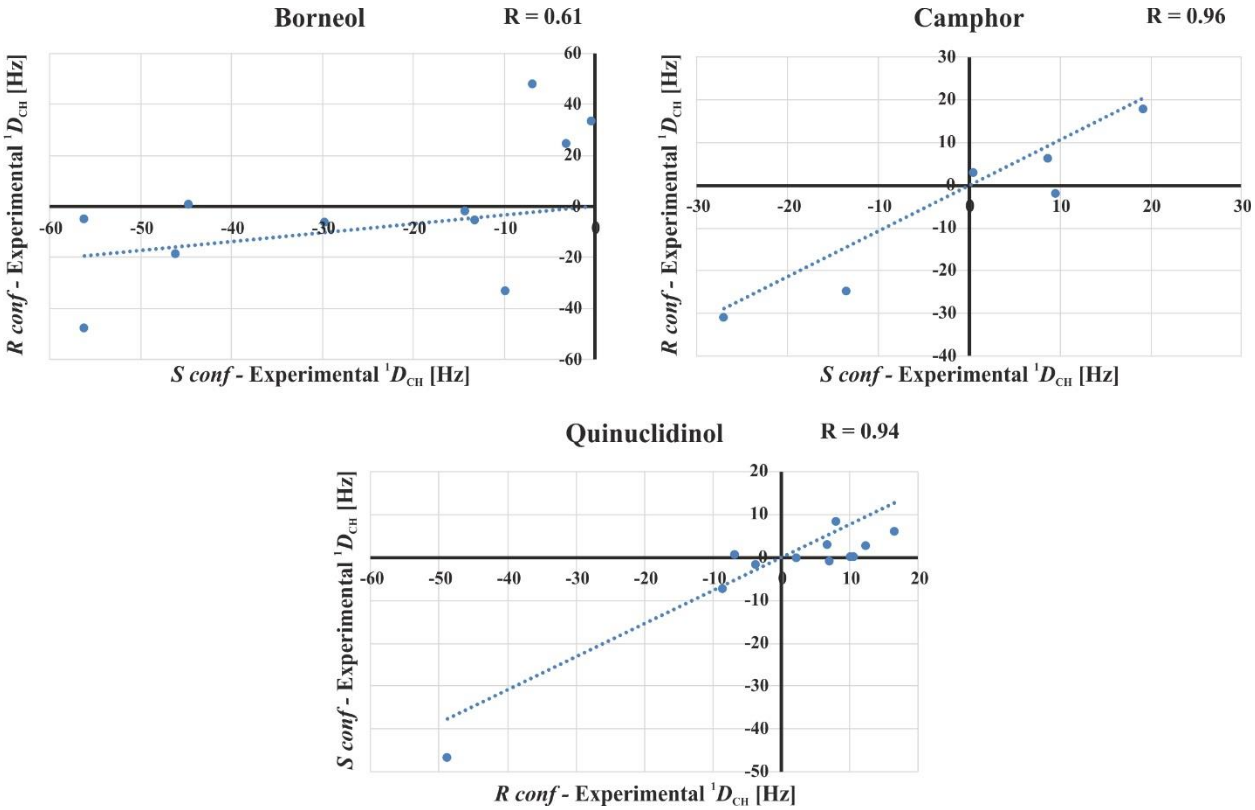

Figure 65: Comparison of the experimental RDCs extracted from experiments acquired with VASS.
For each enantiomeric pair, the experimental RDCs measured for the individual enantiomer are plotted and a correlation coefficient (R) determined.

For quinuclidinol and camphor, very high correlation coefficients of R=0.96 and R=0.94 were determined. However, for camphor, less RDCs were extractable compared to the RDCs extracted from the 5 mm NMR samples. For quinuclidinol, a better correlation (R=0.94) was obtained compared to the correlation observed with the 5 mm NMR samples (R=0.78). However, with the single conformer single alignment tensor SVD approach, the experimental values obtained with VASS gave a bad fit compared to the 5 mm NMR samples. With the VASS sample, a Cornilescu quality factor of 0.75 is obtained while with the 5 mm NMR tube, a quality of 0.11 is obtained. Since the value of the Cornilescu quality factor is inversely correlated with the quality of the fit, (*i.e.* the smaller the value the better is the fit), the experimental VASS data obtained for camphor and quinuclidinol was not sufficient to distinguish the two enantiomers. The sensitivity of the VASS probe head is significantly lower than the sensitivity of probe heads used for the 5 mm NMR samples which include the use of cryo-probe heads. The rotors are only filled with 50 µL volume and therefore contain less sample amount compared to the 5 mm NMR tubes which adds to lower poor signal to noise. Longer experiments with better resolution need to be measured for camphor and quinuclidinol in order to obtain more accurate RDCs with smaller error.

For borneol, the same number of RDCs were extractable compared to the 5 mm NMR samples. The SVD approach with MSpin provided a good fit with a low Cornilescu quality factor (Q=0.15) for the *R*-enantiomer. However, the experimental RDCs extracted for the *S* enantiomer result in a quality factor of Q= 0.53, and the errors of these RDCs are larger compared to the data of the *R*-enantiomer. The data quality of the *S*-enantiomer is not sufficient to extract accurate RDCs and consequently to assign the absolute stereochemistry of this molecule.

6.7. Conclusion

In summary, 5 enantiomeric pairs were measured in the chiral medium PBLG in order to compare the experimentally determined data to assess the correlation and to identify possible interactions with PBLG for the assignment of the absolute configuration. Understanding the interaction of the analyte with PBLG can support the set-up of the MD simulation with an appropriate force field. This is critical since the available calculation methods limit the application of NMR spectroscopy for the assignment of absolute stereochemistry. Calculated RDCs can be provided by MD simulation of the liquid crystal PBLG and its interaction with the analyte. The time of the MD need to be long enough to ensure the proper average of the dipolar parameters. More realistic MD capture the steric and dynamic interactions between the molecule and PBLG, and as a result calculated RDCs will be closer to reality. Remarkably, all molecules having a hydrogen bond donor (borneol, quinuclidinol, HMIP and POMT) display a strong similarity in their alignment tensor (**Figure 59**) deduced by the experimental RDCs obtained in PBLG. The hydrogen bond donors point into the same direction, which suggests that the analyte forms a hydrogen bond with PBLG which possesses a carbonyl group as hydrogen bond acceptor. Two MD simulations have been performed for the HMIP molecule, one *in vacuo* and one with explicit solvent. Comparison of the experimental data of the *R*- and *S*-enantiomers with the calculated data of *R* vs *S* enantiomers shows a very good correlation (R=0.98 for the experimental data, R=0.92 for the MD *in vacuo* and R=0.97 for the MD with explicit solvent). Consequently, these MD simulations can be considered as an adequate tool for the prediction of alignment and absolute configuration. Nevertheless, the direct comparison of the experimental data with the calculated data provides good correlation with both enantiomers, hence the distinction of the two enantiomers is not possible. However, the comparison of the difference observed between the experimental data and the calculated data could allow the assignment of the absolute stereochemistry. This method named chirality-driven difference in alignment (CDDA) has been applied on HMIP and has allowed to assign correctly the absolute configuration.

Further investigations will be performed in order to prove and characterize the interaction between PBLG and analyte such as measurement of NOESY experiments on PBLG samples with an HR-MAS probe head at the magic angle. As a consequence dipolar couplings will be averaged to zero and thus the NMR spectra be simplified, allowing potentially to observe NOE correlations between PBLG and the analyte if the interaction exists and if it is not too weak. Saturation-Transfer Difference (STD) experiment could be another solution to show the binding of the analyte to the LC, this technique is often used biomolecular NMR in order to characterize the binding of small molecule to protein [157].

To demonstrate the feasibility of the CDDA approach, for all enantiomeric pairs, the theoretical RDCs need to be simulated and compared to the respective experimental RDCs like the HMIP molecule. Other molecules need also to be measured to prove the robustness of this new promising approach.

7. Summary and outlook

In this thesis, by using *residual* dipolar couplings (RDCs) in complement to the standard NMR parameters, the determination of the relative stereochemistry of challenging natural products was accomplished. These natural products are reserpine derivatives containing seven stereocenters including a tertiary amine which was treated as a chiral centre. According to their complexity, either only one bond CH RDCs ($^1D_{CH}$) or a combination of $^1D_{CH}$ with standard NMR parameters were used for the determination of the relative configuration. To achieve this, molecular dynamics with orientational constraints (MDOC) was used in order to accommodate molecular flexibility which cannot be handled properly by the singular value decomposition (SVD) approach. In the latter, the small number of utilized conformers is a major shortcoming, which results in a limitation in the treatment of flexibility. MDOC runs cover the full range of possible conformers present in solution and thus lead to a good agreement with the experimental data. For larger and more flexible, *i.e.* more complex molecules, the use of additional RDCs such as $^2D_{CH}$ or $^2D_{HH}$ and even $^nD_{CH}$ becomes essential. The measurement of these coupling constants is possible using P.E.HSQC [55] and IPAP-type HSQC-TOCSY experiments [158]. Compared to $^1D_{CH}$ RDC, $^nD_{CH}$ have a relatively small magnitude and hence they are difficult to measure precisely. The existing experiments for the measurement of long range RDCs are less sensitive compared to the experiments allowing the measurement of one bond coupling. Consequently, determining RDCs for samples with a limited amount of material such as natural products becomes challenging. Long range RDCs like $^nD_{CH}$ are significantly smaller than 10 Hz under weak alignment conditions and as the quality of structure determinations depends on the relative error of each coupling, the extracted values have to be even more accurate than corresponding one-bond coupling. Hence, NMR spectra with a very good resolution need to be measured with the smallest possible linewidths. The use of homonuclear decoupled experiments [159-161] allows the extraction of one-bond coupling constants from clean doublets and could be a way to gain resolution. Indeed, the doublets don’t contain the contribution of the homonuclear interactions and are hence simplified and better resolved. Therefore the use of this type of experiment could help to obtain more accurate values and can be valuable for an automated extraction of $^1J_{CH}$ or $^1T_{CH}$. Homonuclear decoupling for experiments measuring long range RDCs, however, are not yet available. Since manual inspection usually takes several hours depending on the size of the molecule, the complexity of the spectra, as well as personal experience and skills, an automated procedure for the extraction of residual dipolar couplings including their individual errors would be highly valuable in the future.

Subsequently, for efficient measurements of anisotropic parameters with small amounts of sample, the adaptation of the existing 5 mm device to 3 mm was developed, allowing the scaling of the alignment of small volumes with high accuracy. Another advantage of this device is the gain in homogeneity translating into a better resolution of the NMR spectra, which results in more accurate extraction of the anisotropy data such as RDCs. Indeed, the 3 mm device provides much sharper resonance lines for anisotropic samples than the corresponding 5 mm device. This effect might be due to easier shimming of a sample with small diameter, but could also arise from the more homogeneous gel in the smaller volume. With the development of this device, RDC measurements and stereochemical elucidations of natural products or synthesized samples which are only available in small quantities are significantly facilitated. Furthermore, the elaboration of a device to control the swelling process, which can take several weeks depending on the gel and the solvent used, was another aim of this study. While further room for improvements exist, the current version of the apparatus is able to speed up sample preparation, the measurements of the NMR spectra and the data extraction process to obtain the residual anisotropic parameters. Simplified preparation of individual samples and subsequent measurement steps would allow being more routinely used anisotropic NMR parameters for structure verification and elucidations of challenging samples. In a very recent paper in Nature Protocols (2019) [47], Liu *et al.* provided a practical guide for the acquisition and the utilization of anisotropic NMR data for chemical structure elucidation. The use of anisotropic parameters is a time consuming process but different steps still could be accelerated by using automation.

Finally, in the presented thesis, RDCs have been utilized to assess the absolute configuration of enantiomeric molecules. Pairs of enantiomers were aligned in a known chiral liquid crystalline phase (PBLG) with which the molecules are able to interact. Consequently, each enantiomer should be differently aligned resulting in different RDCs. Five enantiomeric pairs were measured in order to compare their alignment tensor based on the interactions with PBLG for the assignment of the absolute configuration. Three small molecules having very similar overall shapes but different functional groups were chosen, *i.e.* containing a hydrogen bond donor (alcohol - borneol), a hydrogen bond acceptor (carbonyl – camphor), or both with an alcohol and a tertiary amine (quinuclidinol). In addition, two rigid, more complex natural products were also investigated in this study. Remarkably, all molecules with a hydrogen bond donor display a similar alignment tensor with the alcohol pointing into the same direction. This suggests that a hydrogen bond is formed between the molecule and PBLG and that this interaction could allow differentiating the enantiomers by comparing experimental RDCs with calculated RDCs. However, the currently available calculation methods still remains a major limitation and a continued, intense collaboration between NMR and MD scientists is essential to improve and develop MD simulations closely representing the experimental conditions. For the natural product HMIP, two different MD simulations have been performed and both gave similar results with a good correlation between calculated and experimental RDCs for each enantiomer, but a clear distinction of enantiomers was not possible. This result was expected because the comparison of experimental data of *R vs. S* isomers provided a very high correlation coefficient close to 1, equivalent to the comparison of calculated data of *R vs. S* forms. This indicates a small potential to distinguish enantiomers, but on the other hand also reveals MD simulations to be the adequate tool for prediction of alignment and absolute configuration determination. Indeed, the MD simulations were able to reproduce the experimental data, however, due to a small difference between the enantiomers the absolute configuration determination was not possible. In order to reach this point, further investigations are needed. More advanced experiments, such as NOESY experiments performed on an HR-MAS probe head or STD experiments could be a way to further characterize the interaction between PBLG and the analyte. Furthermore, the measurement of a DOSY experiment on the aligned sample with an HR-MAS probe head could reveal different diffusion coefficients of the enantiomers which could be explained by differential interactions of the analyte with PBLG.

In summary, the interaction between the analyte and PBLG can be considered the critical point for the assignment of absolute stereochemistry. Since the interaction is believed to be weak and limited to certain classes of molecules with H-bond donors, different interactions might be exploited for other classes of molecules in the future. Currently, there are only few alignment media available which allow the differentiation of enantiomers, and therefore further investigations to identify new chiral media which potentially could be used with organic solvent could help the advancement of this field. If the interaction between the analyte and the chiral medium is of an adequate strengths and is sufficiently able to differentiate the enantiomers the distinction of all types of enantiomers and potentially the assignment of the absolute stereochemistry will be possible.

8. Bibliography

1. *Guidance for Industry: Drug Substance Chemistry, Manufacturing, and Controls Information*. Available from: https://www.fda.gov/downloads/AnimalVeterinary/GuidanceComplianceEnforcement/GuidanceforIndustry/ucm052498.pdf.
2. Jones, C.G., et al., *The CryoEM Method MicroED as a Powerful Tool for Small Molecule Structure Determination.* ACS Cent. Sci., 2018. **4**(11): p. 1587-1592.
3. Shi, D., et al., *Three-dimensional electron crystallography of protein microcrystals.* eLife, 2013. **2**: p. e01345.
4. De la Cruz, M.J., et al., *Atomic-resolution structures from fragmented protein crystals with the cryoEM method MicroED.* Nat. Methods, 2017. **14**: p. 399.
5. Nannenga, B.L., et al., *Structure of catalase determined by MicroED.* eLife, 2014. **3**: p. e03600.
6. Cram, D.J. and N.L. Allinger, *Macro Rings. XII. Stereochemical Consequences of Steric Compression in the Smallest Paracyclophane1*. J. Am. Chem. Soc., 1955. **77**(23): p. 6289-6294.
7. Therapontos, C., et al., *Thalidomide induces limb defects by preventing angiogenic outgrowth during early limb formation.* Proc. Natl. Acad. Sci., 2009. **106**(21): p. 8573.
8. Kang, Y.K., et al., *Intrinsic Torsional Potential Parameters for Conformational Analysis of Peptides and Proteins.* J. Phys. Chem., 1996. **100**(38): p. 15588-15598.
9. Blackledge, M., *Recent progress in the study of biomolecular structure and dynamics in solution from residual dipolar couplings.* Prog. Nucl. Magn. Reson. Spectrosc., 2005. **46**(1): p. 23-61.
10. Nguyen, L.A., et al., *Chiral drugs: an overview.* Int. J. Biomed. Sci., 2006. **2**(2): p. 85-100.
11. Berova, N., *Circular dichroism : principles and applications / ed. by Nina Berova, Koji Nakanishi, and Robert W. Woody*. 2nd ed. ed. 2000: New York N.Y. [etc.] : Wiley-VCH.
12. Seco, J.M., et al., *The Assignment of Absolute Configuration by NMR.* Chem. Rev., 2004. **104**(1): p. 17-118.
13. Koos, M.R.M., et al., *Differentiation of enantiomers by 2D NMR spectroscopy at 1 T using residual dipolar couplings.* Magn. Reson. Chem., 2016. **54**(6): p. 527-530.
14. Saupe, A. and G. Englert, *High-Resolution Nuclear Magnetic Resonance Spectra of Orientated Molecules.* Phys. Rev. Lett., 1963. **11**(10): p. 462-464.
15. Saupe, A., *Kernresonanzen in kristallinen Flüssigkeiten und in kristallinflüssigen Lösungen. Teil I.* Z. Naturforsch., C, J. Biosci., 1964. **19**(2): p. 161.
16. Deloche, B. and E.T. Samulski, *Short-range nematic-like orientational order in strained elastomers: a deuterium magnetic resonance study.* Macromolecules, 1981. **14**(3): p. 575-581.
17. Samulski, E.T., *Investigations of polymer chains in oriented fluid phases with deuterium nuclear magnetic resonance.* Polymer, 1985. **26**(2): p. 177-189.
18. Prosser, R.S., et al., *Magnetically Aligned Phospholipid Bilayers with Positive Ordering: A New Model Membrane System.* Biophys. J., 1998. **74**(5): p. 2405-2418.
19. Sanders, C.R. and J.H. Prestegard, *Magnetically orientable phospholipid bilayers containing small amounts of a bile salt analogue, CHAPSO.* Biophys. J., 1990. **58**(2): p. 447-460.

20. Tjandra, N. and A. Bax, *Direct measurement of distances and angles in biomolecules by NMR in a dilute liquid crystalline medium.* Science, 1997. **278**(5340): p. 1111-4.
21. Hansen, M.R., et al., *Tunable alignment of macromolecules by filamentous phage yields dipolar coupling interactions.* Nat. Struct. Biol., 1998. **5**: p. 1065.
22. Park, S.H., et al., *Phage-Induced Alignment of Membrane Proteins Enables the Measurement and Structural Analysis of Residual Dipolar Couplings with Dipolar Waves and λ-Maps.* J. Am. Chem. Soc., 2009. **131**(40): p. 14140-14141.
23. Tycko, R., et al., *Alignment of Biopolymers in Strained Gels: A New Way To Create Detectable Dipole−Dipole Couplings in High-Resolution Biomolecular NMR.* J. Am. Chem. Soc., 2000. **122**(38): p. 9340-9341.
24. Kramer, F., et al., *Residual dipolar coupling constants: An elementary derivation of key equations.* Concepts Magn. Reson., 2004. **21A**(1): p. 10-21.
25. Robinson, C., et al., *Liquid crystalline structure in polypeptide solutions. Part 2.* Discuss. Faraday Soc., 1958. **25**(0): p. 29-42.
26. Sarfati, M., et al., *Theoretical and experimental aspects of enantiomeric differentiation using natural abundance multinuclear nmr spectroscopy in chiral polypeptide liquid crystals.* Chem. Commun., 2000(21): p. 2069-2081.
27. Deloche, B. and E.T. Samulski, *Short-range nematic-like orientational order in strained elastomers: a deuterium magnetic resonance study.* Macromolecules, 1981. **14**.
28. Sass, H.-J., et al., *Solution NMR of proteins within polyacrylamide gels: Diffusional properties and residual alignment by mechanical stress or embedding of oriented purple membranes.* J. Biomol. NMR, 2000. **18**(4): p. 303-309.
29. Luy, B., et al., *An Easy and Scalable Method for the Partial Alignment of Organic Molecules for Measuring Residual Dipolar Couplings.* Angew. Chem. Int. Ed. Engl., 2004. **43**(9): p. 1092-1094.
30. Freudenberger, J.C., et al., *Stretched Poly(dimethylsiloxane) Gels as NMR Alignment Media for Apolar and Weakly Polar Organic Solvents: An Ideal Tool for Measuring RDCs at Low Molecular Concentrations.* J. Am. Chem. Soc., 2004. **126**(45): p. 14690-14691.
31. Freudenberger, J.C., et al., *Stretched Poly(vinyl acetate) Gels as NMR Alignment Media for the Measurement of Residual Dipolar Couplings in Polar Organic Solvents.* Angew. Chem. Int. Ed. Engl., 2005. **44**(3): p. 423-426.
32. Haberz, P., et al., *A DMSO-Compatible Orienting Medium: Towards the Investigation of the Stereochemistry of Natural Products.* Angew. Chem. Int. Ed. Engl., 2005. **44**(3): p. 427-429.
33. Kummerlöwe, G., et al., *Stretched Poly(acrylonitrile) as a Scalable Alignment Medium for DMSO.* J. Am. Chem. Soc., 2007. **129**(19): p. 6080-6081.
34. Gayathri, C., et al., *Residual Dipolar Couplings (RDCs) Analysis of Small Molecules Made Easy: Fast and Tuneable Alignment by Reversible Compression/Relaxation of Reusable PMMA Gels.* Chemistry – A European Journal, 2010. **16**(12): p. 3622-3626.
35. Kuchel, P.W., et al., *Apparatus for rapid adjustment of the degree of alignment of NMR samples in aqueous media: verification with residual quadrupolar splittings in (23)Na and (133)Cs spectra.* J. Magn. Reson., 2006. **180**(2): p. 256-65.
36. Kummerlöwe, G., et al., *Precise Measurement of RDCs in Water and DMSO Based Gels Using a Silicone Rubber Tube for Tunable Stretching.* The Open Spectrosc. J., 2008. **2**: p. 29-33.
37. Trigo-Mouriño, P., et al., *Probing Spatial Distribution of Alignment by Deuterium NMR Imaging.* Chem. – Eur. J., 2013. **19**(22): p. 7013-7019.

38. Luy, B., et al., *Orientational Properties of Stretched Polystyrene Gels in Organic Solvents and the Suppression of Their Residual ^1H NMR Signals.* J. Am. Chem. Soc., 2005. **127**(17): p. 6459-6465.
39. Courtieu, J., et al., *Variable-Angle Sample-Spinning Nmr in Liquid-Crystals.* Prog. Nucl. Magn. Reson. Spectrosc., 1994. **26**: p. 141-169.
40. Emsley, J.W., *Liquid-Crystalline Materials*, in *Solid-State NMR Spectroscopy Principles and Applications*, M.J. Duer, Editor. 2002, Blackwell Science. p. 512-562.
41. Ishii, Y., et al., *Controlling residual dipolar couplings in high-resolution NMR of proteins by strain induced alignment in a gel.* J. Biomol. NMR, 2001. **21**(2): p. 141-151.
42. Chou, J.J., et al., *A simple apparatus for generating stretched polyacrylamide gels, yielding uniform alignment of proteins and detergent micelles*.* J. Biomol. NMR, 2001. **21**(4): p. 377-382.
43. Naumann, C., et al., *Tunable-Alignment Chiral System Based on Gelatin for NMR Spectroscopy.* J. Am. Chem. Soc., 2007. **129**(17): p. 5340-5341.
44. Kummerlöwe, G., et al., *Tunable Alignment for All Polymer Gel/Solvent Combinations for the Measurement of Anisotropic NMR Parameters.* Chem. – Eur. J., 2010. **16**(24): p. 7087-7089.
45. Frank, A.O., et al., *Direct prediction of residual dipolar couplings of small molecules in a stretched gel by stochastic molecular dynamics simulations.* Magn. Reson. Chem., 2015. **53**(3): p. 213-7.
46. Li, G.-W., et al., *Residual Dipolar Couplings in Structure Determination of Natural Products.* Nat Prod Bioprospect, 2018. **8**(4): p. 279-295.
47. Liu, Y., et al., *Application of anisotropic NMR parameters to the confirmation of molecular structure.* Nat. Protoc., 2019. **14**(1): p. 217-247.
48. Zong, W., et al., *An Alignment Medium for Measuring Residual Dipolar Couplings in Pure DMSO: Liquid Crystals from Graphene Oxide Grafted with Polymer Brushes.* Angew. Chem. Int. Ed. Engl., 2016. **55**(11): p. 3690-3693.
49. Enthart, A., et al., *The CLIP/CLAP-HSQC: Pure absorptive spectra for the measurement of one-bond couplings.* J. Magn. Reson., 2008. **192**(2): p. 314-322.
50. Skinner, T.E., et al., *Application of optimal control theory to the design of broadband excitation pulses for high-resolution NMR.* J. Magn. Reson., 2003. **163**(1): p. 8-15.
51. Skinner, T.E., et al., *Reducing the duration of broadband excitation pulses using optimal control with limited RF amplitude.* J. Magn. Reson., 2004. **167**(1): p. 68-74.
52. Kobzar, K., et al., *Exploring the limits of broadband excitation and inversion pulses.* J. Magn. Reson., 2004. **170**(2): p. 236-243.
53. Luy, B., et al., *Construction of universal rotations from point-to-point transformations.* J. Magn. Reson., 2005. **176**(2): p. 179-186.
54. Kummerlowe, G., et al., *Cross-Fitting of Residual Dipolar Couplings.* The Open Spectrosc. J., 2010(4): p. 16-27.
55. Tzvetkova, P., et al., *P.E.HSQC: A simple experiment for simultaneous and sign-sensitive measurement of ($^1J_{CH}+D_{CH}$) and ($^2J_{HH}+D_{HH}$) couplings.* J. Magn. Reson., 2007. **186**(2): p. 193-200.
56. Griesinger, C., et al., *Two-dimensional correlation of connected NMR transitions.* J. Am. Chem. Soc., 1985. **107**(22): p. 6394-6396.
57. Griesinger, C., et al., *Correlation of connected transitions by two-dimensional NMR spectroscopy.* J. Chem. Phys., 1986. **85**(12): p. 6837-6852.

58. Griesinger, C., et al., *Practical aspects of the E.COSY technique. Measurement of scalar spin-spin coupling constants in peptides.* J. Magn. Reson., 1987. **75**(3): p. 474-492.
59. Mueller, L., *P.E.COSY, a simple alternative to E.COSY.* J. Magn. Reson., 1987. **72**(1): p. 191-196.
60. Bendiak, B., *Sensitive Through-Space Dipolar Correlations between Nuclei of Small Organic Molecules by Partial Alignment in a Deuterated Liquid Solvent.* J. Am. Chem. Soc., 2002. **124**(50): p. 14862-14863.
61. Thiele, C.M., *Simultaneous Assignment of All Diastereotopic Protons in Strychnine Using RDCs: PELG as Alignment Medium for Organic Molecules.* J. Org. Chem., 2004. **69**(22): p. 7403-7413.
62. Edden, R.A.E. and J. Keeler, *Development of a method for the measurement of long-range* ^{13}C*–*^{1}H *coupling constants from HMBC spectra.* J. Magn. Reson., 2004. **166**(1): p. 53-68.
63. Koźmiński, W., *Simplified Multiplet Pattern HSQC-TOCSY Experiment for Accurate Determination of Long-Range Heteronuclear Coupling Constants.* J. Magn. Reson., 1999. **137**(2): p. 408-412.
64. Gubensäk, N., et al., *Disentangling scalar coupling patterns by real-time SERF NMR.* Chem. Commun., 2014. **50**(82): p. 12254-12257.
65. Parella, T. and J. Belloc, *Spin-State-Selective Excitation in Selective 1D Inverse NMR Experiments.* J. Magn. Reson., 2001. **148**(1): p. 78-87.
66. Meissner, A., et al., *Integration of spin-state-selective excitation into 2D NMR correlation experiments with heteronuclear ZQ/2Q π rotations for* $^{1}J_{XH}$. J. Biomol. NMR, 1997. **10**(1): p. 89-94.
67. Soerensen, M.D., et al., *Spin-state-selective coherence transfer via intermediate states of two-spin coherence in IS spin systems: Application to E.COSY-type measurement of J coupling constants.* J. Biomol. NMR, 1997. **10**(2): p. 181-186.
68. Losonczi, J.A., et al., *Order Matrix Analysis of Residual Dipolar Couplings Using Singular Value Decomposition.* J. Magn. Reson., 1999. **138**(2): p. 334-342.
69. Almond, A. and J.B. Axelsen, *Physical Interpretation of Residual Dipolar Couplings in Neutral Aligned Media.* J. Am. Chem. Soc., 2002. **124**(34): p. 9986-9987.
70. Zweckstetter, M., *NMR: prediction of molecular alignment from structure using the PALES software.* Nat. Protoc., 2008. **3**: p. 679.
71. Zweckstetter, M. and A. Bax, *Prediction of Sterically Induced Alignment in a Dilute Liquid Crystalline Phase: Aid to Protein Structure Determination by NMR.* J. Am. Chem. Soc., 2000. **122**(15): p. 3791-3792.
72. Navarro-Vázquez, A., *MSpin-RDC. A program for the use of residual dipolar couplings for structure elucidation of small molecules.* Magn. Reson. Chem., 2012. **50**(S1): p. S73-S79.
73. Banks, J.L., et al., *Integrated Modeling Program, Applied Chemical Theory (IMPACT).* J. Comput. Chem., 2005. **26**(16): p. 1752-1780.
74. Jorgensen, W.L., et al., *Development and Testing of the OPLS All-Atom Force Field on Conformational Energetics and Properties of Organic Liquids.* J. Am. Chem. Soc., 1996. **118**(45): p. 11225-11236.
75. Sánchez-Pedregal, V.M., et al., *Residual Dipolar Couplings of Freely Rotating Groups in Small Molecules. Stereochemical Assignment and Side-Chain Conformation of 8-Phenylmenthol.* Org. Lett., 2009. **11**(7): p. 1471-1474.
76. Sun, H., et al., *Bijvoet in Solution Reveals Unexpected Stereoselectivity in a Michael Addition.* Chem. – Eur. J., 2011. **17**(6): p. 1811-1817.

77. Thiele, C.M., et al., *Determination of the relative configuration of a five-membered lactone from residual dipolar couplings.* Angew. Chem. Int. Ed. Engl., 2006. **45**(27): p. 4455-60.
78. Cornilescu, G., et al., *Validation of Protein Structure from Anisotropic Carbonyl Chemical Shifts in a Dilute Liquid Crystalline Phase.* J. Am. Chem. Soc., 1998. **120**(27): p. 6836-6837.
79. Tzvetkova, P., et al., *Configuration Determination by Residual Dipolar Couplings: Accessing the Full Conformational Space by Molecular Dynamics with Tensorial Constraints.* J. Am. Chem. Soc., Submitted.
80. Möllhoff, M. and U. Sternberg, *Molecular mechanics with fluctuating atomic charges – a new force field with a semi-empirical charge calculation.* J. Mol. Model., 2001. **7**(4): p. 90-102.
81. Derome, A.E. and M.P. Williamson, *Rapid-pulsing artifacts in double-quantum-filtered COSY.* J. Magn. Reson., 1990. **88**(1): p. 177-185.
82. Bax, A. and D.G. Davis, *MLEV-17-based two-dimensional homonuclear magnetization transfer spectroscopy.* J. Magn. Reson., 1985. **65**(2): p. 355-360.
83. Hwang, T.L. and A.J. Shaka, *Cross relaxation without TOCSY: transverse rotating-frame Overhauser effect spectroscopy.* J. Am. Chem. Soc., 1992. **114**(8): p. 3157-3159.
84. Kay, L., et al., *Pure absorption gradient enhanced heteronuclear single quantum correlation spectroscopy with improved sensitivity.* J. Am. Chem. Soc., 1992. **114**(26): p. 10663-10665.
85. Bax, A. and M.F. Summers, *Proton and carbon-13 assignments from sensitivity-enhanced detection of heteronuclear multiple-bond connectivity by 2D multiple quantum NMR.* J. Am. Chem. Soc., 1986. **108**(8): p. 2093-2094.
86. Kiran, M.U., et al., *RDC Enhanced NMR Spectroscopy in Organic Solvent Media: The Importance for the Experimental Determination of Periodic Hydrogen Bonded Secondary Structures.* J. Am. Chem. Soc., 2009. **131**(43): p. 15590-15591.
87. Ward, J.M. and N.R. Skrynnikov, *Very large residual dipolar couplings from deuterated ubiquitin.* J. Biomol. NMR, 2012. **54**(1): p. 53-67.
88. Bein, H.J., *[Pharmacology of reserpin, a new alkaloid from Rauwolfia serpentina Benth].* Experientia, 1953. **9**(3): p. 107-10.
89. Muller, J.M., et al., *[Reserpin, the sedative principle from Rauwolfia serpentina B].* Experientia, 1952. **8**(9): p. 338.
90. Chakravarty, N.K. and M.N. Rai Chaudhuri, *Rauwolfia serpentina in essential hypertension.* Ind. Med. Gaz., 1951. **86**(8): p. 348-354.
91. Hensler, L., *[Serpasil, an alkaloid of Rauwolfia serpentina, in therapy of hypertension].* Schweiz Med Wochenschr, 1953. **83**(48): p. 1162-6.
92. Rauk, A., et al., *Pyramidal Inversion.* Angew. Chem. Int. Ed. Engl., 1970. **9**(6): p. 400-414.
93. Yunusov, T.K., et al., *Investigation of the lability of the conformations of some alkaloids of the quinolizidine series.* Chem. Nat. Compd., 1971. **7**(1): p. 44-48.
94. Sternberg, U., et al., *All-atom molecular dynamics simulations using orientational constraints from anisotropic NMR samples.* J. Biomol. NMR, 2007. **38**(1): p. 23-39.
95. Witter, R., et al., *Chemical shift driven geometry optimization.* J. Comput. Chem., 2002. **23**(2): p. 298-305.
96. Merle, C., et al., *Crosslinked Poly(ethylene oxide) as a Versatile Alignment Medium for the Measurement of Residual Anisotropic NMR Parameters.* Angew. Chem. Int. Ed. Engl., 2013. **52**(39): p. 10309-10312.

97. Lei, X., et al., *Graphene Oxide Liquid Crystals as a Versatile and Tunable Alignment Medium for the Measurement of Residual Dipolar Couplings in Organic Solvents.* J. Am. Chem. Soc., 2014. **136**(32): p. 11280-11283.
98. Stevensson, B., et al., *Conformational Distribution Function of a Disaccharide in a Liquid Crystalline Phase Determined Using NMR Spectroscopy.* J. Am. Chem. Soc., 2002. **124**(21): p. 5946-5947.
99. Kummerlöwe, G., et al., *Artifact-free measurement of residual dipolar couplings in DMSO by the use of cross-linked perdeuterated poly(acrylonitrile) as alignment medium.* Chem. Commun., 2010. **46**(43): p. 8273-8275.
100. Sadowski, J., et al., *Comparison of Automatic Three-Dimensional Model Builders Using 639 X-ray Structures.* J. Chem. Inf. Comput. Sci., 1994. **34**(4): p. 1000-1008.
101. Flack, H.D., *On enantiomorph-polarity estimation.* Acta Crystallogr., Sect. A, 1983. **39**(6): p. 876-881.
102. Karplus, M., *Contact Electron-Spin Coupling of Nuclear Magnetic Moments.* J. Chem. Phys., 1959. **30**(1): p. 11-15.
103. Karplus, M., *The analysis of molecular wave functions by nuclear magnetic resonance spectroscopy.* J. Phys. Chem., 1960. **64**(12): p. 1793-1798.
104. Karplus, M., *Vicinal Proton Coupling in Nuclear Magnetic Resonance.* J. Am. Chem. Soc., 1963. **85**(18): p. 2870-2871.
105. Bothner-By, A.A., et al., *Structure determination of a tetrasaccharide: transient nuclear Overhauser effects in the rotating frame.* J. Am. Chem. Soc., 1984. **106**(3): p. 811-813.
106. Lewis, I., et al., *A Detailed Investigation on Conformation, Permeability and PK Properties of Two Related Cyclohexapeptides.* Int J Pept Res Ther, 2015. **21**(2): p. 205-221.
107. Di Pietro, M.E., et al., *Conformational investigation in solution of a fluorinated anti-inflammatory drug by NMR spectroscopy in weakly ordering media.* J. Phys. Chem., 2014. **118**(30): p. 9007-16.
108. Di Pietro, M.E., et al., *Assessing the stable conformations of ibuprofen in solution by means of Residual Dipolar Couplings.* Eur. J. Pharm. Sci., 2017. **106**: p. 113-121.
109. Emsley, J.W., et al., *The conformation and orientational order of a 1,2-disubstituted ethane nematogenic molecule (I22) in liquid crystalline and isotropic phases studied by NMR spectroscopy.* Phys. Chem. Chem. Phys., 2010. **12**(12): p. 2895-2914.
110. Gil, R.R., *Constitutional, Configurational, and Conformational Analysis of Small Organic Molecules on the Basis of NMR Residual Dipolar Couplings.* Angew. Chem. Int. Ed. Engl., 2011. **50**(32): p. 7222-7224.
111. Gschwind, R.M., *Residual Dipolar Couplings—A Valuable NMR Parameter for Small Organic Molecules.* Angew. Chem. Int. Ed. Engl., 2005. **44**(30): p. 4666-4668.
112. Kummerlöwe, G. and B. Luy, *CHAPTER 4 - Residual Dipolar Couplings for the Configurational and Conformational Analysis of Organic Molecules*, in *Ann. Rep. NMR Spectrosc.*, G.A. Webb, Editor. 2009, Academic Press. p. 193-232.
113. Yan, J., et al., *Complete Relative Stereochemistry of Multiple Stereocenters Using Only Residual Dipolar Couplings.* J. Am. Chem. Soc., 2004. **126**(15): p. 5008-5017.
114. Yan, J., et al., *A Novel Method for the Determination of Stereochemistry in Six-Membered Chairlike Rings Using Residual Dipolar Couplings.* J. Org. Chem., 2003. **68**(5): p. 1786-1795.
115. Yan, J. and E.R. Zartler, *Application of residual dipolar couplings in organic compounds.* Magn. Reson. Chem., 2005. **43**(1): p. 53-64.

116. Bijvoet, J.M., et al., *Determination of the Absolute Configuration of Optically Active Compounds by Means of X-Rays.* Nature, 1951. **168**: p. 271.
117. Allenmark, S. and J. Gawronski, *Determination of absolute configuration—An overview related to this Special Issue.* Chirality, 2008. **20**(5): p. 606-608.
118. Nicolaou, K.C. and S.A. Snyder, *Chasing Molecules That Were Never There: Misassigned Natural Products and the Role of Chemical Synthesis in Modern Structure Elucidation.* Angew. Chem. Int. Ed. Engl., 2005. **44**(7): p. 1012-1044.
119. Ana, G.P., et al., *From Relative to Absolute Configuration of Complex Natural Products: Interplay Between NMR, ECD, VCD, and ORD Assisted by ab initio Calculations.* Curr. Org. Chem., 2010. **14**(15): p. 1612-1628.
120. Leichnitz, D., et al., *Total synthesis and functional analysis of microbial signalling molecules.* Chem. Soc. Rev., 2017. **46**(20): p. 6330-6344.
121. Engh, R.A., *X-Ray Crystallography, Basic Principles*, in *Encyclopedic Reference of Genomics and Proteomics in Molecular Medicine*. 2006, Springer Berlin Heidelberg: Berlin, Heidelberg. p. 2026-2029.
122. Flack, H.D. and G. Bernardinelli, *The use of X-ray crystallography to determine absolute configuration.* Chirality, 2008. **20**(5): p. 681-690.
123. Parsons, S., et al., *Use of intensity quotients and differences in absolute structure refinement.* Acta Crystallogr., Sect. B: Struct. Sci, 2013. **69**(Pt 3): p. 249-259.
124. Freedman, T.B., et al., *Absolute configuration determination of chiral molecules in the solution state using vibrational circular dichroism.* Chirality, 2003. **15**(9): p. 743-758.
125. Burlingame, T.G. and W.H. Pirkle, *The Nonequivalence of Physical Properties of Enantiomers in Optically Active Solvents. Differences in Proton Magnetic Resonance Spectra. II.* J. Am. Chem. Soc., 1966. **88**(18): p. 4294-4294.
126. Pirkle, W.H. and D.L. Sikkenga, *The use of chiral solvating agent for nuclear magnetic resonance determination of enantiomeric purity and absolute configuration of lactones. Consequences of three-point interactions.* J. Org. Chem., 1977. **42**(8): p. 1370-1374.
127. Doty, P., et al., *Polypeptides II. The configuration of polymers of γ-benzyl-L-glutamate in solution.* J. Am. Chem. Soc., 1954. **76**(17): p. 4493-4494.
128. Panar, M. and W.D. Phillips, *Magnetic ordering of poly(.gamma.-benzyl L-glutamate) solutions.* J. Am. Chem. Soc., 1968. **90**(14): p. 3880-3882.
129. Aroulanda, C., et al., *Investigation of the enantioselectivity of three polypeptide liquid-crystalline solvents using NMR spectroscopy.* Enantiomer, 2001. **6**(5): p. 281-7.
130. Kobzar, K., et al., *Stretched Gelatin Gels as Chiral Alignment Media for the Discrimination of Enantiomers by NMR Spectroscopy.* Angew. Chem. Int. Ed. Engl., 2005. **44**(23): p. 3509-3509.
131. Eliav, U. and G. Navon, *Collagen Fibers as a Chiral Agent: A Demonstration of Stereochemistry Effects.* J. Am. Chem. Soc., 2006. **128**(50): p. 15956-15957.
132. Ma, J., et al., *Weak Alignment of Biomacromolecules in Collagen Gels: An Alternative Way to Yield Residual Dipolar Couplings for NMR Measurements.* J. Am. Chem. Soc., 2008. **130**(48): p. 16148-16149.
133. Kummerlöwe, G., et al., *Covalently Cross-linked Gelatin Allows Chiral Distinction at Elevated Temperatures and in DMSO.* Chem. – Eur. J., 2009. **15**(45): p. 12192-12195.
134. Naumann, C. and P.W. Kuchel, *NMR (Pro)chiral Discrimination Using Polysaccharide Gels.* Chem. – Eur. J., 2009. **15**(45): p. 12189-12191.

135. Lesot, P., et al., *^{2}H and ^{13}C NMR-based Enantiodetection using Polyacetylene versus Polypeptide Aligning Media: Versatile and Complementary Tools for Chemists.* ChemPlusChem, 2018. **0**(ja).
136. Meyer, N.-C., et al., *Polyacetylenes as Enantiodifferentiating Alignment Media.* Angew. Chem. Int. Ed. Engl., 2012. **51**(33): p. 8334-8338.
137. Reller, M., et al., *Biphasic Liquid Crystal and the Simultaneous Measurement of Isotropic and Anisotropic Parameters by Spatially Resolved NMR Spectroscopy.* Chem. – Eur. J., 2017. **23**(54): p. 13351-13359.
138. Sakurai, S.-i., et al., *Two-Dimensional Surface Chirality Control by Solvent-Induced Helicity Inversion of a Helical Polyacetylene on Graphite.* J. Am. Chem. Soc., 2006. **128**(17): p. 5650-5651.
139. Ziani, L., et al., *Empirical determination of the absolute configuration of small chiral molecules using natural abundance 2H NMR in chiral liquid crystals.* Chem. Commun., 2007(45): p. 4737-4739.
140. Marathias, V.M., et al., *Stereochemical identification of (R)- and (S)-ibuprofen using residual dipolar couplings, NMR, and modeling.* Chirality, 2007. **19**(9): p. 741-750.
141. Berger, R., et al., *Is Enantiomer Assignment Possible by NMR Spectroscopy Using Residual Dipolar Couplings from Chiral Nonracemic Alignment Media?—A Critical Assessment.* Angew. Chem. Int. Ed. Engl., 2012. **51**(33): p. 8388-8391.
142. Azurmendi, H.F. and C.A. Bush, *Tracking Alignment from the Moment of Inertia Tensor (TRAMITE) of Biomolecules in Neutral Dilute Liquid Crystal Solutions.* J. Am. Chem. Soc., 2002. **124**(11): p. 2426-2427.
143. Wu, B., et al., *Prediction of molecular alignment of nucleic acids in aligned media.* J. Biomol. NMR, 2006. **35**(2): p. 103-115.
144. Catalano, D., et al., *A maximum‐entropy analysis of the problem of the rotameric distribution for substituted biphenyls studied by 1H nuclear magnetic resonance spectroscopy in nematic liquid crystals.* J. Chem. Phys., 1991. **94**(5): p. 3928-3935.
145. Ehni, S. and B. Luy, *Robust INEPT and refocused INEPT transfer with compensation of a wide range of couplings, offsets, and B1-field inhomogeneities (COB3).* J. Magn. Reson., 2014. **247**: p. 111-117.
146. Brooks, B.R., et al., *CHARMM: A program for macromolecular energy, minimization, and dynamics calculations.* J. Comput. Chem., 1983. **4**(2): p. 187-217.
147. Grest, G.S. and K. Kremer, *Molecular dynamics simulation for polymers in the presence of a heat bath.* Phys. Rev. A, 1986. **33**(5): p. 3628-3631.
148. Berendsen, H.J.C., et al., *GROMACS: A message-passing parallel molecular dynamics implementation.* Comput. Phys. Commun., 1995. **91**(1): p. 43-56.
149. Wang, J., et al., *Automatic atom type and bond type perception in molecular mechanical calculations.* . Mol. Graph. Model., 2006. **25**(2): p. 247-260.
150. Wang, J., et al., *Development and testing of a general amber force field.* J. Comput. Chem., 2004. **25**(9): p. 1157-1174.
151. Sousa da Silva, A.W. and W.F. Vranken, *ACPYPE - AnteChamber PYthon Parser interfacE.* BMC Research Notes, 2012. **5**(1): p. 367.
152. Bussi, G., et al., *Canonical sampling through velocity rescaling.* J. Chem. Phys., 2007. **126**(1): p. 014101.
153. Luy, B., *Distinction of enantiomers by NMR spectroscopy using chiral orienting media.* J. Indian Inst. Sci., 2010. **90**(1): p. 119-132.

154. Marx, A., et al., *How different are diastereomorphous orientations of enantiomers in the liquid crystalline phases of PBLG and PBDG: a case study.* Magn. Reson. Chem., 2009. **47**(9): p. 734-740.
155. Schmidt, M., et al., *Determining the Absolute Configuration of (+)-Mefloquine HCl, the Side-Effect-Reducing Enantiomer of the Antimalaria Drug Lariam.* J. Am. Chem. Soc., 2012. **134**(6): p. 3080-3083.
156. Sun, H., et al., *Absolute Configuration and Docking Study of Canescensterone, a Potent Phytoecdysteroid, with Non-Lepidopteran Ecdysteroid Receptor Selectivity.* Eur. J. Org. Chem., 2010. **2010**(30): p. 5791-5799.
157. Viegas, A., et al., *Saturation-Transfer Difference (STD) NMR: A Simple and Fast Method for Ligand Screening and Characterization of Protein Binding.* J. Chem. Educ., 2011. **88**(7): p. 990-994.
158. Trigo-Mouriño, P., et al., *Structural Discrimination in Small Molecules by Accurate Measurement of Long-Range Proton–Carbon NMR Residual Dipolar Couplings.* Angew. Chem. Int. Ed. Engl., 2011. **50**(33): p. 7576-7580.
159. Paudel, L., et al., *Simultaneously Enhancing Spectral Resolution and Sensitivity in Heteronuclear Correlation NMR Spectroscopy.* Angew. Chem. Int. Ed. Engl., 2013. **52**(44): p. 11616-11619.
160. Reinsperger, T. and B. Luy, *Homonuclear BIRD-decoupled spectra for measuring one-bond couplings with highest resolution: CLIP/CLAP-RESET and constant-time-CLIP/CLAP-RESET.* J. Magn. Reson., 2014. **239**: p. 110-120.
161. Sakhaii, P., et al., *Experimental access to HSQC spectra decoupled in all frequency dimensions.* J. Magn. Reson., 2009. **199**(2): p. 192-198.

9. Appendix

9.1. List of Figures

Figure 1: Chemical structures of two regioisomers with the chemical formula C_6H_7NO. 4

Figure 2: Example of stereoisomers. 6

Figure 3: Example of conformers. 7

Figure 4: Magnetic dipole (I) – dipole (S) coupling interaction (D_{IS}) and the spectrum obtained with the dipolar coupling. 13

Figure 5: Comparison between isotropic and the anisotropic conditions. 14

Figure 6: Schematic representation of laboratory and molecular frames. 16

Figure 7: Chemical structure of poly-γ-benzyl-*L*-glutamate (PBLG). 19

Figure 8: Several ^{2}H imaging spectra of deuterated solvent measured with LC in $CDCl_3$ (**A B** and **C**) and gel samples in DMSO-d_6 (**D, E** and **F**). 22

Figure 9: Modulation of the alignment strength by using different degrees of cross-linking. 23

Figure 10: Scaling of the alignment with variable angle sample spinning (VASS). 25

Figure 11: Scaling of the alignment strength of a polyacrylamide gel with the 5 mm stretching device. .. 27

Figure 12: 5 mm stretching device designed by Kummerlöwe for polar solvents. 27

Figure 13: 5 mm stretching device designed by Kummerlöwe for all commonly used solvents. 28

Figure 14: Excerpt of a CLIP-HSQC acquired on a reserpine derivative molecule studied in section 5. .. 30

Figure 15: Illustration of the extraction of $^nJ_{CH}/^nT_{CH}$ values and of the corresponding error estimation. .. 31

Figure 16: Excerpt of a P.E.HSQC recorded on the POMT molecule described in section 6 aligned in PBLG/$CDCl_3$. 32

Figure 17: Procedure for the extraction of the long range RDCs $^nJ_{CH}$ from HSQC-TOCSY experiments. 34

Figure 18: Technical description of the silicone rubber tube. 44

Figure 19: Impact of apolar solvents on silicone tubes used in this study. 44

Figure 20: T-shaped Teflon plug. 45

Figure 21: Design and dimension of the novel Teflon lock. 46

Figure 22: Chemical structure and numbering of 4-(Phosphonomethyl)-2-piperidinecarboxylic acid. 46

Figure 23: Chemical reaction for the preparation of the polyacrylamide gel. 47

Figure 24: Correlation schemes showing NMR connectivities. 50

Figure 25: Deuterium spectra of D_2O measured at different stretching strengths with the 3 and the 5 mm stretching devices. 51

Figure 26: Scaling of the alignment strength dependent on the extension factor with the 3 and 5 mm stretching devices. 52

Figure 27: Design and dimensions of the swelling device. 54

Figure 28: Procedure to transfer a swollen gel from the swelling device to the tubing. 55

Figure 29: Chemical structure and numbering used in this study of Reserpine Derivate 1 (RD-1) 58

Figure 30: Chemical structure and numbering used in this study of Reserpine Derivate 2 (RD-2) 58

Figure 31: LC-MS and ^{1}H proton NMR spectrum of RD-2 59

Figure 32: Quality factors n/χ^2 calculated for *cis*- and *trans*-conformations of Selfotel. 62

Figure 33: Experimental RDCs for the *cis*- and *trans*-conformations of Selfotel plotted against back calculated RDCs obtained with MSpin and COSMOS. 63

Figure 34: MSpin (SVD) quality factors n/χ2 calculated for all possible configurations of RD-1. 69

Figure 35: Plot of back calculated RDCs obtained with MSpin (SVD), against experimental RDCs for the best configuration 11 (*RRSSSSR*). 69

Figure 36: MSpin (SVD) quality factors n/χ^2 calculated for all possible configurations of RD-1 from multiple conformers. 71

Figure 37: Plot of back calculated RDCs obtained with MSpin (Single Tensor Fit), against experimental RDCs for the best configuration 11 (*RRSSSSR*). 71

Figure 38: COSMOS quality factors n/χ^2 calculated for all possible relative configurations of RD-1 defined in **Table 14** 73

Figure 39: Study of the dihedral angle C_{11}-C_{12}-C_{23}-N_8 during the MDOC run for the configurations 11 and 27 of RD-1. 74

Figure 40: Quinolizidine system of RD-1. 75

Figure 41: COSMOS quality factors n/χ^2 calculated for all possible configurations of RD-1. 76

Figure 42: Plot of averaged back calculated RDCs obtained with COSMOS against experimental RDCs for configuration 11 (*RRSSSSR*) of RD-1. 77

Figure 43: The crystal structure of RD-1. 77

Figure 44: MSpin (SVD) quality factors n/χ^2 calculated for all possible configurations of RD-2. 79

Figure 45: Plot of back calculated RDCs obtained with MSpin (SVD), against experimental RDCs for the best configuration 1 (*RRSSSSS*) of RD-2. 79

Figure 46: MSpin (SVD) quality factors n/χ^2 calculated for all possible configurations of RD-2 from multiple conformers. 80

Figure 47: Plot of back calculated RDCs obtained with MSpin (SVD) against experimental RDCs for the ensemble of conformers for the best configuration 1 (*RRSSSSS*) of RD-2. 81

Figure 48: COSMOS quality factors n/χ^2 calculated for all possible configurations of RD-2 with only $^1D_{CH}$ orientational constraints. 82

Figure 49: COSMOS quality factors n/χ^2 calculated for all possible configurations of RD-2 with $^1D_{CH}$ and $^3J_{HH}$ orientational constraints. 83

Figure 50: Quinolizidine system of RD-2 84

Figure 51: COSMOS quality factors n/χ^2 calculated for all possible relative configuration of RD-2 defined in **Table 14** 85

Figure 52: Three-dimensional representation of configurations 1 (*RRSSSSS*) and 6 (*RSSSSSS*) of RD-2. 86

Figure 53: Structural ensemble derived from experimental RDC constraints of RD-1. 91

Figure 54: Flexibility of RD-2. 92

Figure 55: Chemical structures, generic names and arbitrary numbering of the five pairs of enantiomers described in this study........ 101

Figure 56: Vertical rotating shaker 360° PTR-35 Grant-Bio adapted for 5 mm NMR tubes. 103

Figure 57: Selectively coupled ^{13}C-detected 1D-INEPT spectra of HMIP measured for CH_3-21, CH_2-8 and CH-3........ 104

Figure 58: Comparison of the experimental RDCs extracted for the five pairs of enantiomers. 108

Figure 59: Graphical representation of the alignment tensors of the enantiomeric pairs........ 109

Figure 60: Comparison of the calculated RDCs for HMIP obtained from the MD simulation *in vacuo*. 114

Figure 61: Snapshot from the MD simulation of *R*-(-) HMIP with PBLG in chloroform solution. 115

Figure 62: Comparison of the calculated RDCs for HMIP obtained from the MD simulation with explicit solvent. 118

Figure 63: Comparison of the experimental RDC differences (*R*-*S*) with the calculated RDCs differences (*R*-*S*) in panel **A** and (*S*-*R*) in panel **B**. 121

Figure 64: 1D ^{2}H NMR spectra of $CDCl_3$ in PBLG of *R*-quinuclidinol sample recorded at various angles. 123

Figure 65: Comparison of the experimental RDCs extracted from experiments acquired with VASS. .. 125

Figure 66: ^{1}H NMR spectrum with assignment of Selfotel in D_2O. 155

Figure 67: ^{13}C NMR spectrum with assignment of Selfotel in D_2O. 155

Figure 68: ^{31}P NMR spectrum of Selfotel in D_2O........ 156

Figure 69: edited-HSQC NMR spectrum with assignment of Selfotel in D_2O........ 156

Figure 70: COSY NMR spectrum with assignment of Selfotel in D_2O........ 157

Figure 71: TOCSY NMR spectrum with assignment of Selfotel in D_2O. 157

Figure 72: ROESY NMR spectrum with assignment of Selfotel in D_2O. 158

Figure 73: ^{13}C-HMBC spectrum with assignment of Selfotel in D_2O. 158

Figure 74: ^{1}H,^{13}C-CLIP-HSQC of Selfotel in D_2O........ 159

Figure 75: ^{1}H,^{13}C-CLIP-HSQC of Selfotel acquired inside a stretched gel PAA/D_2O gel with the 5 mm stretching device with a quadrupolar splitting $\Delta\nu_Q$ of D_2O of 23 Hz. 159

Figure 76: ^{1}H,^{13}C-CLIP-HSQC of Selfotel acquired inside a stretched gel PAA/D_2O gel with the 3 mm stretching device with a quadrupolar splitting $\Delta\nu_Q$ of D_2O of 9.5 Hz. 160

Figure 77: ^{1}H NMR spectrum with assignment of RD-1 in DMSO-d_6........ 160

Figure 78: ^{1}H,^{13}C-Edited-HSQC spectrum with assignment of RD-1 in DMSO-d_6. 161

Figure 79: ^{1}H NMR spectrum with assignment of RD-2 in DMSO-d_6........ 161

Figure 80: ^{1}H,^{13}C-Edited-HSQC spectrum with assignment of RD-2 in DMSO-d_6. 162

Figure 81: ^{1}H and ^{1}H,^{13}C-HSQC NMR spectra of HMIP in $CDCl_3$. 169

Figure 82: ^{1}H and ^{1}H,^{13}C-HSQC NMR spectra of POMT in $CDCl_3$. 170

Figure 83: ^{1}H and ^{1}H,^{13}C-HSQC NMR spectra of borneol in $CDCl_3$. 171

Figure 84: ^{1}H and ^{1}H,^{13}C-HSQC NMR spectra of camphor in CDCl$_3$. 172
Figure 85: ^{1}H and ^{1}H,^{13}C-HSQC NMR spectra of quinuclidinol in CDCl$_3$. 173

9.2. List of Tables

Table 1: NMR spectrometers used to acquire experiments described in the thesis and their specifications. 39

Table 2: Software packages used for data analysis. 40

Table 3: NMR experiments recorded for the resonance assignment. 41

Table 4: Dimensions of the T-shaped Teflon plugs for 3 and 5 mm stretching devices. 45

Table 5: Reactants and reagents used for the synthesis of the PAA gel. 47

Table 6: ^{1}H, ^{13}C, ^{15}N, and ^{31}P NMR assignments of Selfotel in D_2O. 49

Table 7: Extension factors obtained from the gel lengths in the 3 and 5 mm devices. 52

Table 8: Chemical shifts of Selfotel in D_2O and one-bond ^{1}H, ^{13}C-couplings for Selfotel in D_2O and in the stretched 15 %-PAA/D_2O-gels 53

Table 9: Chemical shifts of Selfotel in D_2O and one-bond ^{1}H, ^{13}C-couplings for Selfotel in D_2O and in the stretched 30 %-PAA/D_2O-gels 61

Table 10: Experimental and computed RDC values for Selfotel. 61

Table 11: Properties of isotropic and anisotropic sample of RD-1 and RD-2. 64

Table 12: Experimental $^{1}J_{CH}$, $^{1}T_{CH}$, and $^{1}D_{CH}$ coupling constants of RD-1. 66

Table 13: Experimental $^{1}J_{CH}$, $^{1}T_{CH}$, and $^{1}D_{CH}$ coupling constants of RD-2. 67

Table 14: Possible relative configurations of RD-1 and RD-2. 68

Table 15: Experimental data for the CH_2 and CH in close proximity of the amine of RD-1. 75

Table 16: Experimental data for the CH_2-7 and 9 and CH-23 in close proximity of the amine of RD-2. 84

Table 17: Experimental *vs*. calculated $^{1}D_{CH}$ values for configuration 1 *RRSSSSS* of RD-2. 87

Table 18: Experimental *vs*. calculated $^{3}J_{HH}$ values for configuration 1 *RRSSSSS* of RD-2. 87

Table 19: Experimental *vs*. calculated ROE distances for configuration 1 *RRSSSSS* of RD-2. 88

Table 20: Experimental *vs.* calculated values for configuration *RRSSSSR* of RD-1. 90

Table 21: Generic and systematic names of the compound described in this section**.** 100

Table 22: Composition and properties of isotropic and anisotropic samples of the 5 pairs of enantiomers. 102

Table 23: NMR spectrometers used to acquire experiments for the 5 pairs of enantiomers. 103

Table 24: Experimental $^{1}J_{CH}$ and $^{1}T_{CH}$ constant of *R*-HMIP obtained from 4 different samples. 105

Table 25: Experimental $^{1}J_{CH}$ and $^{1}T_{CH}$ constants of *S*-HMIP obtained from 4 different samples. 106

Table 26: Coefficient correlations obtained from the comparison of the quadrupolar splittings and the obtained coupling constants $^{1}J_{CH}$ and $^{1}T_{CH}$. 106

Table 27: Experimental $^{1}D_{CH}$ coupling constants of the five pairs of enantiomers. 107

Table 28: Calculated $^{1}D_{CH}$ RDCs for enantiomers HMIP obtained with the MD simulation in vacuo. 113

Table 29: Correlation coefficients obtained from the comparison of predicted alignment with experimental data. 114

Table 30: Calculated $^{1}D_{\mathrm{CH}}$ RDCs for enantiomers HMIP obtained with the MD simulation with explicit co-solvent. 117

Table 31: Correlation coefficients obtained from the comparison of predicted alignment with experimental data. 118

Table 32: Difference of the experimental and calculated RDCs obtained for the enantiomers of HMIP. 121

Table 33: Experimental $^{1}D_{\mathrm{CH}}$ coupling constants of the 3 pairs of enantiomers measured with the VASS probe head. 124

Table 34: Experimental *vs.* calculated $^{1}D_{\mathrm{CH}}$ values for all configurations of RD-1 obtained with MSpin. 163

Table 35: Experimental *vs.* calculated $^{1}D_{\mathrm{CH}}$ values for all configurations of RD-1 obtained with COSMOS. 164

Table 36: Experimental *vs.* calculated $^{1}D_{\mathrm{CH}}$ values for all configurations of RD-2 obtained with MSpin. 165

Table 37: Experimental *vs.* calculated $^{1}D_{\mathrm{CH}}$ values for all configurations of RD-2 obtained with COSMOS. 166

Table 38: Experimental *vs.* calculated $^{3}J_{\mathrm{HH}}$ values for all configurations of RD-2 obtained with COSMOS. 167

Table 39: Experimental *vs.* calculated ROE distances values for all configurations of RD-2 obtained with COSMOS. 168

9.3. List of Abbreviations and Symbols

°	degree symbol (angle)
°C	degree Celsius
μ_0	permeability of vacuum
μs	Microsecond, 10^{-6} s
1D	one-Dimensional
2D	two-Dimensional
^{2}H	deuterium atom
3D	three-Dimensional
A	Alignment tensor
Å	Angstrom, 10^{-10} m
ACD	Advanced Chemistry Development
AMBER	Assisted Model Building with Energy Refinement
APS	Ammonium-PerSulfate
AQ	AcQuisition time
B_0	static magnetic field (strength)
BBFO	Broad Band Fluorine Observation
BBI	Broad Band Inverse
BEBOP	Broadband Excitation By Optimized Pulses
BIBOP	Broadband Inversion By Optimized Pulses
br	broad
BURBOP	Broadband Universal Rotation By Optimized Pulses
C	Carbon atom
calc	calculated
CD	Circular Dichroism
CDA	Chiral Derivatizing Agent
CDDA	Chirality-Driven Difference in Alignment
CHARMm	Chemistry at HARvard Macromolecular mechanics
CLIP-HSQC	CLean-InPhase-HSQC
cm	centimetre
COSY	COrrelated SpectroscopY
CPD	Composite Pulse Decoupling
CPMG	Carr-Purcell-Meiboom-Gill
CS	Chemical Shift
D	*Dextrorotatory*
d	doublet
D_2O	Deuterium Oxide
D_{CH}	Dipolar coupling or Dipolar splitting
DFT	Density Functional Theory

DMSO	DiMethylSulOxide
DOSY	Diffusion-Ordered SpectroscopY
E	*Entgegen*
e.g.	*exempli gratia*
ECD	Electronic Circular Dichroism
EFG	Electric Field Gradient
enan	enantiomer
et al.	*et alia*
exp	experimental
F1 / F2	indirect / direct NMR dimension
FDA	Food and Drug Administration
FID	Free Induction Decay
fs	femtosecond 10^{-15}
g	gram
GAFF	General Amber Force Field
H	Hydrogen atom
ħ	reduced Planck constant
HD	High Definition
HMBC	Heteronuclear Multiple Bond Correlation
HMIP	HexahydroMethylIndoloPhenanthridine
HPLC	High Performance Liquid Chromatography
HR-MS	High-Resolution Mass Spectroscopy
HSQC	Heteronuclear Single Quantum Coherence
Hz	Hertz
i.e.	*id est*
INEPT	Insensitive Nuclei Enhanced by Polarization Transfer
Int	Interaction
IPAP	In-Phase Anti-Phase
IR	InfraRed
IUPAC	International Union of Pure and Applied Chemistry
J	scalar coupling constant
K	degree Kelvin
kcal	kilocalorie
Kel-F/PCTFE	Kellogg-Fluoropolymer/PolyChloroTetraFluoroEthylene
kGy	kiloGray
kHz	kiloHertz
L	*Levorotatory*
LC	Liquid Crystalline
LC-MS	Liquid Chromatography Mass Spectrometry
m	multiplet
m/z	mass divided by charge number

MA	Magic Angle
MAS	Magic Angle Spinning
MC	Multiple Conformers
MD	Molecular Dynamics
MDOC	Molecular Dynamics with Orientational Constraints
MEE	Maximum Error Estimate
mg	milligram
MHz	Mega Hertz
MicroED	Micro-Electron Diffraction
mL	milliLitre
mm	millimetre
mM	milliMolar
mol	mole
MS	Mass Spectrometry
MTPA	Methoxy-Trifluoro-methyl-Phenyl-Acetic acid
Mult	Multiplet
MW	Molecular Weight
N	Nitrogen atom
n/χ^2	quality factor
NaRb	sodium rubidium
NMR	Nuclear Magnetic Resonance
NOE	Nuclear Overhauser Effect
Nr.	Number
ns	nanosecond 10^{-9} s
NS	Number of Scan
O	Oxygen atom
OPLS	Optimized Potential for Liquid Simulations
ORD	Optical Rotary Dispersion
OS	Optical Spectroscopy
P	Probability tensor
P	Phosphor atom
P.E.HSQC	Primitive Exclusive Heteronuclear Single Quantum Coherence
PAA	PolyAcrylAmide
PAN	PolyAcryloNitrile
PBLG	Poly-γ-Benzyl-*L*-Glutamate
PCBLL	Poly-ε-CarboBenzyloxy-*L*-Lysine
PCTFE	PolyChloroTetraFluoroEthylene
pdb	protein data bank
PDMS	PolyDiMethylSiloxane
POMT	PhenanthrenolOctahydroMethoxyTrimethyl
ppm	parts per million

PS	PolyStyrene
ps	picosecond 10^{-12} s
Q	quality factor by Cornilescu
q	quartet
R	correlation coefficient
R	*Rectus*
RCSA	Residual Chemical Shift Anisotropy
RD-1	Reserpine Derivatives 1
RD-2	Reserpine Derivatives 2
RDC	Residual Dipolar Coupling
RESET	Reducing nuclEar Spin multiplitiEs to singuleTs
rf	radiofrequency
ROA	Raman Optical Activity
ROE	Rotating frame Overhauser Effect
ROESY	Rotating frame Overhauser Effect SpectroscopY
RQC	Residual Quadrupolar Coupling
RT	Room Temperature
S	*Sinister*
s	singlet
S/N	signal to noise
SAG	Strain induced Alignment in a Gel
s_{AM}	scaling factor
SAR	Structure Activity Relationship
SC	Single Conformer
SmartVT	Smart Variable Temperature
SSB	Spinning SideBand
STD	Saturation-Transfer Difference
SVD	Singular Value Decomposition
T	Total coupling constant J + D
t	triplet
TEMED	TEtraMethylEthyleneDiamine
TOCSY	TOtal Correlation SpectroscopY
TSP	TrimethylSilylPropanoic acid
U	Unitary tensor
UV-VIS	UltraViolet–VISible
VASS	Variable Angle Sample Spinning
VCD	Vibrational Circular Dichroism
vs.	*versus*
w/v	Weight/Volume
WF	Weighting Factor
XRD	X-Ray powder Diffraction

List of Abbreviations and Symbols

Z	*Zusammen*
Zr	Zirconium
γ	Gyromagnetic ratio
δ	chemical shift
$\Delta\nu_Q$	quadrupolar splitting
μL	microLitre
μM	microMolar
Ξ	extension factor
ξ	alignment factor

9.4. Appendix

9.4.1. Isotropic NMR spectra of Selfotel

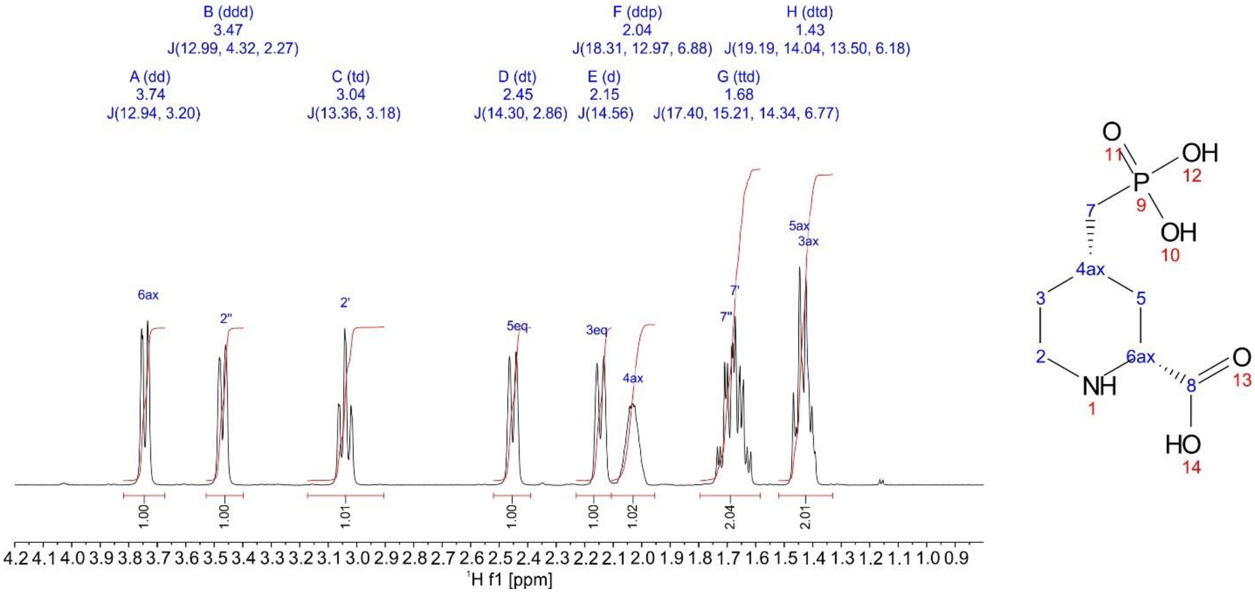

Figure 66: ^{1}H NMR spectrum with assignment of Selfotel in D_2O.

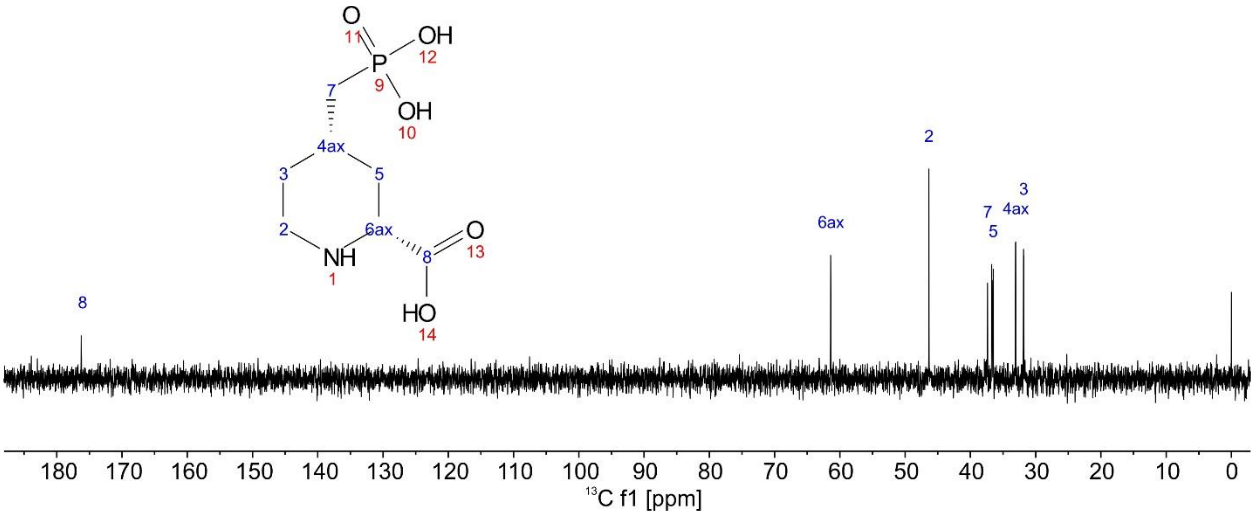

Figure 67: ^{13}C NMR spectrum with assignment of Selfotel in D_2O.

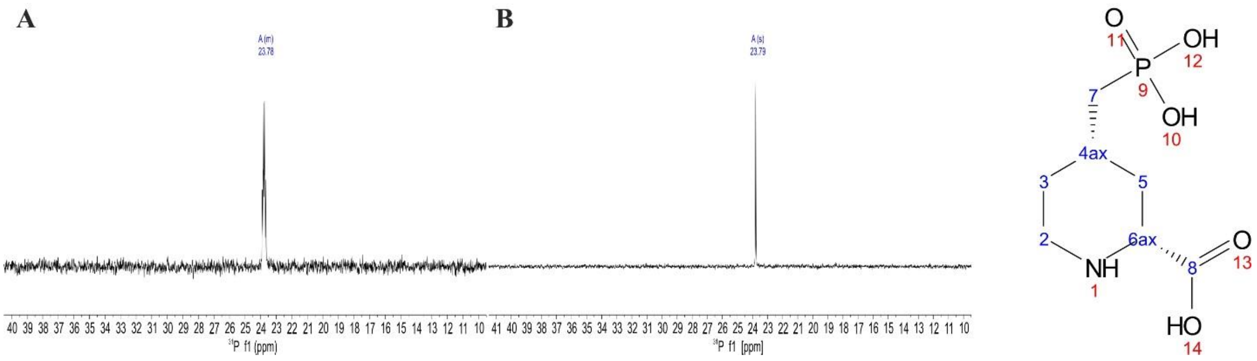

Figure 68: ^{31}P NMR spectrum of Selfotel in D_2O.
In panel **A**, ^{31}P spectrum is coupled to proton while in panel **B,** the ^{31}P spectrum is decoupled.

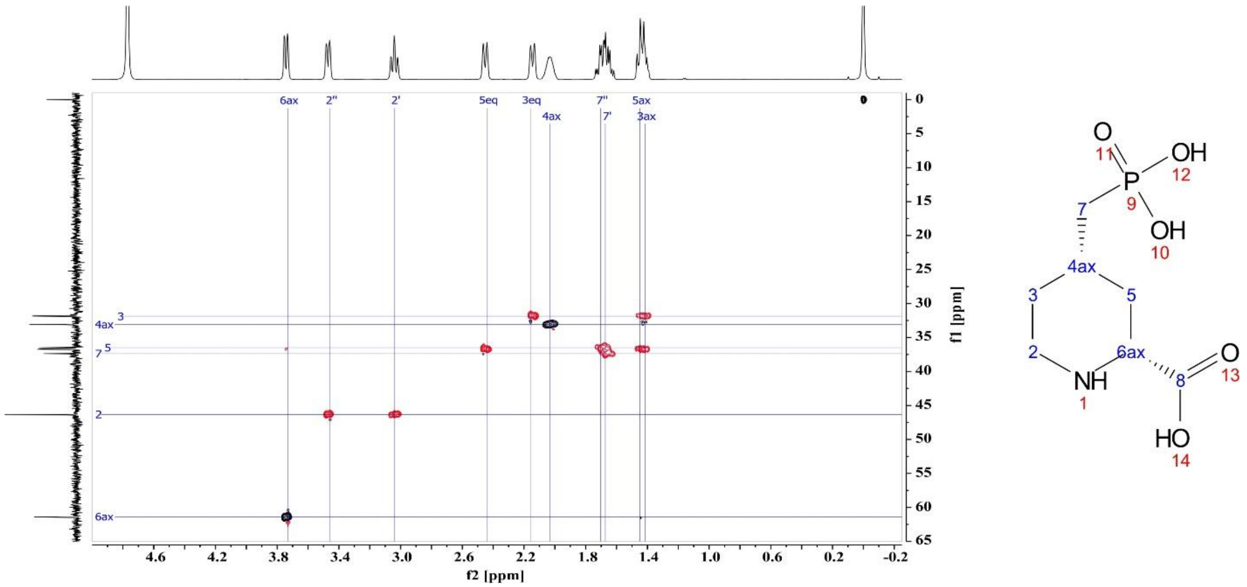

Figure 69: edited-HSQC NMR spectrum with assignment of Selfotel in D_2O.

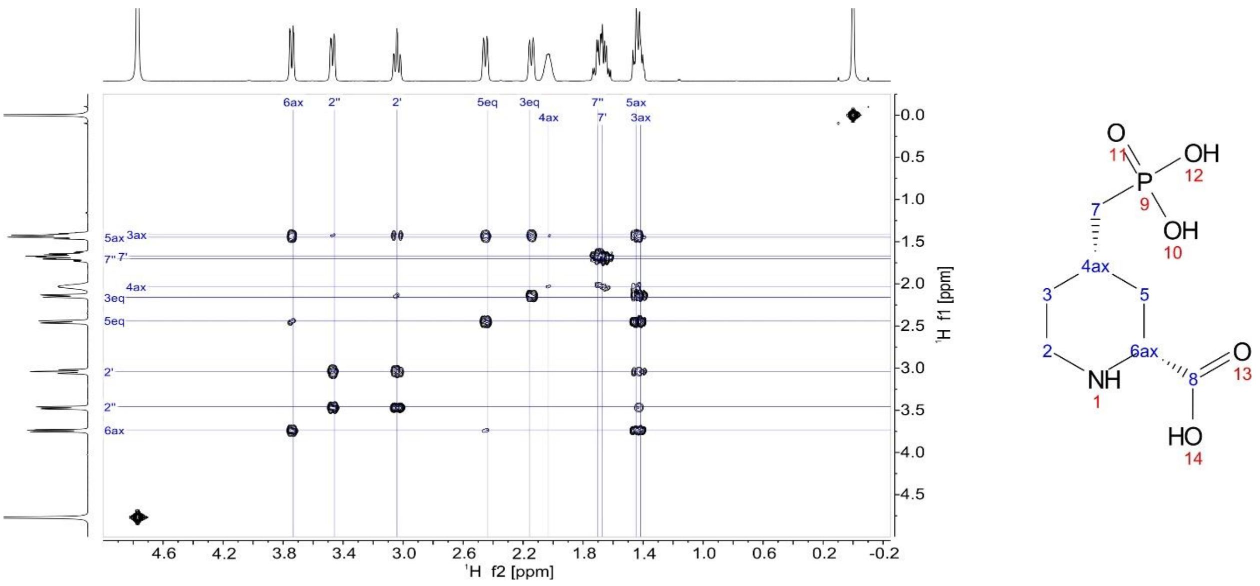

Figure 70: COSY NMR spectrum with assignment of Selfotel in D_2O.

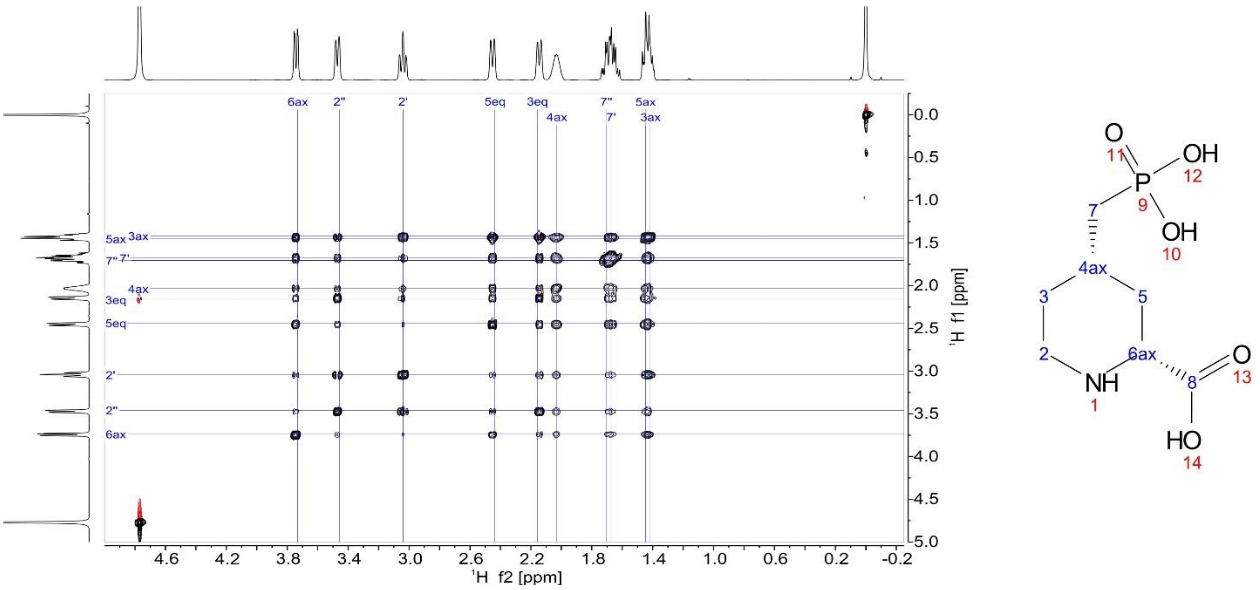

Figure 71: TOCSY NMR spectrum with assignment of Selfotel in D_2O.

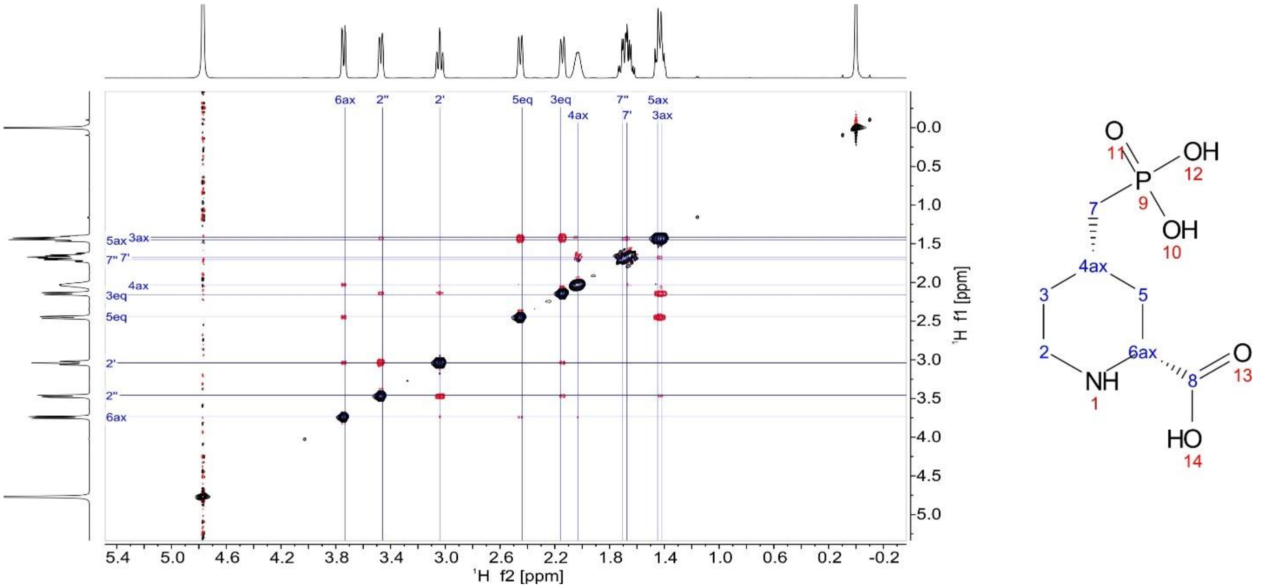

Figure 72: ROESY NMR spectrum with assignment of Selfotel in D_2O.

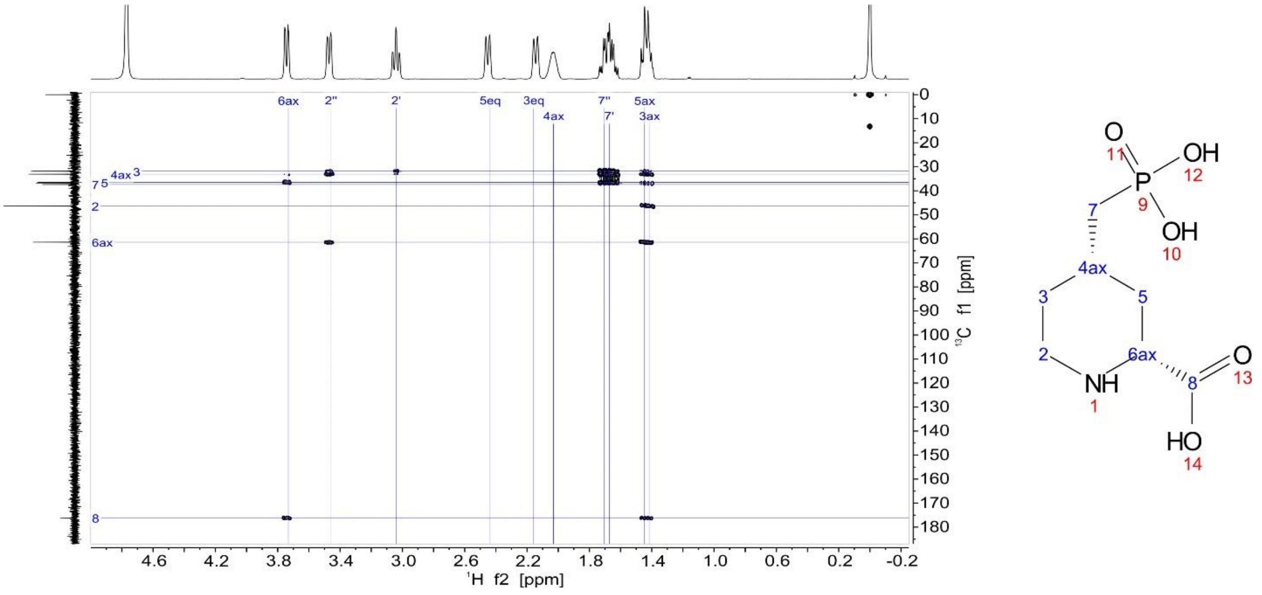

Figure 73: ^{13}C-HMBC spectrum with assignment of Selfotel in D_2O.

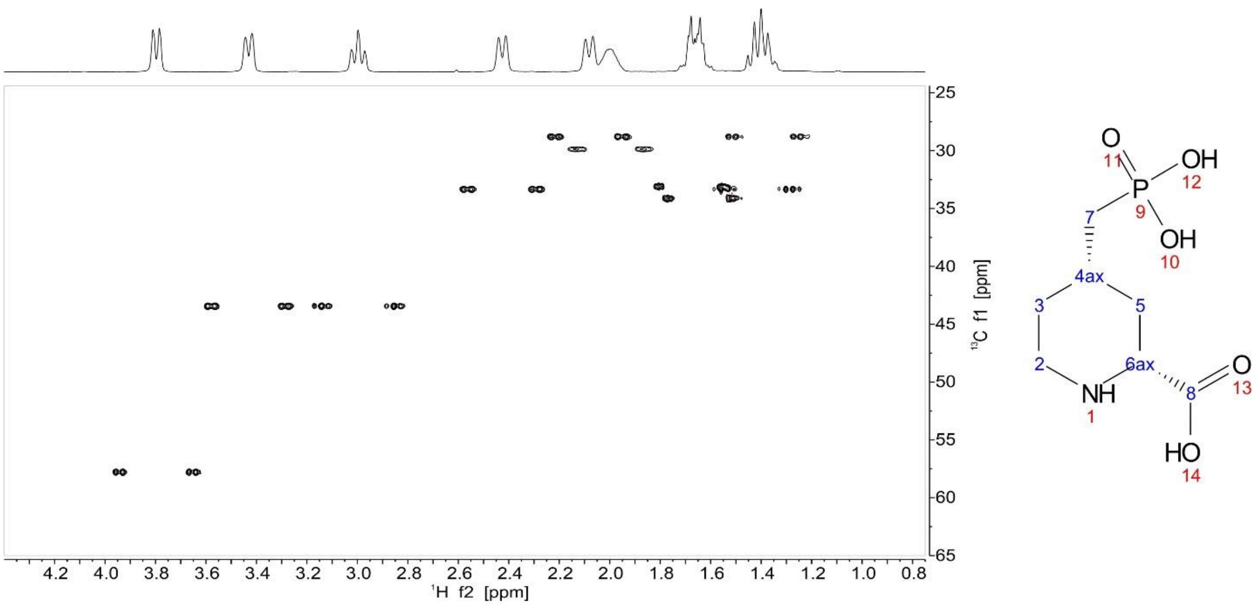

Figure 74: ^{1}H,^{13}C-CLIP-HSQC of Selfotel in D_2O.

9.4.2. Anisotropic NMR spectra of Selfotel.

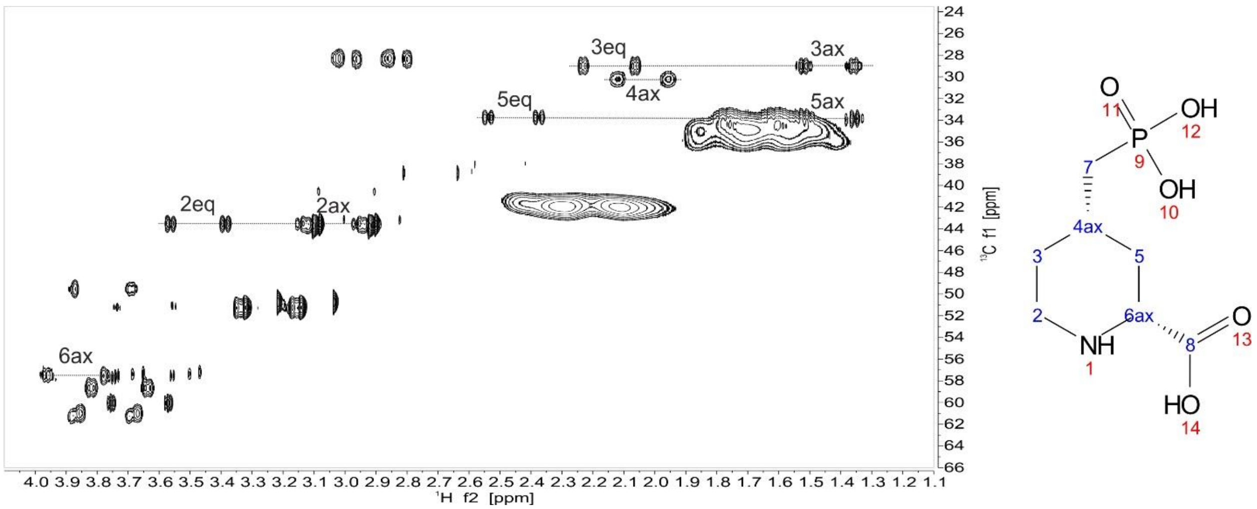

Figure 75: ^{1}H,^{13}C-CLIP-HSQC of Selfotel acquired inside a stretched gel PAA/D_2O gel with the 5 mm stretching device with a quadrupolar splitting $\Delta\nu_Q$ of D_2O of 23 Hz.

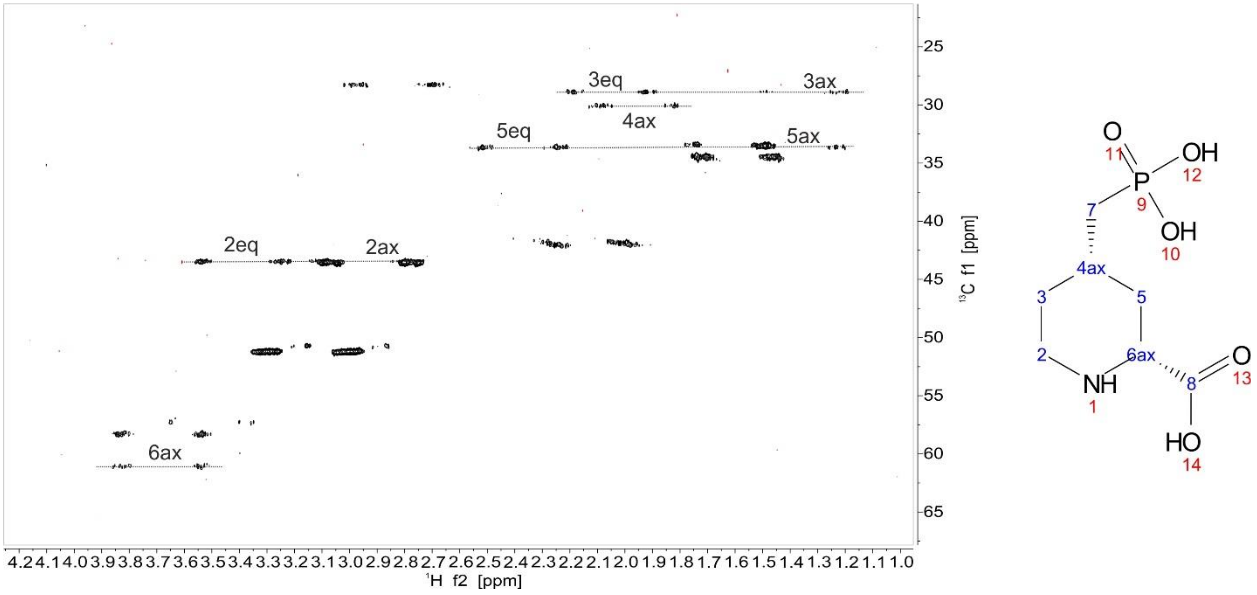

Figure 76: ^{1}H,^{13}C-CLIP-HSQC of Selfotel acquired inside a stretched gel PAA/D$_2$O gel with the 3 mm stretching device with a quadrupolar splitting $\Delta\nu_Q$ of D$_2$O of 9.5 Hz.

9.4.3. NMR spectra of RD-1 and RD-2

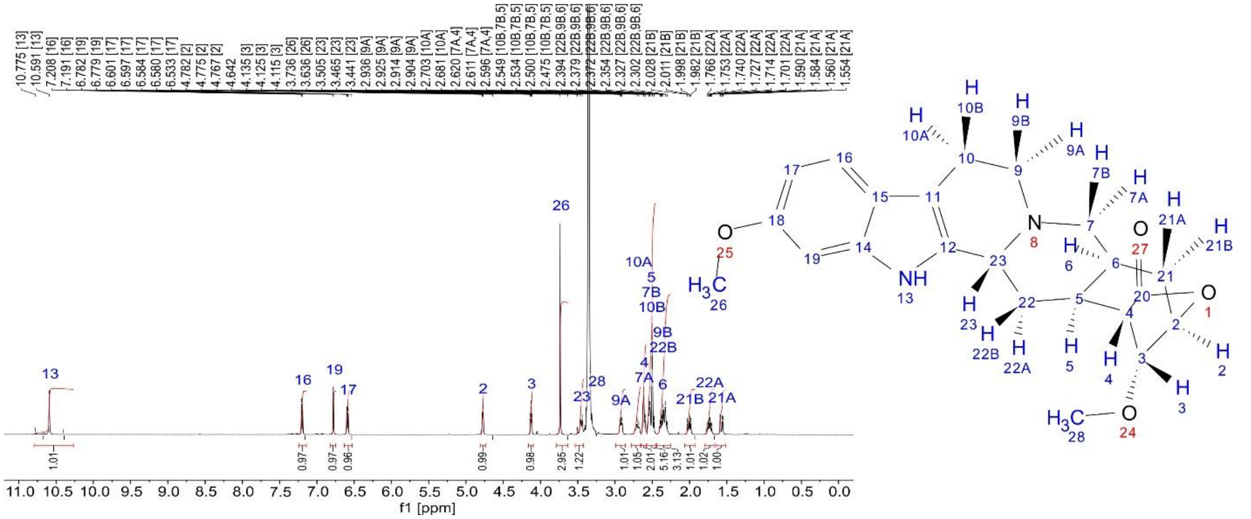

Figure 77: ^{1}H NMR spectrum with assignment of RD-1 in DMSO-d_6.

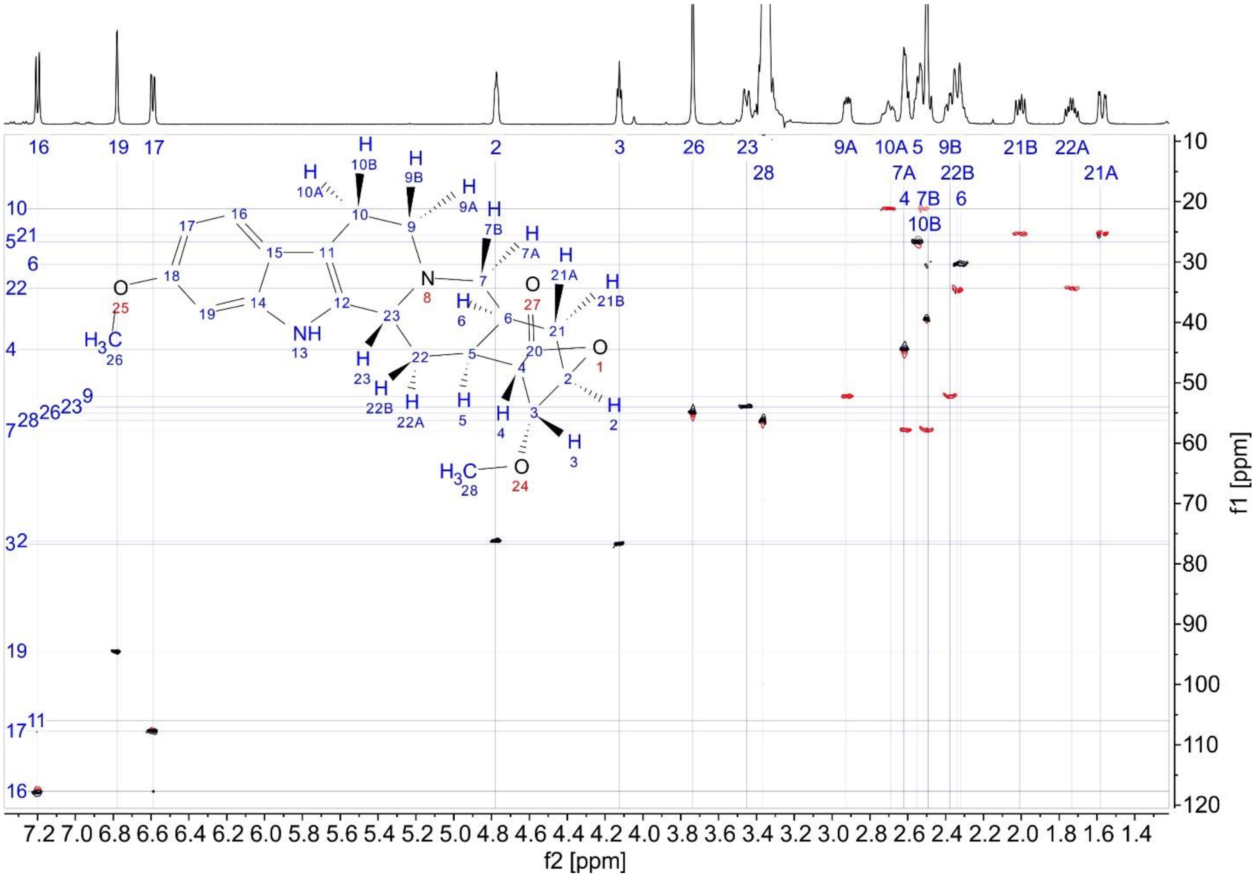

Figure 78: ^{1}H,^{13}C-Edited-HSQC spectrum with assignment of RD-1 in DMSO-d_6.

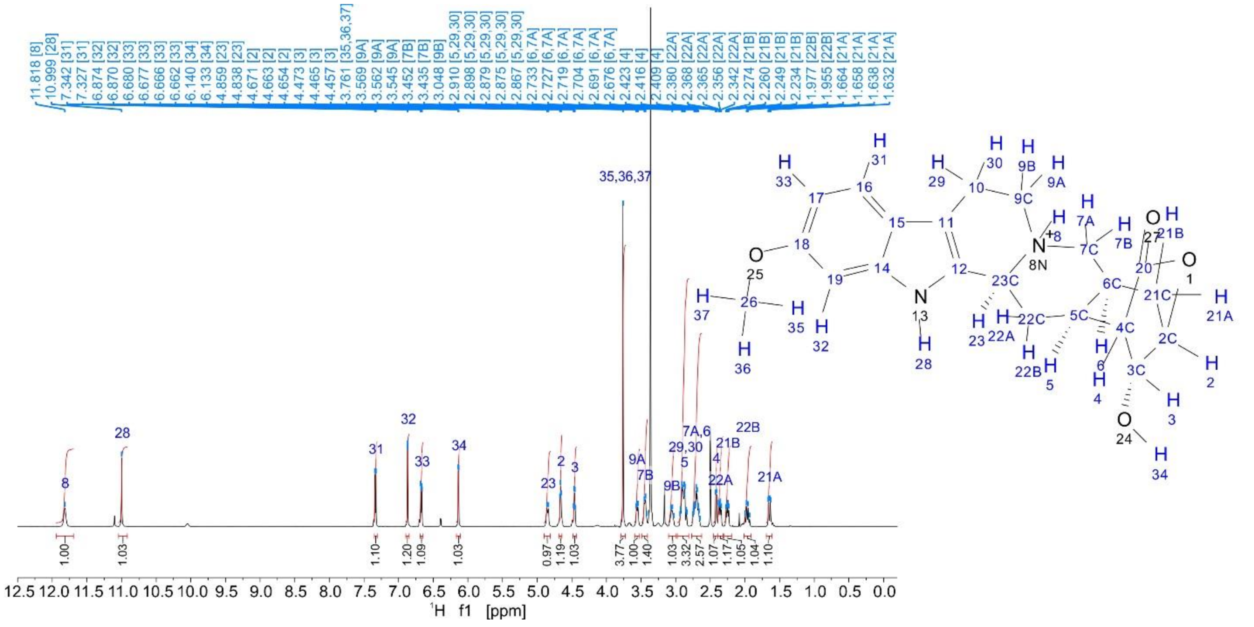

Figure 79: ^{1}H NMR spectrum with assignment of RD-2 in DMSO-d_6.

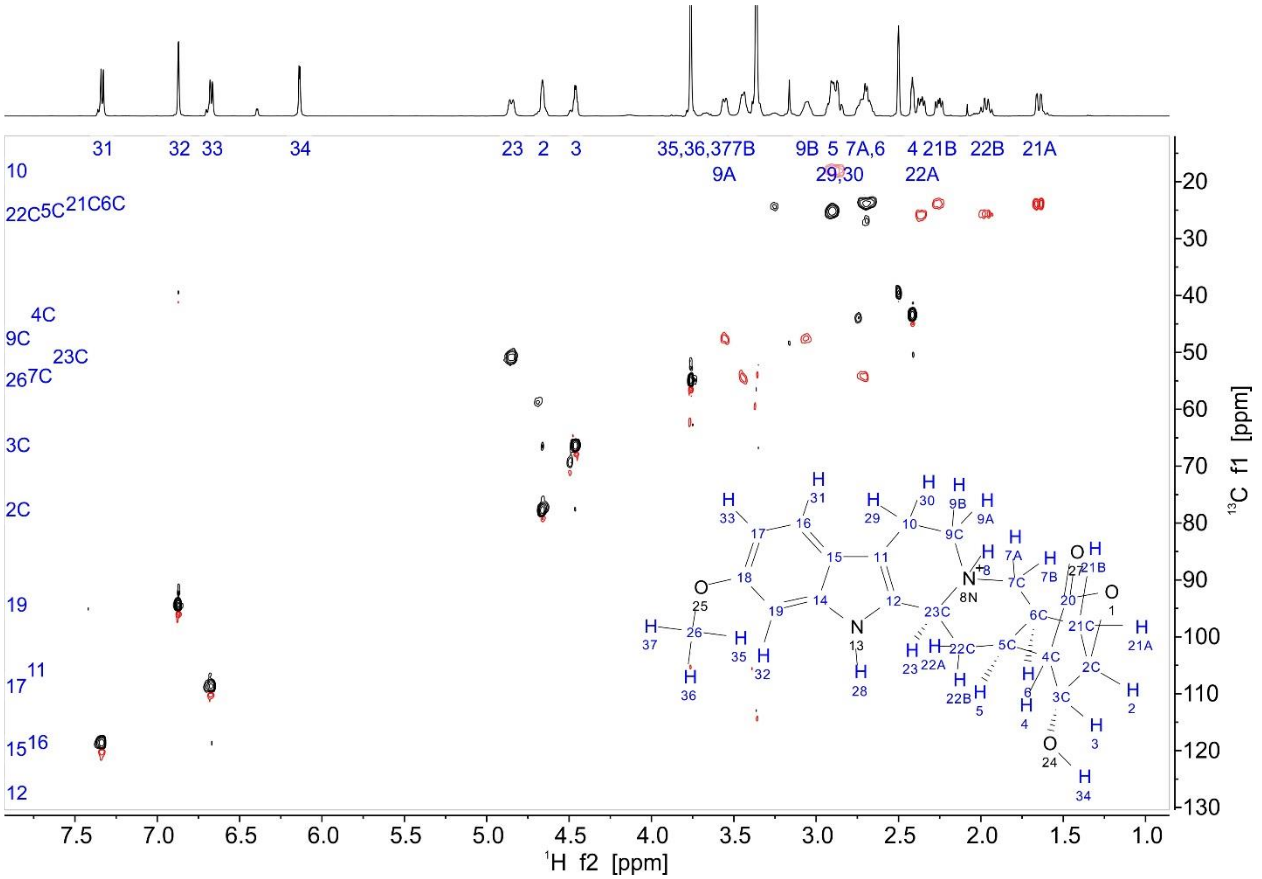

Figure 80: ^{1}H,^{13}C-Edited-HSQC spectrum with assignment of RD-2 in DMSO-d_6.

9.4.4. MSpin and COSMOS results for all configurations of RD-1

Table 34: Experimental *vs.* calculated $^{1}D_{CH}$ values for all configurations of RD-1 obtained with MSpin. The 32 different configurations are listed using the numbering of **Table 14**. Number of outliers is provided in the last row.

	Exp	Err.	1	2	3	4	5	6	7	8	9	10	11	12	13	14	15	16	17	18
$C_{10}H_{10B}$	14.3	5.0	6.7	5.8	6.3	10.7	12.4	4.4	-1.9	-4.4	-0.2	-4.0	10.4	8.1	-6.1	-11.9	10.4	11.1	-3.5	6.9
$C_{10}H_{10A}$	22.7	5.0	13.9	24.2	24.4	27.3	26.5	16.4	9.8	8.8	-11.2	-7.0	23.7	22.1	-10.0	-9.1	29.1	28.9	-9.4	4.5
$C_{21}H_{21A}$	-4.0	0.3	-3.9	-1.1	-0.9	13.6	14.4	-3.8	-8.1	-9.9	-11.3	-15.3	-3.8	-3.2	6.3	2.4	10.5	10.6	-5.6	7.8
$C_{21}H_{21B}$	18.2	0.3	10.6	14.3	16.2	8.1	6.5	7.9	12.1	13.6	25.2	28.1	18.8	13.1	7.6	9.9	8.3	7.5	20.3	7.4
C_5H_5	24.1	1.3	13.5	11.1	13.8	28.1	28.1	10.7	19.4	19.9	15.3	13.4	27.2	22.3	11.2	9.1	20.0	19.2	-1.1	8.9
C_6H_6	25.8	1.0	26.7	7.7	9.0	22.4	21.7	24.9	18.3	19.8	17.2	17.6	25.7	24.1	18.3	23.7	22.6	22.2	7.2	3.5
$C_{22}H_{22A}$	25.4	0.3	-6.4	2.2	1.9	25.6	25.3	-7.6	32.8	33.9	15.7	15.0	24.3	24.2	13.6	14.4	7.9	7.2	8.7	8.5
$C_{22}H_{22B}$	-7.5	0.3	22.4	10.9	13.0	-5.7	-5.7	19.1	-18.1	-18.9	-6.3	-9.1	-11.2	-11.0	-3.0	-5.4	2.6	2.0	5.2	6.9
C_4H_4	-13.8	0.6	-3.5	3.9	3.8	-20.4	-20.0	-3.8	-9.8	-10.9	-5.3	-7.2	-13.9	-13.8	-12.9	-21.7	-6.2	-6.1	2.8	9.2
C_9H_{9B}	32.1	1.5	19.9	24.0	26.2	29.7	29.6	21.0	22.6	20.0	-3.3	-4.8	30.0	27.3	-0.8	-1.4	32.8	32.9	9.3	8.9
C_9H_{9A}	-13.3	0.3	-5.5	0.5	0.6	-13.0	-12.7	-6.8	-18.7	-19.0	7.1	6.5	-14.4	-14.4	0.3	1.6	-19.7	-19.5	1.4	10.6
C_7H_{7B}	26.4	5.0	26.9	4.2	3.5	26.1	25.8	24.8	29.3	26.3	11.4	9.4	29.3	27.5	16.1	18.9	26.7	27.3	8.4	8.6
C_7H_{7A}	-16.6	5.0	-2.9	9.1	10.7	-6.1	-6.1	-2.8	-17.7	-17.2	-4.9	-6.7	-11.3	-11.0	-1.9	-2.9	-2.6	-2.9	4.0	7.0
$C_{23}H_{23}$	26.7	0.3	19.6	8.8	10.7	26.2	25.9	16.3	32.4	31.4	11.8	12.1	26.2	25.6	5.0	9.5	27.9	27.4	5.6	6.4
C_2H_2	-25.7	1.8	-23.8	-28.4	-28.9	-11.5	-10.2	-24.2	-18.5	-15.4	-8.3	-13.7	-26.0	-23.3	-12.2	-24.4	-26.6	-26.2	-18.4	-17.2
C_3H_3	5.0	0.3	9.2	19.1	5.8	6.2	7.5	19.2	4.8	-3.5	18.0	-7.7	4.2	26.0	25.7	-2.9	5.8	7.9	-5.1	14.7
$C_{19}H_{19}$	-5.2	0.3	0.8	2.2	0.5	0.7	1.1	1.0	-2.5	-2.5	-2.3	-0.6	-5.4	-3.4	-7.5	-6.0	-7.1	-7.5	7.3	5.9
$C_{17}H_{17}$	-19.4	1.0	-19.2	-17.4	-22.0	-11.5	-13.0	-17.0	-17.4	-12.5	-8.7	-10.4	-16.6	-12.8	-6.6	-15.6	-9.2	-10.0	-19.9	-24.1
$C_{16}H_{16}$	-6.1	1.0	0.8	2.2	0.5	0.6	1.1	1.0	-2.5	-2.5	-2.2	-0.5	-5.4	-3.5	-7.3	-5.8	-7.2	-7.6	7.5	6.0
outliers			15	18	18	15	15	15	16	17	19	19	10	16	19	17	15	15	18	19

	Exp	Err.	19	20	21	22	23	24	25	26	27	28	29	30	31	32
$C_{10}H_{10B}$	14.3	5.0	6.0	3.5	0.1	-1.4	6.3	1.5	14.0	9.1	-2.9	-2.8	15.4	16.5	-14.1	-16.0
$C_{10}H_{10A}$	22.7	5.0	8.8	18.8	19.7	-13.2	28.1	29.1	-4.5	0.6	22.2	20.9	-3.4	0.5	9.6	12.8
$C_{21}H_{21A}$	-4.0	0.3	6.1	15.6	18.0	-2.6	6.5	8.8	0.3	4.7	-2.5	0.3	18.2	17.8	-4.8	-4.5
$C_{21}H_{21B}$	18.2	0.3	8.8	8.6	8.3	18.3	12.4	14.7	16.3	13.9	16.1	12.0	-4.2	-4.7	6.0	9.3
C_5H_5	24.1	1.3	10.3	23.1	23.4	0.6	16.9	17.1	2.5	-2.7	18.8	15.5	14.9	14.5	-1.4	1.7
C_6H_6	25.8	1.0	2.9	20.2	21.1	6.4	19.3	24.4	22.6	13.4	25.7	22.4	18.7	20.0	11.1	11.4
$C_{22}H_{22A}$	25.4	0.3	7.5	22.1	22.9	10.9	27.7	27.9	12.8	-3.0	24.2	22.9	15.3	14.7	-3.2	-2.3
$C_{22}H_{22B}$	-7.5	0.3	7.5	0.3	1.3	4.1	-4.4	-3.9	-15.2	1.5	-2.0	-1.8	-8.1	-10.6	3.0	4.7
C_4H_4	-13.8	0.6	8.6	-6.6	-3.3	4.6	1.9	1.7	-8.8	4.3	-4.0	-2.0	-5.1	-7.9	-2.9	-1.7
C_9H_{9B}	32.1	1.5	8.3	-3.1	-1.1	11.6	-4.5	-3.1	14.9	9.7	-2.2	-1.1	8.3	6.7	16.0	15.1
C_9H_{9A}	-13.3	0.3	11.8	8.8	6.0	0.1	7.5	2.5	8.2	10.4	9.5	8.1	11.8	13.6	-1.4	-1.5
C_7H_{7B}	26.4	5.0	7.7	21.6	22.2	10.7	23.7	23.1	14.4	9.4	27.8	25.3	17.2	17.4	-1.7	-1.4
C_7H_{7A}	-16.6	5.0	7.4	0.1	0.8	2.0	-3.6	-3.0	7.5	8.2	-3.5	-2.8	1.5	2.7	7.4	8.2
$C_{23}H_{23}$	26.7	0.3	6.7	22.6	23.0	4.0	22.2	22.0	2.5	5.2	26.4	23.8	7.3	7.3	22.5	20.3
C_2H_2	-25.7	1.8	-19.5	-10.7	-8.7	-10.7	-15.0	-14.0	-16.1	-20.6	-17.2	-14.0	-16.8	-20.0	-1.7	-0.2
C_3H_3	5.0	0.3	0.4	-4.6	5.6	16.6	-9.2	-3.4	12.1	-3.1	-3.7	24.8	13.0	-1.2	-0.8	-6.1
$C_{19}H_{19}$	-5.2	0.3	6.2	9.1	7.9	6.5	-5.3	-5.6	11.9	4.3	2.2	0.2	7.0	6.4	3.0	1.4
$C_{17}H_{17}$	-19.4	1.0	-27.5	-9.7	-10.2	-16.0	0.3	3.3	-14.0	-21.1	-19.6	-17.9	-12.5	-12.9	-17.6	-12.3
$C_{16}H_{16}$	-6.1	1.0	6.3	9.1	7.8	6.6	-5.3	-5.6	11.9	4.4	2.2	0.2	7.0	6.4	3.1	1.5
outliers			19	16	16	18	16	17	18	19	15	17	18	18	19	19

Table 35: Experimental *vs.* calculated $^{1}D_{CH}$ values for all configurations of RD-1 obtained with COSMOS. The 32 different configurations are listed using the numbering of **Table 14**. Number of outliers is provided in the last row.

	Exp	**Err.**	**1**	**2**	**3**	**4**	**5**	**6**	**7**	**8**	**9**	**10**	**11**	**12**	**13**	**14**	**15**	**16**	**17**	**18**
$C_{23}H_{23}$	26.7	0.3	23.5	23.7	24.2	26.6	26.7	24.1	26.3	26.4	25.5	25.4	26.6	26.6	23.0	22.9	24.3	23.8	22.6	21.2
C_6H_6	25.8	1.0	25.2	22.8	23.3	25.1	25.0	25.0	22.8	23.4	24.4	24.6	25.3	25.4	24.9	25.0	23.3	22.8	23.4	22.4
C_5H_5	24.1	1.3	22.9	22.1	22.6	24.0	24.1	21.9	22.3	22.7	22.1	20.4	23.4	22.8	23.2	23.0	22.6	22.1	20.7	21.6
$C_{22}H_{22B}$	-7.5	0.3	-7.0	-5.5	-5.2	-7.3	-7.2	-7.2	-8.0	-7.8	-7.7	-7.8	-7.5	-7.5	-7.5	-7.6	-5.4	-5.9	-6.9	-5.3
$C_{22}H_{22A}$	25.4	0.3	24.5	23.9	23.9	25.3	25.3	24.4	24.5	24.7	23.8	23.1	25.1	25.2	24.9	24.8	24.0	23.8	24.6	24.4
$C_{10}H_{10A}$	22.7	5.0	19.1	20.4	20.6	21.2	21.1	19.3	20.1	20.0	17.1	16.8	21.9	22.0	16.9	16.6	20.7	20.5	18.1	16.1
$C_{10}H_{10B}$	14.3	5.0	9.3	11.4	11.6	11.5	11.4	9.5	9.9	9.5	9.3	8.8	12.7	12.6	8.5	7.5	11.7	11.5	9.4	9.0
C_7H_{7A}	-16.6	5.0	-14.1	-6.3	-5.8	-12.4	-12.1	-14.2	-16.1	-15.6	-13.6	-13.8	-13.1	-13.1	-12.1	-12.5	-6.6	-7.4	-12.9	-6.6
C_7H_{7B}	26.4	5.0	25.9	22.3	21.9	26.8	26.9	25.7	24.3	24.8	23.6	22.7	26.8	27.0	25.1	24.8	22.1	22.7	24.9	23.4
C_9H_{9B}	32.1	1.5	28.3	30.2	30.5	31.6	31.6	28.2	30.6	30.8	29.5	29.5	31.6	31.6	28.4	28.2	30.6	30.3	30.5	31.1
C_9H_{9A}	-13.3	0.3	-13.1	-12.4	-12.4	-13.0	-12.9	-13.1	-13.4	-13.3	-12.3	-12.3	-13.1	-13.1	-13.0	-13.0	-12.3	-12.4	-12.1	-12.1
$C_{16}H_{16}$	-6.1	1.0	-5.9	-5.7	-5.7	-5.8	-5.8	-5.9	-6.0	-6.0	-5.9	-5.9	-5.9	-5.9	-6.0	-6.0	-5.7	-5.7	-5.8	-5.7
$C_{19}H_{19}$	-5.2	0.3	-5.2	-5.0	-5.0	-5.1	-5.1	-5.2	-5.3	-5.3	-5.2	-5.2	-5.1	-5.1	-5.2	-5.2	-5.0	-5.1	-5.0	-5.0
C_4H_4	-13.8	0.6	-13.6	-11.9	-12.6	-13.7	-13.5	-13.4	-13.8	-13.6	-13.6	-13.6	-13.5	-13.4	-13.3	-13.7	-12.6	-12.1	-13.4	-10.1
$C_{17}H_{17}$	-19.4	1.0	-19.0	-19.2	-19.3	-19.4	-19.5	-19.0	-19.0	-19.0	-19.1	-19.1	-19.3	-19.3	-18.8	-18.9	-19.3	-19.2	-19.3	-19.5
$C_{21}H_{21B}$	18.2	0.3	18.0	18.0	18.1	17.9	17.9	17.6	17.8	17.9	18.1	18.2	18.1	17.8	17.9	17.8	18.1	18.0	18.1	18.2
$C_{21}H_{21A}$	-4.0	0.3	-4.2	-3.6	-3.6	-3.4	-3.4	-4.2	-4.8	-4.5	-4.3	-4.2	-4.2	-4.2	-3.5	-3.7	-3.7	-3.7	-3.9	-3.5
C_3H_3	5.0	0.3	5.0	6.0	4.9	4.7	5.3	6.4	4.2	5.7	6.0	3.4	5.2	6.6	6.3	4.0	5.0	5.9	4.6	5.9
C_2H_2	-25.7	1.8	-24.5	-25.1	-25.8	-24.1	-23.6	-24.1	-16.7	-13.7	-14.7	-20.2	-25.7	-25.4	-23.4	-24.3	-25.7	-25.0	-23.9	-24.5
$CH_{3\text{-}26}$	1.4	0.3	1.3	1.3	1.3	1.3	1.3	1.3	1.3	1.3	1.3	1.3	1.3	1.3	1.3	1.3	1.3	1.3	1.3	1.3
$CH_{2\text{-}28}$	3.0	0.4	3.0	2.9	2.9	3.0	2.9	3.0	3.0	3.0	3.0	3.0	3.0	3.0	2.9	2.9	2.9	2.9	3.0	2.9
outliers			4	10	9	2	5	6	8	8	9	9	0	3	9	8	8	10	8	12

	Exp	**Err.**	**19**	**20**	**21**	**22**	**23**	**24**	**25**	**26**	**27**	**28**	**29**	**30**	**31**	**32**
$C_{23}H_{23}$	26.7	0.3	21.2	26.4	26.4	22.0	25.9	26.2	23.5	25.0	26.3	26.3	25.2	25.0	25.2	25.7
C_6H_6	25.8	1.0	22.8	25.0	25.0	23.2	23.1	24.0	24.5	24.7	25.2	25.1	24.7	24.9	22.4	22.5
C_5H_5	24.1	1.3	22.0	23.8	23.9	19.7	22.3	22.5	20.9	12.7	21.8	21.0	23.7	23.3	18.6	19.7
$C_{22}H_{22B}$	-7.5	0.3	-5.4	-6.9	-6.8	-7.0	-7.9	-7.6	-7.4	-7.8	-7.3	-7.4	-6.9	-7.1	-7.2	-7.2
$C_{22}H_{22A}$	25.4	0.3	24.4	25.3	25.3	24.5	24.5	24.7	24.4	23.7	24.5	24.4	25.3	25.2	18.1	20.5
$C_{10}H_{10A}$	22.7	5.0	17.2	21.4	21.2	17.5	20.7	20.2	18.5	18.7	20.8	20.7	18.4	18.4	18.9	19.5
$C_{10}H_{10B}$	14.3	5.0	9.5	12.3	11.9	9.3	10.3	9.1	9.9	10.0	11.2	11.0	10.4	10.3	9.3	9.7
C_7H_{7A}	-16.6	5.0	-6.4	-10.9	-10.8	-12.6	-14.8	-14.2	-9.6	-10.9	-13.6	-13.9	-10.9	-10.5	-11.1	-10.8
C_7H_{7B}	26.4	5.0	23.1	25.8	25.9	24.8	23.4	23.6	26.2	26.4	24.5	23.9	25.7	25.9	18.1	20.5
C_9H_{9B}	32.1	1.5	31.0	28.7	29.2	30.4	20.7	24.8	31.3	31.1	29.2	29.4	30.8	30.9	29.9	30.3
C_9H_{9A}	-13.3	0.3	-12.1	-12.0	-12.0	-12.2	-13.1	-13.0	-11.5	-11.7	-12.2	-12.4	-11.3	-11.6	-12.9	-12.6
$C_{16}H_{16}$	-6.1	1.0	-5.7	-5.7	-5.7	-5.8	-5.9	-5.9	-5.8	-5.9	-5.8	-5.8	-5.7	-5.7	-5.9	-5.8
$C_{19}H_{19}$	-5.2	0.3	-5.0	-5.0	-5.0	-5.1	-5.2	-5.2	-5.0	-5.1	-5.1	-5.0	-5.0	-5.0	-5.1	-5.1
C_4H_4	-13.8	0.6	-11.7	-13.5	-13.3	-12.9	-13.6	-13.5	-13.4	-13.5	-13.3	-13.0	-13.3	-13.4	-13.1	-12.5
$C_{17}H_{17}$	-19.4	1.0	-19.5	-19.3	-19.3	-19.3	-18.7	-18.8	-19.4	-19.3	-19.3	-19.3	-19.5	-19.4	-19.1	-19.2
$C_{21}H_{21B}$	18.2	0.3	18.2	18.0	18.0	18.0	17.9	18.0	18.2	18.2	18.0	17.8	18.1	18.2	18.0	18.0
$C_{21}H_{21A}$	-4.0	0.3	-3.6	-3.2	-3.2	-3.9	-4.5	-4.2	-4.0	-4.0	-4.0	-3.9	-3.5	-3.4	-4.0	-3.8
C_3H_3	5.0	0.3	4.6	4.8	5.4	6.2	3.9	5.8	5.7	4.2	5.0	6.4	5.5	4.5	4.2	5.6
C_2H_2	-25.7	1.8	-25.1	-24.2	-23.8	-23.1	-17.1	-12.9	-20.8	-22.9	-25.2	-24.6	-23.9	-24.5	-21.5	-21.4
$CH_{3\text{-}26}$	1.4	0.3	1.3	1.3	1.3	1.3	1.3	1.3	1.3	1.3	1.3	1.3	1.3	1.3	1.3	1.3
$CH_{2\text{-}28}$	3.0	0.4	2.9	3.0	2.9	3.0	2.9	2.9	2.9	3.0	3.0	3.0	2.9	2.9	3.0	2.9
outliers			11	6	8	11	9	9	8	8	5	8	7	6	13	12

9.4.5. MSpin and COSMOS results for all configurations of RD-2

Table 36: Experimental *vs.* calculated ${}^{1}D_{CH}$ values for all configurations of RD-2 obtained with MSpin. The 32 different configurations are listed using the numbering of **Table 14**. Number of outliers is provided in the last row.

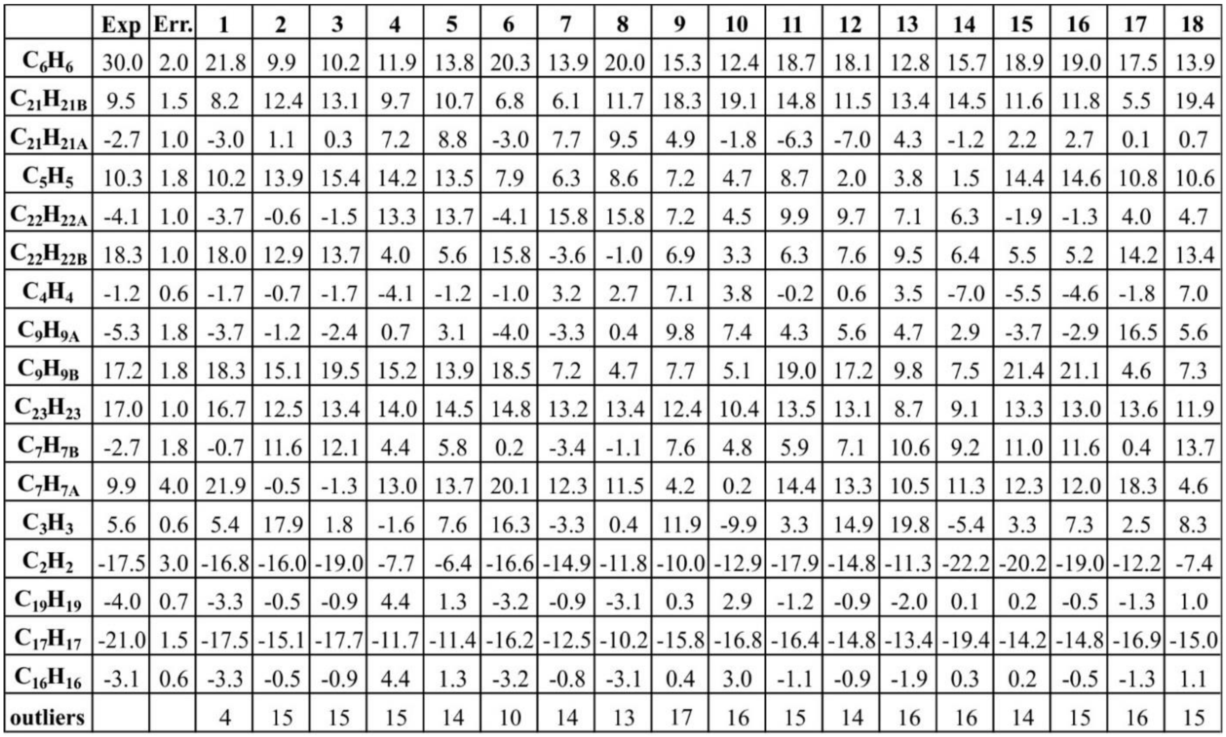

	Exp	**Err.**	**1**	**2**	**3**	**4**	**5**	**6**	**7**	**8**	**9**	**10**	**11**	**12**	**13**	**14**	**15**	**16**	**17**	**18**
C_6H_6	30.0	2.0	21.8	9.9	10.2	11.9	13.8	20.3	13.9	20.0	15.3	12.4	18.7	18.1	12.8	15.7	18.9	19.0	17.5	13.9
$C_{21}H_{21B}$	9.5	1.5	8.2	12.4	13.1	9.7	10.7	6.8	6.1	11.7	18.3	19.1	14.8	11.5	13.4	14.5	11.6	11.8	5.5	19.4
$C_{21}H_{21A}$	-2.7	1.0	-3.0	1.1	0.3	7.2	8.8	-3.0	7.7	9.5	4.9	-1.8	-6.3	-7.0	4.3	-1.2	2.2	2.7	0.1	0.7
C_5H_5	10.3	1.8	10.2	13.9	15.4	14.2	13.5	7.9	6.3	8.6	7.2	4.7	8.7	2.0	3.8	1.5	14.4	14.6	10.8	10.6
$C_{22}H_{22A}$	-4.1	1.0	-3.7	-0.6	-1.5	13.3	13.7	-4.1	15.8	15.8	7.2	4.5	9.9	9.7	7.1	6.3	-1.9	-1.3	4.0	4.7
$C_{22}H_{22B}$	18.3	1.0	18.0	12.9	13.7	4.0	5.6	15.8	-3.6	-1.0	6.9	3.3	6.3	7.6	9.5	6.4	5.5	5.2	14.2	13.4
C_4H_4	-1.2	0.6	-1.7	-0.7	-1.7	-4.1	-1.2	-1.0	3.2	2.7	7.1	3.8	-0.2	0.6	3.5	-7.0	-5.5	-4.6	-1.8	7.0
C_9H_{9A}	-5.3	1.8	-3.7	-1.2	-2.4	0.7	3.1	-4.0	-3.3	0.4	9.8	7.4	4.3	5.6	4.7	2.9	-3.7	-2.9	16.5	5.6
C_9H_{9B}	17.2	1.8	18.3	15.1	19.5	15.2	13.9	18.5	7.2	4.7	7.7	5.1	19.0	17.2	9.8	7.5	21.4	21.1	4.6	7.3
$C_{23}H_{23}$	17.0	1.0	16.7	12.5	13.4	14.0	14.5	14.8	13.2	13.4	12.4	10.4	13.5	13.1	8.7	9.1	13.3	13.0	13.6	11.9
C_7H_{7B}	-2.7	1.8	-0.7	11.6	12.1	4.4	5.8	0.2	-3.4	-1.1	7.6	4.8	5.9	7.1	10.6	9.2	11.0	11.6	0.4	13.7
C_7H_{7A}	9.9	4.0	21.9	-0.5	-1.3	13.0	13.7	20.1	12.3	11.5	4.2	0.2	14.4	13.3	10.5	11.3	12.3	12.0	18.3	4.6
C_3H_3	5.6	0.6	5.4	17.9	1.8	-1.6	7.6	16.3	-3.3	0.4	11.9	-9.9	3.3	14.9	19.8	-5.4	3.3	7.3	2.5	8.3
C_2H_2	-17.5	3.0	-16.8	-16.0	-19.0	-7.7	-6.4	-16.6	-14.9	-11.8	-10.0	-12.9	-17.9	-14.8	-11.3	-22.2	-20.2	-19.0	-12.2	-7.4
$C_{19}H_{19}$	-4.0	0.7	-3.3	-0.5	-0.9	4.4	1.3	-3.2	-0.9	-3.1	0.3	2.9	-1.2	-0.9	-2.0	0.1	0.2	-0.5	-1.3	1.0
$C_{17}H_{17}$	-21.0	1.5	-17.5	-15.1	-17.7	-11.7	-11.4	-16.2	-12.5	-10.2	-15.8	-16.8	-16.4	-14.8	-13.4	-19.4	-14.2	-14.8	-16.9	-15.0
$C_{16}H_{16}$	-3.1	0.6	-3.3	-0.5	-0.9	4.4	1.3	-3.2	-0.8	-3.1	0.4	3.0	-1.1	-0.9	-1.9	0.3	0.2	-0.5	-1.3	1.1
outliers			4	15	15	15	14	10	14	13	17	16	15	14	16	16	14	15	16	15

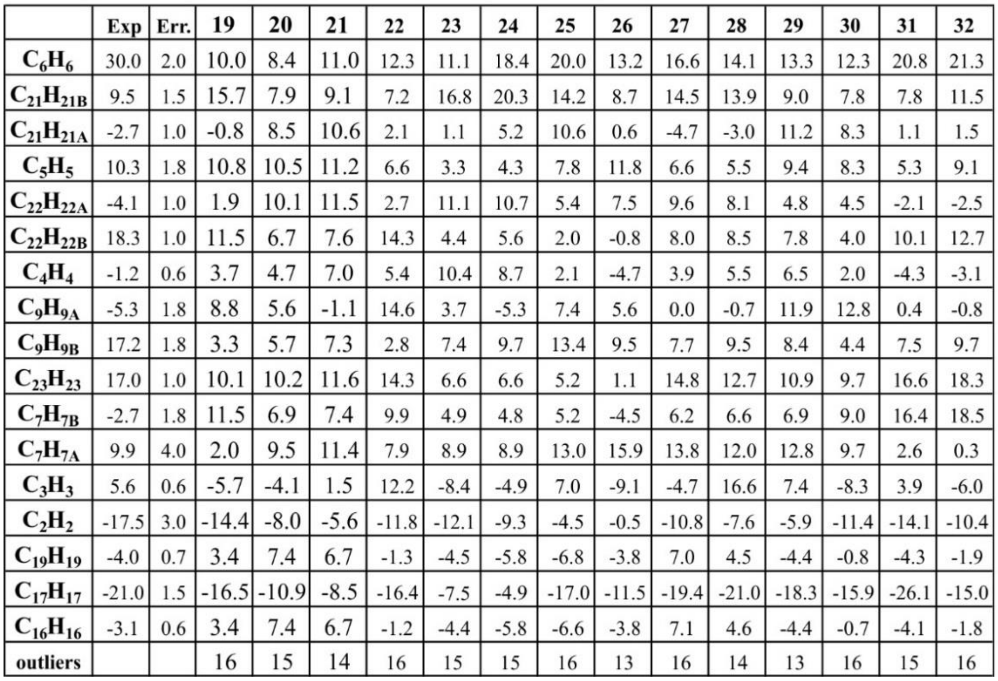

	Exp	**Err.**	**19**	**20**	**21**	**22**	**23**	**24**	**25**	**26**	**27**	**28**	**29**	**30**	**31**	**32**
C_6H_6	30.0	2.0	10.0	8.4	11.0	12.3	11.1	18.4	20.0	13.2	16.6	14.1	13.3	12.3	20.8	21.3
$C_{21}H_{21B}$	9.5	1.5	15.7	7.9	9.1	7.2	16.8	20.3	14.2	8.7	14.5	13.9	9.0	7.8	7.8	11.5
$C_{21}H_{21A}$	-2.7	1.0	-0.8	8.5	10.6	2.1	1.1	5.2	10.6	0.6	-4.7	-3.0	11.2	8.3	1.1	1.5
C_5H_5	10.3	1.8	10.8	10.5	11.2	6.6	3.3	4.3	7.8	11.8	6.6	5.5	9.4	8.3	5.3	9.1
$C_{22}H_{22A}$	-4.1	1.0	1.9	10.1	11.5	2.7	11.1	10.7	5.4	7.5	9.6	8.1	4.8	4.5	-2.1	-2.5
$C_{22}H_{22B}$	18.3	1.0	11.5	6.7	7.6	14.3	4.4	5.6	2.0	-0.8	8.0	8.5	7.8	4.0	10.1	12.7
C_4H_4	-1.2	0.6	3.7	4.7	7.0	5.4	10.4	8.7	2.1	-4.7	3.9	5.5	6.5	2.0	-4.3	-3.1
C_9H_{9A}	-5.3	1.8	8.8	5.6	-1.1	14.6	3.7	-5.3	7.4	5.6	0.0	-0.7	11.9	12.8	0.4	-0.8
C_9H_{9B}	17.2	1.8	3.3	5.7	7.3	2.8	7.4	9.7	13.4	9.5	7.7	9.5	8.4	4.4	7.5	9.7
$C_{23}H_{23}$	17.0	1.0	10.1	10.2	11.6	14.3	6.6	6.6	5.2	1.1	14.8	12.7	10.9	9.7	16.6	18.3
C_7H_{7B}	-2.7	1.8	11.5	6.9	7.4	9.9	4.9	4.8	5.2	-4.5	6.2	6.6	6.9	9.0	16.4	18.5
C_7H_{7A}	9.9	4.0	2.0	9.5	11.4	7.9	8.9	8.9	13.0	15.9	13.8	12.0	12.8	9.7	2.6	0.3
C_3H_3	5.6	0.6	-5.7	-4.1	1.5	12.2	-8.4	-4.9	7.0	-9.1	-4.7	16.6	7.4	-8.3	3.9	-6.0
C_2H_2	-17.5	3.0	-14.4	-8.0	-5.6	-11.8	-12.1	-9.3	-4.5	-0.5	-10.8	-7.6	-5.9	-11.4	-14.1	-10.4
$C_{19}H_{19}$	-4.0	0.7	3.4	7.4	6.7	-1.3	-4.5	-5.8	-6.8	-3.8	7.0	4.5	-4.4	-0.8	-4.3	-1.9
$C_{17}H_{17}$	-21.0	1.5	-16.5	-10.9	-8.5	-16.4	-7.5	-4.9	-17.0	-11.5	-19.4	-21.0	-18.3	-15.9	-26.1	-15.0
$C_{16}H_{16}$	-3.1	0.6	3.4	7.4	6.7	-1.2	-4.4	-5.8	-6.6	-3.8	7.1	4.6	-4.4	-0.7	-4.1	-1.8
outliers			16	15	14	16	15	15	16	13	16	14	13	16	15	16

Table 37: Experimental *vs.* calculated $^{1}D_{CH}$ values for all configurations of RD-2 obtained with COSMOS. These values correspond to the MD simulation with $^{1}D_{CH}$, $^{3}J_{HH}$ and ROE distances constraints. The 32 different configurations are listed using the numbering of **Table 14**. Number of outliers is provided in the last row.

	Exp	**Err.**	**1**	**2**	**3**	**4**	**5**	**6**	**7**	**8**	**9**	**10**	**11**	**12**	**13**	**14**	**15**	**16**	**17**	**18**
$C_{23}H_{23}$	17.0	1.0	17.0	16.8	16.8	16.6	16.8	17.0	16.8	16.7	16.8	16.8	16.7	16.7	16.9	16.9	16.6	16.5	16.9	16.8
$C_{6}H_{6}$	30.0	2.0	27.7	27.9	28.0	26.7	27.0	27.7	27.6	27.8	27.9	27.9	27.7	27.7	27.0	27.0	28.1	28.0	27.5	28.0
$C_{5}H_{5}$	10.3	1.8	10.6	10.9	11.0	10.3	10.6	10.5	9.9	9.9	9.6	9.6	10.1	10.2	10.6	10.6	10.8	10.7	10.3	10.8
$C_{22}H_{22B}$	18.3	1.0	18.0	18.0	18.1	17.9	17.9	18.0	17.8	17.7	17.7	17.7	17.9	18.0	17.9	17.8	17.8	17.9	18.0	18.0
$C_{22}H_{22A}$	-4.0	1.0	-4.0	-4.0	-4.0	-3.9	-3.8	-3.9	-4.2	-4.1	-4.3	-4.3	-4.2	-4.1	-3.8	-3.7	-4.0	-4.0	-4.0	-3.8
$C_{7}H_{7B}$	-2.7	1.8	-2.4	-2.2	-2.2	-2.5	-2.5	-2.5	-2.8	-2.7	-2.6	-2.6	-2.6	-2.5	-2.2	-2.3	-2.2	-2.3	-2.3	-1.7
$C_{7}H_{7A}$	9.9	4.0	12.0	10.4	10.6	11.4	11.3	11.9	10.1	10.1	10.0	10.1	11.9	11.9	11.8	11.8	11.0	10.6	11.3	9.9
$C_{9}H_{9B}$	17.2	1.8	17.0	16.9	17.0	16.9	16.7	16.9	16.6	16.8	16.9	16.9	17.0	17.1	17.1	17.0	16.9	16.8	16.8	16.7
$C_{9}H_{9A}$	-5.3	1.8	-5.1	-5.1	-5.1	-5.1	-5.1	-5.2	-5.2	-5.2	-5.1	-5.1	-5.1	-5.0	-5.0	-5.0	-5.1	-5.1	-4.9	-5.0
$C_{16}H_{16}$	-3.1	0.6	-3.0	-3.0	-3.0	-3.0	-3.1	-3.0	-3.1	-3.1	-3.0	-3.0	-3.1	-3.1	-3.0	-3.0	-3.0	-3.0	-3.0	-3.0
$C_{19}H_{19}$	-4.0	0.7	-3.8	-3.8	-3.8	-3.9	-3.9	-3.8	-3.9	-3.9	-3.9	-3.8	-4.0	-4.0	-3.8	-3.8	-3.8	-3.9	-3.8	-3.9
$C_{4}H_{4}$	-1.2	0.6	-1.3	-1.3	-1.2	-1.3	-1.3	-1.3	-1.4	-1.3	-1.3	-1.3	-1.4	-1.3	-1.2	-1.2	-1.1	-1.2	-1.2	-1.2
$C_{17}H_{17}$	-21.0	1.5	-20.7	-20.7	-20.7	-20.7	-20.7	-20.7	-20.6	-20.6	-20.6	-20.7	-20.5	-20.5	-20.8	-20.8	-20.6	-20.5	-20.7	-20.7
$C_{21}H_{21B}$	9.5	1.5	9.5	9.6	9.7	9.7	9.6	9.3	9.5	9.5	9.7	9.7	9.5	9.5	9.6	9.5	9.8	9.7	9.5	9.7
$C_{21}H_{21A}$	-2.7	1.0	-2.6	-2.6	-2.4	-2.5	-2.5	-2.7	-2.6	-2.6	-2.5	-2.6	-2.6	-2.6	-2.3	-2.3	-2.4	-2.5	-2.5	-2.4
$C_{3}H_{3}$	5.6	0.6	5.7	5.9	5.6	5.2	5.9	5.8	5.4	5.9	5.8	5.4	5.5	5.8	5.8	5.5	5.5	5.8	5.5	5.9
$C_{2}H_{2}$	-17.5	3.0	-17.8	-17.6	-18.2	-17.2	-17.1	-17.6	-16.4	-15.8	-15.9	-16.2	-17.0	-16.7	-17.3	-17.7	-17.6	-17.0	-17.4	-16.6
$CH_{3\text{-}26}$	0.8	0.3	0.7	0.7	0.7	0.7	0.7	0.7	0.7	0.7	0.7	0.7	0.7	0.7	0.7	0.7	0.7	0.7	0.7	0.7
outliers			1	1	0	1	1	1	1	1	1	1	1	1	1	1	0	1	1	0

	Exp	**Err.**	**19**	**20**	**21**	**22**	**23**	**24**	**25**	**26**	**27**	**28**	**29**	**30**	**31**	**32**
$C_{23}H_{23}$	17.0	1.0	16.8	16.2	16.4	16.8	16.1	16.1	16.4	16.4	16.2	16.1	16.8	16.8	16.4	16.1
$C_{6}H_{6}$	30.0	2.0	27.8	27.2	27.1	27.2	27.8	27.9	27.4	27.2	27.6	27.4	26.5	26.9	27.9	27.5
$C_{5}H_{5}$	10.3	1.8	10.8	10.4	10.6	10.4	9.5	9.6	9.3	9.5	10.1	10.1	10.2	10.3	10.9	10.8
$C_{22}H_{22B}$	18.3	1.0	18.0	17.6	17.8	18.0	17.3	17.4	17.7	-4.2	18.0	18.0	18.2	18.1	17.9	17.8
$C_{22}H_{22A}$	-4.0	1.0	-3.8	-4.0	-4.0	-3.9	-4.3	-4.2	-4.3	17.6	-4.2	-4.1	-3.7	-3.8	-4.1	-4.0
$C_{7}H_{7B}$	-2.7	1.8	-1.8	-2.4	-2.3	-2.4	-2.6	-2.6	-2.6	-2.4	-2.7	-2.7	-1.8	-2.2	-2.1	-2.0
$C_{7}H_{7A}$	9.9	4.0	10.2	11.7	11.6	11.2	9.7	9.7	10.0	10.2	11.4	11.3	11.1	11.1	10.7	10.8
$C_{9}H_{9B}$	17.2	1.8	16.8	16.4	16.6	16.8	16.5	16.6	16.6	16.6	16.4	16.5	16.8	16.7	16.6	16.5
$C_{9}H_{9A}$	-5.3	1.8	-5.1	-5.7	-5.5	-5.0	-5.5	-5.5	-5.1	-5.0	-5.5	-5.4	-4.7	-4.9	-5.5	-5.5
$C_{16}H_{16}$	-3.1	0.6	-3.0	-3.1	-3.1	-3.1	-3.2	-3.2	-3.2	-3.1	-3.1	-3.1	-3.0	-3.1	-3.0	-3.0
$C_{19}H_{19}$	-4.0	0.7	-3.8	-3.9	-3.9	-3.9	-4.0	-4.0	-4.0	-3.9	-3.9	-3.9	-3.8	-3.9	-3.9	-3.8
$C_{4}H_{4}$	-1.2	0.6	-1.2	-1.4	-1.4	-1.2	-1.3	-1.3	-1.4	-1.3	-1.4	-1.4	-1.2	-1.3	-1.3	-1.2
$C_{17}H_{17}$	-21.0	1.5	-20.8	-20.5	-20.5	-20.7	-20.4	-20.4	-20.4	-20.5	-20.5	-20.5	-20.8	-20.8	-20.6	-20.4
$C_{21}H_{21B}$	9.5	1.5	9.7	9.7	9.7	9.5	9.5	9.5	9.6	9.6	9.4	9.4	10.1	9.9	9.7	9.7
$C_{21}H_{21A}$	-2.7	1.0	-2.4	-2.4	-2.4	-2.5	-2.6	-2.5	-2.5	-2.6	-2.6	-2.7	-2.3	-2.4	-2.5	-2.4
$C_{3}H_{3}$	5.6	0.6	5.3	5.3	5.9	5.8	5.1	5.9	5.8	5.3	5.5	5.8	5.7	5.4	5.5	6.1
$C_{2}H_{2}$	-17.5	3.0	-17.2	-17.0	-17.0	-17.0	-15.9	-15.7	-15.6	-15.8	-16.8	-16.4	-17.4	-17.5	-17.7	-17.2
$CH_{3\text{-}26}$	0.8	0.3	0.7	0.7	0.7	0.7	0.7	0.7	0.7	0.7	0.7	0.7	0.7	0.7	0.7	0.7
outliers			1	1	1	1	1	1	1	1	1	1	1	1	1	1

Table 38: Experimental *vs.* calculated $^3J_{HH}$ values for all configurations of RD-2 obtained with COSMOS. These values correspond to the MD simulation with $^1D_{CH}$, $^3J_{HH}$ and ROE distances constraints. The 32 different configurations are listed using the numbering of **Table 14**. Number of outliers is provided in the last row.

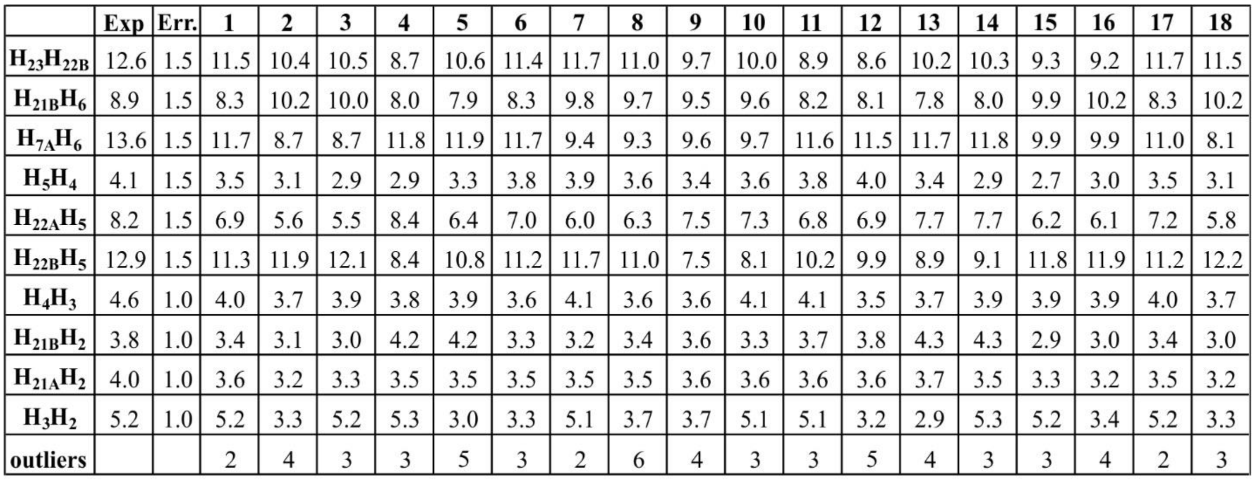

	Exp	**Err.**	**1**	**2**	**3**	**4**	**5**	**6**	**7**	**8**	**9**	**10**	**11**	**12**	**13**	**14**	**15**	**16**	**17**	**18**
$H_{23}H_{22B}$	12.6	1.5	11.5	10.4	10.5	8.7	10.6	11.4	11.7	11.0	9.7	10.0	8.9	8.6	10.2	10.3	9.3	9.2	11.7	11.5
$H_{21B}H_6$	8.9	1.5	8.3	10.2	10.0	8.0	7.9	8.3	9.8	9.7	9.5	9.6	8.2	8.1	7.8	8.0	9.9	10.2	8.3	10.2
$H_{7A}H_6$	13.6	1.5	11.7	8.7	8.7	11.8	11.9	11.7	9.4	9.3	9.6	9.7	11.6	11.5	11.7	11.8	9.9	9.9	11.0	8.1
H_5H_4	4.1	1.5	3.5	3.1	2.9	2.9	3.3	3.8	3.9	3.6	3.4	3.6	3.8	4.0	3.4	2.9	2.7	3.0	3.5	3.1
$H_{22A}H_5$	8.2	1.5	6.9	5.6	5.5	8.4	6.4	7.0	6.0	6.3	7.5	7.3	6.8	6.9	7.7	7.7	6.2	6.1	7.2	5.8
$H_{22B}H_5$	12.9	1.5	11.3	11.9	12.1	8.4	10.8	11.2	11.7	11.0	7.5	8.1	10.2	9.9	8.9	9.1	11.8	11.9	11.2	12.2
H_4H_3	4.6	1.0	4.0	3.7	3.9	3.8	3.9	3.6	4.1	3.6	3.6	4.1	4.1	3.5	3.7	3.9	3.9	3.9	4.0	3.7
$H_{21B}H_2$	3.8	1.0	3.4	3.1	3.0	4.2	4.2	3.3	3.2	3.4	3.6	3.3	3.7	3.8	4.3	4.3	2.9	3.0	3.4	3.0
$H_{21A}H_2$	4.0	1.0	3.6	3.2	3.3	3.5	3.5	3.5	3.5	3.5	3.6	3.6	3.6	3.6	3.7	3.5	3.3	3.2	3.5	3.2
H_3H_2	5.2	1.0	5.2	3.3	5.2	5.3	3.0	3.3	5.1	3.7	3.7	5.1	5.1	3.2	2.9	5.3	5.2	3.4	5.2	3.3
outliers			2	4	3	3	5	3	2	6	4	3	3	5	4	3	3	4	2	3

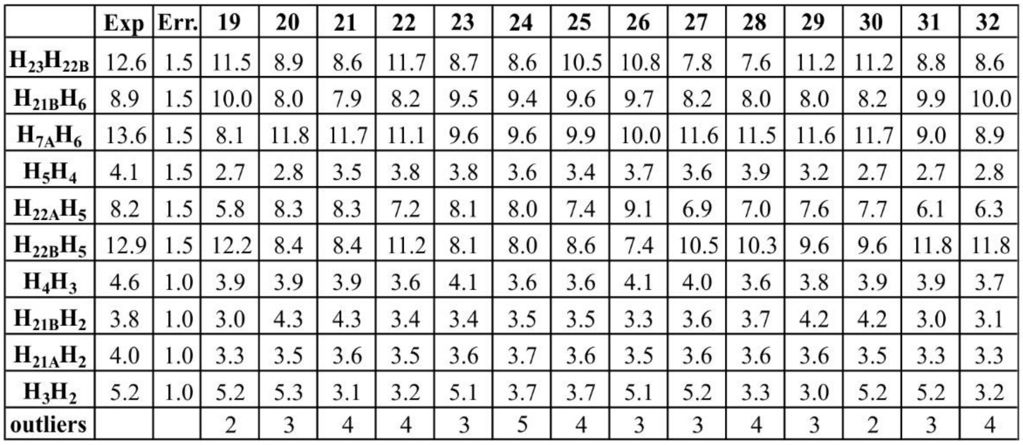

	Exp	**Err.**	**19**	**20**	**21**	**22**	**23**	**24**	**25**	**26**	**27**	**28**	**29**	**30**	**31**	**32**
$H_{23}H_{22B}$	12.6	1.5	11.5	8.9	8.6	11.7	8.7	8.6	10.5	10.8	7.8	7.6	11.2	11.2	8.8	8.6
$H_{21B}H_6$	8.9	1.5	10.0	8.0	7.9	8.2	9.5	9.4	9.6	9.7	8.2	8.0	8.0	8.2	9.9	10.0
$H_{7A}H_6$	13.6	1.5	8.1	11.8	11.7	11.1	9.6	9.6	9.9	10.0	11.6	11.5	11.6	11.7	9.0	8.9
H_5H_4	4.1	1.5	2.7	2.8	3.5	3.8	3.8	3.6	3.4	3.7	3.6	3.9	3.2	2.7	2.7	2.8
$H_{22A}H_5$	8.2	1.5	5.8	8.3	8.3	7.2	8.1	8.0	7.4	9.1	6.9	7.0	7.6	7.7	6.1	6.3
$H_{22B}H_5$	12.9	1.5	12.2	8.4	8.4	11.2	8.1	8.0	8.6	7.4	10.5	10.3	9.6	9.6	11.8	11.8
H_4H_3	4.6	1.0	3.9	3.9	3.9	3.6	4.1	3.6	3.6	4.1	4.0	3.6	3.8	3.9	3.9	3.7
$H_{21B}H_2$	3.8	1.0	3.0	4.3	4.3	3.4	3.4	3.5	3.5	3.3	3.6	3.7	4.2	4.2	3.0	3.1
$H_{21A}H_2$	4.0	1.0	3.3	3.5	3.6	3.5	3.6	3.7	3.6	3.5	3.6	3.6	3.6	3.5	3.3	3.3
H_3H_2	5.2	1.0	5.2	5.3	3.1	3.2	5.1	3.7	3.7	5.1	5.2	3.3	3.0	5.2	5.2	3.2
outliers			2	3	4	4	3	5	4	3	3	4	3	2	3	4

Table 39: Experimental *vs.* calculated ROE distances values for all configurations of RD-2 obtained with COSMOS.

These values correspond to the MD simulation with $^{1}D_{CH}$, $^{3}J_{HH}$ and ROE distances constraints. The 32 different configurations are listed using the numbering of **Table 14**. Number of outliers is provided in the last row.

	Exp	**Err.**	**1**	**2**	**3**	**4**	**5**	**6**	**7**	**8**	**9**	**10**	**11**	**12**	**13**	**14**	**15**	**16**	**17**	**18**
$H_{24}H_3$	2.6	0.3	2.3	2.2	2.3	2.3	2.2	2.2	2.3	2.2	2.2	2.3	2.3	2.2	2.2	2.3	2.3	2.2	2.3	2.2
$H_{23}H_{13}$	2.9	0.3	3.1	3.1	3.1	3.4	3.4	3.1	3.3	3.3	3.1	3.1	3.4	3.5	3.1	3.1	3.4	3.5	3.4	3.4
$H_{23}H_{22B}$	3.2	0.3	3.0	3.0	3.0	2.1	2.7	3.0	3.0	2.8	2.9	2.9	2.2	2.2	2.9	3.0	2.2	2.2	3.0	3.1
$H_{23}H_{22A}$	2.5	0.3	2.4	2.3	2.3	3.0	2.6	2.5	2.5	2.6	2.4	2.4	2.7	2.7	2.4	2.4	2.8	2.8	2.5	2.4
$H_{23}H_8$	2.3	0.3	2.2	2.2	2.2	3.0	3.0	2.2	3.0	3.0	2.3	2.2	3.0	3.0	2.2	2.2	3.0	3.0	3.0	3.0
$H_{22B}H_{22A}$	1.7	0.3	1.8	1.8	1.8	1.8	1.8	1.8	1.8	1.8	1.8	1.8	1.8	1.8	1.8	1.8	1.8	1.8	1.8	1.8
$H_{22B}H_{9B}$	2.5	0.3	3.7	3.9	4.0	4.8	4.9	3.6	4.9	4.8	5.0	5.0	4.6	4.6	5.0	5.0	4.9	4.9	4.6	4.8
$H_{7B}H_{21A}$	2.3	0.3	2.6	3.0	3.0	2.9	2.9	2.6	2.7	2.7	2.8	2.8	2.8	2.8	3.0	2.9	2.9	2.9	2.7	3.1
$H_{9B}H_{9A}$	1.8	0.3	1.8	1.8	1.8	1.8	1.8	1.8	1.8	1.8	1.8	1.8	1.8	1.8	1.8	1.8	1.8	1.8	1.8	1.8
$H_{9A}H_8$	2.6	0.3	2.3	2.3	2.3	2.3	2.3	2.3	2.3	2.4	2.3	2.3	2.4	2.3	2.4	2.4	2.3	2.3	3.0	3.0
$H_{16}H_{17}$	2.5	0.3	2.5	2.5	2.5	2.5	2.5	2.5	2.5	2.5	2.5	2.5	2.5	2.5	2.5	2.5	2.5	2.5	2.5	2.5
H_4H_3	2.4	0.3	2.4	2.6	2.4	2.5	2.7	2.6	2.5	2.7	2.7	2.5	2.4	2.7	2.6	2.5	2.4	2.6	2.4	2.6
$H_{21B}H_{21A}$	1.7	0.3	1.7	1.7	1.7	1.8	1.8	1.7	1.7	1.7	1.7	1.7	1.7	1.7	1.8	1.8	1.7	1.7	1.7	1.7
$H_{21B}H_2$	2.3	0.3	2.5	2.5	2.5	2.3	2.3	2.4	2.5	2.4	2.4	2.5	2.4	2.4	2.3	2.3	2.5	2.4	2.5	2.5
$H_{21A}H_2$	2.3	0.3	2.5	2.4	2.4	2.7	2.6	2.5	2.5	2.5	2.5	2.5	2.6	2.5	2.6	2.7	2.4	2.4	2.5	2.4
H_3H_2	2.4	0.3	2.5	2.6	2.5	2.6	2.7	2.6	2.5	2.6	2.6	2.5	2.5	2.7	2.7	2.6	2.5	2.6	2.5	2.6
outliers			3	3	3	7	9	4	6	7	6	4	5	7	5	4	7	8	5	6

	Exp	**Err.**	**19**	**20**	**21**	**22**	**23**	**24**	**25**	**26**	**27**	**28**	**29**	**30**	**31**	**32**
$H_{24}H_3$	2.6	0.3	2.3	2.3	2.2	2.2	2.3	2.2	2.2	2.3	2.3	2.2	2.2	2.3	2.3	2.4
$H_{23}H_{13}$	2.9	0.3	3.4	3.1	3.1	3.4	3.1	3.2	3.3	3.3	3.1	3.2	3.2	3.2	3.2	3.2
$H_{23}H_{22B}$	3.2	0.3	3.1	2.2	2.2	3.0	2.2	2.2	3.0	2.4	2.2	2.2	3.0	3.0	2.3	2.2
$H_{23}H_{22A}$	2.5	0.3	2.3	2.9	2.9	2.5	2.9	2.9	2.4	3.0	2.6	2.6	2.4	2.4	2.7	2.7
$H_{23}H_8$	2.3	0.3	3.0	2.2	2.2	3.0	2.3	2.3	3.0	3.0	2.1	2.1	3.0	3.0	2.2	2.1
$H_{22B}H_{22A}$	1.7	0.3	1.8	1.8	1.8	1.8	1.8	1.8	1.8	1.8	1.8	1.8	1.8	1.8	1.8	1.8
$H_{22B}H_{9B}$	2.5	0.3	4.8	5.0	5.0	4.6	5.0	4.9	4.8	4.7	4.9	4.8	4.8	4.7	5.0	5.0
$H_{7B}H_{21A}$	2.3	0.3	3.1	2.9	2.9	2.7	2.8	2.8	2.9	2.8	2.7	2.7	3.0	3.0	3.0	3.0
$H_{9B}H_{9A}$	1.8	0.3	1.8	1.8	1.8	1.8	1.8	1.8	1.8	1.8	1.8	1.8	1.8	1.8	1.8	1.7
$H_{9A}H_8$	2.6	0.3	3.0	2.8	2.8	3.0	2.8	2.8	3.0	3.0	2.8	2.8	3.0	3.0	2.8	2.7
$H_{16}H_{17}$	2.5	0.3	2.5	2.5	2.5	2.5	2.5	2.5	2.5	2.5	2.5	2.5	2.5	2.5	2.5	2.5
H_4H_3	2.4	0.3	2.4	2.5	2.7	2.7	2.5	2.7	2.7	2.5	2.4	2.7	2.7	2.5	2.4	2.6
$H_{21B}H_{21A}$	1.7	0.3	1.7	1.8	1.8	1.7	1.7	1.7	1.7	1.7	1.7	1.7	1.8	1.7	1.7	1.7
$H_{21B}H_2$	2.3	0.3	2.5	2.3	2.3	2.4	2.5	2.4	2.4	2.5	2.5	2.4	2.3	2.3	2.5	2.4
$H_{21A}H_2$	2.3	0.3	2.4	2.7	2.6	2.5	2.5	2.5	2.5	2.5	2.6	2.5	2.6	2.7	2.4	2.4
H_3H_2	2.4	0.3	2.5	2.6	2.7	2.7	2.5	2.6	2.6	2.5	2.5	2.7	2.7	2.6	2.5	2.7
outliers			5	5	6	7	5	6	7	7	3	5	8	6	3	3

9.4.6. Isotropic NMR spectra of HMIP with assignments

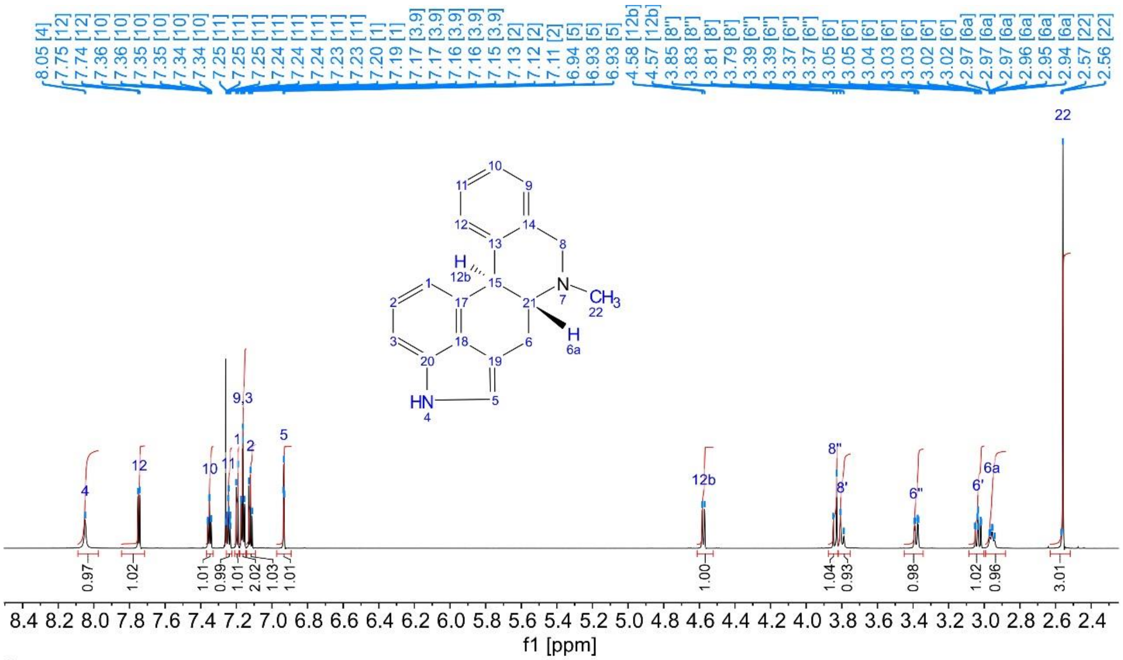

^{1}H NMR (800 MHz, Chloroform-*d*) δ 8.05 (s, 1H), 7.75 (d, J = 7.7 Hz, 1H), 7.35 (td, J = 7.5, 1.3 Hz, 1H), 7.26 – 7.22 (m, 1H), 7.20 (d, J = 8.0 Hz, 1H), 7.18 – 7.15 (m, 2H), 7.12 (t, J = 7.6 Hz, 1H), 6.93 (t, J = 1.8 Hz, 1H), 4.58 (d, J = 10.1 Hz, 1H), 3.84 (d, J = 14.7 Hz, 1H), 3.80 (d, J = 14.9 Hz, 1H), 3.38 (dd, J = 14.0, 3.5 Hz, 1H), 3.03 (ddd, J = 13.7, 11.6, 1.7 Hz, 1H), 2.99 – 2.88 (m, 1H), 2.56 (s, 3H).

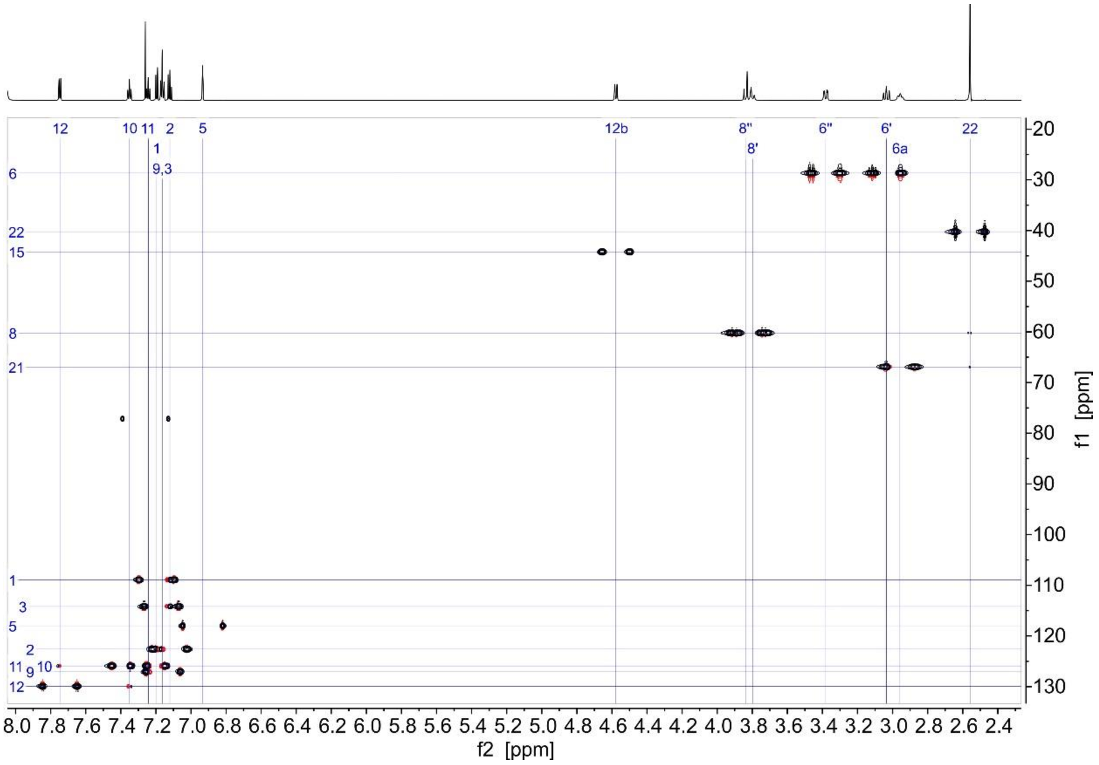

Figure 81: ^{1}H and ^{1}H,^{13}C-HSQC NMR spectra of HMIP in $CDCl_3$.

9.4.7. Isotropic NMR spectra of POMT with assignments

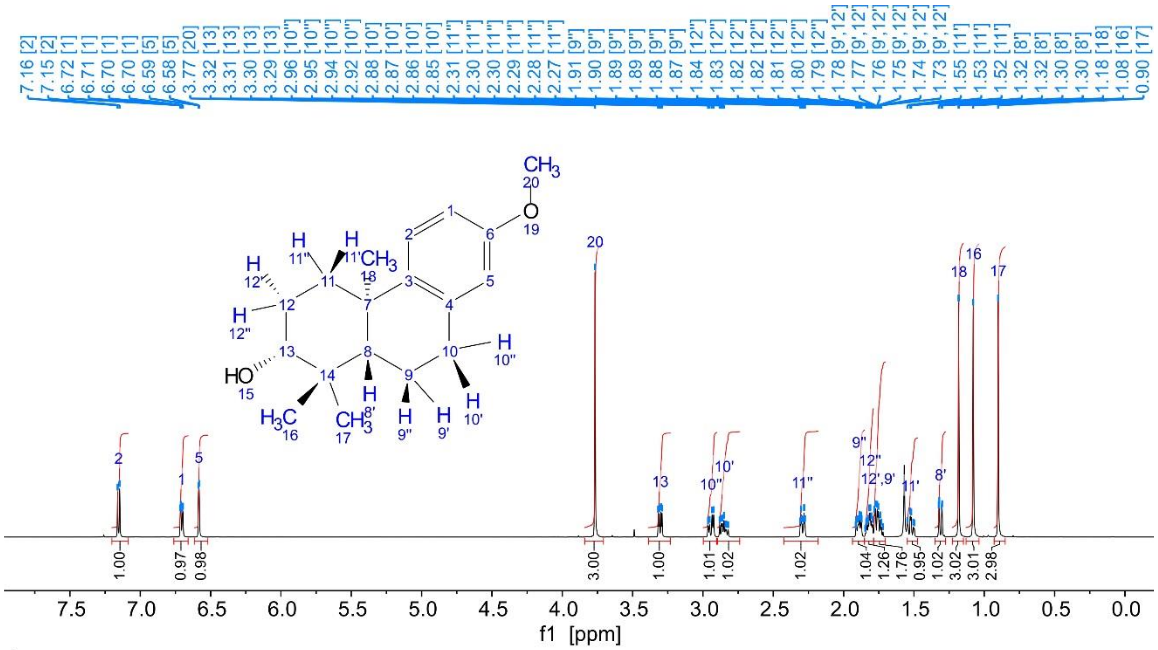

^{1}H NMR (600 MHz, Chloroform-d) δ 7.15 (d, J = 8.7 Hz, 1H), 6.71 (dd, J = 8.8, 2.7 Hz, 1H), 6.58 (d, J = 2.7 Hz, 1H), 3.77 (s, 3H), 3.30 (dd, J = 11.6, 4.6 Hz, 1H), 2.94 (dd, J = 17.2, 6.6 Hz, 1H), 2.85 (ddd, J = 17.8, 11.6, 7.5 Hz, 1H), 2.29 (dt, J = 13.2, 3.6 Hz, 1H), 1.89 (dt, J = 9.3, 4.7 Hz, 1H), 1.81 (td, J = 9.2, 4.8 Hz, 1H), 1.79 – 1.70 (m, 2H), 1.52 (td, J = 13.2, 4.0 Hz, 1H), 1.31 (dd, J = 12.3, 2.2 Hz, 1H), 1.18 (s, 3H), 1.08 (s, 3H), 0.90 (s, 3H).

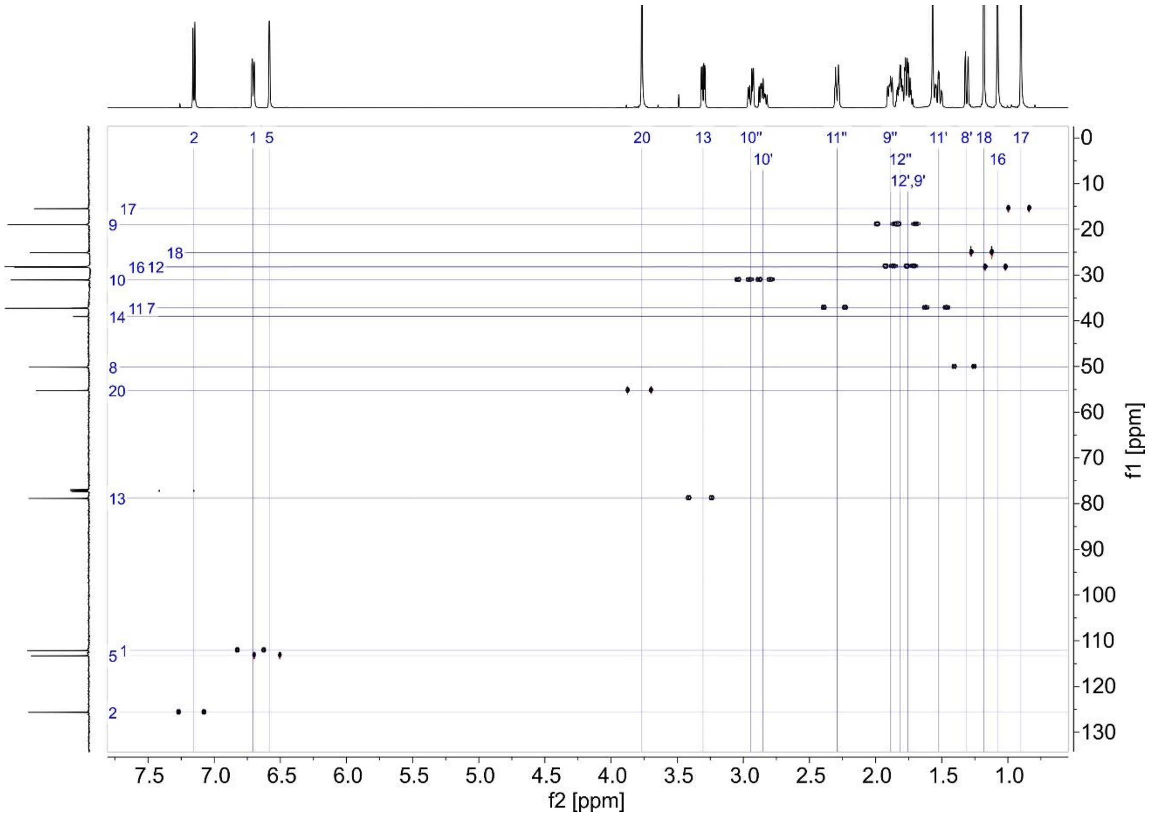

Figure 82: ^{1}H and ^{1}H,^{13}C-HSQC NMR spectra of POMT in $CDCl_3$.

9.4.8. Isotropic NMR spectra of borneol with assignments

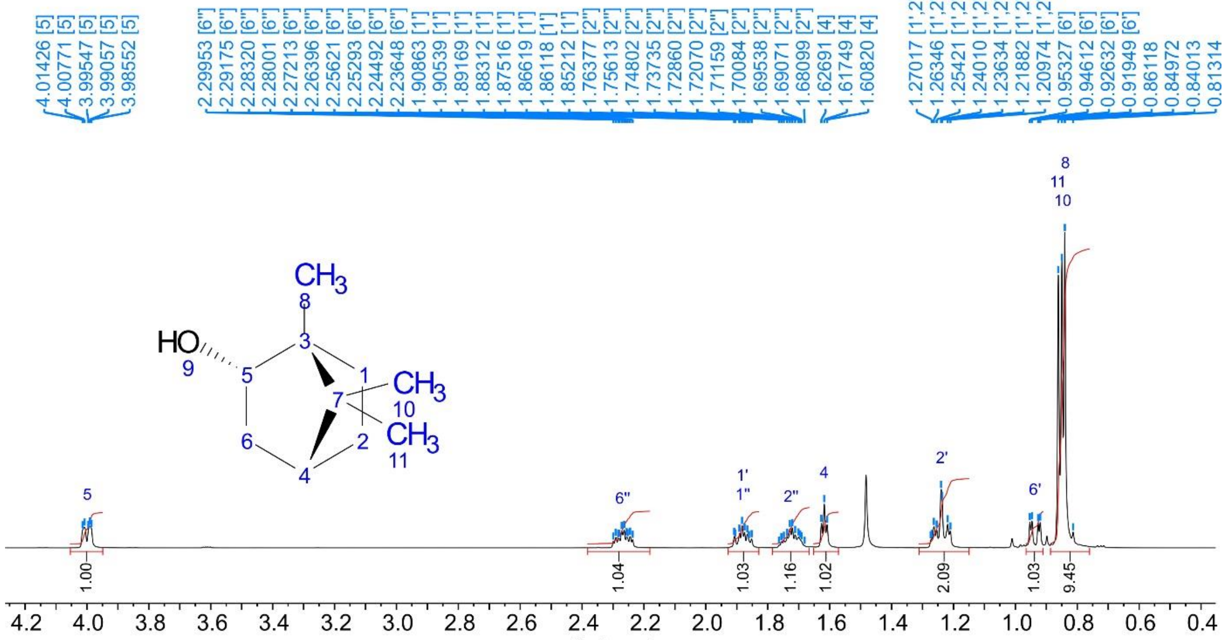

^{1}H NMR (500 MHz, Chloroform-d) δ 4.05 – 3.95 (m, 1H), 2.27 (ddt, J = 13.7, 9.9, 4.1 Hz, 1H), 1.88 (ddd, J = 15.5, 10.0, 4.3 Hz, 1H), 1.72 (ddt, J = 15.0, 10.4, 4.6 Hz, 1H), 1.62 (t, J = 4.7 Hz, 1H), 1.24 (td, J = 13.3, 12.5, 4.6 Hz, 2H), 0.94 (dd, J = 13.4, 3.5 Hz, 1H), 0.89 – 0.76 (m, 9H).

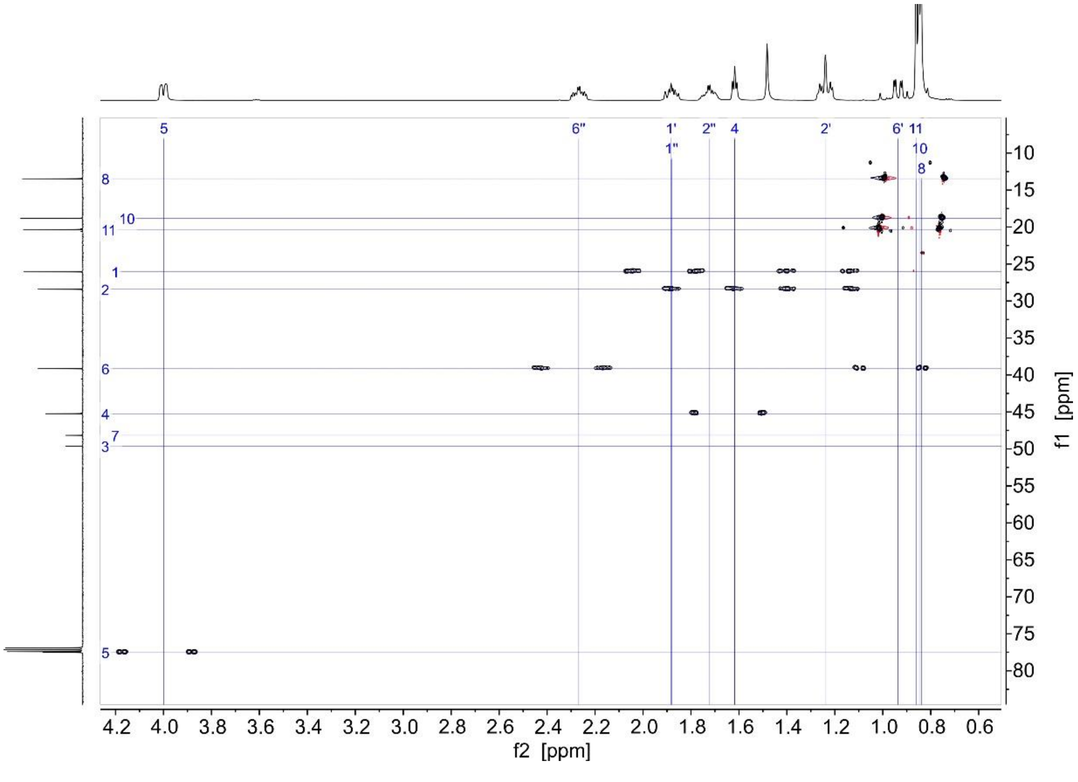

Figure 83: ^{1}H and ^{1}H,^{13}C-HSQC NMR spectra of borneol in $CDCl_3$.

9.4.9. Isotropic NMR spectra of camphor with assignments

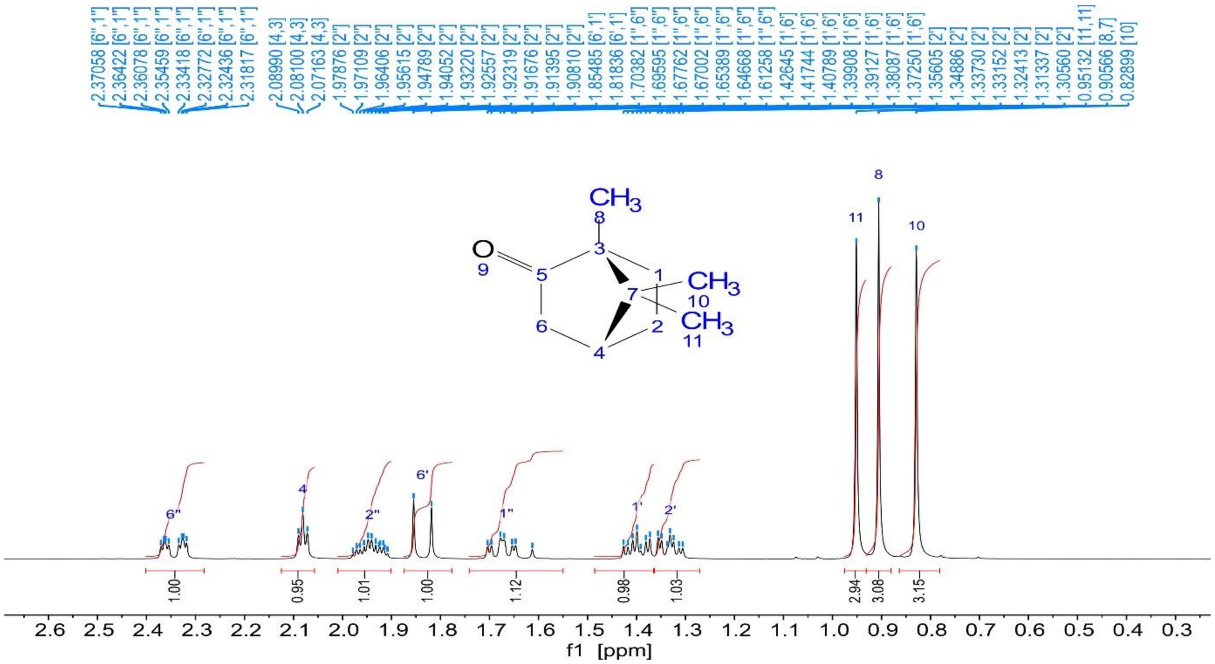

1H NMR (500 MHz, Chloroform-d) δ 2.34 (ddd, J = 18.2, 4.8, 3.1 Hz, 1H), 2.08 (t, J = 4.6 Hz, 1H), 2.01 – 1.90 (m, 1H), 1.84 (d, J = 18.2 Hz, 1H), 1.74 – 1.55 (m, 1H), 1.40 (ddd, J = 13.3, 9.3, 4.3 Hz, 1H), 1.33 (ddd, J = 13.0, 9.3, 3.7 Hz, 1H), 0.95 (s, 3H), 0.91 (s, 3H), 0.83 (s, 3H).

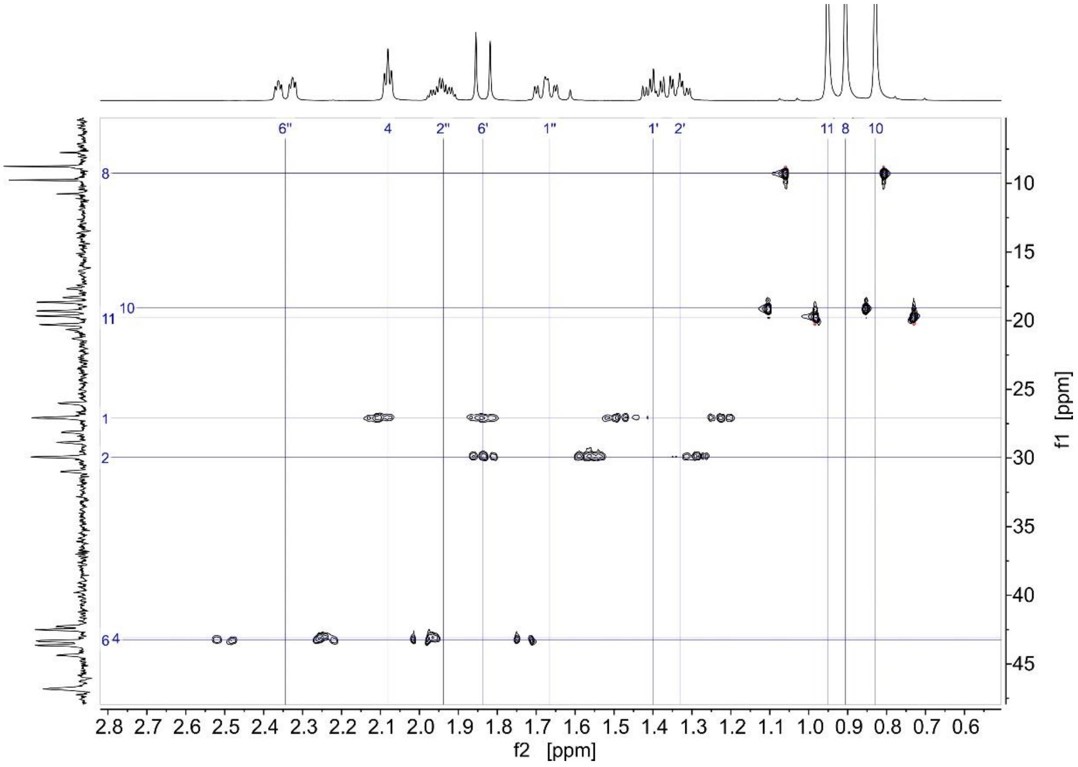

Figure 84: ^{1}H and ^{1}H,^{13}C-HSQC NMR spectra of camphor in CDCl$_3$.

9.4.10.Isotropic NMR spectra of quinuclidinol with assignments

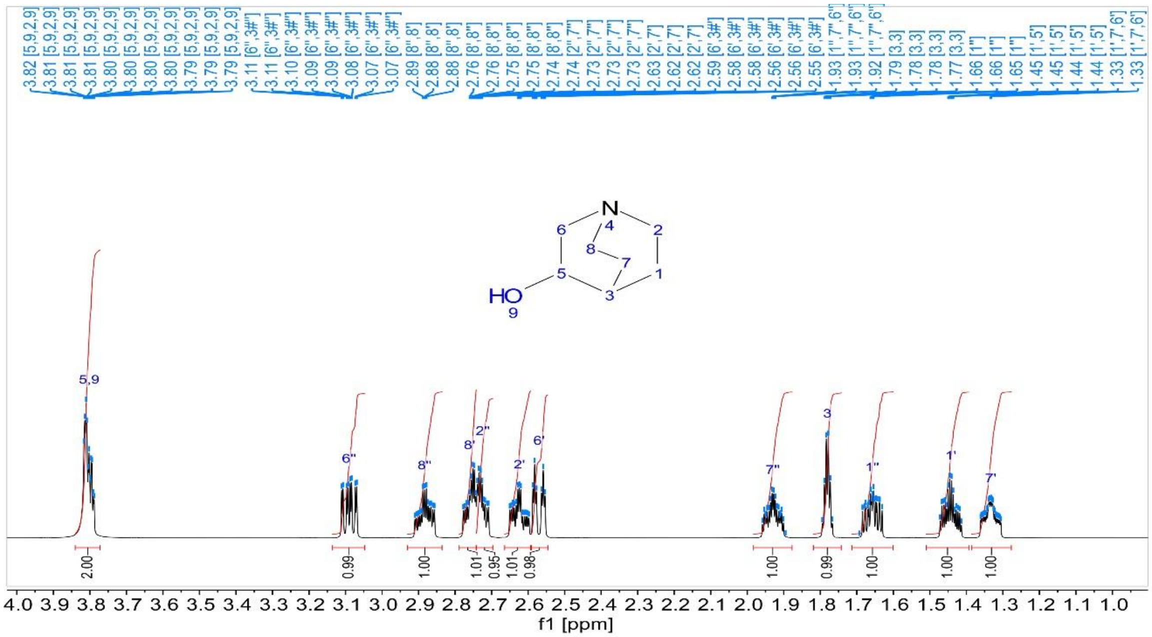

^{1}H NMR (600 MHz, Chloroform-d) δ 3.80 (dtd, J = 8.3, 3.5, 1.4 Hz, 2H), 3.09 (ddd, J = 14.1, 8.4, 2.4 Hz, 1H), 2.88 (dddd, J = 13.2, 10.6, 5.6, 2.5 Hz, 1H), 2.76 (ddt, J = 10.0, 4.8, 2.4 Hz, 1H), 2.72 (ddd, J = 10.2, 5.7, 2.6 Hz, 1H), 2.62 (dddd, J = 13.3, 10.6, 5.0, 2.5 Hz, 1H), 2.57 (dt, J = 14.1, 3.0 Hz, 1H), 1.93 (dddd, J = 15.9, 10.8, 5.6, 3.0 Hz, 1H), 1.78 (h, J = 3.3 Hz, 1H), 1.66 (dddd, J = 14.0, 10.3, 5.0, 3.7 Hz, 1H), 1.44 (dddt, J = 13.3, 10.9, 5.6, 2.8 Hz, 1H), 1.33 (ddddd, J = 13.2, 10.3, 5.6, 2.9, 1.3 Hz, 1H).

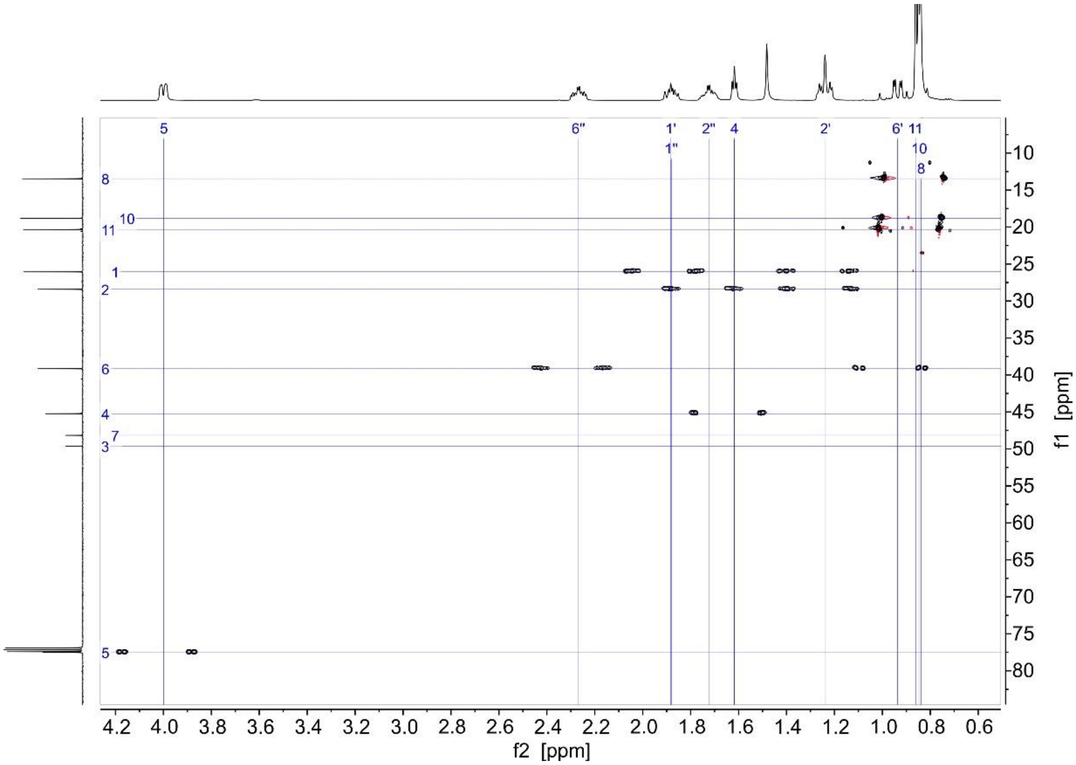

Figure 85: ^{1}H and ^{1}H,^{13}C-HSQC NMR spectra of quinuclidinol in CDCl$_3$.

Acknowledgements

It has been a long, arduous and painful road but it is often in moments of difficulty and trials that beautiful stories are written. During this long journey, I was lucky to have the help and support from many people. Writing a thesis is both a lonely task requiring much sacrifices but also teamwork where everyone has a part to play.

As such, I particularly would like to thank **Dr. Trixie Wagner**, Director of GDC AX Novartis, who - after asking her for new challenges - not only suggested but also gave me the opportunity to successfully complete my doctoral period while working. This proved to be the biggest challenge I could have wished for. I would like to extend my thanks to **Dr. Stephen Martin** and **Dr. John Hastewell**, for supporting this decision.

I would like to express my appreciation for **Prof. Dr. Burkhard Luy**, for the honour and trust confided in me by welcoming me into his laboratory in Karlsruhe Institute of Technology while I left the academic world seven years ago. Our scientific discussions have been interesting, rewarding and fulfilling.

I would like to express my special appreciation to **Dr. Pavleta Tzvetkova** for the extensive support and the time taken to guide, teach and supervise me during my thesis and also for carefully reading this thesis. All her advices and time spent with me have been very precious.

Dr. Alvar Gossert deserves particular mentioning. Despite his new professional activities in the last years of my PhD, he has managed to keep a watchful eye on my work. His ongoing support and faultless observations have helped me through the completion of my thesis.

I extend my deepest gratitude to **Dr. Andreas Lingel** who has been by my side during the last years of the writing and finalisation of my thesis. His precious scientific advices, his patience and his time taken to correct my work have contributed in the successful completion of my thesis. I believe he didn’t become my manager by accident, he has been a catalyst with my work and kept me motivated, helping me carry out this challenging project.

Someone else who didn’t enter in my life accidentally is **Mrs. Zeynep Jaggi**, a most amazing English teacher who became my friend. I would like to thank Zeynep for her help and moral support throughout writing my thesis over the last year. She kept me motivated all the time and helped me a lot in the writing of this thesis, in my time management and improving my English.

I am also grateful to the entirety of the Novartis GDC team, for being so thorough and, for their continued support and encouragement. Thanks also to the AK Bulu team from KIT, and everyone else who collaborated for the scientific research completed. I have had the pleasure to work with them during this project:

- **Dr. Alvar Gossert**, **Dr. Axel Meissner** and **Dr. Andreas Lingel** for their mentoring.
- **Armin Widmer**, **Dr. Konstantin Klenin** and **Dr. Ivan Kondov** for the molecular dynamics simulations.
- **Dr. Ulrich Sternberg**, **Dr. Sebastien Ehni**, **Thomas Gloge** and **Dr. Pavleta Tzvetkova** for their help and advice for the use of COSMOS.
- **Dr. Armando Navarro-Vázquez** for the program MSpin.
- **Muhammet Ali Sağer** and **Matthias Brechbuehl** for the technical help and work on the stretching and swelling devices. **Berthold Grundwald** for his advice about the rotating shaker.
- **Dr. Ina Dix**, **Philippe Piechon** and **Dr. Trixie Wagne**r for the crystallization and the X-ray results of my compounds.
- **Dr. Philippe Lesot** for his advice concerning PBLG.
- **Alexandre Luneau**, **Dr. Mustafa Sağer** and **Hasan Sağer** for their amazing scripts which allow me to gain time and avoid repetitive tasks.
- **Dr. Sebastien Ehni** and **Dr. Pavleta Tzvetkova** for the MatLab and Mathematica scripts without them the processing of my data would have been arduous.
- **Frank Ehret** for his help with Photoshop.
- Novartis compound archive for the nice molecules on which I worked.
- The entire Analytics group (GDC AX) in Novartis for their help, support, measurements and the opportunity to work on the different spectrometers.
- A special thanks to the Chemical Biology & Therapeutics group in Novartis (CBT) allowing me to work on the 800 MHz NMR spectrometer, a real gem.
- **Pinar Sancar**, **Janine Moritz**, **Dr. Pavleta Tzvetkova** and **Dr. PD. Claudia Mulhe** for their support in the administrative part of this PhD.
- **Hacer Sağer** for her valuable help and support over the final weeks of my thesis and the abbreviations list.

- **Dr. Andreas Lingel**, **Dr. Pavleta Tzvetkova**, **Prof. Dr. Burkhard Luy**, **Zeynep Jaggi**, **Sabah Alloui Imaaingfen**, **Aziza Imaaingfen** and **Alexander Smith** for their corrections and advice on English writing throughout my PhD thesis. A special thanks to **Dr. Manuel Koller** and **Renate Moser** for the help with the translation of my abstract in German.

And last but not least, I want to thank my brothers and sisters, and my whole family and close friends (they are too numerous to be listed here) who showed me huge support, trust, and for their patience. Mevlana (Rumi) is right in saying that "Life is a balance between letting go and holding on", however, finding this balance during these several years has not always been easy: balance between work and study, balance between 4 different countries (France, Switzerland, Germany and Turkey), balance between professional and personal life, balance between different ways to work with different people... Thanks to my family and close friends (especially Sabah) who provided me unconditional love and care to help me complete this adventure. I know I always have my wonderful family and close friends to count on when times are rough. I truly thank all of them.